MATHEMATICAL INVESTIGATIONS OF HEAT AND MASS TRANSFER OF NANOFLUIDS FLOW OVER STRETCHABLE SURFACES WITH RADIATION AND ENTROPY GENERATION

Girma Tafesse Workneh

A Dissertation Submitted to the Department of Applied Mathematics

School of Applied Natural Sciences

Presented in Fulfillment of the Requirement for the Degree of Doctor of Philosophy in Applied Mathematics (Specialization in Computational Fluid Dynamics)

Office of Graduate Studies

Adama Science and Technology University

June, 2024

Adama, Ethiopia

MATHEMATICAL INVESTIGATIONS OF HEAT AND MASS TRANSFER OF NANOFLUIDS FLOW OVER STRETCHABLE SURFACES WITH RADIATION AND ENTROPY GENERATION

Girma Tafesse Workneh

Supervisor: Dr. Mitiku Daba Firdi (Associate Professor)
Co-Supervisor: Dr. Naidu V G (Associate Professor)
Co-Supervisor: Dr. Tekle Gemechu Dinka (Associate Professor)

A Dissertation Submitted to the Department of Applied Mathematics
School of Applied Natural Sciences

Presented in Fulfillment of the Requirement for the Degree of Doctor of Philosophy in Applied Mathematics (Specialization in Computational Fluid Dynamics)

Office of Graduate Studies
Adama Science and Technology University

June, 2024
Adama, Ethiopia

Declaration

I, hereby declare that this dissertation entitled **"Mathematical Investigations of Heat and Mass Transfer of Nanofluids Flow over Stretchable Surfaces with Radiation and Entropy Generation"** is my own, original work. Thus, it has not been submitted to any university for analogous purpose. The references used in this dissertation have been properly recognized through appropriate and correct citations.

Mr. Girma Tafesse Workneh	________________	________________
Name of Student	Signature	Date

Recommendation

We, the supervisors of this dissertation work, hereby certify that we have read and revised the dissertation entitled **"Mathematical Investigations of Heat and Mass Transfer of Nanofluids Flow over Stretchable Surfaces with Radiation and Entropy Generation"** prepared under our guidance by Girma Tafesse submitted in partial fulfillment of the requirements for the degree of Doctor of Philosophy in Applied Mathematics. Therefore, we recommend the submission of dissertation to the department for further review and defense.

Dr. Mitiku Daba Firdi	________________	________________
Supervisor	Signature	Date
Dr. Naidu V G	________________	________________
Co-Supervisor	Signature	Date
Dr. Tekle Gemechu Dinka	________________	________________
Co-Supervisor	Signature	Date

Approval Page

We, hereby certify that the recommendation and suggestion made by the board of examiners are appropriately incorporated into the final version of the dissertation entitled **"Mathematical Investigations by Heat and Mass Transfer of Nanofluids Flow over Stretchable Surfaces with Radiation and Entropy Generation"** by Girma Tafesse.

Dr. Mitiku Daba Firdi Supervisor	____________ Signature	____________ Date
Dr. Naidu V G Co-Spervisor	____________ Signature	____________ Date
Dr. Tekle Gemechu Dinka Co- Supervisor	____________ Signature	____________ Date

We, the undersigned, members of the Board of Examiners for this dissertation open defense by Girma Tafesse have read and evaluated the dissertation entitled **"Mathematical Investigations of Heat and Mass Transfer of Nanofluids Flow over Stretchable Surfaces with Radiation and Entropy Generation"** and examined the candidate during open defense. This is, therefore, to certify that the dissertation is accepted for the fulfillment of the requirements of the degree of Doctor of Philosophy in Applied Mathematics.

____________ Chairperson	____________ Signature	____________ Date
____________ Internal Examiner 1	____________ Signature	____________ Date
____________ Internal Examiner 2	____________ Signature	____________ Date
____________ External Examiner 1	____________ Signature	____________ Date
____________ External Examiner 2	____________ Signature	____________ Date

Finally, approval and acceptance of the dissertation is contingent upon submission of its final copy to the Office of Postgraduate Studies (OPGS) through the candidate's Department Graduate Council (DGC) and the School of Graduate Committee (SGC).

____________ Department Head	____________ Signature	____________ Date
____________ School Dean	____________ Signature	____________ Date
____________ Office of Postgraduate Studies, Dean	____________ Signature	____________ Date

ACKNOWLEDGMENTS

This study would not have been possible without the exceptional support of my supervisor, Dr. Mitiku Daba (PhD, Associate Professor). His excitement, expertise, and remarkable attention in detail have been a source of motivation. It is also my great pleasure to express my sincere gratitude to my co-supervisors Dr. V G Naidu (PhD, Associate Professor) and Dr. Tekle Gemechu (PhD, Associate Professor) for their guidance, support and encouragement throughout the courses and research work.

My appreciation also goes to Adama Science and Technology University (ASTU) for the financial support (Grant No. $ASTU/SP-R/188/22$) and Haramaya University for sponsoring my PhD study at ASTU.

My grateful thanks is extended to the department heads of the Applied Mathematics; Dr. Belay Mitiku and Dr. Mitiku Daba, all instructors and members of the Applied Natural Science School at ASTU, for providing supportive and clear information during my stay. Particularly, the remarks given by Dr. Eba Hindebu and Dr. Feleke Buta play a crucial role in making this dissertation strong, which includes different assumptions. A heartfelt appreciation should also go out to all of the ASTU lab technicians and the secretaries of Applied Mathematics Department.

I am also thankful to all my family members, my classmates, and my friends at Haramaya University (HU), who have supported me financially and psychologically and shown me unending love. To list some from HU, Mathematics Department: Dr. Getachew Teshome (PhD, Associate Professor), Dr. Mekonen Yimam, Dr. Henok Desalegn, Mr. Agegnehu Tesfaye, Mr. Basha Haile, Mr. Zerihun Mekoya, Mr. Dawit Negera and Mr. Negash Tessema (Irrigation Engineering). Their suggestions and supportive ideas make me stronger.

Finally, my special thanks should go to my beloved wife, Aynalem Abera Abebe, my daughter, Nohamin Girma, my son, Elnathan Girma, my father, Tafesse Workneh, and all of my siblings. Sincere gratitude should also be expressed to Mr. Eshetu Amen, his family, and his siblings. In my success, they played a key role.

Dedication

This dissertation work is dedicated to all my family members.

List of Publications

This PhD dissertation contributed the following original papers which were published (to be published) in peer reviewed indexed and Scopus journals.

1. Workneh G. T., Firdi M. D., & Naidu V. G., (2023). Convective heat exchanger from renewable Sun radiation by nanofluids flow in direct absorption solar collectors with entropy. *Frontiers in Heat and Mass Transfer*, 20(1): 1-12.
   DOI: http://dx.doi.org/10.5098/hmt.20.27.

2. Workneh, G. T., Firdi, M. D., & Naidu, V. G. (2023). Heat and Mass Transfer via Flowing Nanofluid on Porous Medium with the Presence of Renewable Solar Radiation and Entropy. (Under review)

3. Workneh, G. T., Firdi, M. D., & Naidu, V. G. (2023). Heat and Mass Transfer by Stirring Nanofluids with the Presence of Renewable Solar Rays, Joule Heating, and Entropy Procreation. *Heliyon*, 9(10).
   https://doi.org/10.1016/j.heliyon.2023.e20053

4. Workneh, G. T., Firdi, M. D., & Naidu, V. G. (2023). Convective Heat Transfer via Slip Moving Nanofluids Across a Porous Medium with Thermal Radiation and Entropy. (Under review)

5. Workneh, G. T. & Firdi, M. D. (2024). Heat and Mass Transfer within Unsteady Nanofluid Movement in the Presence of Sustained Solar Radiation. Accepted in Journal of Nanofluid.

CONTENTS

List of Tables

List of Figures

Nomenclature and Acronym

Nomenclature

B, E	Magnetic and electric fields	Re_x	Local Reynolds number
L	Dimensionless concentration	$\bar{T}$	Temperature
$\bar{C}_\infty$	Ambient concentration	$\bar{T}_\infty$	Ambient temperature
H	Dimensionless temperature	$\bar{C}$	Concentration
V'	Dimensionless velocity	u, v	Velocity components along x & y axis
$\mathbb{L}$	Characteristic length	x, y	Coordinate along the plate
H_f	Heat transfer coefficient	$\mathbf{g}$	Acceleration due to gravity
$\mathbf{J}$	Current density	V_w	Mass propagation at the plate
$\mathbf{v}$	Velocity vector	q_{rd}	Incident radiation flux
	Greek symbols		
β_t	Volumetric thermal expansion	$(\rho c)_p$	Heat capacity of the nanoparticles
β_c	Volumetric concentration expansion	σ_e	Electrical conductivity
ϵ	Similarity variable	ψ	Stream function
τ_h	Heat capacity ratio	μ	Dynamic viscosity
ν	kinematic viscosity	ρ, ρ_p	Density of the fluid and nanoparticles
θ	Angle of inclination	τ, σ	Shear and normal stress
τ_w	Shear wall stress		

Acronym

ADM:	Adomian decomposition method	1D:	One Dimension
CVD:	Chemical vapor deposition	2D:	Two Dimension
DASC:	Direct absorption solar collector	3D:	Three Dimension
HAM:	Homotopy Analysis Method	ODE:	Ordinary differential equation
IDASC:	In Direct absorption solar collector	PDE:	Partial differential equation
IEA:	International Energy Agency	SWP:	Solar Water Pump
MHD:	Magnetohydrodynamics	SPS:	Solar-powered ship
PTSC:	Parabolic trough solar collector	TEC:	Thermoelectric Cooling
SI:	International System	RRT:	Reynolds's Transport Theorem

Abstract

Currently, various industries are utilizing heat and mass transfer techniques involving the flow of fluids and nanofluids. Due to the high thermal conductivity of nanoparticles, nanofluids play a crucial role in heat and mass transfer processes. Electrically conducting nanofluids flowing over a stretchable, permeable surface demonstrate superior performance in heat and mass transfer. The Darcy and Darcy-Forchheimer laws were applied to understand the impact of porous media. The characteristics of nanofluids were examined using the Buongiorno and Tiwari-Das flow models. Heat from the Sun is transferred by radiation, which does not require a transmission medium. Solar radiation can be described using Rosseland's approximation and Beer's law. Hence, this dissertation focuses on exploring the role of unsteady, viscous nanofluid flow over an expandable surface in relation to heat and mass transfer through radiation and entropy generation. Using conservation laws, the governing non-linear partial differential equations were derived, and simplified based on boundary layer approximations. These equations were then transformed into systems of ordinary differential equations using similarity transformations. Convective heat transfer, velocity slip, and mass suction were incorporated as boundary conditions, and solved using the Homotopy Analysis Method on Mathematica and numerically on MATLAB. Comparisons with previously published articles confirm the applicability of these methods. The influence of parameters on dimensionless velocity, temperature, concentration, entropy, Bejan number, skin friction coefficient, and Nusselt and Sherwood numbers were presented graphically and in tables. The magnetic field and porosity parameters slowed the flow while improving temperature, concentration, and drag force formation. Solar radiation, heat sources, thermophoresis, Eckert, and Biot numbers increased the nanofluid's temperature. The Grashof number increased the flow and concentration of the nanofluid. The nanofluid's velocity, as well as the local Nusselt and Sherwood numbers, rose when the surface changed from horizontal to vertical. Increasing the unsteadiness and absorption parameters lowered the nanofluid's temperature. Low entropy generation occurred with increased velocity slip and mass suction parameters, while high drag forces slowed the flow. More entropy was generated with higher temperature distributions.

Keywords: Heat Transfer; Nanofluid; Radiation; Homotopy Analysis Method; Entropy.

CHAPTER ONE

Introduction

1.1 Background of the Study

1.1.1 Heat Transfer

Heat is a form of energy that is transferred from one body or system to another because of the temperature variation between the two bodies. We can not see heat but we can felt it by the effect of hotness it produces. In general, heat transfer is defined as the convey of heat from a hot body to a cooler body which is dominant in direct solar, geothermal and biomass sources (Twidell, 2021). In the branch of engineering, heat transfer deals with the convey of thermal energy with in/out of a medium due to a temperature difference. Thus, the main driving force for heat transfer is temperature difference. Conduction, convection, and radiation are the three basic modes of heat transfer. They can be observed in different states of matter, practically. For examples:

- In solids, heat is transferred from one point to another through conduction,
- In liquids and gases, heat transfer takes place by convection and
- In an empty space or vacuum heat is transferred by radiation.

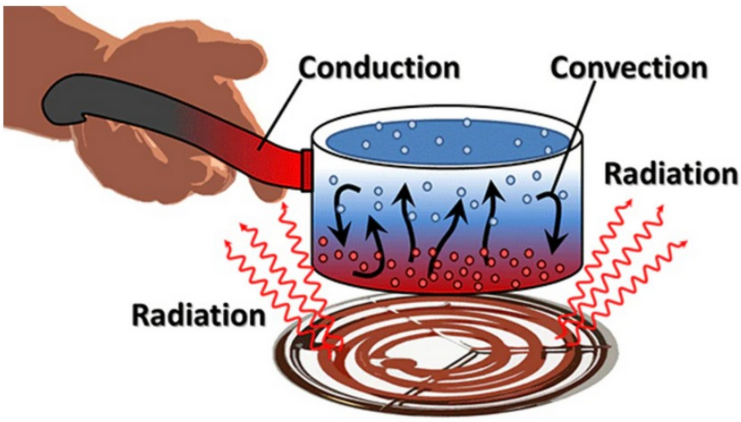

Figure 1.1.1: Three modes of heat transfer from www.theengineeringconcepts.com

Figure 1.1.1 illustrates how these three kinds of heat transfer happen. There are brief explanations regarding these basic heat transfer mechanisms from Welty et al. (2014).

1. **Conduction heat transfer** is the process in which the transfer of heat takes place within the medium due to diffusion process. So, it is the transfer of heat from the hot to cold by contact without the actual movement of the particles. For heat conduction occur, there must be temperature variations between neighboring points. Fourier's law states that heat flow is proportional to the temperature gradient and the governed equation is

$$\frac{q_x}{Ar} = -k\frac{dT}{dx}, \tag{1.1.1}$$

where q_x (W) is heat-transfer rate in the x direction, Ar (m^2) is the area normal to the direction of heat flow, dT/dx (K/m) is the temperature gradient in the x direction, and k ($W/(mK)$) is the thermal conductivity, which is the transportation of energy due to the random movement of molecules across the temperature gradient. It measures the material's ability to conduct heat. The negative sign in equation (1.1.1) indicates that heat flows towards temperature gradient.

2. **Convection heat transfer** is the process in which heat is transferred from one place to another by the actual movement of heated particles. As a result of fluid motion, convection allows more heat transfer than conduction which used stationary fluid for transferring heat.

   There are two types of convective heat transfer. Those are free (natural) and forced convective heat transfer. The formation of fluid movement above the surface due to the temperature difference between the fluid and any hot plate is called free convection. This leads to form buoyancy as a result of density gradient between the layers of fluid above the surface (Boujelbene et al., 2023). Thus, in free convection, the heat flow occurs naturally from hot to cold. In forced convection, the fluid moves across a surface by an external agency like pressure difference, pump or wind, with out depending on the heat transfer.

   In practice, the phenomena of convective heat transfer is partial forced and partial free, but one process usually dominates (Twidell, 2021). The convective heat transfer between two different media is governed by Newton's law of cooling which states that the heat flow is proportional to the difference of temperatures in two media. Mathematically it is formulated as

$$\frac{q_x}{Ar} = h\Delta T, \tag{1.1.2}$$

where q (Watt) is the rate of convective heat transfer, ΔT is the temperature difference between surface and fluid, and $h(W/Km^2)$ is the convective heat transfer coefficient. It is applicable in engineering and industry for heating and cooling process, energy production, heat exchanger and cooling of nuclear reactant.

3. **Radiation** is an electromagnetic mechanism, which allows energy transport with the speed of light through regions of space that are devoid of any matter. So, it is the process in which heat is transmitted from one place to another directly without intervening medium. Some characteristics of radiation are

   - The presence of matter is not required for effective radiant heat transfer. Thus, it occurs through electromagnetic waves without having particles.
   - Cloud cover is observed to reduce maximum daytime temperatures and to increase minimum evening temperature.
   - The color of incandescent objects is changed with temperature which is very important in determining the radiant-energy exchange between bodies .

   Radiant energy exchange takes place between surface/region and its surroundings. This relationship is described by the Stefan Boltzmann law. It states that the radiant energy transmitted is proportional to the fourth power of the surface's temperature. Rate of energy emission from a perfect radiator (black body) is:

   $$\frac{q_r}{Ar} = \sigma^* \bar{T}^4, \tag{1.1.3}$$

   where q_r is the rate of radiant energy emission, in W, and σ^* is the Stefan Boltzmann constant in $W/(m^2K^4)$.

The energy transfer by radiation is maximum when the two heat exchanger surfaces are separated by a perfect vacuum. Both convective heat transfer and electromagnetic radiation are necessary for high-temperature processes found in combustion engines, nuclear power generation, heating and cooling systems (Boujelbene et al., 2023).

In general, radiation travels at the speed of light, having both wave properties and particle like characters. The radiation between wavelengths of 0.1 and 100 microns (0.1×10^{-6} and 100×10^{-6}) is termed as thermal radiation. The incident thermal radiation upon a surface as shown in Figure 1.1.2 may be either absorbed, reflected or transmitted. If r, a, and t are the fractions of incident radiation that are reflected,

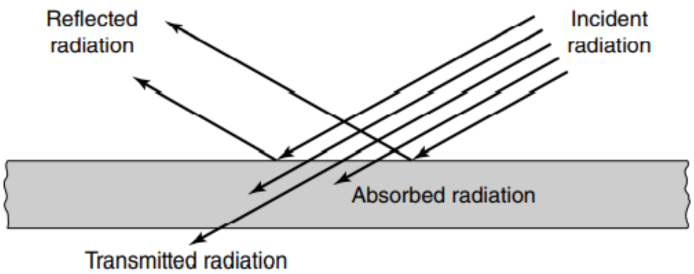

Figure 1.1.2: Chance of radiation incident upon a surface (Welty et al., 2014).

absorbed, and transmitted, respectively, then (Welty et al., 2014)

$$r + a + t = 1. \tag{1.1.4}$$

For most solids, the transmissivity (t) is zero, and is called opaque to thermal radiation. For opaque body, $r + a = 1$ from equation (1.1.4). Ideally absorbing body, for which $a = 1$, is called a black body which neither reflects nor transmits thermal radiation.

In an optically thick medium, it is possible to express the radiative energy by a diffusion relation similar to that of heat conduction. In this medium, the radiation travels only a short distance before being scattered or absorbed. Due to this, energy transfer depends only on the conditions in the immediate vicinity of position. Therefore, the diffusion approximation provides a substantial simplification for standard techniques such as finite difference schemes for solving the radiative diffusion differential equation. Hence, in the interior of an optically thick medium with small temperature gradients, the intensity is nearly isotropic, which is important for diffusion approximation. Thus, the Rosseland diffusion approximation for grey medium in 1D simplifies the total radiative flux with $\boldsymbol{D}$ is optical thickness in the following manner (Howell et al., 2020).

$$q(X) = -\frac{4\sigma^*}{3\boldsymbol{D}(X)}\frac{d\bar{T}^4}{dX} = -\frac{16\sigma^*\bar{T}^3}{3\boldsymbol{D}(X)}\frac{d\bar{T}}{dX}. \tag{1.1.5}$$

1.1.2 Applications and Models of Nanofluid Flow

Fluid is a class of idealized materials that cannot sustain any shearing stresses during the motion of a rigid body (including the state of rest). The inability of fluids to stand shearing stresses without continuously deforming is one of the distinctions between fluids and solids. There are different kinds of fluids, such as compressible/incompressible, steady/unsteady flow, viscous, Newtonian, and non-Newtonian (Lai et al., 2009).

Mixing nanoparticles whose size is between 1 and 100 nanometers (1-100 nm) with convectional fluid is called nanofluid. The nanoparticles are made up of metals ($Cu, Ag, Al,\ Fe, Au$), metallic oxides (Al_2O_3, Fe_2O_3, CuO) and carbonates ($CNTS$, $MWCNT$). Examples of convectional fluids are water, ethanol, oil, toluene, ethylene, kerosin oil and glycol. The idea of nanofluid was first coined by Choi and Eastman (1995). They presented thermo-physical features of nanofluids, such as thermal conductivity, thermal diffusivity, viscosity, and convective heat-transfer coefficients. Accordingly, nanofluid amended these thermophysical characteristics. Currently, nanofluids are more applicable in water heaters, solar gathering, cooling systems, absorption refrigeration systems, solar cells, and a combination of various solar devices than the base fluids (Elsheikh et al., 2018). Due to the merits of nanofluids, they are highly applicable in heat transfer processes. The applications nanofluids can be summarized in the following three fields.

- **In industries:** controlling heat transfer valves, cooling pipe and the radiator temperature of vehicles, oil industry, nuclear energy, coolant, lubricant, heat exchanger, micro-channel, chemical process, microelectronic, avoiding heat from the computer processor and drying process.

- **Bio-medicine:** disease diagnosis, heart surgery, cancer treatment, drug dispersal, antimicrobial treatments, pharmaceutical, food processing, blood circulation system in our body, sensing and imaging.

- **Engineering:** heating and cooling system, thermal extraction, improvement of solar system, transportation, air ventilation, agricultural, power plant, storing solar energy, astronautic, aerodynamic and geothermal energy.

As it can be explained above, nanofluids have a key role in heat and mass transfer in various fields. Thus, it is important to analyze the behaviour of nanofluids in order to elaborate their function, particularly concerning the transformation of heat from renewable solar energy. For this, Buongiorno (2006) introduced the two main slip mechanisms out of seven that describe the movement of nanoparticles inside the nanofluids. These are Brownian diffusion and thermophoresis, which are included in the energy equation. Due to these slip mechanisms, Buongiorno considered nanofluids as a two-phase model. Those are small solid particles and fluids in which they have a role in heat transfer separately. But, Tiwari and Das (2007) proposed a single-phase model first in which the nanofluid is more likely fluid due to tiny solid particles. Hence, in a one-phase model, both the nanoparticles and convectional fluid are in thermal equilibrium and have similar local velocities. Even though both models are employed to study the characteristics of nanofluids, each has benefits and drawbacks.

1.1.3 Flow of Magnetic Nanofluid over Porous Medium

Electrically conducting nanofluids flowing over a permeable sheet enhances the heat transfer system. In fact, magnetohydrodynamics (MHD) is the study of electrically conducting fluid under the impact of magnetic field. For instance salt water, electrolyte, liquid metal and plasma are considered as MHD fluid. An electrically conducting fluid induces an electric current and consequently polarize the materials. Some applications of MHD are boundary layer controller of aerodynamics, electrostatic filter, MHD accelerators, sensor, raidioactive reactors, crystal intensification, chemotherapy treatment, tumor analysis and therapy, star formation, X-ray radiation, power generation from solar and wind, design of heat exchangers, electrolytes, fusion and fission reactions, etc (Khan et al., 2022b; Reddy et al., 2022). In MHD, there is a mutual interaction between magnetic flux and electrically conducting nanofluids. This process can produce excessive heat in moving nanofluid either due to applied magnetic force or electric current. This excessive heat is referred as Joule heating (Swain et al., 2020). It can be observed in electric heater and iron.

Furthermore, various scholars investigated that the nanofluids movement on porous surface has a possibility to improve the heat transfer process. A porous media is a solid substance having sufficient open space in which nanofluids enable to pass through it. For example, rocks, soils, cements, sandstone, limestone, beach sand, human lung, ceramics, bones, woods and corks are considered as a porous media. In fact, porosity refers to the amount of void space within a given material and it is the volume fraction of the void space over the whole volume. As Mahdi et al. (2015) state, a permeable surface has large dissipation area and irregular movement of fluid around the distinct drops. These are the two vital merits which make the surface to transfer more heat. Hence, the contact between small-sized solid particles and fluid occur highly in porous sheet which yields a high heat transfer due to more expansion of nanoparticles. The result of this phenomena enhances thermal conductivity (Siavashi et al., 2021).

According to Noghrehabadi et al. (2013), there are two drag forces that resist the movement of nanofluid across permeable surface. Those are

1. **The linear form of Darcy law:** In this, only the surface drag forces considered and called classical Darcy law. It is limited for slow movement of nanofluid or low Reynolds number ($Re < 1$) to observe the effect of porosity. Classical Darcy law is applicable when there is a direct relation between flow rate and pressure gradient (Takhanov, 2011). Hence, the flow is linearly dependent upon the pressure gradient without inertia. Mathematically, it can be expressed as

$$\nabla P = -\frac{\mu \mathbf{v}}{k_p}, \tag{1.1.6}$$

where ∇P is the pressure gradient and $\mathbf{v}$ is velocity of the nanofluid.

2. **The drag form by solid impede force which Darcy law disregards:** In this case, the pressure drop is considered due to the form drag, which was neglected by Darcy. This is true especially when the nanofluid moves quickly, having high Reynolds number and flow on highly permeable surface (Charreh et al., 2023). As a result of the inertial and boundary impact, the Darcy's law can be modified by the Darcy-Forchheimer which account for the influence of inertial in terms of a quadratic velocity under the momentum equation (Khan et al., 2022b). In this way, Forchheimer extends the Darcy law in equation (1.1.6) as follows:

$$\nabla P = -\frac{\mu \mathbf{v}}{k_p} - \frac{F_d}{\sqrt{k_p}}\rho_l |\mathbf{v}|\mathbf{v}, \tag{1.1.7}$$

where F_d is a dimensionless form drag constant, and ρ_l is the fluid density.

Modeling the porous surface by Darcy-Forchheimer is applicable in scientific fields like atomic waste archive, artificial dialysis, catalytic converters, gas turbine, improved oil recuperation, atherosclerosis, grain stockpiling, geo-energy production, and warm protection designing (Khan et al., 2022b). Generally, nanofluid moving on porous media have many applications in hydrology, agriculture, civil, petroleum engineering, environmental and industrial systems such as designing heat exchange, catalytic reactors, fermentation processes, grain storage, groundwater pollution, movement of water in reservoirs, crude oil production, geothermal energy, ground water and recovery systems as explained by Hayat et al. (2016a, 2017a); Seth and Mandal (2018).

1.1.4 Mass Transfer

Mass transfer in a system happens when there is a difference in concentration of two or more components at various points. In this case, there is a natural tendency for mass to be transported due to a driving force such as concentration, temperature or pressure gradients. Thus, mass transfer is defined as the transport of one constituent from a region of higher concentration to that of a lower concentrations. Apart from this, if there is no concentration gradient, then equilibrium of mass transfer will occur. In real life, the mass transfer is observed practically, in the following manner.

- A cup of tea dissolved sugar and diffuses uniformly throughout the tea.
- Due to the evaporation of water from lakes or ponds, increases the humidity of the passing air stream.
- Considering perfume that diffuses throughout the surrounding atmosphere.

Mass transfer is fundamental for biological process which includes oxygenated blood and the transport of ions across membranes within the kidney and chemical processes such as the chemical vapor deposition (CVD) of silane (SiH_4) onto a silicon wafer, the doping of a silicon wafer to form a semiconducting thin film, the aeration of wastewater and the purification of ores and isotopes. Furthermore, mass transfer is applied on various chemical separation processes. Baehr and Stephan (2011) pointed out that the mass transfer processes have many applications in various ways on both natural and technological industries.

Mass can be transferred via two different methods. One is by random molecular motion in quiescent (inactive) fluids which is called molecular mass transfer. The second one is when the mass transferred from a surface into a moving fluid, by the aid of dynamic characteristics of the flow which is called convective mass transfer. These molecular and convective modes of mass transport are analogous to conduction and convective heat transfer respectively. Even if, the two modes of mass transfers occur simultaneously, one mechanism can dominate quantitatively. Thus, the dominate one is used to approximate the solutions of assumed problem (Welty et al., 2014).

1.1.5 Stretchable Surface

A substance that can be stretched or extended without breaking or irreversibly deforming referred as a stretchable surface. The time dependent fluid flow across a stretching sheet in engineering problem has an essential applications in industries. As an example, melt-spinning, polymer extrusion, continuous casting, manufacturing plastic film, tinning of copper wires, crystal growth, a polymer sheet, wire drawing, glass-fiber production, rubber sheets and cooling of a large metallic plate in a bath are some of the applications (Haile and Shankar, 2014; Khan et al., 2022d). Moreover, Khan et al. (2022d) explained the importance of heat transfer toward cooling of a machine tool, pasteurization of food and heat treatment on stretchable surface. In addition, utilizing heat transfer instruments such as heat swaps, desiccation, condensers, boilers and heat sinks, the chemical reactions are started by controlling temperature or furnaces in industries (Khan et al., 2022d). Stretchable surface also used to collect and convert energy from the Sun or other sources. In general, the surface of materials that have an ability to expand is considered a stretchable surface such as stretch fabric, electronic and expandable metals film (Mechael et al., 2018).

1.1.6 Solar Collectors and Thermal Radiation

It is difficult to use the total energy that is obtained from the Sun. A part of sunlight converted into heat when it is absorbed by an object or a surface is known as solar thermal radiation. It is an essential source of heat in the climate, oceans and ecological system. Solar radiation is an important form of power in gas turbines, nuclear power plants and thermal energy storage (Boujelbene et al., 2023). In industrial and residential, desalination systems, air heaters, solar water heating and dryers are the applications of solar (Tabarhoseini and Sheikholeslami, 2022).

Hence, collecting solar radiation adequately, increases the supply of energy. A device used to collect and/or concentrate solar radiation from the Sun is called a solar collector. In fact, many scientists focused their attention toward upgrading the efficient way of collecting and using solar radiation. Bhalla and Tyagi (2018) stated that there are two methods of gathering solar radiation.

1. **Solar photovoltaic cells:** Using semiconductor cell, these mechanism alter energy from the Sun into electric power directly by solar panels and produce electricity (Al-Waeli et al., 2017; Sathe and Dhoble, 2017).

2. **Solar thermal collectors:** In these, the solar energy induce electricity after bringing it into mechanical energy. Solar thermal collectors used to heat air, water or other fluids (Gorji and Ranjbar, 2017).

Bhalla and Tyagi (2018) also noted that practically the solar thermal collectors have greater potential of harvesting the Sun's radiation than solar photovoltaic cell. The solar thermal collector can be classified as concentrated, which gives energy from the solar radiation via transport medium, and non-concentrated solar collector where the energy is used directly for industry, equipment for washing air, controlling humidity, endemic water and solar space heating (Gorji and Ranjbar, 2017).

The two kinds of solar collectors are indirect absorption solar collector (IASC) and direct absorption solar collectors (DASC). IASC uses working fluid to convert heat energy from solar into another form of energy. However, it is not suitable to collect more solar radiation like DASC. In DASC, there is a straight relationship between the Sun's radiation and the transport medium without any interface. As a result, the loss of solar energy by convection and conduction detracts (Dugaria et al., 2018). Since there is no plate that takes the solar radiation.

The ultimate need of people in the world mostly accomplished by applying energy and thus, the role of energy has been uncountable in our day to day activities. Practically, this energy is obtained from limited source called non-renewable energy such as coal, fossil fuels, natural gas, oil, and nuclear energy which cause a problem on environmental conditions with less in amount and high cost of power (Ikram, 2021). Based on the Central Statistics Office report (Statistics, 2016) in India, the usage of non-renewable energy in many industries, convey system, residential, agricultural and educational sectors are increasing from time to time. In this kind of utilization, there have been a bulky amount of carbon dioxide emitted which leads to alter the existing climate and cause global warming (Szulejko et al., 2017). For the last 10 years, more heat was captured in lower part of the Earth's atmosphere by the occurrence of CO_2 and other air pollutants in the atmosphere. This leads to the global warming which is usually recognized as the greenhouse effect that make the planet extremely warm (Jamshed et al., 2021a).

Thus, increasing the utilization of fossil fuels resulted in several environmental impact such as air pollution, acid rain, ozone layer depletion, and global climate change. A tangible reason for these phenomena is the effect of global warming that make extreme weather conditions such as hurricanes, flooding, droughts, heat waves, etc. Gorji and Ranjbar (2017). These challenges are rising from time to time as a result of the growth in energy demand, global economic and population number. Hence, it is a crucial work to find viable, clean and unlimited power sources called renewable energy because of uprising of the Earth's temperature and power demand.

The energy that can be acquired from nature in recurrence manner, and occurring in consistence with out affecting the climate called renewable energy. For instance, solar, wind, wave, tidal, nuclear, water, biomass and geothermal considered as renewable energy (Tiwari and Mishra, 2012; Everett et al., 2012). Because of limited resources and high cost observed in fossil fuels, scientists paid attention and devoted their research work towards renewable energy resources. However, requiring high initial cost, hard to produce large amount, need wide area on the Earth, and consistence on supplement are some demerits in the implementation renewable energy (Bhalla and Tyagi, 2018). Owing to the advantage of renewable energy, today researchers attracted towards it for deprecating the world's climate change and economic problems.

Among different kinds of renewable energy, solar is the one which is inconstant, unlimited, free from air pollutant, occurring repeatedly and obtained everyplace in abundant on the Earth. These properties of solar improves energy availability, environmental suitability and power sustainability. It is a kind of electromagnetic wave emitted by the Sun in large amount for thermonuclear activities (Boujelbene et al., 2023). The Earth's surface gained approximately $3,400,000EJ$ solar radiation in one year which is more than 7500 times the world's total annual primary energy consumption of $450EJ$ (Gorji and Ranjbar, 2017). Thus, solar power is more preferable to satisfy the need of current and planned energy for different activities. It is applicable for cooking, water heating and electricity producing.

1.1.7 Entropy

Entropy is the measure of randomness or disorder of particles. The value of entropy changes based on the amount of existing substances. This implies that entropy has the extensive property of a thermodynamic systems. The SI units of entropy is Joule per Kelvin (J/K). Thus, smaller entropy means the system is highly ordered. It is the hottest issue relating to the analysis of heat transfer and designing the minimum production based on the second law of thermodynamics. Bejan (1996) was a beginner on the concept of entropy. As Tyagi et al. (2007) stated, the production of irreversibility leads to a decrease in existing work.

The idea of entropy is analyzed by thermodynamic second law. According to the Biswal and Basak (2017) discussion, energy loss due to irreversibility is evaluated by the second law of thermodynamics, which explains the entropy generation. Since the first law of thermodynamic does not give enough information to identify whether the existing energy is used efficiently or not. Thus, based on the second law of thermodynamics, the total entropy of an isolated system either remains constant or increases (Jameel et al., 2023). The maximum achievable efficiency of energy is reduced by the loss of exergy which is proportional to entropy generation. In any system, exergy is defined as the ideal maximum amount of usable energy (Bayrak et al., 2017). Moreover, the idea of entropy generation has been used for different flow frames like pipe flow, boundary layer over a flat plate, single cylinder in cross-flow, and flow in the entrance region of a flat rectangular duct based on thermodynamics second law (Bejan, 1979).

1.2 Statement of the Problem

Currently, the biggest challenges faced in the world are global warming and energy supply deficiency, which are caused by using non-renewable energy sources (fuels, coal). One means of reducing these problems is by finding alternative energy sources such as solar, wind, and water that are sustainable, renewable and environmental friendship.

Due to the use of solar energy, different scholars pay attention to analyze the efficient way of collecting and transforming solar thermal radiation by nanofluids flow across stretchable surface. For instance, Elsheikh et al. (2018) concluded that using nanofluid as a working fluid enhances heat transfer in the solar energy system. The cause of heat exploration from renewable Sun's radiation in parabolic trough solar collector (PTSC) through Maxwell nanofluid was examined by Jamshed et al. (2021a) using Keller box technique. Jamshed et al. (2021a) critically analyzed the viscous Prandtl-Eyring hybrid nanofuid over porous media to improve Solar Water Pump (SWP) production. Alkathiri et al. (2022) also elaborated this idea using Galerkin finite element. Seethamahalakshmi et al. (2023) study unsteady flowing nanofluid over porous media employing finite difference method. Considering permeable surface, Jyothi and Avula Golla (2023) used Non-Newtonian fluid for solar energy application and Hussain and Sheremet (2023) took radiative nanofluid flow with slanted magnetic field.

In heat transfer process, there is a loss of energy as a result of irreversibility process which is measured by entropy. Different authors examined the generation of entropy on various kinds of nanofluids. As an evidence, entropy analysis in MHD flow of nanofluid with effects of thermal radiation, viscous dissipation and chemical reaction was studied by Daniel et al. (2017) and solved numerically. Aziz et al. (2018) analyzed the entropy in terms of Mathematical model for thermal solar collectors using Maxwell nanofluids and solved by Keller box method. Tabarhoseini and Sheikholeslami (2022) explained the entropy generation and thermal analysis of nanofluid flow inside the evacuated tube solar collector. Entropy is examined based on property of random and thermophoresis motion by Khan et al. (2022a) for unsteady flow of Prandtl nanofuid. Khan et al. (2022b) studied entropy generation in highly porous media.

Based on the latest research work, there was little information on the Mathematical analysis of heat and mass transfer via unsteady moving viscous nanofluid over a stretchable surface using a semi-analytic approach. Thus, the researchers aspired to look at the transfer of heat and mass when the Sun's radiation directly touches the unsteady, viscous, moving nanofluid over an expandable surface. The problems were solved by the Homotopy Analysis Method (HAM) and compared with a numerical approach. In line with this, the following specific problems have been addressed in this dissertation:

(i) Convective heat exchanger from renewable Sun's radiation through nanofluids flow in direct absorption solar collectors (DASC) with entropy generation.

(ii) Heat and mass transfer via nanofluid flow on porous medium in the presence of a renewable solar radiation with entropy.

(iii) Heat and mass transfer by stirring nanofluids with the presence of renewable solar rays, Joule heating, and entropy generation.

(iv) Convective heat transfer via slip moving nanofluids across a porous medium with thermal radiation and entropy.

(v) Heat and mass transfer within unsteady nanofluid flow in the presence of sustained solar radiation.

1.3 Objectives of the Study

1.3.1 General Objective

The objective of this dissertation is to analyze mathematically the heat and mass transfer of unsteady viscous nanofluid flow over a stretchable surface by radiation with entropy generation.

1.3.2 Specific Objectives

The specific objectives of this dissertations are to

1. formulate the mathematical model for each of the above specific problems from the governing equations.

2. simplify the derived PDEs by applying the concept of boundary layer and Boussinesq approximations.

3. develop ODEs from governing simplified PDEs by using suitable similarity transformation.

4. solve the problems by using the semi-analytic approach (HAM) and numerical technique.

5. identify the impact of potential parameters generated during the non-dimensional process on velocity, temperature, concentration, entropy, local skin friction coefficient, local Nusselt and Sherwood numbers.

1.4 Significance of the Study

Generally, the unsteady flowing nanofluid over a stretchable surface has an advantage in enhancing the heat and mass transfer from solar thermal radiation and another heat sources. This process contributes to supplying energy by reducing the problem caused by using fuels. Thus, this dissertation has the following specific significance.

- It initiates the scholars to think on the practical use of solar radiation as an alternative power source.
- It provides information for the scientific community about nanofluids.
- It has a role in the development of science and technology regarding the heat and mass transfer by radiation, considering flowing nanofluids.
- It is a means of obtaining published articles in reputable journals.
- The dissertation work is used as a reference for further study.

1.5 Organization of the Dissertation

This dissertation is classified into eight chapters with five research articles. The general points of this work were discussed in the first three chapters. Hence, chapter ONE includes a brief description of the dissertation in a background of the study, a statement of the problem, objectives, significance and organization of this dissertation. Summarized literature has been presented in chapter TWO. Approaches used in this dissertation are discussed under methodology (chapter THREE).

Chapter FOUR, includes the first problem. Its extension is presented in Chapter FIVE as a second problem. Chapter SIX discusses the third problem that the researchers needed to address. The fourth problem is included in chapter SEVEN. From chapters 4 to 7, the impact of potential parameters on velocity, temperature, concentration, entropy, skin friction, Nusselt, and Sherwood numbers is displayed in graphical and tabular form by applying Buongiorno's model using HAM.

Chapter EIGHT is presented which is the fifth problem by applying the Tiwari-Das and Darcy-Forchheimer models, and solved by Numerical method using fourth order Runge Kutta with shooting scheme. Then, the conclusions and recommendations are made. At the end, there were references and appendices.

CHAPTER TWO

Review of the Related Literature

In this chapter, the researchers summarize different recent studies relating to heat and mass transfer analysis of a moving nanofluid in the presence of solar thermal radiation with entropy generation. They are important for indicating the research gap.

2.1 Heat and Mass Transfer by Nanofluid Flow

The existence of small sized particles (1-100 nm) called nanoparticles in the host fluid like water referred as nanofluid. These solid particles have better performance in heat transfer process since they have high thermal conductivity. Because of this, the less performance of convectional fluids toward heat transfer have been enhanced by mixing the nanoparticles with them which form nanofluids. Due to the properties of nanofluids, currently numerous scholars pay attention toward the application of nanofluids as a working fluid. Some of the studies which focus on the application of moving nanofluids with respect to heat and mass transfer are explained in the following manner.

Pang et al. (2015) revised the properties of nanofluid in both mass and heat transfer system. They concluded that, the application of nanofluids increased exponentially. Besides, from the two methods (one-step and two-step) of nanofluid preparations, the two-step approach is mostly applicable in laboratories. The thermal conductivity, convective, boiling and mechanism of heat transfer have been explained. Accordingly, the thermal conductivity of nanofluids depend on temperature, concentration, material, shape and size of nanoparticles. Further, the convective heat transfer also rely on thermal conductivity, density, specific heat capacity, and dynamic viscosity of nanofluids. Mass transfer is defined as the flow of chemical species from a high concentration region toward a lower concentration (Pang et al., 2015). For the occurrence of mass transfer, there must be two regions with various concentration. They also state that the driving force for mass transfer is concentration difference. The improvement of heat transfer enhances the mass transfer where both are studied in analogous way. Generally, due to the application of nanofluid on industries, transportation, energy conversion, heating and cooling process, the heat and mass transfer via moving nanofluids are the hottest researchable concept for the future generation.

Because of this, Sheremet (2021) explained the applicability of nanofluid toward heat and mass transfer. Specifically, they are applicable on varies fields of human activities, comprising power, chemical engineering, medicine, electronics, and others. The presence of low concentration tiny solid particles have a role to improve heat and mass transfer. Moreover, nanofluid has a function on managing the convey system like drag delivery process due to having low concentration nanoparticles. Sheremet (2021) reported the work of various authors regarding the applications of nanofluid. As an evidence, nanofluids are used to avoid heat efficiently in various cooling systems.

In general, different researchers investigate the practical applications of nanofluid currently. For instance, Hamzat et al. (2022) indicated the use of nanofluids to improve the performance of solar collectors. This is because of the properties that nanofluids have toward thermal conductivity. It is one of the main work in upgrading the efficiency of solar energy. The utilization of nanofluids starting from nano-medicine to renewable energy was examined by (Souza et al., 2022). Here, the impact of various parameters on the thermal properties of nanofluid were studied. Thus, due to suspending nanoparticles in the base fluid, the heat transfer via nanofluids enhanced. They suggested that, the heat and mass transfer can be improved by nanofluid flow on various media. Moreover, Enjavi et al. (2022) illuminated the application of nanofluid toward drug delivery and disease treatment. Can et al. (2022) showed the applications of nanofluid to control the thermal properties of a battery.

2.1.1 Viscous Nanofluid

In this subsection, the researchers summarized some published researches related to heat and mass transfer due to viscous nanofluid flow on stretchable surfaces. This is applicable in various fields such as in fluid mechanics, civil and bio-mechanical engineering. Thus, the researchers would like to review a number of works as follows.

Haile and Shankar (2014) considered the time dependent viscous nanofluid for the sake of transforming heat and mass in the existence of magnetic field interaction, thermal radiation, heat generation and chemical reaction. They considered moving nanofluids over vertically expandable surface. Further, they explained the essential applications of stretchable sheet on industry with MHD boundary layer flow, radiative heat transfer, impact of solid particles and thermal buoyancy movement of the fluid. By considering the viscous dissipation and chemical reaction, the non-linear PDEs are rearranged. Then, using suitable similarity transformation a coupled system of non-linear higher order ODEs are obtained and solved by Keller box method. Moreover, they used Buongiorno's model where the Brownian motion and thermophoresis properties of nanofluid are taken in to account. Finally, they displayed the obtained outcomes in tabular and graphical form with brief explanations. Consequently, the buoyancy ratio number and magnetic field parameters delay the flow of nanofluid but they increase the temperature and concentration profiles of nanofluid. Prandtl number rises the flow and volume fraction of nanoparticles whereas it reduces the temperature profile. Viscous dissipation decreases the formation of local skin friction coefficient whereas it enhances the distribution of temperature profile. The Brownian motion parameter rises the velocity and temperature profiles of nanofluid but it decreases the micro-sized particles volume fraction.

Considering a thin film nanofluid flow, Qasim et al. (2016) examined the heat and mass transfer on expandable sheet due to time-dependent. They explained the application of heat and mass transfer by moving film nanofluid in food processing, insulating materials, polymer, reactor fluidization, heat exchangers, cooling industry and so on. Particularly, it is more applicable in coating industries such as wire and fiber coating. Like Haile and Shankar (2014), they used Buongiorno's model to see the impact of Brownian motion and thermophoresis on film nanofluid. They also included the impact of viscous dissipation and transverse magnetic field in their model without the effect of thermal radiation and entropy generation. Using appropriate similarity transformation, the non-linear PDEs were converted into non-linear coupled ODEs and solved numerically by Maple's built-in 'dsolve' solver. Accordingly, the unsteadiness and magnetic field interaction decrease the flow of thin film nanofluid. The temperature distribution enhanced by viscous dissipation. They obtained a similar result on rate of heat and mass transfer due to the parameters of film thickness, unsteadiness, magnetic field interaction and viscous dissipation. Brownian motion constant increases the temperature profile whereas it decreases the concentration of nanofluid.

In addition to viscous dissipation, the impact of radiation and internal heat generation were investigated by Jalili et al. (2023) in heat transfer system via the boundary layer flow of nanofluid over movable surface. In thermal field, viscous dissipation has an important role and it behaves as a source of internal heat generation due to the work done by shearing stresses on distinct fluid layers. It is applicable in electronic chips and cigarettes, systems of power generation, food processing, cooling nuclear reactor and metallic sheet (Nandi et al., 2022). The governing equations of this model incorporated the internal heat generation and radiative heat flux under the energy equation. Here, they did not consider the impact of Brownian motion and thermophoresis in the steady flow of nanofluid. After the work of dimensionalization, the problem was solved by Akbari-Ganji Method (AGM) on Maple Mathematical software. They explained the impact of velocity slip and mass suction parameters on the nanofluids' flow rate and temperature distribution. Nanofluids was constructed by $Cu - H_2O$ and $Al_2O_3 - H_2O$.

Ullah et al. (2023) also elaborated the advantage of viscous dissipation with thermal density towards heat and mass transfer by chemically reactive moving nanofluid over an expandable surface. They also examined the thermophoresis properties of an electrically conducting nanofluid with physical impact of entropy during heat and mass transfer process. In the Boussinesq model, they considered non linear temperature profile in which the fluid density has an exponential component of it. The governing PDEs were converted into non linear ODEs by suitable similarity transformation. Applying Keller Box method, these ODEs were solved. They found that due to the rises of Brownian motion parameter, the rate of heat transfer reduces but Sherwood number shows an increment. Generally, they displayed their results graphical and tabular manner with brief discussion for prominent parameters such as magnetic-force parameter, thermophoretic, buoyancy, Eckert and Prandtl numbers on velocity, temperature and concentration distribution.

2.1.2 Nanofluid Flow in Porous Media

The existence of porous medium in a boundary layer flow has an influence on the flow and temperature fields. The nanofluid flowing over a permeable stretchable surface is applicable in geothermal extraction, petroleum industry, heat exchanger, electronic cooling by fan, solar system, separation and filtration in chemical industry, fiber insulation, human lung, small blood vessels, and so on. Hence, numerous researchers consider the movement of nanofluid on porous media which produces a good potential in boosting thermal capacity. Some of them are summarized below.

Yirga and Tesfay (2015) investigated the convective heat and mass transfer through steady, an electrical conducting moving nanofluid over a permeable expandable surface by considering the impact of viscous dissipation, chemical reaction and Soret. They have taken two kinds of nanofluids, those are Cu-water and Ag-water. The fundamental controlling PDEs are converted into non-linear ODEs using suitable similarity transformations with out considering the thermal radiation and Brownian motion effects. These ODEs were solved numerically by Keller box method. There was no slip between nanoparticles and base fluid, hence they were in thermal equilibrium. For the potential parameters, the findings were presented graphical and tabular form. Accordingly, the volume fraction of nanoparticles parameter delays the motion of nanofluid whereas it rises the temperature and concentration profiles. The impact of mass suction/injection, porosity, chemical reactive, Eckert, Soret, Prandtl and Schmidt numbers were seen on velocity, heat and concentration of nanofluid. Moreover, they explained the impact of these parameters on local coefficient of skin friction, Nusselt and Sherwood numbers.

The research work of Yirga and Tesfay (2015) is examined again by Chanie et al. (2018) in which the impact of viscous dissipation replaced by thermal radiation. Hence, Chanie et al. (2018) explained the heat and mass transfer by steady nanofluid flow over a permeable expandable surface. Mainly, they considered the influence of porosity, thermal radiation, magnetic field interaction and chemical reaction in their study. The transformed non-linear higher order ODEs from the basic PDEs were solved analytically by optimal homotopy asymptotic method (OHAM). The findings of this problem was presented with the help of graphs and tables. Henceforth, the porosity and nanoparticles concentration have the ability to retard the flow and increase the formation of local skin friction. Thermal radiation enhances the temperature field. Suction parameter raises heat transfer rate and decreases temperature profile. Concentration of nanofluid rises with Soret but declines with chemical reaction parameter and Schmidt number.

A permeable exponentially expandable surface was also considered by Li et al. (2021) to study the heat and mass transfer in an electrically conducting MHD boundary layer flow of Williamson nanofluid with the presence of heat generation/absorption and mass suction. They also considered an exterior aligned magnetic field, Brownian diffusion and thermophoresis of nanofluid in the governing PDEs with out thermal radiation and viscous dissipation impacts. By applying suitable similarity transformation, the PDEs were reformulated into ODEs, then they were solved by bvp4c package on MATLAB software.

Khan et al. (2022d) also analyzed the time dependent flow over a permeable expandable media for heat transfer purpose. The thin film flow incorporated the effect of thermal radiation and viscous dissipation. The porous surface was modeled by Darcy-Forchheimer. With these assumptions, the developed PDEs were transformed into ODEs by using suitable similarity transformation. Then, these ODEs were solved by analytic approach called HAM on Mathematica software. According to their discussion, analyzing the heat source with thermal radiation played a key role in manufacturing engineering procedures such as the production of electric power, solar energy modernization and astrophysical flow. They also clarified the necessity of Mathematical tools toward solving the problems of fluid flow and visualizing any dynamic characters. The obtained outcomes were displayed in pictures and tables with a brief natural interpretation for the most prominent parameters. The magnetic field and porosity parameter delay the flow of thin film liquid and enhance the formation of drag force. The thermal radiation enhances the distribution of temperature while tapers the rate of heat transfer.

2.1.3 Joule Heating Effect

In addition to considering porous stretchable surface where the fluid flow, the electrically conducting fluids have their own roles in heat and mass transfer processes. Cooling of nuclear reactors during emergency shutdown, glass fiber production, manufacture of plastic and rubber sheets, the utilization of geothermal energy, food processing, textile and paper industries are some of the applications of electrically conducting fluids (Yirga and Shankar, 2015). The role of Joule heating on heat and mass transfer with other factors have been summarized in the next four paragraphs from published articles.

Swain et al. (2020) investigated the MHD boundary layer flow for heat system using Newtonian fluid across a permeable exponentially stretchable surface. The energy sources such as viscous dissipation and Joule heating affected the rate of heat transfer. The interaction between electrically conducting fluid and externally applied magnetic field yields Joule heating which has many advantages in industries (Swain et al., 2020). The fundamental PDEs are stated for steady Newtonian fluid flow by applying the Boussinesq approximations and Darcy model for porous media. Using appropriate similarity transformation, these PDEs were altered into ODEs. Then, these non-linear ODEs were solved by both numerically (fourth order Runge-Kutta with shooting technique) and analytically (Homotopy Perturbation Method). The obtained results were illustrated graphically and tabular form by employing MATLAB software for the selected parameters. Magnetic field interaction and mass suction retarded the fluid flow and regulated the function of fluid flow in clinical or mechanical processes. Darcy number fastens the fluid movement and decrease the temperature distribution. Moreover, the Prandtl number and mass suction have the ability to lower the fluid temperature. Besides, the Joule heating parameters (Eckert number and magnetic field interaction) have a role to rise the temperature distribution inside the fluid while reducing the rate of heat transfer. This implies that the energy is collected in the fluid region due to dissipation. In addition to these, they discussed the impact of some parameters on local skin friction coefficient and Nusselt number.

Using electrically conducting steady nanofluids flow over sinusoidal wavy vertical sheet, Zeeshan et al. (2021) studied the radiative heat and mass transfer by incorporating the impact of natural convective, thermal radiation, heat generation, viscous dissipation and Joule heating. In this investigation, they added the impact of Brownian motion and thermophoresis to the study of Swain et al. (2020). At a specific temperature, the heat transfer between the fluid flow and surface termed as convective heat transfer (Zeeshan et al., 2021). They also discussed the three kinds of convective heat transfer: namely natural, forced and mixed. After, expressing the fundamental controlling PDEs into simple form of first order ODEs with the help of appropriate streamline functions, then they were solved by applying the well known implicit finite difference scheme called Keller Box method. Pictorially, the influence of different physical parameters were viewed and discussed. As a result, increasing the amplitude of waviness rises the concentration, Nusselt number and temperature whereas it reduces the local skin friction and Sherwood number. The Buoyancy Ratio, Brownian motion and thermophoresis parameters have an inverse relation with local drag formation, heat and mass transfer rate.

Moreover, Abbas et al. (2023) considered the impact of Joule heating, viscous dissipation, variable density, heat generation on optically dense gray steady moving Williamson fluid across an inclined permeable surface. With the presumed fluid, the governing PDEs were formulated and made dimensionless by applying non-dimensional variables. Due to the difficulties arising from solving PDEs directly, the researchers formulated an appropriate stream function to reduce the PDEs into ODEs. Then, the numerical results were obtained in the form of figures using the bvp4c solver on MATLAB software. Consequently, porous medium, magnetic field and density variation parameters have a role to retard the flow and increase the temperature distribution. Increasing Eckert number, heat generation, Williamson fluid and radiation parameters, produce rapid movement of fluid and high temperature distribution. But, Prandtl number leads to decline the fluid's temperature. Finally, the radiation and density variation parameters rise the rate of heat transfer while reducing the formation of drag force.

The impact of Joule heating together with magnetic flux in wave oscillations over a porous cone medium was reported by Boujelbene et al. (2023) including solar radiations and lower gravitational region. They defined the Joule heating, as it is the process where a moving current inside an electric conducting material produce thermal energy. In real life, Joule heating is applicable in house equipment such as electronic heaters, electrical iron, toaster ovens and industrial energy processes encompassing heating and drying products, heating boilers, dissolving and fusing metals (Boujelbene et al., 2023).

2.2 Solar Thermal Radiation

Currently, a number of scientists pay attention toward upgrading the heat transfer process from solar radiation due to its sustainability, environmental friendly and abundance of the Sun rays. In general, solar radiation can be used to satisfy our energy demand. In practice, solar can be utilized in industrial and household electricity needs, controlling wastes at a moisture stage, drinking water from sea and salt production (Mahian et al., 2013). As an evidence, Esfe and Toghraie (2022) showed the applications of solar radiation to produce fresh water using Thermoelectric Cooling System (TCS). Here, a renewable solar energy is necessary for the implement of solar stills. Since, solar still works based on the evaporation of salt water which needs sunlight.

For this purpose, various kinds of nanofluids are applied as working fluids in solar collectors, to convert solar radiation into various forms of energy such as heat and electric power. Even, the heat transfer via nanofluids from renewable and sustainable energy system (solar) evaluated using machine learning which is the latest trend (Ma et al., 2021). In line with these, the following points summarize some of the published research works regarding heat and mass transfer from solar radiation by nanofluid flow.

The boundary layer flow of an electrically conducting nanofluid over a vertically expandable sheet in the existence of thermal stratification due to solar radiation was discussed by Kandasamy et al. (2013). The character of nanofluid is modeled by Buongiorno model which considers the main two slip mechanisms namely, thermophoresis and Brownian motion. They explained the role of solar radiation as a renewable energy source to reduce environmental problems and scarcity of power. In the solar thermal system, utilizing nanofluid as a heat transport fluid is profitable because of the nanoparticles' excellent thermal conductivity. The basic governing PDEs are formulated for 2D, incompressible, steady flow of nanofluid over a porous vertical stretchable surface in terms of standard boundary layer approximation. Here, they assumed the non-transparent porous medium for self-emitted thermal radiation, and parallel Sun rays' are perpendicular to the surface. The PDEs were reduced into ODEs of the boundary value problem type using Lie-group transformation. Then, the non-linear ODEs solved numerically by Runge Kutta Gill algorithm with shooting method on MATLAB software. The obtained solutions depend on Lewis number, magnetic field, Brownian motion parameter, thermal stratification and thermophoretic parameters. They have their own consequential effects on flow field, temperature and nanoparticle volume fraction.

The application of nanofluid with its optical characters flowing over direct absorption solar collectors (DASCs) was revised by Gorji and Ranjbar (2017). In the 1970s Minardi and Chuang started the idea of DASC to design a collector where the flowing working fluid in the transparent tube directly absorbs solar energy. They employed nanofluid as a working fluid to reduce sedimentation and agglomeration problem as well improving the conductive and convective heat transfer characters of basic transport mediums. Thus, mixing tiny nanoparticles (0.01% volume) enhance the optical properties which is necessary for their potential use in DSACs since the incident radiation directly touch the working fluid without barriers. The performance of DASC systems is directly related to nanofluids concentration. Mostly, the incident radiation absorbed more by thin top layer of nanofluid than volumetrically fluid medium with increasing the nanoparticles volume fraction above maximum value. As a result, the system approaches surface-based absorber case (Gorji and Ranjbar, 2017). They concluded that optimizing the nanofluids optical properties and the volumetric solar collectors, ensured the maximum thermal performance.

Regarding solar energy, the impact of non-linear thermal radiation on the time dependent MHD cross nanofuid flow over a stretching surface was examined by Azam et al. (2019). Buongiorno's nanofluid model with convective boundary condition and zero nanoparticles mass flux were incorporated in the flow. Non-linear thermal radiation played a key role on the ability of nanofluid in absorbing solar radiation. It is obtained naturally from the Sun and transferred into electricity and heat energy (Azam et al., 2019). Without considering the impact of viscous dissipation and joule heating, the basic PDEs were formulated according to the assumed nanofluid properties. Then, following appropriate similarity transformation, these PDEs and boundary conditions were reduced into a set of ODEs. Due to the complex non-linear ODEs, numerical method (Runge-Kutta-Fehlberg technique with shooting approach) was the applied rather than analytic method. Based on this investigation, the magnetic parameter decrease the momentum boundary layer thickness. Both the temperature and nanoparticles concentration profiles were increased by magnetic field parameters. The magnitude of skin friction coefficient decreased for growing values of Weissenberg number. They concluded that Nusselt number was enhancing function of the temperature ratio parameter, Prandtl number and Biot number. Higher value of Brownian motion parameter resulted in declining nanoparticles concentration.

Due to the thermophysical properties of nanofluid, various researchers have upgraded the effectiveness of solar collectors using nanofluid in the thermal transfer of non-polluting renewable solar energy. For instance, Jamshed et al. (2021a) considered unsteady moving Maxwell nanofluid for the enhancement of heat transfer from renewable Sun's radiation in a parabolic trough solar collector (PTSC). They took Copper-methanol ($Cu - Ch_3OH$) and Titanium-methanol ($TiO_2 - Ch_3OH$) for Maxwell nanofluids flowing over an exponentially uniform, horizontal permeable expandable plate inside the PTSC. Exterior resources assumed in this problems are thermal radiative, viscous dissipative flow and Joule heating parameters. They explained about solar collectors, where nanofluid travels through them for the purpose of being a heat exchanger from solar radiation. The large solar collectors can be used to produce electrical energy for industries. The team conclude that nanofluids are crucial tools for improving the performance of solar collectors inside PTSC. By applying the monotonic Tiwari-Das model, the fundamental higher order non-linear PDEs are constructed with the help of standard boundary layer approximations including radiation heat flux, viscous dissipation, inclined MHD and Joule heating. Due to difficulties arise in solving these PDEs, the suitable transformation variables are used to convert PDEs into ODEs. Numerically, using the Keller box technique, the ODEs are solved. By comparing the heat transfer potential of the two different nanofluids, they found that Copper-methanol nanofluid has the ability to transfer heat more compared to Titanium-methanol nanofluid. Based on these findings, the velocity and temperature profiles are controlled by the Maxwell constant factor. Moreover, they considered entropy generation. As a result, higher values of the Reynolds and Brinkmann numbers maximize the generation of entropy.

Recently, Irfan et al. (2023) also used Maxwell nanofluid for heat transfer process, having better thermal conductivity for the progressive activity of solar energy. They included the impact of Joule heating, heat sink/source, and chemical reactions. The transformed ODEs from controlling PDEs are solved by a homotopic algorithm. The effects of potential parameters are discussed and examined in detail. The temperature of Maxwell nanofluid increased with the Eckert number and variable conductivity factors. The Brownian motion and thermophoretic parameters have opposite impacts on the concentration of the fluid. Heat transfer rate decays because of raising the values of Brownian motion and thermophoretic factors.

2.3 Entropy Generation

During the process of heat transfer, the existence of energy loss (entropy) has been expected due to the irreversible reactions. The idea of entropy was explained by the second law of thermodynamics (Daniel et al., 2017). Hence, the achievement of collecting energy from solar collector needs enhancement by adopting the thermodynamic second law analysis-based scheme (Yousefi et al., 2012). Since the first law thermodynamics is used for the law of conservation of energy, it is more applicable to explain the concept of entropy (Khan et al., 2022b). Different studies examined the generation of energy loss based on heat irreversibility or conduction impact and other. As an example, Khan et al. (2022b) suggested, due to molecular vibration, thermal radiation, rate of mass and heat transfer, friction between fluid particles, porous medium, diffusion and Joule heating in the thermal process, there is a creation of energy loss.

Consequently, owing to high fluid friction, mixing some electrical resistance, reactions and fluid vibrations, the entropy and energy disappearance are studied by Alkathiri et al. (2022). The generation of entropy is also analyzed by Qureshi (2022) in the case of solar aircraft implementation under linearly flowing hybrid nanofluid that passes through a PTSC. As usual, let us see the works of some published articles relating to the generation of entropy in mass and heat transfer via nanofluid in the presence of thermal solar radiation.

Loganathan and Rajan (2020) explained about the loss of energy in the flow and heat transfer process which is measured by entropy. The energy used to maximize the product is affected by energy loss. Thus, entropy has a role in decreasing the useful energy. They analyzed the influence of entropy production on the MHD, 2D flow of a Williamson nanofluid across a permeable porous surface. The research group considered Christov-Cattaneo heat flux, thermal radiation and Buongiorno model. Using suitable similarity transformation, the governing PDEs were transformed into ODEs which were solved by the homotopy analysis method (HAM). Besides, the entropy that is used to calculate the irreversible process, is formulated as a result of fluid friction, magnetic field interaction, porous media, heat and mass transmission. Bejan number is defined as the ratio of entropy production by heat and mass transformation to total entropy generation. They concluded that heat cannot be converted totally into work. The parameters such as radiation, magnetic, porosity, Eckert and Brinkman numbers raise the rate of formation of entropy but Weissenberg number has an opposite trend. Brinkman number has a role in decreasing the Bejan number.

The production of entropy with thermal analysis of nanofuid flow was examined by Tabarhoseini and Sheikholeslami (2022) inside the evacuated tube solar collector. Utilizing CuO nanoparticles in the base fluid, the thermal properties are optimized. During the flow of nanofluid, the irreversibility of fluid friction increased. The rate of local entropy generation has been derived in terms of velocity and temperature fields based on the second law of thermodynamics. In this study, the analysis of entropy generation was made due to fluid viscosity and heating. According to their findings, the production of entropy is lower in nanofluid than in pure water. In addition, fluid friction generated more entropy using nanofluid as a heat transfer.

The entropy generation in a binary nanofluid flowing over an infinite flat surface in a porous medium was analyzed by Alkathiri et al. (2022). They also elaborated on the cause of heat expansion in renewable solar energy with the binary nanofluid in the parabolic trough solar collector (PTSC) using Galerkin finite element. A PTSC is used as an extended medium for the non-linear binary nanofluid movement. In this study, the magnetic field parameter decreases the Nusselt number but raises the drag force factor formation. Moreover, parameters such as Reynolds, Brinkmann and Eckert numbers increase the total entropy generation. They concluded that a binary nano-based fluid improved the thermal prospector in the PTSC. According to this result, the heat transfer rate of $Cu - EO$ is better than $Fe_3O_4 - EO$.

The entropy formation was examined by Nandi et al. (2022), as a result of fluid friction, non-linear thermal radiation, magnetic field, porous media, heat and mass transmission. Generally, their research work focused on steady-moving Casson nanofluid over a slanted porous expandable surface in the existence of multiple slips, non-uniform heat source/sink, Arrhenius activation energy, Joule heating, viscous dissipation, thermal radiation, magneto-convective and chemically reactive with analysis of entropy formation. The natural irreversibility between the system and the surroundings is referred to as entropy. In every kind of heat transfer process, the formation of entropy is related to thermodynamic irreversibility. In general, the performance of useful energy is reduced by the high rate of entropy production. However, it is applicable in refrigerators, air conditioners, combustion engines and heat pumps, etc. According to presumed nanofluid movement, the controlling PDEs were transformed into ODEs by a suitable similarity transformation. Then, the ODEs were solved numerically by using Runge-Kutta Cash-Karp approach based on the shooting technique using MATLAB Mathematical language. Here, their findings show the growth of Brinkmann number, diffusive, thermal radiation and concentration ratio parameters, produce more formation of energy loss.

Before one year, the formation of entropy is also examined by Sharma et al. (2023) considering steady bio-convective Jeffrey fluid flow under the influence of solar radiation. In this study, the heat and mass transfer on such a flow through a non-linear expandable surface of non-uniform thickness was studied numerically with the effect of Joule heating, viscous dissipation and the exponential heat source. Based on the second law of thermodynamics, Jameel et al. (2023) formulated and investigated the rate of volumetric entropy procreation within the Maxwell nanofluid, by considering the impact of thermal radiation, viscous dissipation and joule heating. In general, from these inquiries, the total entropy increases concerning parameters such as temperature difference, Brinkman number, porosity, radiation and magnetic parameters.

In this way, numerous scholars explained the heat and mass transfer process through flowing nanofluids on a stretchable surface. To facilitate this processes, different assumptions on moving nanofluids are added. Some of them are horizontal or inclined permeable surfaces, steady or unsteady flow, using Tiwari-Das or Buongiorno's nanofluid models, convective heat transfer, mass suction/injection, slip, heat generation, viscous dissipation, Joule heating and thermal radiation. With the help of defined similarity transformations, the governing PDEs of the problems were converted into non-linear higher-order ODEs. Then, these ODEs were solved either numerically or semi-analytically. Generally, the researchers observed that there is little information about the problem of heat and mass transfer through unsteady nanofluid flow in a solar collector by radiation with entropy generation, which is solved by the Homotopy Ananlysis Method (HAM). Hence, the novelty of this dissertation work is considering radiation heat transfer, examining entropy generation, and solving the reduced ODEs by HAM with various boundary conditions.

Therefore, this dissertation focuses on heat and mass transfer by radiation via time-dependent nanofluid flow over a stretchable surface with entropy formation. The obtained equations were solved using a well-known robust method called HAM, implemented in Mathematica 12.1 software. Using HAM, the series solutions are close to exact solutions. Moreover, this method is justified by comparing it with the familiar finite difference approach coded with bvp4c, operated on MATLAB software.

CHAPTER THREE

Research Methodology

The researchers used the semi-analytic technique called HAM and the numerical approach to solve the non linear systems of higher-order ODEs which were transformed from the governed non linear PDEs using suitable similarity transformations. Thus, this chapter explained the governing equations with relating concepts, HAM, numerical approach, boundary layer approximation, and boundary conditions applied for solving the considered problems in this dissertation.

3.1 Governing Equations with Related Concepts

In this dissertation work, the Buongiorno model (Buongiorno, 2006) is used to examine the impact of Brownian motion and thermophoresis on nanofluid flow, heat and mass transfer in the presence of thermal radiation. This model considers the nanofluid as two phase. In another way, due to small sized solid particles suspended in the base fluid, the nanofluid is assumed to be a single phase, which is initiated by Tiwari and Das (2007). Both models have their own advantages and disadvantages. As a consequence, this dissertation has encompassed the two models on different problems. In line with this, the fundamental Mathematical model for the considered problems are derived based on the principles of mass, momentum, energy, and concentration conservation on the boundary layer. These basic physical principles can be expressed either in integral equations or PDEs. The following subsections describe the derivation of those four conservation laws and their simplifications in 2D and 3D rectangular geometry.

3.1.1 The Continuity Equation

The equation of continuity derived from mass conservation is the initial step for other fundamental laws of fluid mechanics. The law of mass conservation states as "mass is neither created nor destroyed". Thus, in a control volume, this law is

$$M_e - M_i + M_a = 0. \tag{3.1.1}$$

In equation (3.1.1), M_e, M_i, and M_a are rate of mass efflux from the control volume, flow into the control volume, and accumulation within control volume, respectively.

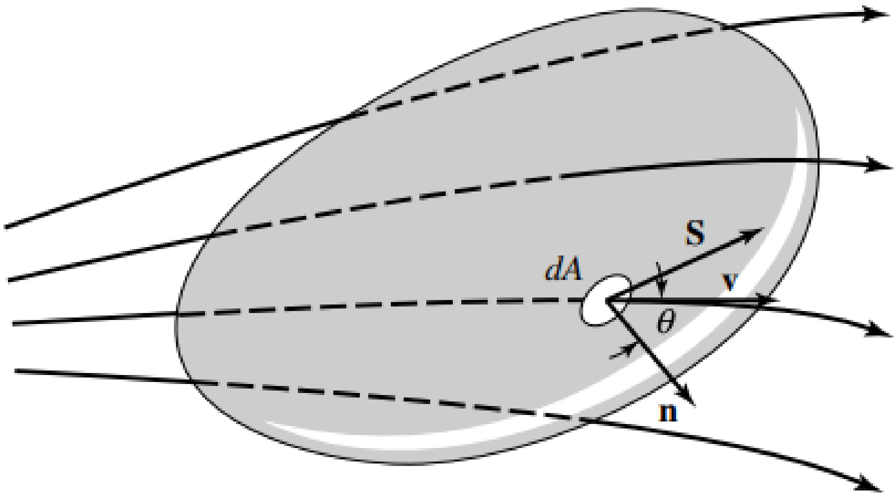

Figure 3.1.1: Flow and shear work for a general control volume (Welty et al., 2014).

According to Figure 3.1.1 (Welty et al., 2014), dA is the infinitesimal area on the assumed control volume in the fluid field. Then, $M_e = (\rho v)(dA\cos\theta)$, where $dA\cos\theta$ is the projection of the area dA in a plane normal to the velocity vector ($\mathbf{v}$) and θ is the angle between $\mathbf{v}$ and the outward directed unit normal vector ($\mathbf{n}$) to dA. Based on the property of vector dot product, it is obtained as

$$\rho v dA\cos\theta = \rho dA|\mathbf{v}||\mathbf{n}|\cos\theta = \rho(\mathbf{v}\cdot\mathbf{n})dA. \tag{3.1.2}$$

Equation (3.1.2) indicates that the net rate of mass efflux through dA and ρv, refereed as mass velocity. Physically, the product ρv, shows the amount of mass flowing through a unit cross-sectional area per unit time. Now, by integrating equation (3.1.2) over the entire control surface, the rate net of mass efflux is obtained as follows:

$$M_e - M_i = \iint_{c.s.} \rho(\mathbf{v}\cdot\mathbf{n})dA. \tag{3.1.3}$$

Thus, equation (3.1.3) describes the rate of net mass efflux in the given control volume. From this integral, the following points are investigated.

- There is a net efflux of mass if the integral is positive in a control volume.
- There is a net influx of mass if the integral is negative in a control volume.
- The mass within the control volume is constant if the integral is zero.

On the other hand, the rate of accumulation of mass within the control volume can be

$$M_a = \frac{\partial}{\partial t} \iiint_{c.v.} \rho dV. \tag{3.1.4}$$

By summing the integral expressions of equations (3.1.3) and (3.1.4) for conservation law of mass, the mass balance over a general control volume has been expressed as

$$\iint_{c.s.} \rho(\mathbf{v} \cdot \mathbf{n}) dA + \frac{\partial}{\partial t} \iiint_{c.v.} \rho dV = 0. \tag{3.1.5}$$

Mathematically, equations (3.1.5) can be expressed as

$$\frac{\partial}{\partial t} \int_V \rho dV + \int_S \rho(\mathbf{v} \cdot \mathbf{n}) dS = 0, \tag{3.1.6}$$

where V: volume, S: surface area, and $\mathbf{v} = (u_1, u_2, u_3)$: velocity along the x, y and z-axis respectively. The surface integral in equation (3.1.6) is converted to volume integral by applying the Gauss divergence theorem to the convection term as follows:

$$\int_V \frac{\partial \rho}{\partial t} dV + \int_V \nabla \cdot (\rho \mathbf{v}) dV = 0 \implies \int_V \left[\frac{\partial \rho}{\partial t} + \nabla \cdot (\rho \mathbf{v}) \right] dV = 0. \tag{3.1.7}$$

The result in equation (3.1.7) is true irrespective of the size, shape or location of volume V, which is only possible if $\frac{\partial \rho}{\partial t} + \nabla \cdot (\rho \mathbf{v}) = 0$. Hence, by allowing the control volume to become infinitesimally small leads to a differential coordinate-free form of the continuity equation, which results equations in Cartesian coordinates.

$$\begin{aligned}
&\frac{\partial \rho}{\partial t} + \nabla \cdot (\rho \mathbf{v}) = 0 \implies \frac{\partial \rho}{\partial t} + \frac{\partial}{\partial x}(\rho u_1) + \frac{\partial}{\partial y}(\rho u_2) + \frac{\partial}{\partial z}(\rho u_3) = 0 \\
&\frac{\partial \rho}{\partial t} + \rho \frac{\partial u_1}{\partial x} + \rho \frac{\partial u_2}{\partial y} + \rho \frac{\partial u_3}{\partial z} + u_1 \frac{\partial \rho}{\partial x} + u_2 \frac{\partial \rho}{\partial y} + u_3 \frac{\partial \rho}{\partial z} = 0 \\
&\implies \frac{\partial \rho}{\partial t} + \rho \nabla \cdot \mathbf{v} + \mathbf{v} \cdot \nabla \rho = 0.
\end{aligned} \tag{3.1.8}$$

Specifically, in 2D and 3D rectangular geometry, incompressible fluid where there is insignificance change in density of fluid, the continuity equation (3.1.8) is simplified as

$$\begin{aligned}
&\frac{\partial \rho}{\partial t} + \rho \nabla \cdot \mathbf{v} + \mathbf{v} \cdot \nabla \rho = 0 \implies \nabla \cdot \mathbf{v} = 0 \implies \frac{\partial u_1}{\partial x} + \frac{\partial u_2}{\partial y} = 0 \\
&\frac{\partial \rho}{\partial t} + \rho \nabla \cdot \mathbf{v} + \mathbf{v} \cdot \nabla \rho = 0 \implies \nabla \cdot \mathbf{v} = 0 \implies \frac{\partial u_1}{\partial x} + \frac{\partial u_2}{\partial y} + \frac{\partial u_3}{\partial z} = 0.
\end{aligned} \tag{3.1.9}$$

3.1.2 The Momentum Equation

In contrast to mass, momentum can be changed by the action of forces and its conservation equation is based on Newton's second law. This principle states that the rate of change of momentum for fluid particles equals to the sum of forces acting on the particles. Mathematically, it can be expressed as

$$\frac{d(m\mathbf{v})}{dt} = \sum \mathbf{F}. \tag{3.1.10}$$

From equations (3.1.10), t stands for time, m for mass, $\mathbf{v}$ for velocity vector and $\mathbf{F}$ for forces acting on the control mass. Then, the conservation of linear momentum in terms of control volume method, can be expressed as

$$\sum \mathbf{F} = Mo_o - Mo_i + Mo_a, \tag{3.1.11}$$

where Mo_o, Mo_i and Mo_a are the rate of momentum out of the control volume, into the control volume and accumulation within the control volume respectively. Actually, in equation (3.1.11) the term $Mo_o - Mo_i$ is called net rate of momentum efflux from control volume and $\sum \mathbf{F}$ represents the total force acting on the control volume which includes both surface and body forces. Surface forces occurred due to the interactions between the control-volume fluid and its surroundings through direct contact, like shear force. But the body forces resulted from the location of the control volume in a force field. The gravitational field and its resultant forces are the most common examples of body forces. Hence, for a small area dA on the control surface, the rate of momentum efflux can be defined and simplified as

$$\mathbf{v}(\rho v)(dA\cos\theta) = \mathbf{v}(\rho dA)(|\mathbf{v}||\mathbf{n}|\cos\theta) = \rho\mathbf{v}(\mathbf{v}\cdot\mathbf{n})dA. \tag{3.1.12}$$

We can recall that the product $(\rho v)(dA\cos\theta)$ is the rate of mass efflux from the control volume through dA. Thus, the rate of momentum efflux is obtained by multiplying the rate of mass efflux and $\mathbf{v}$ through dA as equation (3.1.12). Integrating this quantity over the entire control surface, the following expression is obtained (3.1.13).

$$Mo_o - Mo_i = \iint_{c.s.} \rho\mathbf{v}(\mathbf{v}\cdot\mathbf{n})dA \implies \text{ rate net momentum efflux.} \tag{3.1.13}$$

On the other hand, the rate of momentum accumulation within the control volume is

$$\frac{\partial}{\partial t}\iiint_{c.v.} \mathbf{v}\rho dV. \tag{3.1.14}$$

Therefore, the overall linear-momentum balance for a control volume becomes

$$\frac{\partial}{\partial t}\iiint_{c.v.} \mathbf{v}\rho dV + \iint_{c.s.} \rho\mathbf{v}(\mathbf{v}\cdot\mathbf{n})dA = \sum \mathbf{F}. \tag{3.1.15}$$

Equation (3.1.15) is called momentum theorem which is a base in fluid mechanics.

In another way, the law of momentum conservation is Navier-Stokes equation which is the differential form of Newton's second law of motion. It states that the product of mass and acceleration is equal to the sum of external forces acting on a body. This law is equivalent with momentum theorem and used to develop Navier-Stokes equations for an arbitrary control volume. That is the external force acting on the control volume is equal to the sum of net rate of linear momentum efflux and time rate change of linear momentum with the control volume.

The development of this law can be simplified by dividing volume in the control and taking limit as the dimensions approach to zero. The equation (3.1.15) becomes

$$\underbrace{\lim_{\Delta x\Delta y\Delta z\to 0}\frac{\sum \mathbf{F}}{\Delta x\Delta y\Delta z}}_{\text{First}} = \underbrace{\lim_{\Delta x\Delta y\Delta z\to 0}\frac{\iint \rho\mathbf{v}(\mathbf{v}.\mathbf{n})dA}{\Delta x\Delta y\Delta z}}_{\text{Second}} + \underbrace{\lim_{\Delta x\Delta y\Delta z\to 0}\frac{\frac{\partial}{\partial t}\iiint \rho\mathbf{v}dV}{\Delta x\Delta y\Delta z}}_{\text{Third}}. \tag{3.1.16}$$

Each terms in equation (3.1.16), has the following explanation.

1. The first term is the sum of external forces: It includes both body and surface forces. The gravity and magnetic forces are considered as a body force, while the friction force and forces due to normal and shear stress acting on the control volume are considered as a surface force.

2. The second term is the net momentum flux through the control volume.

3. The third term is the time rate of change of momentum within the control volume.

Now, let us discuss the three terms in equation (3.1.16) one by one considering some of the body and surface forces.

1. From the first term of equation (3.1.16), the external forces is the sum of the body force (gravitational force) and surface forces (normal and shear stress forces). Thus, it is expressed in the following manner according to Figure 3.1.2.

$$
\begin{aligned}
\sum \mathbf{F}_x =& (\sigma_{xx}|_{x+\Delta x} - \sigma_{xx}|_x)\Delta y \Delta z + (\tau_{yx}|_{y+\Delta y} - \tau_{yx}|_y)\Delta x \Delta z \\
&+ (\tau_{zx}|_{z+\Delta z} - \tau_{zx}|_z)\Delta y \Delta x + g_x \rho \Delta x \Delta y \Delta z \\
\sum \mathbf{F}_y =& (\sigma_{yy}|_{y+\Delta y} - \sigma_{yy}|_y)\Delta x \Delta z + (\tau_{xy}|_{x+\Delta x} - \tau_{xy}|_x)\Delta y \Delta z \\
&+ (\tau_{zy}|_{z+\Delta z} - \tau_{zy}|_z)\Delta y \Delta x + g_y \rho \Delta x \Delta y \Delta z \\
\sum \mathbf{F}_z =& (\sigma_{zz}|_{z+\Delta z} - \sigma_{zz}|_z)\Delta y \Delta x + (\tau_{xz}|_{x+\Delta x} - \tau_{xz}|_x)\Delta z \Delta y \\
&+ (\tau_{yz}|_{y+\Delta y} - \tau_{yz}|_y)\Delta z \Delta x + g_z \rho \Delta x \Delta y \Delta z
\end{aligned}
\tag{3.1.17}
$$

where g_x, g_y, g_z are the component of gravitational acceleration in the x, y and z directions respectively.

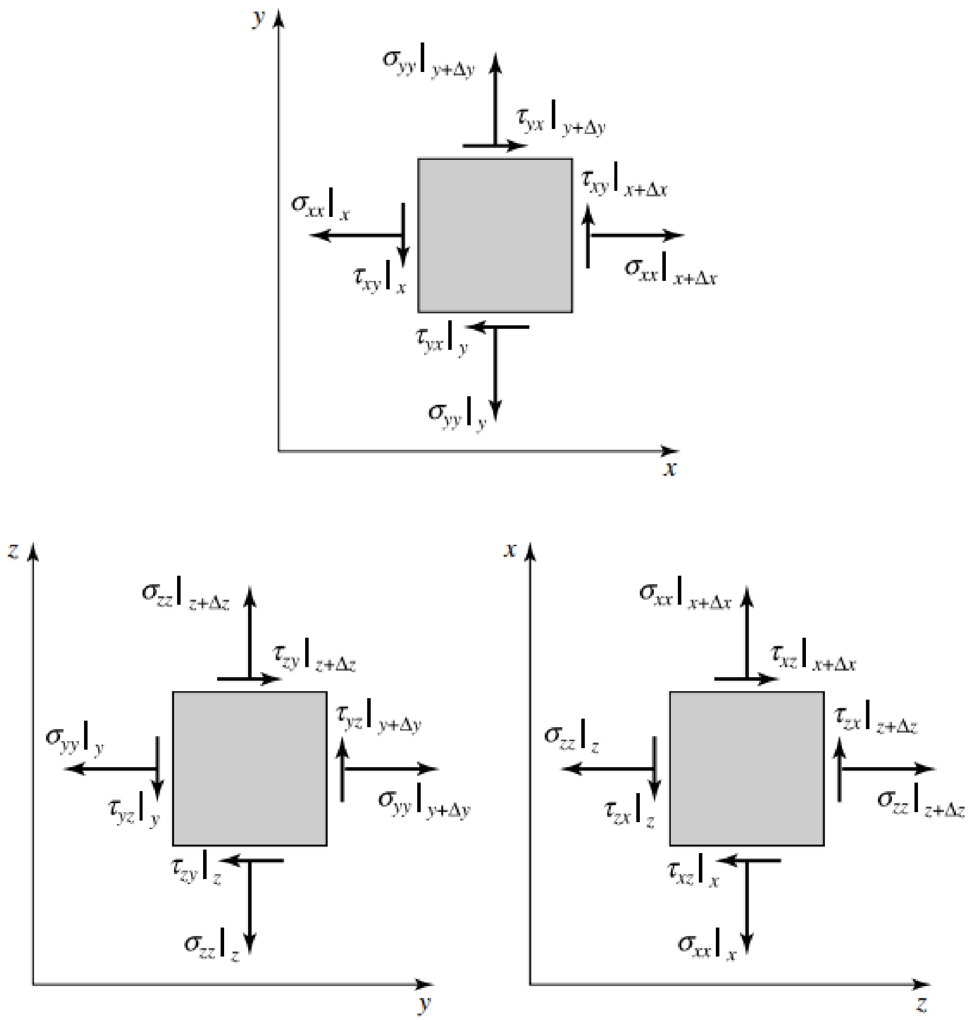

Figure 3.1.2: Forces acting on a differential control volume (Welty et al., 2014).

Applying limit as the infinitesimal dimensions approach zero ($\Delta x \Delta y \Delta z \to 0$), the following expression has been obtained from equation (3.1.17).

$$
\begin{aligned}
\lim_{\Delta x \Delta y \Delta z \to 0} \frac{\sum \mathbf{F}_x}{\Delta x \Delta y \Delta z} &= \frac{\partial \sigma_{xx}}{\partial x} + \frac{\partial \tau_{yx}}{\partial y} + \frac{\partial \tau_{zx}}{\partial z} + g_x \rho \\
\lim_{\Delta x \Delta y \Delta z \to 0} \frac{\sum \mathbf{F}_y}{\Delta x \Delta y \Delta z} &= \frac{\partial \sigma_{yy}}{\partial y} + \frac{\partial \tau_{xy}}{\partial x} + \frac{\partial \tau_{zy}}{\partial z} + g_y \rho \\
\lim_{\Delta x \Delta y \Delta z \to 0} \frac{\sum \mathbf{F}_z}{\Delta x \Delta y \Delta z} &= \frac{\partial \sigma_{zz}}{\partial z} + \frac{\partial \tau_{xz}}{\partial x} + \frac{\partial \tau_{yz}}{\partial y} + g_z \rho.
\end{aligned}
\tag{3.1.18}
$$

The vector forms of equation (3.1.18) in Cartesian coordinates is

$$
\begin{aligned}
\lim_{\Delta x \Delta y \Delta z \to 0} \frac{\sum \mathbf{F}}{\Delta x \Delta y \Delta z} =& \left(\frac{\partial \sigma_{xx}}{\partial x} + \frac{\partial \tau_{yx}}{\partial y} + \frac{\partial \tau_{zx}}{\partial z} + g_x \rho\right) e_x \\
&+ \left(\frac{\partial \sigma_{yy}}{\partial y} + \frac{\partial \tau_{xy}}{\partial x} + \frac{\partial \tau_{zy}}{\partial z} + g_y \rho\right) e_y \\
&+ \left(\frac{\partial \sigma_{zz}}{\partial z} + \frac{\partial \tau_{xz}}{\partial x} + \frac{\partial \tau_{yz}}{\partial y} + g_z \rho\right) e_z,
\end{aligned}
\tag{3.1.19}
$$

where $e_x = (1,0,0), e_y = (0,1,0)$ and $e_z = (0,0,1)$ are unit vectors along x, y and z axes in that order.

2. The second term in equation (3.1.16) is the rate of net momentum flux through the control volume. Based on Figure 3.1.3 where $v_x = u_1, v_y = u_2, v_z = u_3$ and applying limit on dimensional element, the following differential form is obtained.

$$
\begin{aligned}
\lim_{\Delta x \Delta y \Delta z \to 0} \frac{\iint \rho \mathbf{v}(\mathbf{v}.\mathbf{n}) dA}{\Delta x \Delta y \Delta z} =& \lim_{\Delta x \Delta y \Delta z \to 0} \Big[\frac{\rho \mathbf{v} (u_1|_{x+\Delta x} - u_1|_x) \Delta y \Delta z}{\Delta x \Delta y \Delta z} + \\
& \frac{\rho \mathbf{v} (u_2|_{y+\Delta y} - u_2|_y) \Delta x \Delta z}{\Delta x \Delta y \Delta z} + \frac{\rho \mathbf{v} u_3|_{z+\Delta z} - u_3|_z) \Delta y \Delta x}{\Delta x \Delta y \Delta z} \Big] \\
=& \frac{\partial}{\partial x}(\rho \mathbf{v} u_1) + \frac{\partial}{\partial y}(\rho \mathbf{v} u_2) + \frac{\partial}{\partial z}(\rho \mathbf{v} u_3).
\end{aligned}
\tag{3.1.20}
$$

Equation (3.1.20) can be further simplified by using $-\frac{\partial \rho}{\partial t} = \frac{\partial}{\partial x}(\rho u_1) + \frac{\partial}{\partial y}(\rho u_2) + \frac{\partial}{\partial z}(\rho u_3)$ from continuity equation in (3.1.8).

$$
\begin{aligned}
& \frac{\partial}{\partial x}(\rho \mathbf{v} u_1) + \frac{\partial}{\partial y}(\rho \mathbf{v} u_2) + \frac{\partial}{\partial z}(\rho \mathbf{v} u_3) = \\
& \mathbf{v} \left(\frac{\partial}{\partial x}(\rho u_1) + \frac{\partial}{\partial y}(\rho u_2) + \frac{\partial}{\partial z}(\rho u_3) \right) + \rho \left(u_1 \frac{\partial \mathbf{v}}{\partial x} + u_2 \frac{\partial \mathbf{v}}{\partial y} + u_3 \frac{\partial \mathbf{v}}{\partial z} \right) \\
& = -\mathbf{v} \frac{\partial \rho}{\partial t} + \rho \left(u_1 \frac{\partial \mathbf{v}}{\partial x} + u_2 \frac{\partial \mathbf{v}}{\partial y} + u_3 \frac{\partial \mathbf{v}}{\partial z}\right)
\end{aligned}
\tag{3.1.21}
$$

Therefore, the net momentum flux through a control volume can be written as

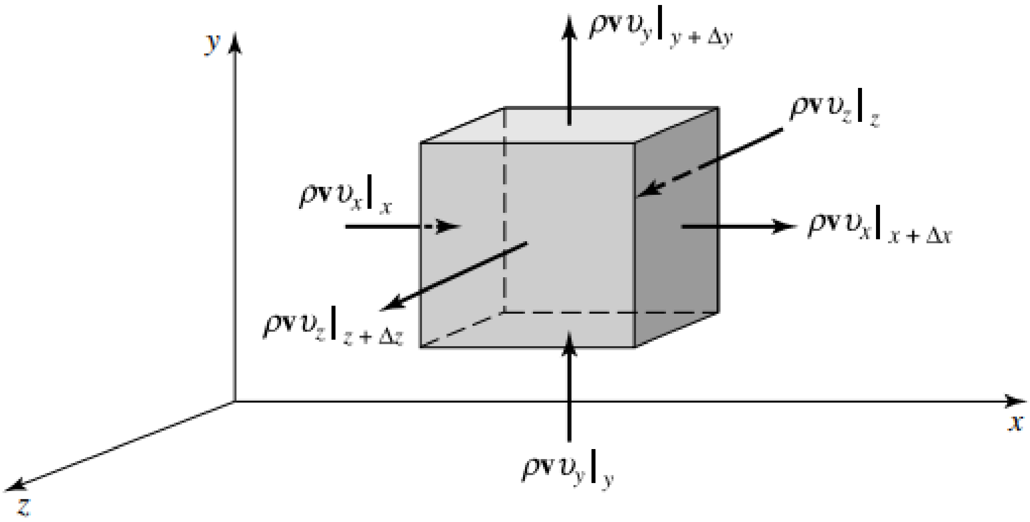

Figure 3.1.3: Momentum flux in a differential control volume (Welty et al., 2014).

$$\lim_{\Delta x \Delta y \Delta z \to 0} \frac{\iint \rho \mathbf{v}(\mathbf{v}.\mathbf{n})dA}{\Delta x \Delta y \Delta z} = -\mathbf{v}\frac{\partial \rho}{\partial t} + \rho\left(u_1\frac{\partial \mathbf{v}}{\partial x} + u_2\frac{\partial \mathbf{v}}{\partial y} + u_3\frac{\partial \mathbf{v}}{\partial z}\right). \tag{3.1.22}$$

3. The third term of equation (3.1.16) can be simplified directly from the integration concept by considering ρ and $\mathbf{v}$ constant with respect of volume.

$$\lim_{\Delta x \Delta y \Delta z \to 0} \frac{\frac{\partial}{\partial t}\iiint \rho \mathbf{v} dV}{\Delta x \Delta y \Delta z} = \frac{\partial}{\partial t}(\mathbf{v}\rho) = \rho\frac{\partial \mathbf{v}}{\partial t} + \mathbf{v}\frac{\partial \rho}{\partial t}. \tag{3.1.23}$$

The sum of equations (3.1.22) and (3.1.23 yields the following simplified form.

$$\begin{aligned}
&\lim_{\Delta x \Delta y \Delta z \to 0} \frac{\iint \rho \mathbf{v}(\mathbf{v}.\mathbf{n})dA}{\Delta x \Delta y \Delta z} + \lim_{\Delta x \Delta y \Delta z \to 0} \frac{\dfrac{\partial}{\partial t}\iiint \rho \mathbf{v} dV}{\Delta x \Delta y \Delta z} \\
&= -\mathbf{v}\frac{\partial \rho}{\partial t} + \rho\left(u_1\frac{\partial \mathbf{v}}{\partial x} + u_2\frac{\partial \mathbf{v}}{\partial y} + u_3\frac{\partial \mathbf{v}}{\partial z}\right) + \rho\frac{\partial \mathbf{v}}{\partial t} + \mathbf{v}\frac{\partial \rho}{\partial t} \\
&= \rho\left(u_1\frac{\partial \mathbf{v}}{\partial x} + u_2\frac{\partial \mathbf{v}}{\partial y} + u_3\frac{\partial \mathbf{v}}{\partial z}\right) + \rho\frac{\partial \mathbf{v}}{\partial t}
\end{aligned} \tag{3.1.24}$$

The component wise momentum terms of equation (3.1.24) can be expressed as:

$$\begin{aligned}
\rho\left(u_1\frac{\partial \mathbf{v}}{\partial x} + u_2\frac{\partial \mathbf{v}}{\partial y} + u_3\frac{\partial \mathbf{v}}{\partial z}\right) + \rho\frac{\partial \mathbf{v}}{\partial t} &= \left(\frac{\partial u_1}{\partial t} + u_1\frac{\partial u_1}{\partial x} + u_2\frac{\partial u_1}{\partial y} + u_3\frac{\partial u_1}{\partial z}\right)\rho e_x \\
+ \left(\frac{\partial u_2}{\partial t} + u_1\frac{\partial u_2}{\partial x} + u_2\frac{\partial u_2}{\partial y} + u_3\frac{\partial u_2}{\partial z}\right)\rho e_y &+ \left(\frac{\partial u_3}{\partial t} + u_1\frac{\partial u_3}{\partial x} + u_2\frac{\partial u_3}{\partial y} + u_3\frac{\partial u_3}{\partial z}\right)\rho e_z.
\end{aligned}$$

Now, the three term in equation (3.1.16) have been reduced. These expressions are also based on Newton's second law. Hence, equating equations (3.1.19) and (3.1.24) in the component wise yields the following expression.

$$\begin{aligned}
\rho\left(\frac{\partial u_1}{\partial t}+u_1\frac{\partial u_1}{\partial x}+u_2\frac{\partial u_1}{\partial y}+u_3\frac{\partial u_1}{\partial z}\right)&=\frac{\partial \sigma_{xx}}{\partial x}+\frac{\partial \tau_{yx}}{\partial y}+\frac{\partial \tau_{zx}}{\partial z}+g_x\rho\\
\rho\left(\frac{\partial u_2}{\partial t}+u_1\frac{\partial u_2}{\partial x}+u_2\frac{\partial u_2}{\partial y}+u_3\frac{\partial u_2}{\partial z}\right)&=\frac{\partial \sigma_{yy}}{\partial y}+\frac{\partial \tau_{xy}}{\partial x}+\frac{\partial \tau_{zy}}{\partial z}+g_y\rho\\
\rho\left(\frac{\partial u_3}{\partial t}+u_1\frac{\partial u_3}{\partial x}+u_2\frac{\partial u_3}{\partial y}+u_3\frac{\partial u_3}{\partial z}\right)&=\frac{\partial \sigma_{zz}}{\partial z}+\frac{\partial \tau_{yz}}{\partial y}+\frac{\partial \tau_{xz}}{\partial x}+g_z\rho.
\end{aligned}\tag{3.1.25}$$

It will be noted that in equation (3.1.25) above, the terms on the left-hand side represent the time rate of change of momentum ($\frac{\partial \mathbf{v}}{\partial t}$), called local acceleration, and the velocity change from point to points is called convective acceleration. These two kinds of acceleration are known as the total acceleration. While terms in the right-hand side represent the forces which are valid for any type of fluid, regardless of the nature on stress to strain relationships. It can be further simplified using the following notation.

$$\begin{aligned}
\rho\frac{Du_1}{Dt}&=\frac{\partial \sigma_{xx}}{\partial x}+\frac{\partial \tau_{yx}}{\partial y}+\frac{\partial \tau_{zx}}{\partial z}+\rho g_x\\
\rho\frac{Du_2}{Dt}&=\frac{\partial \sigma_{yy}}{\partial y}+\frac{\partial \tau_{xy}}{\partial x}+\frac{\partial \tau_{zy}}{\partial z}+\rho g_y\\
\rho\frac{Du_3}{Dt}&=\frac{\partial \sigma_{zz}}{\partial z}+\frac{\partial \tau_{xz}}{\partial x}+\frac{\partial \tau_{yz}}{\partial z}+\rho g_z,
\end{aligned}\tag{3.1.26}$$

where D in equation (3.1.26) is the substantial derivative notation, and is defined as

$$\frac{Du_i}{Dt}=(\frac{\partial}{\partial t}+u_1\frac{\partial}{\partial x}+u_2\frac{\partial}{\partial y}+u_3\frac{\partial}{\partial z})u_i, \quad \text{where } i=1,2,3.$$

The Stoke's viscosity relation regarding shear (τ) and normal (σ) stresses expressed as

- **Shear stress:** Using the rate of shear-stress, the shear stress components in laminar flow can be written in rectangular coordinates form as

$$\begin{aligned}
&\tau_{ij}=\tau_{ji}=\mu\left(\frac{\partial u_i}{\partial j}+\frac{\partial u_j}{\partial i}\right)\implies \tau_{xy}=\tau_{yx}=\mu\left(\frac{\partial u_1}{\partial y}+\frac{\partial u_2}{\partial x}\right),\\
&\tau_{xz}=\tau_{zx}=\mu\left(\frac{\partial u_1}{\partial z}+\frac{\partial u_3}{\partial x}\right)\text{ and }\tau_{zy}=\tau_{yz}=\mu\left(\frac{\partial u_3}{\partial y}+\frac{\partial u_2}{\partial z}\right)
\end{aligned}\tag{3.1.27}$$

- **Normal stress:** Stress to strain relationship used to formulate the normal stress.

It is developed based on the generalized Hooke's law for an elastic medium. Thus, normal stress for Newtonian fluid in rectangular coordinates is

$$\begin{aligned}
&\sigma_{xx} = \mu\left(2\frac{\partial u_1}{\partial x} - \frac{2}{3}\nabla\cdot\mathbf{v}\right) - P,\ \sigma_{yy} = \mu\left(2\frac{\partial u_2}{\partial y} - \frac{2}{3}\nabla\cdot\mathbf{v}\right) - P \\
&\sigma_{zz} = \mu\left(2\frac{\partial u_3}{\partial z} - \frac{2}{3}\nabla\cdot\mathbf{v}\right) - P
\end{aligned}. \qquad (3.1.28)$$

Then, using equations (3.1.27) and (3.1.28), equation (3.1.26) simplified as follows

$$\begin{aligned}
\rho\frac{Du_1}{Dt} =& \frac{\partial \sigma_{xx}}{\partial x} + \frac{\partial \tau_{yx}}{\partial y} + \frac{\partial \tau_{zx}}{\partial z} + \rho g_x = \rho g_x - \frac{\partial P}{\partial x} - \frac{2\partial}{3\partial x}\nabla\cdot(\mu\mathbf{v}) \\
&+\mu\left(2\frac{\partial^2 u_1}{\partial x^2} + \frac{\partial}{\partial y}\left(\frac{\partial u_1}{\partial y} + \frac{\partial u_2}{\partial x}\right) + \frac{\partial}{\partial z}\left(\frac{\partial u_1}{\partial z} + \frac{\partial u_3}{\partial x}\right)\right) \\
\implies \rho\frac{Du_1}{Dt} =& \rho g_x - \frac{\partial P}{\partial x} - \frac{\partial}{\partial x}(\frac{2}{3}\mu\nabla\cdot\mathbf{v}) + \mu\frac{\partial}{\partial x}\left(\frac{\partial u_1}{\partial x} + \frac{\partial u_2}{\partial y} + \frac{\partial u_3}{\partial z}\right) \\
&+\mu\left(\frac{\partial^2 u_1}{\partial x^2} + \frac{\partial^2 u_1}{\partial y^2} + \frac{\partial^2 u_1}{\partial z^2}\right) \quad \text{By applying the concept of gradient, we get} \\
\rho\frac{Du_1}{Dt} =& \rho g_x - \frac{\partial P}{\partial x} - \frac{\partial}{\partial x}(\frac{2}{3}\mu\nabla\cdot\mathbf{v}) + \nabla\cdot(\mu\frac{\partial\mathbf{v}}{\partial x}) + \nabla\cdot(\mu\nabla u_1).
\end{aligned}$$

Applying similar approach, each components of equation (3.1.26) is reduced as

$$\left\{\begin{aligned}
\rho\frac{Du_1}{Dt} =& \rho g_x - \frac{\partial P}{\partial x} - \frac{\partial}{\partial x}(\frac{2}{3}\mu\nabla\cdot\mathbf{v}) + \nabla\cdot(\mu\frac{\partial\mathbf{v}}{\partial x}) + \nabla\cdot(\mu\nabla u_1) \\
\rho\frac{Du_2}{Dt} =& \rho g_y - \frac{\partial P}{\partial y} - \frac{\partial}{\partial y}(\frac{2}{3}\mu\nabla\cdot\mathbf{v}) + \nabla\cdot(\mu\frac{\partial\mathbf{v}}{\partial y}) + \nabla\cdot(\mu\nabla u_2) \\
\rho\frac{Du_3}{Dt} =& \rho g_z - \frac{\partial P}{\partial z} - \frac{\partial}{\partial z}(\frac{2}{3}\mu\nabla\cdot\mathbf{v}) + \nabla\cdot(\mu\frac{\partial\mathbf{v}}{\partial z}) + \nabla\cdot(\mu\nabla u_3).
\end{aligned}\right. \qquad (3.1.29)$$

Equation (3.1.29) is valid for both compressible and incompressible fluid. For incompressible flow, ($\nabla\cdot\mathbf{v} = \frac{\partial u_1}{\partial x} + \frac{\partial u_2}{\partial y} + \frac{\partial u_3}{\partial z} = 0$), equation (3.1.29) becomes

$$\left\{\begin{aligned}
\rho\frac{Du_1}{Dt} =& \rho g_x - \frac{\partial P}{\partial x} + \mu(\frac{\partial^2 u_1}{\partial x^2} + \frac{\partial^2 u_1}{\partial y^2} + \frac{\partial^2 u_1}{\partial z^2}) \\
\rho\frac{Du_1}{Dt} =& \rho g_y - \frac{\partial P}{\partial y} + \mu(\frac{\partial^2 u_2}{\partial x^2} + \frac{\partial^2 u_2}{\partial y^2} + \frac{\partial^2 u_2}{\partial z^2}). \\
\rho\frac{Du_3}{Dt} =& \rho g_z - \frac{\partial P}{\partial z} + \mu(\frac{\partial^2 u_3}{\partial x^2} + \frac{\partial^2 u_3}{\partial y^2} + \frac{\partial^2 u_3}{\partial z^2})
\end{aligned}\right. \qquad (3.1.30)$$

Equation (3.1.30) can be expressed in more compact single way as follows:

$$\rho\frac{D\mathbf{v}}{Dt} = \rho\mathbf{g} - \nabla P + \mu\nabla^2\mathbf{v}, \quad \text{where } \mathbf{g} = (g_x, g_y, g_z). \qquad (3.1.31)$$

Euler consider the Navier-Stokes equation when the flow is inviscid, that is $\mu = 0$. This is called Euler equation. It reduces the Navier-Stokes equation (3.1.31) to (3.1.32):

$$\rho \frac{D\mathbf{v}}{Dt} = \rho\mathbf{g} - \nabla P. \tag{3.1.32}$$

3.1.3 The Energy Equation

In fluid flow analysis, the third basic law is the first law of thermodynamics. It is based on energy conservation which is stated as energy is neither created nor destroyed. An integral expression for the conservation of energy applied to a control volume will be developed from the first law of thermodynamics. The energy conservation is also called the first law of thermodynamics which states that if a system is carried through a cycle, the total heat added to the system from its surroundings is proportional to the work done by the system on its surroundings (Welty et al., 2014). Unlike the momentum equations, the resulting formula from the first law of thermodynamics is scalar. The integral form of energy conservation based on the first law of thermodynamics is

$$\oint \delta Q = \frac{1}{J} \oint \delta W. \tag{3.1.33}$$

The integral in equation (3.1.33) represents the quantity evaluated over a cycle and the symbols δQ and δW represent differential operator for heat transfer and work done, respectively. Hence, δ is a path function which is used for both heat transfer and work done. Actually, the well known differential operator, d, is used as a point function. The quantity J is known as mechanical equivalent of heat, numerically $J = 778.17 ftlb/Btu$ in engineering units with SI system, $J = 1\frac{Nm}{J}$ which is dimensionless. Therefore, the general thermodynamic cycle can be describe as in Figure 3.1.4 where the cycle occurs between points 1 and 2 by the paths indicated. Applying equation (3.1.33), the next expression has been developed as

$$\int_{1a}^{2} \delta Q + \int_{2a}^{1} \delta Q = \int_{1a}^{2} \delta W + \int_{2a}^{1} \delta W. \tag{3.1.34}$$

Considering another path, the equation (3.1.33) written as

$$\int_{1a}^{2} \delta Q + \int_{2b}^{1} \delta Q = \int_{1a}^{2} \delta W + \int_{2b}^{1} \delta W. \tag{3.1.35}$$

The difference between equations (3.1.34) and (3.1.35), implies equation (3.1.36), which is stated as

$$\int_{2a}^{1} \delta Q - \int_{2b}^{1} \delta Q = \int_{2a}^{1} \delta W - \int_{2b}^{1} \delta W \implies \int_{2a}^{1} (\delta Q - \delta W) = \int_{2b}^{1} (\delta Q - \delta W). \tag{3.1.36}$$

Here, the expression $\delta Q - \delta W = dE$. Including the time interval dt during the system undergoing a process, the equation (3.1.36) ca be written in equation (3.1.37) as follows.

$$\frac{\delta Q}{dt} - \frac{\delta W}{dt} = \frac{dE}{dt}. \tag{3.1.37}$$

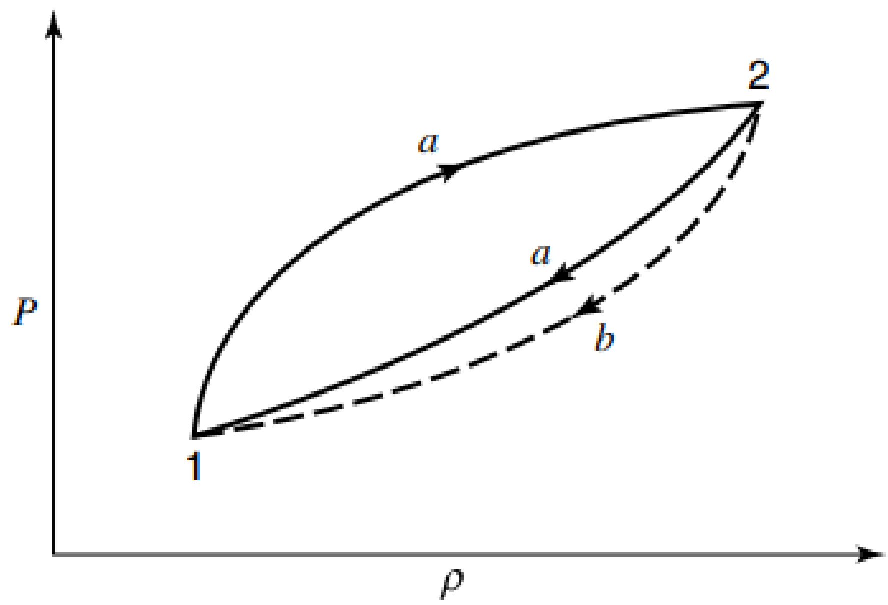

Figure 3.1.4: Reversible and irreversible thermodynamic cycles (Welty et al., 2014).

Like equation (3.1.11), the thermodynamics first law can be modeled in a control volume in the following manner.

$$H_i - W_d = E_o - E_i + E_a, \tag{3.1.38}$$

where H_i is rate of heat added from the surrounding, W_d is rate of work done by the control volume on its surroundings, E_o, E_i and E_a are the rates of energy out of, into and accumulation with in the control volume due to the flow of fluid respectively. The left side of the equation (3.1.38) is equivalent to (3.1.37). Then, the following result is obtained.

$$H_i - W_d = \frac{\delta Q}{dt} - \frac{\delta W}{dt} = \frac{dE}{dt}. \tag{3.1.39}$$

The rate of energy leaving the control volume through small area dA on the control surface can be formulated in the following manner

$$\text{Rate of energy efflux} = e(\rho v)(dA\cos\theta) = e\rho dA(|\mathbf{v}|\mathbf{n}|\cos\theta) = e\rho(\mathbf{v}\cdot\mathbf{n})dA.$$

Here, the product $dA\cos\theta$ is the rate of mass efflux from the control volume through dA, as discussed in the previous section. Then, like the expression for mass and momentum, the integral of this quantity over the control surface becomes

$$E_o - E_i = \iint_{c.s.} e\rho(\mathbf{v}\cdot\mathbf{n})dA. \tag{3.1.40}$$

Equation (3.1.40) indicates the net efflux of energy from the control volume and the scalar product, $\mathbf{v}\cdot\mathbf{n}$, accounts both for efflux and influx of mass across the control surface as considered. The quantity e is the specific energy or the energy per unit mass and it includes the potential energy (gy), by the position of fluid continuum in the gravitational field; the kinetic energy of the fluid $(u^2/2)$, due to its velocity; and the internal energy (U) of the fluid by its thermal state $(e = gy + u^2/2 + U)$.

The rate of accumulation of energy within the control volume can be expressed as

$$E_a = \frac{\partial}{\partial t}\iiint_{c.v.} e\rho dV. \tag{3.1.41}$$

Finally, combining equations (3.1.38) and (3.1.39), then the integral form of energy conservation can be expressed by using (3.1.40) and (3.1.41) as

$$\frac{dE}{dt} = \frac{\delta Q}{dt} - \frac{\delta W}{dt} = E_o - E_i + E_a = \iint_{c.s.} e\rho(\mathbf{v}\cdot\mathbf{n})dA + \frac{\partial}{\partial t}\iiint_{c.v.} e\rho dV. \tag{3.1.42}$$

In equation (3.1.42), the term $\delta W/dt$ stands for the rate of work done or power. It includes the following three types of work.

- **Shaft work (W_s):** It is the work done by the control volume on its surrounding that could cause a shaft to rotate or accomplish raising weight in a distance.

- **Flow work (W_σ):** This is the work done on the surroundings to overcome normal stresses on the control surface due to the existence of fluid flow.

- **Shear work (W_τ):** It is performed on the surroundings

Now, let us discuss the shear work of fluid flow based on Figure 3.1.1 in the control volume. The elemental portion of the control surface is denoted by dA. Assume the vector $\mathbf{S}$ is the force intensity (stress) having components σ_{ii} and τ_{ij} in the directions normal and tangential to the surface, respectively. In terms of $\mathbf{S}$, the force on dA is $\mathbf{S}dA$, and the rate of work done by the fluid flowing through dA is $\mathbf{S}dA \cdot \mathbf{v}$. Thus, the net rate of work done in the control volume on its surroundings by $\mathbf{S}$ is

$$\frac{\delta W}{dt} = \frac{\delta W_s}{dt} + \frac{\delta W_\sigma}{dt} + \frac{\delta W_\tau}{dt} = \frac{\delta W_s}{dt} - \iint_{c.s.} \mathbf{S} \cdot \mathbf{v} dA. \tag{3.1.43}$$

In equation (3.1.43), $-\mathbf{S}$ comes from the force per unit area on the surroundings. Then, equation (3.1.42) becomes

$$\begin{aligned} \iint_{c.s.} e\rho(\mathbf{v} \cdot \mathbf{n}) dA + \frac{\partial}{\partial t} \iiint_{c.v.} e\rho dV &= \frac{\delta Q}{dt} - \frac{\delta W_s}{dt} + \iint_{c.s.} \mathbf{S} \cdot \mathbf{v} \; dA \\ &= \frac{\delta Q}{dt} - \frac{\delta W_s}{dt} + \iint_{c.s.} \sigma_{ii}(\mathbf{n} \cdot \mathbf{v}) dA + \frac{\delta W_\tau}{dt}. \end{aligned} \tag{3.1.44}$$

In equation, (3.1.44), $\dfrac{\delta W_s}{dt}$ is the shaft work rate. Here, $\mathbf{S}$ contains the normal stress which is expressed as $\sigma_{ii}\mathbf{n}$, and the remaining shear stress is expressed as $\dfrac{\delta W_\tau}{dt}$.

The term containing normal stress is the sum of pressure and viscous effects. The work done can be combined the viscous portion of normal stress with shear work to get a single term. This is denoted by $\dfrac{\delta W_\mu}{dt}$ where the work rate is accomplished in overcoming viscous effects at the control surface. The rest part of the normal stress term that is associated with pressure may be written in slightly different form. As it is known that the bulk stress, σ_{ii}, is the negative of thermodynamic pressure, P. The shear and flow work terms can now be written as follows:

$$\iint_{c.s.} \sigma_{ii}(\mathbf{v} \cdot \mathbf{n}) dA + \frac{\delta W_\tau}{dt} = -\iint_{c.s.} P(\mathbf{v} \cdot \mathbf{n}) dA + \frac{\delta W_\mu}{dt}. \tag{3.1.45}$$

Using equation (3.1.45), equation (3.1.44) becomes

$$
\begin{aligned}
&\frac{\delta Q}{\partial t}-\frac{\delta W}{\partial t}=\frac{\delta Q}{dt}-\frac{\delta W_s}{dt}+\iint_{c.s.}\sigma_{ii}(\mathbf{n}\cdot\mathbf{v})dA+\frac{\delta W_\tau}{dt}\implies\\
&\frac{\delta Q}{dt}-\frac{\delta W_s}{dt}-\iint_{c.s.}P(\mathbf{v}\cdot\mathbf{n})dA+\frac{\delta W_\mu}{dt}=\iint_{c.s.}e\rho(\mathbf{v}\cdot\mathbf{n})dA+\frac{\partial}{\partial t}\iiint_{c.v.}e\rho dV\\
&\implies\frac{\delta Q}{dt}-\frac{\delta W_s}{dt}+\frac{\delta W_\mu}{dt}=\iint_{c.s.}\left(e+\frac{P}{\rho}\right)\rho(\mathbf{v}\cdot\mathbf{n})dA+\frac{\partial}{\partial t}\iiint_{c.v.}e\rho dV.
\end{aligned}
\tag{3.1.46}
$$

Similar to the fundamental equations of momentum in a differential control volume, the first law of thermodynamics is expressed in a control-volume as a basic analytical tool. Moreover, certain differential equations already developed in previous sections ca be applicable in energy term. Thus, equation (3.1.46), represents the general integral expression for energy transfer in the control volume. Considering the dimensions Δx, Δy and Δz, equation (3.1.46) can be expressed as follows by referring Figure 3.1.5.

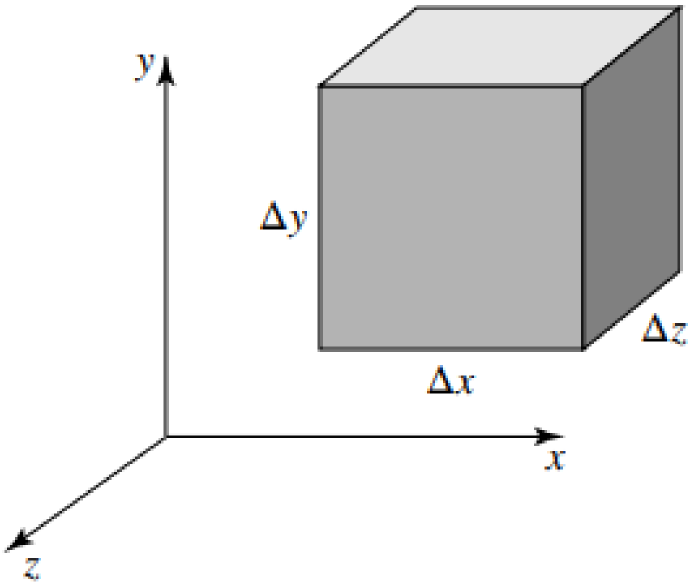

Figure 3.1.5: A differential control volume (Welty et al., 2014).

Thus, the term $\dfrac{\delta Q}{dt}$ is net rate heat added to the control volume including all conduction effects, net release of thermal energy in control volume, and is expressed as

$$
\begin{aligned}
\frac{\delta Q}{dt}=&\left[k\frac{\partial\bar{T}}{\partial x}|_{x+\Delta x}-k\frac{\partial\bar{T}}{\partial x}|_{x}\right]\Delta y\Delta z+\left[k\frac{\partial\bar{T}}{\partial y}|_{y+\Delta y}-k\frac{\partial\bar{T}}{\partial y}|_{y}\right]\Delta x\Delta z\\
&+\left[k\frac{\partial\bar{T}}{\partial z}|_{z+\Delta z}-k\frac{\partial\bar{T}}{\partial z}|_{z}\right]\Delta y\Delta x+\bar{q}\Delta x\Delta y\Delta z,
\end{aligned}
\tag{3.1.47}
$$

where $\bar{q}$ stands for the volumetric rate of thermal energy in W/m^3 or Btu/hft^3 unit.

In this case, the shaft work rate or power term will be taken as zero. It has no particular effect in the control volume, the shaft work rate is thus vanished.

$$\frac{\delta W_s}{dt} = 0. \tag{3.1.48}$$

The term $\dfrac{\delta W_\mu}{dt}$ is called viscous work rate, occurring at the control surface, and it is evaluated by integrating the dot product of the viscous stress with velocity over the control surface. As this process is tedious, the viscous work rate can e expressed as

$$\frac{\delta W_\mu}{dt} = \Lambda \Delta x \Delta y \Delta z, \tag{3.1.49}$$

where Λ is viscous work rate per unit volume. From the right side of equation (3.1.46), the surface integral includes all energy transfer occur by fluid flow over control surface which is explained in the following manner.

$$\begin{aligned}\iint_{c.s.} \left(e + \frac{P}{\rho}\right) \rho(\mathbf{v} \cdot \mathbf{n}) dA = &\left[\rho u_1 \left(e + \frac{P}{\rho}\right)|_{x+\Delta x} - \rho u_1 \left(e + \frac{P}{\rho}\right)|_x\right] \Delta y \Delta z \\ &+ \left[\rho u_2 \left(e + \frac{P}{\rho}\right)|_{y+\Delta y} - \rho u_2 \left(e + \frac{P}{\rho}\right)|_y\right] \Delta x \Delta z \\ &+ \left[\rho u_3 \left(e + \frac{P}{\rho}\right)|_{z+\Delta z} - \rho u_3 \left(e + \frac{P}{\rho}\right)|_z\right] \Delta y \Delta x.\end{aligned} \tag{3.1.50}$$

Associating the variation in total energy within the control volume as a function of time, the terms in the accumulation energy become

$$\frac{\partial}{\partial t} \iiint_{c.v.} e \rho dV = \frac{\partial e}{\partial t} \rho \Delta x \Delta y \Delta z \quad \text{where } e = \frac{u^2}{2} + gy + U. \tag{3.1.51}$$

Now, all terms in equation (3.1.46) can be defined and evaluated as from equations (3.1.47) to (3.1.51). Then dividing by $\Delta x \Delta y \Delta z$, equation (3.1.46) looks like

$$\begin{aligned}&\bar{q} + \Lambda + \frac{\left[k\partial \bar{T}/\partial x|_{x+\Delta x} - k\partial \bar{T}/\partial x|_x\right]}{\Delta x} + \frac{\left[k\partial \bar{T}/\partial y|_{y+\Delta y} - k\partial \bar{T}/\partial y|_y\right]}{\Delta y} \\ &+ \frac{\left[k\partial \bar{T}/\partial z|_{z+\Delta z} - k\partial \bar{T}/\partial z|_z\right]}{\Delta z} = \rho \frac{\partial e}{\partial t} + \frac{\left[\rho u_1 (e + P/\rho)|_{x+\Delta x} - \rho u_1 (e + P/\rho)|_x\right]}{\Delta x} \\ &+ \frac{\left[\rho u_2 (e + P/\rho)|_{y+\Delta y} - \rho u_2 (e + P/\rho)|_y\right]}{\Delta y} + \frac{\left[\rho u_3 (e + P/\rho)|_{z+\Delta z} - \rho u_3 (e + P/\rho)|_z\right]}{\Delta z}.\end{aligned} \tag{3.1.52}$$

Applying limit on the dimension of Δx, Δy and Δz approaching to zero, result in

$$\begin{aligned}\bar{q}+\Lambda+\frac{\partial}{\partial x}\left(k\frac{\partial\bar{T}}{\partial x}\right)+\frac{\partial}{\partial y}\left(k\frac{\partial\bar{T}}{\partial y}\right)+\frac{\partial}{\partial z}\left(k\frac{\partial\bar{T}}{\partial z}\right)&=\frac{\partial}{\partial x}\left[\rho u_1\left(e+P/\rho\right)\right]\\ +\frac{\partial}{\partial y}\left[\rho u_2\left(e+P/\rho\right)\right]+\frac{\partial}{\partial z}\left[\rho u_3\left(e+P/\rho\right)\right]+\frac{\partial}{\partial t}(\rho e).\end{aligned}\tag{3.1.53}$$

As a consequence of simplifying equation (3.1.53), it has the following form.

$$\begin{aligned}&\nabla\cdot(k\nabla\bar{T})+\bar{q}+\Lambda=\rho\frac{De}{Dt}+\mathbf{v}\cdot\nabla P=\rho\frac{D(\mathbf{v}^2/2)+gy+U)}{Dt}+\mathbf{v}\cdot\nabla P\\ &\nabla\cdot(k\nabla\bar{T})+\bar{q}+\Lambda=\frac{\rho}{2}\frac{D\mathbf{v}^2}{Dt}+\rho\frac{D(gy)}{Dt}+\rho\frac{DU}{Dt}+\mathbf{v}\cdot\nabla P\\ &\nabla\cdot(k\nabla\bar{T})+\bar{q}+\Lambda=\mathbf{v}\cdot(g\rho)-\mathbf{v}\cdot\nabla P+\mathbf{v}\cdot\mu\nabla^2\mathbf{v}+\rho\frac{D(gy)}{Dt}+\rho\frac{DU}{Dt}+\mathbf{v}\cdot\nabla P,\end{aligned}\tag{3.1.54}$$

where $U=c_p\bar{T}$, and momentum equation (3.1.31) implies $\rho\dfrac{D\mathbf{v}}{Dt}=\rho g-\nabla P+\mu\nabla^2\mathbf{v}$. Now, multiplying this by $\mathbf{v}$, we obtained $\dfrac{\rho}{2}\dfrac{D\mathbf{v}^2}{Dt}=\mathbf{v}\cdot(g\rho)-\mathbf{v}\cdot\nabla P+\mathbf{v}\cdot\mu\nabla^2\mathbf{v}$.

In a closed path, the rate of work done due gravity is zero, and also at the lowest height, the potential energy becomes zero. This implies that, the terms $\mathbf{v}\cdot(g\rho)=\rho\dfrac{D(gy)}{Dt}=0$. The term Λ in equations (3.1.49) and (3.1.54) can be expressed by the viscous portion of normal and shear stress functions. Thus, $\Lambda=\mathbf{v}\cdot\mu\nabla^2\mathbf{v}+\mu\Phi$ is given, where Φ is the dissipation function and always positive. Hence, for 2D and 3D incompressible flow, Φ is

$$\begin{aligned}&\Phi=2\left[\left(\frac{\partial u_1}{\partial x}\right)^2+\left(\frac{\partial u_2}{\partial y}\right)^2\right]+\left(\frac{\partial u_2}{\partial x}+\frac{\partial u_1}{\partial y}\right)^2\\ &\Phi=2\left[\left(\frac{\partial u_1}{\partial x}\right)^2+\left(\frac{\partial u_2}{\partial y}\right)^2+\left(\frac{\partial u_3}{\partial z}\right)^2\right]+\left(\frac{\partial u_2}{\partial x}+\frac{\partial u_1}{\partial y}\right)^2+\left(\frac{\partial u_2}{\partial z}+\frac{\partial u_3}{\partial y}\right)^2+\left(\frac{\partial u_3}{\partial x}+\frac{\partial u_1}{\partial z}\right)^2.\end{aligned}$$

Therefor, equation (3.1.54) further is reduced in the following form

$$\begin{aligned}\nabla\cdot(k\nabla\bar{T})+\bar{q}+\Lambda=\nabla\cdot(k\nabla\bar{T})+\bar{q}+\mathbf{v}\cdot\mu\nabla^2\mathbf{v}+\mu\Phi=\rho c_p\frac{DT}{Dt}+\mathbf{v}\cdot\mu\nabla^2\mathbf{v}\\ \Longrightarrow\ \rho c_p\frac{D\bar{T}}{Dt}=\rho c_p\left(\frac{\partial\bar{T}}{\partial t}+(\mathbf{v}\cdot\nabla)\bar{T}\right)=\nabla\cdot(k\nabla\bar{T})+\mu\Phi+\bar{q}.\end{aligned}\tag{3.1.55}$$

The effect of viscous dissipation is always positive and increasing internal energy at the expense of potential energy or stagnation pressure.

The term $\bar{q}$ includes thermal radiation, joule heating and the impact of slip mechanism. The Brownian and thermophoretic diffusion are the main slip mechanisms on heat transfer out of seven (Buongiorno, 2006). The suspended nanoparticles in the base fluid move randomly that cause Brownian diffusion. It occurs due to the continuous collisions of tiny solid particles. The movement of nanoparticles from a hot surface to cold by temperature difference is called thermophoretic diffusion. It happens as a result of thermophoretic force. Both, the Brownian and thermophoretic diffusion have a significant impact on heat and mass transfer processes. Hence, the total nanoparticles mass flux is defined as the sum of nanoparticles mass fluxes (J_p) due Brownian and thermophoresis diffusion, and is stated as

$$J_p = J_{pb} + J_{pt} = \rho_p D_B \nabla \bar{C} + \rho_p \frac{D_T}{\bar{T}_\infty} \nabla \bar{T} = \rho_p \left(D_B \nabla \bar{C} + \frac{D_T}{\bar{T}_\infty} \nabla \bar{T}\right).$$

The heat source per volume becomes (3.1.56)

$$c_p(\nabla \bar{T}) J_p = c_p \rho_p (\nabla \bar{T}) \left(D_B \nabla \bar{C} + \frac{D_T}{\bar{T}_\infty} \nabla \bar{T} \right),$$

where J_{pb} is denoted the nanoparticles mass flux due to Brownian diffusion, and J_{pt} denotes the nanoparticles mass flux due to thermopheresis diffusion.

3.1.4 The Species Concentration Equation

The species concentration equation is derived from the conservation of mass including the nanoparticles interaction on the physical system with the production or disappearance of a given species due to a chemical reaction. General law of mass balance for the given species concentration in the control volume can be stated as the sum of the net mass efflux rate and net rate of accumulation is equal to the rate of chemical production. Mathematically, it can be expressed as

$$C_i - C_o + C_a = C_p, \tag{3.1.57}$$

where C_i, C_o, C_a, C_p are the rate of mass in and out of the control volume, net rate of mass accumulation and rate of chemical production respectively. The net rate at which mass enters the control volume through the control surface, dS and the rate of fluid mass accumulation within the control volume becomes

$$\begin{aligned}
&C_i - C_o = -\iint_{c.s.} J_p.\mathbf{n}ds \text{ and based on RTT} \\
&C_a = \frac{d}{dt}\iiint_{c.v.} \rho\bar{C}dV = \rho\left(\iiint_{c.v.} \frac{\partial\bar{C}}{\partial t}dV + \iint_{c.s.} \bar{C}(\mathbf{v}\cdot\mathbf{n}dS)\right),
\end{aligned} \tag{3.1.58}$$

where J_p is the mass flux of the chemical species due to the Brownian motion and thermophoresis diffusion given in equation (3.1.56). Moreover, Reynolds's Transport Theorem (RTT) is applied for moving concentration ($\bar{C}$) with velocity vector ($\mathbf{v}$), as stated in Appendix A.1.1. Thus, equations (3.1.57) and (3.1.58), can be expressed as follows with no chemical production ($C_p = 0$).

$$\begin{aligned}
&\frac{d}{dt}\iiint_{c.v.} \rho\bar{C}dV - \iint_{c.s.} J_p.\mathbf{n}ds = 0 \\
\Longrightarrow &\iiint_{c.v.} \left(\frac{\partial\bar{C}}{\partial t} + \nabla\cdot(\bar{C}\mathbf{v})\right)\rho dV = \iiint_{c.v.} \nabla\cdot J_p dV \\
&\iiint_{c.v.} \left(\frac{\partial(\rho\bar{C})}{\partial t} + \nabla\cdot(\rho\bar{C}\mathbf{v}) - \nabla\cdot J_p\right)dV = 0 \Longrightarrow \frac{\partial(\rho\bar{C})}{\partial t} + \nabla\cdot(\rho\bar{C}\mathbf{v}) - \nabla\cdot J_p = 0 \\
&\rho\frac{\partial\bar{C}}{\partial t} + \rho\mathbf{v}\cdot\nabla\bar{C} = \nabla\cdot\left[\rho(D_B\nabla\bar{C} + \frac{D_T}{\bar{T}_\infty}\nabla\bar{T})\right] = \rho\left(D_B\nabla^2\bar{C} + \frac{D_T}{\bar{T}_\infty}\nabla^2\bar{T}\right).
\end{aligned} \tag{3.1.59}$$

Using the continuity equation ($\nabla\cdot\mathbf{v} = 0$) for nano-particle and constant density ($\frac{\partial\rho}{\partial t} = 0$), equation (3.1.59) produced the following species concentration $\bar{C}$ equation (3.1.60).

$$\frac{\partial\bar{C}}{\partial t} + (\mathbf{v}\cdot\nabla)\bar{C} = D_B\nabla^2\bar{C} + \frac{D_T}{\bar{T}_\infty}\nabla^2\bar{T}, \tag{3.1.60}$$

where D_B and D_T are Brownian and thermophoresis diffusion coefficient respectively.

3.1.5 Expression for Entropy

In a system the second law of thermodynamics is used to explain the concept of entropy (Bejan, 2013). Based on Figure 3.1.6, the production of entropy can be expressed as:

$$\int_1^2 \frac{\delta Q}{\bar{T}} = \frac{E_2 - E_1}{\bar{T}} \leq S_2 - S_1. \tag{3.1.61}$$

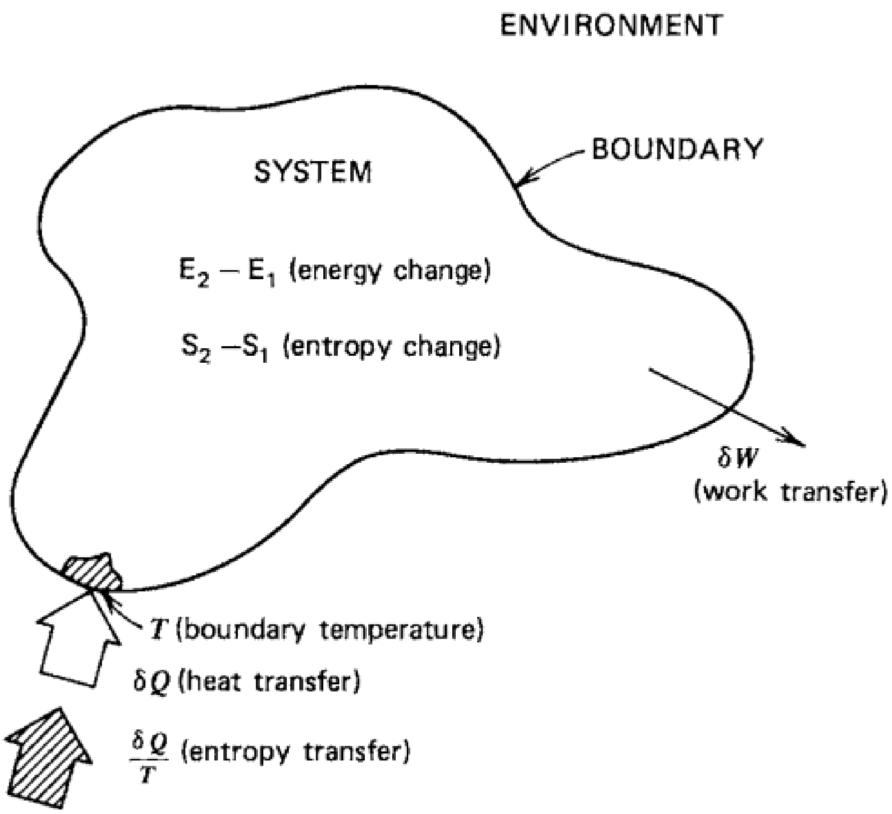

Figure 3.1.6: Closed thermodynamic with environmental interactions (Bejan, 2013).

In equation (3.1.61), the entropy generation is affected by the temperature at the boundary, heat and entropy transfer. The difference between possible paths is explained quantitatively by the amount of entropy generation S_{gen} which is

$$S_{gen} = S_2 - S_1 - \left(\frac{E_2 - E_1}{\bar{T}} \right) \geq 0.$$

The second law of thermodynamic states that any process is occurred by entropy generation. In the case of open system as in Figure 3.1.7, it is formulated as

$$\sum_{in} ms - \sum_{out} ms + \frac{\delta Q}{\bar{T}} \leq \frac{\partial S}{\partial t}. \tag{3.1.62}$$

In equation (3.1.62), ms related with the mass flow in the control volume. For the purpose of measuring the degree of irreversibility from the actual engineering systems, it is convenient to rearrange the second law inequality as

$$S_{gen} = \frac{\partial S}{\partial t} - \sum_{in} ms + \sum_{out} ms - \frac{\delta Q}{\bar{T}} \geq 0. \tag{3.1.63}$$

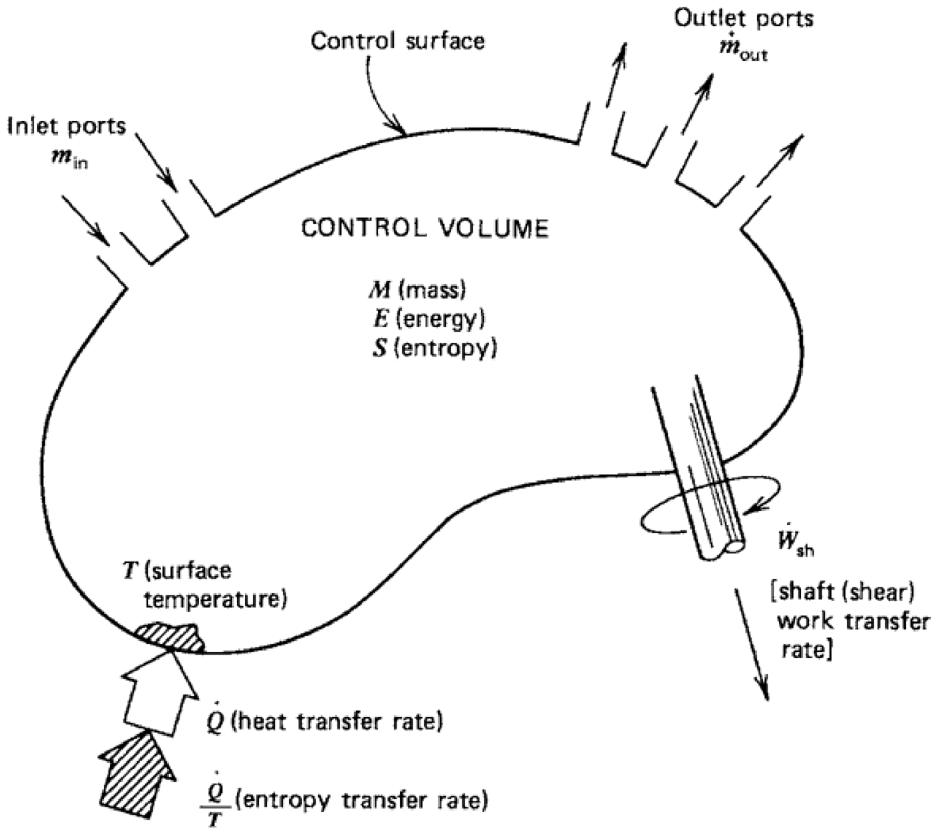

Figure 3.1.7: Open thermodynamic with environmental interactions (Bejan, 2013).

Equation (3.1.63) defines the rate of entropy generation in the system with unit W/K. It is always a positive quantity, and to zero in the reversible process. The relation between work lost or destruction (W_{lost}) available and entropy generation is

$$W_{lost} = \bar{T}_{\infty} S_{gen} = \bar{T}_{\infty} \left(\frac{\partial S}{\partial t} - \sum_{in} ms + \sum_{out} ms - \frac{\delta Q}{\bar{T}} \right). \tag{3.1.64}$$

Equation (3.1.64) is called Gouy-Stodola theorem which states that the available lost work is directly proportional to the entropy production. In fact, the velocity, temperature and concentration distribution in any laminar flow field can be determined analytically or numerically by solving the Navier-Stokes equations subject to an appropriate set of boundary and initial conditions. Once this solution is obtained, the local entropy generation rate can be evaluated in a straightforward manner.

In general, the entropy balance can be expressed as

$$\rho \frac{DS}{Dt} = -\nabla \cdot \left(\frac{\mathbf{q}}{\bar{T}} \right) + S', \tag{3.1.65}$$

where S' in equation (3.1.65) is the local entropy production and $\mathbf{q} = (q_x, q_y, q_z)$ stands for the form of entropy flux as Arpaci (1991).

$$\nabla \cdot \mathbf{q} = \nabla \left[\left(\frac{\mathbf{q}}{\bar{T}} \right) \bar{T} \right] = T \nabla \cdot \left(\frac{\mathbf{q}}{\bar{T}} \right) + \left(\frac{\mathbf{q}}{\bar{T}} \right) \nabla \bar{T}.$$

Assuming the process in local equilibrium, the local entropy production can be expressed as (Bejan, 2013)

$$S' = \frac{1}{\bar{T}} \left[- \left(\frac{\mathbf{q}}{\bar{T}} \right) \nabla \bar{T} + \mu \Phi + u' \right]. \tag{3.1.66}$$

In equation (3.1.66), u' is energy lost due to other energy. In particular, $\mathbf{q}$ denotes the total entropy flux by the sum of conductive and radiative flux, and expresses as

$$\mathbf{q} = -k \nabla \bar{T} + q_r = -k \nabla \bar{T} - \frac{16 T_\infty^3 \sigma^*}{3k^*} \frac{\partial \bar{T}}{\partial y} \text{ where } q_r \approx -\frac{16 T_\infty^3 \sigma^*}{3k^*} \frac{\partial \bar{T}}{\partial y}.$$
$$\text{Then, } \quad S' = \frac{1}{T} \left[\left(\frac{k \nabla \bar{T}}{\bar{T}} + \frac{16 T_\infty^3 \sigma^*}{3 \bar{T} k^*} \frac{\partial T}{\partial y} \right) \nabla T + \mu \Phi + u' \right].$$

Now, according to the entropy balance, the local entropy generation rate per unit volume (S'') for the impact of thermal radiation (Arpaci, 1987), conductive (Arpaci, 1991), Joule heating, porosity, fluid friction (Bejan, 2013), heat and mass irreversibility (San et al., 1987) is given as follows for 2D incompressible Newtonian fluid flow.

$$\begin{aligned} S'' = E_{pr} = & \frac{1}{\bar{T}_\infty} \left[\frac{1}{\bar{T}_\infty} \left(k \frac{\partial \bar{T}}{\partial x} + k \frac{\partial \bar{T}}{\partial y} - q_r \right) \frac{\partial \bar{T}}{\partial y} + \bar{p} + \mu \Phi \right] \\ & + \frac{RD}{\bar{T}_\infty} \left(\frac{\partial \bar{T}}{\partial x} + \frac{\partial \bar{T}}{\partial y} \right) \cdot \left(\frac{\partial \bar{C}}{\partial x} + \frac{\partial \bar{C}}{\partial y} \right) + \frac{RD}{\bar{C}_\infty} \left(\frac{\partial \bar{C}}{\partial x} + \frac{\partial \bar{C}}{\partial y} \right) \cdot \left(\frac{\partial \bar{C}}{\partial x} + \frac{\partial \bar{C}}{\partial y} \right), \end{aligned} \tag{3.1.67}$$

where $\bar{p}$ represents energy lost due to magnetic field interaction and permeability of the surface. Hence, equation (3.1.67) is the general local rate of entropy production per volume and it can adjusted and simplified based on the specific problem.

3.1.6 Boundary Layer Approximation

For solving the problems in fluid dynamics, the boundary layer approximation plays a key role. As a consequence, it is considered in the methodology section. The idea is introduced by Ludwig Prandtl in 1904 (Welty et al., 2014). L. Prandtl suggested that, at low Reynolds number, the impacts of fluid friction are limited to a thin layer near the boundary of a body. Thus, boundary layer is a thin region adjacent to the surface of a body where viscous forces dominate over inertia forces. In fact, the flow around a solid cannot be treated without viscous friction. However, the only thin region near the wall is affected by this friction which is called boundary layer. Moreover, there is no significant pressure change occur across the boundary layer. This means pressure in the boundary layer is the same as pressure in the inviscid flow outside the boundary layer. On the other side, there is a region in the flow where the effect of drag or viscosity is negligible called main (potential) or outer inviscid flow (Schlichting and Gersten, 2000). Although friction exists in all types of flows, the impact of friction on viscous fluid, mass, momentum and heat transfer are felt in the boundary layer.

As Figure 3.1.8 indicates the thickness of boundary layer increase with distance x. Depending on this, there are three regions in the boundary layer. These are laminar, transition and turbulent regions. At the lower values of x, the laminar boundary-layer region is developed with in the boundary layer. However, for a larger value of x, there exists the turbulent region in the boundary layer. Between laminar and turbulent field, there is a region called transition where the fluctuations between laminar and turbulent flows occur within the boundary layer. Moreover, in the turbulent region, there exist, a very thin film of fluid called the laminar sub-layer in which there is still laminar region and high velocity gradients present (Welty et al., 2014).

There is a criteria to identify whether the region of boundary layer is laminar or turbulent. For this purpose, the magnitude of Reynolds number (Re) is critically important. It is the dimensionless parameter that represents the ratio of inertia to viscous forces. Mathematically, Re is expressed as follows (Welty et al., 2014).

$$Re = \frac{xU_\infty \rho}{\mu} = \frac{xU_\infty}{\nu}, \quad \text{where} \quad \mu = \nu\rho.$$

For horizontal flow surfaces like Figure 3.1.8, the experimental result of Re_x shows

- $Re_x < 2 \times 10^5$ indicates laminar boundary layer.
- $2 \times 10^5 < Re_x < 3 \times 10^6$ shows either laminar or turbulent boundary layer.
- $Re_x > 3 \times 10^6$ indicates turbulent boundary layer.

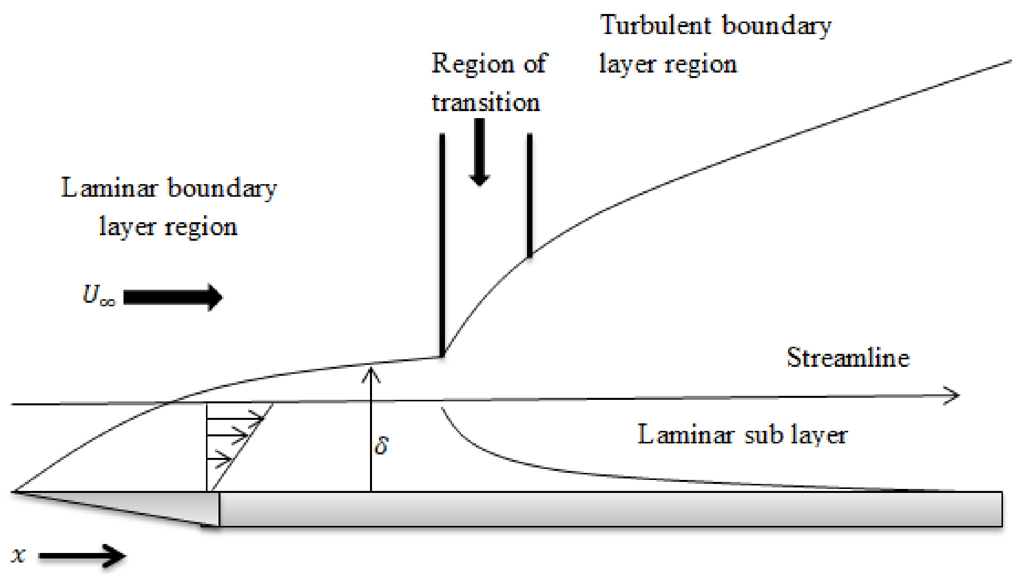

Figure 3.1.8: Boundary layer on a flat surface with small thickness.

Table 3.1.1: The difference between laminar and turbulent boundary layer region

No.	Conditions	Laminar region	Turbulent region
1	Fluid flow	Ordered and streamlined	Randomly and irregular
2	Steady-state	Time independent velocity change	Fluctuating velocity components
3	The diffusion of momentum, temperature and concentration	Occur at the boundary layer	Due to larger transfer, chaotic fluctuation conditions are occurred

The character and formation of boundary layer is basically important for heat and mass transfer process in fluid flow over a solid surface. Now, let us discuss the three kinds of boundary layers when fluid moves over a horizontal surface as Welty et al. (2014). This discussion was depend on the Figure 3.1.9 sketched by assuming the Prandtl number greater than one ($Pr > 1$).

1. **Velocity boundary layer**: is a thin layer where the fluid velocity gradients and shear stress are large. In this layer, the fluid velocity varies from zero at the surface to $0.99U_\infty$ of bulk fluid flow. The velocity boundary layer thickness (δ_{ve}) can be expressed in the following manner with a free stream velocity U_∞

$$\delta_{ve} = y \times 0.99U_\infty.$$

As a result of viscous force or shear stress applied along the x-axis (plane parallel to flow), the movement of fluid is retarded by the particles adjoining fluid layer until at the distance of $y = \delta_{ve}$ from the surface. In a flow over a horizontal surface (Figure 3.1.9), the velocity boundary layer profile changes with flow moving further on a plate. Inside the velocity boundary layer, there is high shear stress force which leads to the formation of velocity gradients in the opposite of the surface direction. The ratio of shear stress (τ_w) and velocity can be measured by dimensionless quantity called local skin friction coefficient which is expressed as

$$Cf_x = \frac{\tau_w}{\rho U_\infty^2/2} = \frac{\mu \frac{\partial u_1}{\partial y}|_{y=0}}{\rho U_\infty^2/2}, \quad \tau_w = \mu \frac{\partial u_1}{\partial y}|_{y=0} \implies \text{for Newtonian fluid.}$$

2. **Thermal boundary layer**: is a region where there exist a difference in the fluid temperature from surface to bulk fluid. So, it is a layer of the fluid in which temperature gradient exists. However, the fluid's particles that touch the surface gain thermal equilibrium which means the solid and the fluid have the same temperatures and also velocity of fluid is zero. Here, the transfer of heat takes place only by random molecular motion (conduction). On the other hand, these solid particles transfer heat with those in the adjoining fluid layer which leads to occur the temperature gradients in the fluid. Therefore, the temperature boundary layer is described by heat transfer and temperature gradients. It is occurred due to the variation in fluids and surface temperature near the plate.

   The thermal and velocity boundary layer will not be identical except $Pr = 1$. Prandtl number (Pr) is a dimensionless constant named after the Germans physicist Ludwig Prandtl and defined as the ratio of momentum to thermal diffusivity. The temperature boundary layer thickness (δ_{Te}) also formulated like (δ_{ve}) as

$$\delta_{Te} = y \times \left(\frac{\bar{T}_w - \bar{T}}{\bar{T}_w - \bar{T}_\infty} \right), \quad \text{where} \quad \frac{\bar{T}_w - \bar{T}}{\bar{T}_w - \bar{T}_\infty} = 0.99.$$

   Based on Figure 3.1.9, for horizontal surface, δ_{Te} and the temperature are functions of both distances from the tip (x) and height from plate (y) in the boundary layer. But, out of the boundary layer, the temperature becomes $\bar{T} = \bar{T}_\infty$. According to Fourier's law with temperature gradient and conductivity, the local plate heat flux at any distance from tip can be formulated as $q_w = -k \frac{\partial \bar{T}}{\partial y}|_{y=0}$

The convection heat flux (q_{cw}) is defined as $q_{cw} = h(\bar{T}_w - \bar{T}_\infty)$. It is clear that at surface convection heat transfer is only due to conduction. That is $q_{cw} = q_w$. Hence, a local convection heat transfer coefficient (h) is

$$q_{cw} = h(\bar{T}_w - \bar{T}_\infty) \implies h = \frac{q_{cw}}{\bar{T}_w - \bar{T}_\infty} = \frac{q_w}{\bar{T}_w - \bar{T}_\infty} = \frac{-k\frac{\partial \bar{T}}{\partial y}|_{y=0}}{\bar{T}_w - \bar{T}_\infty}.$$

3. **Concentration boundary layer**: Like the velocity and thermal boundary layers, concentration boundary layer can be developed when there is a concentration gradient near the surface. It is mainly dependent on the concentration gradients and convection mass transfer rates. The concentration boundary layer thickness (δ_{Co}) is expressed as

$$\delta_{Co} = y \times \left(\frac{\bar{C}_w - \bar{C}}{\bar{C}_w - \bar{C}_\infty}\right), \quad \text{where} \quad \frac{\bar{C}_w - \bar{C}}{\bar{C}_w - \bar{C}_\infty} = 0.99.$$

According to Figure 3.1.9, when the fluid flowing across horizontal surface, there is molar flux by diffusion from the plate at any distance from tip and it can be written with Fick's law and D_B, diffusion coefficient as

$$M_w = -D_B \frac{\partial \bar{C}}{\partial y}|_{y=0}.$$

The convective mass transfer is expressed as $M_{cw} = h_m(\bar{C}_w - \bar{C}_\infty) = M_w$. Similar to heat transfer coefficient, convection mass transfer coefficient can be

$$M_{cw} = h_m(\bar{C}_w - \bar{C}_\infty) \implies h_m = \frac{M_{cw}}{\bar{C}_w - \bar{C}_\infty} = \frac{M_w}{\bar{C}_w - \bar{C}_\infty} = \frac{-D_B\frac{\partial \bar{C}}{\partial y}|_{y=0}}{\bar{C}_w - \bar{C}_\infty}.$$

The boundary layer approximation is applicable to reduce the PDEs developed from conservation principles. Considering 2D incompressible fluid flow over flat surface, it follows $y \ll x, u_2 \ll u_1, \frac{\partial u_1}{\partial x} \approx \frac{\partial u_2}{\partial y}, \frac{\partial u_1}{\partial x} \ll \frac{\partial u_1}{\partial y}, \frac{\partial u_2}{\partial x} \ll \frac{\partial u_1}{\partial y}, \frac{\partial \bar{T}}{\partial x} \ll \frac{\partial \bar{T}}{\partial y}, \frac{\partial \bar{C}}{\partial x} \ll \frac{\partial \bar{C}}{\partial y}$ and using the boundary-layer thickness, $\frac{u_1}{u_2} \approx \frac{x}{y}$, from boundary layer approximation (Welty

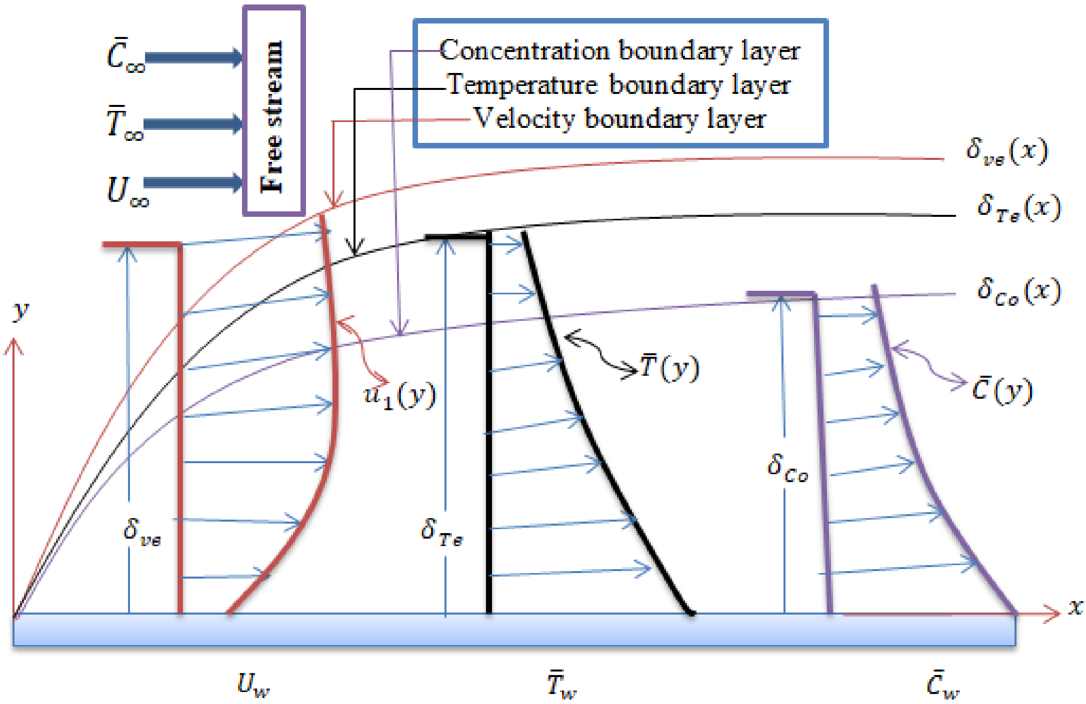

Figure 3.1.9: Velocity, temperature and concentration boundary layer of flow

et al., 2014). Thus, by applying this approximations, equation (3.1.31) becomes

$$
\begin{aligned}
\rho\frac{Du_1}{Dt} &= \rho g_x - \frac{\partial P}{\partial x} + \mu\left(\frac{\partial^2 u_1}{\partial x^2} + \frac{\partial^2 u_1}{\partial y^2}\right) \implies \rho\frac{Du_1}{Dt} = \rho g_x - \frac{\partial P}{\partial x} + \mu\left(\frac{\partial^2 u_1}{\partial y^2}\right) \\
\rho\frac{Du_2}{Dt} &= \rho g_y - \frac{\partial P}{\partial y} + \mu\left(\frac{\partial^2 u_2}{\partial x^2} + \frac{\partial^2 u_2}{\partial y^2}\right) \implies 0 = \frac{\partial P}{\partial y}
\end{aligned}
\tag{3.1.68}
$$

According to equation (3.1.68), $\frac{\partial P}{\partial y} = 0 \implies \frac{\partial P}{\partial x} = \frac{dP}{dx}$ since P depend only by x. The pressure P is constant ($\frac{dP}{dx} = 0$) in the boundary layer flow of fluids. If the flow has a horizontal rectangular geometry, equation (3.1.68) further written as follows.

$$
\rho\frac{Du_1}{Dt} = \rho\left(\frac{\partial u_1}{\partial t} + u_1\frac{\partial u_1}{\partial x} + u_2\frac{\partial u_1}{\partial y}\right) = \mu\left(\frac{\partial^2 u_1}{\partial y^2}\right) \tag{3.1.69}
$$

Similarly, applying boundary layer approximation, equation (3.1.55), becomes

$$
\begin{aligned}
\rho c_p\frac{D\bar{T}}{Dt} &= \rho c_p\left(\frac{\partial \bar{T}}{\partial t} + u_1\frac{\partial \bar{T}}{\partial x} + u_2\frac{\partial \bar{T}}{\partial y}\right) = k\left(\frac{\partial^2 \bar{T}}{\partial x^2} + \frac{\partial^2 \bar{T}}{\partial y^2}\right) + \mu\Phi + \bar{q} \\
&\implies \rho c_p\frac{D\bar{T}}{Dt} = k\left(\frac{\partial^2 \bar{T}}{\partial y^2}\right) + \mu\left(\frac{\partial u_1}{\partial y}\right)^2 + \bar{q} \quad \text{where } \Phi = \left(\frac{\partial u_1}{\partial y}\right)^2
\end{aligned}
\tag{3.1.70}
$$

Applying the boundary layer approximation, equation (3.1.60) can be expressed

$$\begin{aligned}\frac{DC}{Dt} =&\frac{\partial \bar{C}}{\partial t}+u_1\frac{\partial \bar{C}}{\partial x}+u_2\frac{\partial \bar{C}}{\partial y}=D_B\left(\frac{\partial^2 \bar{C}}{\partial x^2}+\frac{\partial^2 \bar{C}}{\partial y^2}\right)+\frac{D_T}{\bar{T}_\infty}\left(\frac{\partial^2 \bar{T}}{\partial x^2}+\frac{\partial^2 \bar{T}}{\partial y^2}\right)\\ \implies \frac{DC}{Dt} =&\frac{\partial \bar{C}}{\partial t}+u_1\frac{\partial \bar{C}}{\partial x}+u_2\frac{\partial \bar{C}}{\partial y}=D_B\left(\frac{\partial^2 \bar{C}}{\partial y^2}\right)+\frac{D_T}{\bar{T}_\infty}\left(\frac{\partial^2 \bar{T}}{\partial y^2}\right)\end{aligned} \tag{3.1.71}$$

Applying the boundary layer approximation on equation (3.1.67), then it is written as

$$\begin{aligned}S'' =&E_{pr}=\frac{1}{\bar{T}_\infty}\left[\frac{1}{\bar{T}_\infty}\left(k\frac{\partial \bar{T}}{\partial x}+k\frac{\partial \bar{T}}{\partial y}+q_r\right)\frac{\partial \bar{T}}{\partial y}+\bar{p}+\mu\Phi\right]\\ &+\frac{RD}{\bar{T}_\infty}\left(\frac{\partial \bar{T}}{\partial x}+\frac{\partial \bar{T}}{\partial y}\right)\cdot\left(\frac{\partial \bar{C}}{\partial x}+\frac{\partial \bar{C}}{\partial y}\right)+\frac{RD}{\bar{C}_\infty}\left(\frac{\partial \bar{C}}{\partial x}+\frac{\partial \bar{C}}{\partial y}\right)\cdot\left(\frac{\partial \bar{C}}{\partial x}+\frac{\partial \bar{C}}{\partial y}\right)\\ \implies E_{pr} =&\frac{1}{\bar{T}_\infty}\left[\frac{1}{\bar{T}_\infty}\left(k\frac{\partial \bar{T}}{\partial y}+q_r\right)\frac{\partial \bar{T}}{\partial y}+\bar{p}+\mu\left(\frac{\partial u_1}{\partial y}\right)^2\right]+\frac{RD}{\bar{T}_\infty}\left(\frac{\partial \bar{T}}{\partial y}\frac{\partial \bar{C}}{\partial y}\right)+\frac{RD}{\bar{C}_\infty}\left(\frac{\partial \bar{C}}{\partial y}\right)^2\end{aligned} \tag{3.1.72}$$

3.1.7 Boundary Conditions

In this dissertation, the problems are solved by considering different boundary conditions which have their own applications in heat and mass transfer. They are used to solve the fluid dynamics problems. Generally, the boundary conditions include no-slip/slip, mass suction/injection and convective heat transfer boundary conditions.

As a result of viscous effect on moving fluid, the no-slip situation is happened. The no slip conditions developed when both the fluid and boundary layer have no motion which implies fluid flow on a surface stick to the plate. To make clear the no-slip condition occurs in fluid flow whenever there is no relative motion between the wall and fluid during the contact with boundary. Although the no-slip condition simplifies the governing equations, it is not sufficient for demonstrating the observable wall slip (Daniel et al., 2020). Commonly, the solid surface is assumed to be rough, which slows down the fluid flow at the surface. Thus, slip condition is applicable in situations where the velocity is small. As Daniel et al. (2020) stated, slip boundary conditions can occur due to the low viscosity, loss of adhesive on the solid surface. Fluid flow over a slippery region is essential for varies industries, modern sciences and technology (Jan et al., 2019; Sehra et al., 2021).

In this dissertation, the researchers consider convective boundary condition to see the role of nanofluid in the process of heat and mass transmission from thermal solar radiation and other heat sources. Convective is a mode of heat transfer in fluids, wherein the moving fluid particles carry heat in the form of internal energy (Welty et al., 2014). Convective boundary condition has several industrial and engineering processes, such as storage of thermal energy, solar panel, nuclear and gas turbines, and so on (Khan et al., 2022c). For controlling the flow, heat transfer and energy loss, the mass suction/injection has an important role as a boundary conditions.

3.2 Mathematical Procedure

To solve each problem in this dissertation, the following steps are used:

1. Deriving the PDEs from the governing equations.
2. Simplifying the derived PDEs by applying the concept of boundary layer and Boussinesq approximations.
3. Converting the simplified PDEs into ODEs by taking suitable similarity transformations. However, these ODEs were non-linear and higher-order.
4. As a result, solving these ODEs using analytical methods is complicated. Therefore, semi-analytical and/or numerical methods have been used to solve them.
5. Finally, the outcomes have been displayed graphical and tabular manner.

3.3 Homotopy Analysis Method (HAM)

In this section, the researchers discuss about one method of solving non-linear higher order system of ODEs of boundary value problem type is called HAM. It works based on the Taylor series expansion with out the need of domain discretization. So, it is called analytic method. Using the next section, the researchers try to explain the background, computational techniques and convergence properties of HAM.

3.3.1 Background on HAM with Comparison

As Liao (2013) explained, any non-linear problem can be examined using physical experiment, numerical simulation and analytic (approximation) method having their own merits and demerits. These points discussed in the following manner.

- Physical experiments: are the basic approach but they are expensive, time-consuming and hard to satisfy all similarity criterion.
- Numerical methods: nonlinear equations can be solved approximately. However, it may be difficult for nonlinear problems with singularity and multiple solutions.
- In analytic (approximation) methods: one can investigate nonlinear problems with singularity and multiple solutions in an infinity interval, but equations should be defined in a simple enough domain (well-defined and clear rule).

In general, for a non linear problem, obtaining an exact and closed form solution is difficult. However, to understand non linear phenomena in a better way and to obtain analytic approximations, mostly perturbation techniques are used which make great contribution to the development of nonlinear sciences. Actually, perturbation method is invalid for strongly non linear problems in general due to their dependence upon physically small parameters. That is why it can not be applicable for any kind of equation.

Then, the non perturbation method called Lyapunov's artificial small-parameter method (LASPM) was developed. It is independent on small parameter. As Zhang and Liang (2015) explained, it works using the linear and non-linear operators for linear and non-linear part of the problem respectively. LASPM has no freedom to choose linear operator for obtaining guaranteed convergence solution. Next, Adomian decomposition method (ADM) was developed in which the linear operator is related with higher order. So that the higher order approximation is easily solved. But still there is a gap on taking any linear operator and lack of guaranteed convergence criteria.

Basically, the two non perturbation methods (LASPM and ADM) can convert the non-linear equation into an infinite number of linear sub-problems. The limitations of these approaches are fixing the linear operators and no way to guarantee the convergence of approximated series. It is known that divergent approximations are useless. Therefore, like perturbation method, the traditional non-perturbation methods (such as LASPM and ADM) are often valid for weakly nonlinear problems in most cases. Henceforth, for any kind of non linear problem, it is valuable to develop a new kind of method which should have the following characteristics:

1. It is independent of small physical parameter;

2. It provides us great freedom and flexibility to choose the equation-type and solution expression of high-order approximation equations;

3. It provides us a convenient way to guarantee convergence of approximation series.

HAM is an analytic approximation technique that satisfies the above three properties. It has been developed by Shijun Liao from 1990s to 2010s together with different scholars (Liao, 2013). In HAM, there is great freedom to choose the auxiliary linear operator, the initial guess, the auxiliary function and the value of convergence-control parameter. This method also exploits the statement of Georg Cantor (1845-1918) which is "the essence of mathematics that lies entirely in its freedom". In spite of the advantages exist in HAM, lacking the criteria for selecting suitable linear operator and initial guess are the major challenges confronted by applying HAM. These difficulties can be managed by trial and error. As Liao (2012) states, the benefits of HAM are:

1. Independent of small/large physical parameters;

2. Guarantee of convergence;

3. Flexibility on the choice of base function and initial guess of solution.

HAM is capable of achieving the solutions of boundary value problems of non linear higher order system of ODEs nicely. It is an analytic tool that solves highly nonlinear problems in science, finance and engineering. In HAM, the solution expressed in an infinite series, hence it is difficult to handle by hand calculation. Instead, it is computed on Mathematica 12.1, using BVBh2.0 package developed by Zhao and Liao (2014).

3.3.2 Computational Techniques of HAM

Here, the basic points in computing the equation by HAM has been discussed briefly. The concept of HAM is based on the idea of homotopy which is a basic term in topology and differential geometry. This subsection starts by defining the term homotopy.

Definition 1. A homotopy is defined as a connection between different things in mathematics, which contains the same characteristics in some aspects.

Liao (2012) also defined the word "homotopy" in general as follows.

Definition 2. A homotopy between two continuous functions $f(x)$ and $g(x)$ from a topological space $\mathbf{X}$ to a topological space $\mathbf{Y}$ is formally defined to be a continuous function $\mathbb{H}:\mathbf{X}\times[0,1]\rightarrow\mathbf{Y}$ from the product of the space $\mathbf{X}$ with the unit interval $[0,1]$ to $\mathbf{Y}$ such that, if $x\in\mathbf{X}$ then $\mathbb{H}(x;0)=f(x)$ and $\mathbb{H}(x;1)=g(x)$

In homotopy, a continuous real function deformed continuously into a continuous function. The discussion of HAM begins by considering the non-linear equation $\mathcal{N}[f(\mathbf{x},t)]=0$ with initial guess $f_0(\mathbf{x},t)$, where $\mathcal{N}$ is a non-linear differential operator, $f(\mathbf{x},t)$ is an unknown function, $\mathbf{x}$ is a vector of spatial independent-variables, t denotes the temporal independent variable.

$$\mathbb{H}(\mathbf{x},t;p)=(1-p)\mathcal{L}[\Phi(\mathbf{x},t;p)-f_0(\mathbf{x},t)]+p\mathcal{N}[\Phi(\mathbf{x},t;p)]. \tag{3.3.1}$$

In equation (3.3.1), $\mathcal{L}$ denotes linear operator and $p\in[0,1]$ is the homotopy embedding parameter without any physical meaning. Now, enforcing $\mathbb{H}(\mathbf{x},t;p)$ to zero results in

$$(1-p)\mathcal{L}[\Phi(\mathbf{x},t;p)-f_0(\mathbf{x},t)]+p\mathcal{N}[\Phi(\mathbf{x},t;p)]=0,\quad 0\leq p\leq 1. \tag{3.3.2}$$

Equation (3.3.2) is the first step and is called the zero$^{\text{th}}$-order deformation equation where $\Phi(\mathbf{x},t,p)$ is an unknown function. Then, for $p=0$ and $p=1$, the next result is obtained.

$$\begin{aligned} &p=0,\quad \mathcal{L}[\Phi(\mathbf{x},t;p)-f_0(\mathbf{x},t)]=0 \implies \Phi(\mathbf{x},t;0)=f_0(\mathbf{x},t)\\ &\text{and } p=1,\quad \mathcal{N}[\Phi(\mathbf{x},t;p)]=0 \implies \Phi(\mathbf{x},t;1)=f(\mathbf{x},t). \end{aligned} \tag{3.3.3}$$

From equation (3.3.3), someone can understand that, as p run from 0 to 1, $\mathbb{H}(\mathbf{x},t;p)$ varies continuously from $\Phi(\mathbf{x},t;0)=f_0(\mathbf{x},t)$ to $\Phi(\mathbf{x},t;1)=f(\mathbf{x},t)$. In another way, as p varies from 0 to 1, $\mathbb{H}(\mathbf{x},t;p)$ varies from the initial guess, $f_0(\mathbf{x},t)$ to the exact unknown solution $f(\mathbf{x},t)$. This type of continuous variation is called deformation in topology. Due to the absence of a physical meaning for p, there exists a freedom for constructing the zero$^{\text{th}}$-order deformation equation. Moreover, HAM has a freedom to select linear operator ($\mathcal{L}$) which is mandatory to fix in LASPM or ADM.

Similar to perturbation techniques, equation (3.3.2) can not guarantee the convergence of homotopy-series. Hence, using the freedom that exists in HAM, equation

(3.3.2) has been constructed in another way to obtain a convergent solution particularly for strong non-linear problems. Thus, as Liao (1997) explained a non-zero auxiliary constant called convergence control parameter (c_0) that introduced to construct a more generalized zero$^{\text{th}}$-order deformation equation. Therefore, equation (3.3.2) becomes

$$(1-p)\mathcal{L}[\Phi(\mathbf{x},t;p)-f_0(\mathbf{x},t)] = c_0 p\mathcal{N}[\Phi(\mathbf{x},t;p)], \quad 0 \leq p \leq 1. \tag{3.3.4}$$

Equation (3.3.4) depends on not only $\mathbf{x}$ and t, but also the non-zero auxiliary parameter c_0. One more 'artificial' degree of freedom is introduced by auxiliary convergent parameter (c_0).. Moreover, c_0 provides a convenient way to control the convergence of homotopy-series by choosing it properly.

The zero$^{\text{th}}$-order deformation equation can also be constructed by introducing a non-zero auxiliary function ($\mathcal{H}(\mathbf{x},t)$). Thus, equation (3.3.4) is expressed as follows:

$$(1-p)\mathcal{L}[\Phi(\mathbf{x},t;p)-f_0(\mathbf{x},t)] = c_0 p\mathcal{H}(\mathbf{x},t)\mathcal{N}[\Phi(\mathbf{x},t;p)], \quad 0 \leq p \leq 1. \tag{3.3.5}$$

$\mathcal{H}(\mathbf{x},t)$ is introduced by Liao (2003). Generally, the implementation of HAM is strongly related to the construction of zero$^{\text{th}}$-order deformation. Improving the development of equation (3.3.2) by introducing c_0 in (3.3.4), and adding $\mathcal{H}(\mathbf{x},t)$ term in (3.3.5), used to guarantee the convergence of homotopy series solutions. In this dissertation, the researchers have constructed zero$^{\text{th}}$-order deformation according to the form of equation (3.3.5). For this, HAM allows us to select $c_0, \mathcal{H}(\mathbf{x},t), f_0(\mathbf{x},t)$, and $\mathcal{L}$. The solution of equation (3.3.5) for $p=0$ and $p=1$ are stated as follows where $c_0 \neq 0, \mathcal{H}(\mathbf{x},t) \neq 0$.

$$\begin{aligned} &p=0,\ \mathcal{L}[\Phi(\mathbf{x},t;0)-f_0(\mathbf{x},t)] = 0 \implies \Phi(\mathbf{x},t;0) = f_0(\mathbf{x},t) \ \text{ and for } p=1 \\ &c_0\mathcal{H}(\mathbf{x},t)\mathcal{N}[\Phi(\mathbf{x},t;1)] = 0 \implies \mathcal{N}[\Phi(\mathbf{x},t;1)] = 0 \implies \Phi(\mathbf{x},t;1) = f(\mathbf{x},t). \end{aligned} \tag{3.3.6}$$

Now, using Taylor series expansion, $\Phi(\mathbf{x},t;p)$ can be expanded about $p=0$ as

$$\begin{aligned} \Phi(\mathbf{x},t;p) &= \Phi(\mathbf{x},t;0) + \frac{p\partial\Phi(\mathbf{x},t;p)}{\partial p}|_{p=0} + \frac{p^2\partial^2\Phi(\mathbf{x},t;p)}{2!\partial p^2}|_{p=0} + \frac{p^3\partial^3\Phi(\mathbf{x},t;p)}{3!\partial p^3}|_{p=0} + \\ &= \Phi(\mathbf{x},t;0) + \sum_{m=1}^{\infty} \frac{p^m\partial^m\Phi(\mathbf{x},t;p)}{m!\partial p^m}|_{p=0} = f_0(\mathbf{x},t) + \sum_{m=1}^{\infty} f_m(\mathbf{x},t)p^m \\ &\implies \Phi(\mathbf{x},t;p) = f_0(\mathbf{x},t) + f_1(\mathbf{x},t)p^1 + f_2(\mathbf{x},t)p^2 + f_3(\mathbf{x},t)p^3 + ..., \end{aligned} \tag{3.3.7}$$

where $m!f_m(\mathbf{x},t) = \dfrac{\partial^m \Phi(\mathbf{x},t;p)}{\partial p^m}|_{p=0}$ is called the m^{th}-order deformation derivative. Hence, equation (3.3.7) helps us to obtain a relation between the initial guess and the exact solution by means of the terms $f_m(\mathbf{x},t), m = 1,2,3,\cdots$. Here, the $f_m(\mathbf{x},t)$ is computed by using the zero$^{\text{th}}$-order deformation equation (3.3.5). That is, $f_m(\mathbf{x},t)$ can be obtained by differentiating equation (3.3.5), m times with respect to the embedding parameter p, then setting $p = 0$ and dividing it by $m!$. Here, in equation (3.3.5), the expression $\Phi(\mathbf{x},t;p)$, is replaced by its Taylor expansion at $p = 0$ in equation (3.3.7). The following equations explain this procedure and constructed the general m$^{\text{th}}$-order deformation equation by observing the expressions for $m = 1,2,3$.

- From the first derivative of equation (3.3.5), that is $m = 1$, $f_1(\mathbf{x},t)$ becomes

$$
\begin{aligned}
&(1-p)\mathcal{L}[f_1(\mathbf{x},t) + 2pf_2(\mathbf{x},t) + 3p^2 f_3(\mathbf{x},t) + \cdots] \\
&- \mathcal{L}[pf_1(\mathbf{x},t) + p^2 f_2(\mathbf{x},t) + p^3 f_3(\mathbf{x},t) + \cdots] = \\
&c_0\mathcal{H}(\mathbf{x},t)\mathcal{N}[f_0(\mathbf{x},t) + pf_1(\mathbf{x},t) + p^2 f_2(\mathbf{x},t) + p^3 f_3(\mathbf{x},t) + \cdots] + \\
&c_0\mathcal{H}(\mathbf{x},t)p\mathcal{N}[f_1(\mathbf{x},t) + 2pf_2(\mathbf{x},t) + 3p^2 f_3(\mathbf{x},t) + \cdots], \ \text{ setting } p = 0 \ \text{ we get} \\
&\mathcal{L}[f_1(\mathbf{x},t)] = c_0 H(\mathbf{x},t)\mathcal{N}[f_0(\mathbf{x},t)] \implies f_1(\mathbf{x},t) = c_0\mathcal{L}^{-1}\{H(\mathbf{x},t)\mathcal{N}[f_0(\mathbf{x},t)]\}.
\end{aligned}
$$

- Given, $f_0(\mathbf{x},t)$ and $f_1(\mathbf{x},t)$, the second derivative of equation (3.3.5) is used to get $f_2(\mathbf{x},t)$ as:

$$
\begin{aligned}
&(1-p)\mathcal{L}[2f_2(\mathbf{x},t) + 6pf_3(\mathbf{x},t) + \cdots] - 2\mathcal{L}[f_1(\mathbf{x},t) + 2pf_2(\mathbf{x},t) + 3p^2 f_3(\mathbf{x},t) + \cdots] = \\
&2c_0\mathcal{H}(\mathbf{x},t)\mathcal{N}[f_1(\mathbf{x},t) + 2pf_2(\mathbf{x},t) + 3p^2 f_3(\mathbf{x},t) + \cdots] + \\
&c_0\mathcal{H}(\mathbf{x},t)p\mathcal{N}[2f_2(\mathbf{x},t) + 6pf_3(\mathbf{x},t) + \cdots] \text{ setting } p = 0,\ 2\mathcal{L}[f_2(\mathbf{x},t) - f_1(\mathbf{x},t)] = \\
&2c_0 H(\mathbf{x},t)\mathcal{N}[f_1(\mathbf{x},t)] \implies f_2(\mathbf{x},t) = f_1(\mathbf{x},t) + c_0\mathcal{L}^{-1}\{H(\mathbf{x},t)\mathcal{N}[f_1(\mathbf{x},t)]\}
\end{aligned}
.
$$

- In this, $f_0(\mathbf{x},t)$, $f_1(\mathbf{x},t)$ and $f_2(\mathbf{x},t)$ are given above, then the third derivative of (3.3.5) $(m = 3)$ is used to obtain $f_3(\mathbf{x},t)$ as follows.

$$
\begin{aligned}
&(1-p)\mathcal{L}[6f_3(\mathbf{x},t) + \cdots] - \mathcal{L}[2f_2(\mathbf{x},t) + 6pf_3(\mathbf{x},t) + \cdots] - 2\mathcal{L}[2f_2(\mathbf{x},t) + 6pf_3(\mathbf{x},t) + \cdots] \\
&= 3c_0\mathcal{H}(\mathbf{x},t)\mathcal{N}[2f_2(\mathbf{x},t) + 6pf_3(\mathbf{x},t) + \cdots] + c_0\mathcal{H}(\mathbf{x},t)p\mathcal{N}[6f_3(\mathbf{x},t) + \cdots] \\
&\text{Then setting } p = 0, \quad 6\mathcal{L}[f_3(\mathbf{x},t) - f_2(\mathbf{x},t)] = 6c_0 H(\mathbf{x},t)\mathcal{N}[f_2(\mathbf{x},t)] \\
&\implies f_3(\mathbf{x},t) = f_2(\mathbf{x},t) + c_0\mathcal{L}^{-1}\{H(\mathbf{x},t)\mathcal{N}[f_2(\mathbf{x},t)]\} \quad \text{and so on.}
\end{aligned}
$$

Therefore, the m$^{\text{th}}$-order deformation equation can be generally written as

$$\mathcal{L}[f_m(\mathbf{x},t) - \chi_m f_{m-1}(\mathbf{x},t)] = c_0 \mathcal{H}(\mathbf{x},t) \mathcal{R}_m(f_{m-1}(\mathbf{x},t)). \tag{3.3.8}$$

$\mathcal{R}_m(f_{m-1}(\mathbf{x},t)) = \dfrac{1}{(m-1)!} \dfrac{\partial^{m-1} \mathcal{N}[\Phi(\mathbf{x},t;p)]}{\partial p^{m-1}}|_{p=0}$ can be expressed in terms of $f_0(\mathbf{x},t), f_1(\mathbf{x},t), f_2(\mathbf{x},t), \cdots, f_{m-1}(\mathbf{x},t), \cdots$ where m starts from 1. The step function χ_m is defined as

$$\chi_m = \begin{cases} 0 & \text{for } m \leq 1 \\ 1 & \text{for } m > 1. \end{cases} \tag{3.3.9}$$

Thus, the m$^{\text{th}}$-order deformation in (3.3.8) is used to find the terms $f_1(\mathbf{x},t), f_2(\mathbf{x},t), f_3(\mathbf{x},t), \cdots$ by taking the inverse of linear operator as explained above and summarized as follows.

$$\begin{aligned}
&f_1(\mathbf{x},t) = c_0 \mathcal{L}^{-1} \left[H(\mathbf{x},t) \mathcal{R}_1(f_0(\mathbf{x},t))\right], \\
&f_2(\mathbf{x},t) = f_1(\mathbf{x},t) + c_0 \mathcal{L}^{-1} \left[H(\mathbf{x},t) \mathcal{R}_2(f_1(\mathbf{x},t))\right] \\
&f_3(\mathbf{x},t) = f_2(\mathbf{x},t) + c_0 \mathcal{L}^{-1} \left[H(\mathbf{x},t) \mathcal{R}_3(f_2(\mathbf{x},t))\right] \text{ and so on.} \\
&\text{Generally, } \ f_m(\mathbf{x},t) = \chi_m f_{m-1}(\mathbf{x},t) + c_0 \mathcal{L}^{-1} \left[H(\mathbf{x},t) \mathcal{R}_m(f_{m-1}(\mathbf{x},t))\right].
\end{aligned} \tag{3.3.10}$$

Finally, according to (3.3.7), the exact solution of the original problem becomes

$$\Phi(\mathbf{x},t;p) = f_0(\mathbf{x},t) + \sum_{m=1}^{\infty} f_m(\mathbf{x},t) p^m. \tag{3.3.11}$$

For $p = 1$, equation (3.3.11) produces an exact solution as formulated below

$$\Phi(\mathbf{x},t;1) = f(\mathbf{x},t) = f_0(\mathbf{x},t) + \sum_{m=1}^{\infty} f_m(\mathbf{x},t). \tag{3.3.12}$$

Equation (3.3.12) becomes accurate as $m \to \infty$. However, evaluating all values of $f_m(\mathbf{x},t)$ is difficult. As a result, the infinite series solutions limited to some value of m by considering the convergence of solutions. This makes the HAM to be semi-analytic. In general, the overall procedures of HAM are exhibited pictorially in the following way using the flow chart give below.

The flow chart 3.3.1 is used for solving the problems by applying HAM on Mathematica mathematical language to employ the package BVPh2.0 that Zhao and Liao (2014) developed. The next subsection discusses about the convergent solutions of

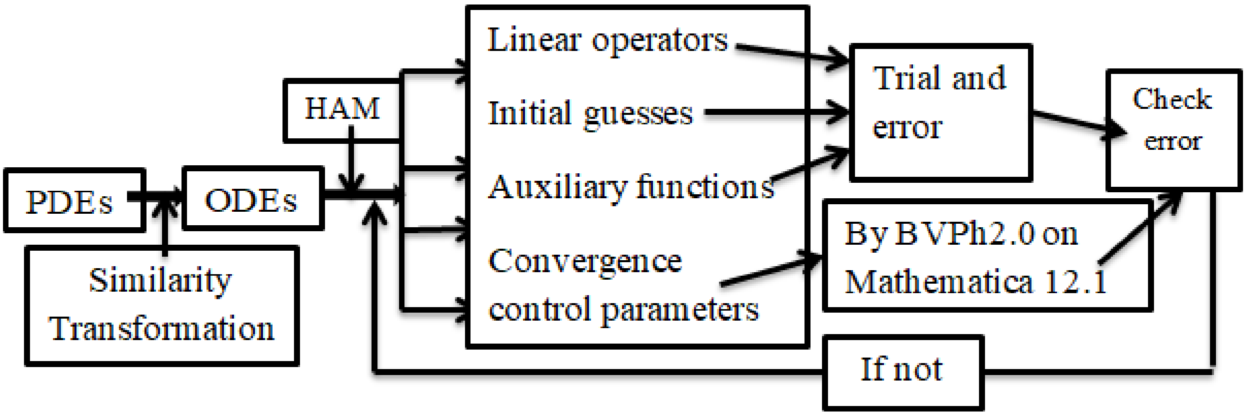

Figure 3.3.1: Flow chart that shows the step of HAM

HAM, since the divergent solution is useless.

3.3.3 Convergence Analysis of HAM

This subsection explains the convergent property of HAM that is expressed as a sum of infinite series. It is known that the truncating order of the analytic solution is applicable when its limit goes to exact. Now, let us start by stating the next Mathematical fact

$$f_M(\mathbf{x},t) = f_0(\mathbf{x},t) + \sum_{m=1}^{M} f_m(\mathbf{x},t) \text{ and } f(\mathbf{x},t) = \lim_{M\to\infty} f_M(\mathbf{x},t). \tag{3.3.13}$$

In fact, the success of HAM substantially depend upon the zero$^{\text{th}}$-order deformation in equation (3.3.5). For this purpose, the auxiliary linear operator ($\mathcal{L}$), initial guess ($f_0(\mathbf{x},t)$), convergence control parameter (c_0) and auxiliary function ($\mathcal{H}(\mathbf{x},t)$) have been chosen properly. As a result, the homotopy series in equation (3.3.11) converges at $p = 1$ which is verified by the next theorem.

Theorem 3.3.1. *Suppose that $A \subset R$ be a Banach space associated with a suitable norm $\|\|$ (depending on the physical problem under consideration), over which the functional sequence $f_m(\boldsymbol{x},t)$ of (3.3.11). Assume also that the initial approximation $f_0(\boldsymbol{x},t)$ remains inside the ball of the solution $f(\boldsymbol{x},t)$ of the original problem. Taking $r \in R^+$ be a constant, based on the prescribed convergence control parameter c_0, if $\|f_{n+1}(\boldsymbol{x},t)\| \leq r\|f_n(\boldsymbol{x},t)\|$ $\forall n$ where $0 < r < 1$, then the series solution $\Phi(\boldsymbol{x},t,p)$ defined in equation (3.3.11) converges absolutely at $p = 1$ to $f(\boldsymbol{x},t)$ given by equation (3.3.12) over the domain of definition of t.*

Proof. Assume $S_n(\mathbf{x},t)$ is the sequence of partial sums of the series in (3.3.12). It is important to show that $S_n(\mathbf{x},t)$ is a Cauchy sequence in A. For this, the following inequalities can be constructed.

$$\|S_{n+1}(\mathbf{x},t)-S_n(\mathbf{x},t)\| = \|f_{n+1}(\mathbf{x},t)\| \leq r\|f_n(\mathbf{x},t)\| \leq r^2\|f_{n-1}(\mathbf{x},t)\| \leq \cdots \leq r^{n+1}\|f_0(\mathbf{x},t)\| \tag{3.3.14}$$

Applying the triangular inequality on equation (3.3.14) for $\forall k,n \in N$ such that $k \leq n$, the following result is obtained:

$$\begin{aligned}
\|S_n(\mathbf{x},t)-S_k(\mathbf{x},t)\| =& \|(S_n(\mathbf{x},t)-S_{n-1}(\mathbf{x},t))+(S_{n-1}(\mathbf{x},t)-S_{n-2}(\mathbf{x},t))+\cdots \\
&+(S_{k+1}(\mathbf{x},t)-S_k(\mathbf{x},t))\| \leq \|S_n(\mathbf{x},t)-S_{n-1}(\mathbf{x},t)\| \\
&+\|S_{n-1}(\mathbf{x},t)-S_{n-2}(\mathbf{x},t)\|+\cdots+\|S_{k+1}(\mathbf{x},t)-S_k(\mathbf{x},t)\| \\
\leq& \|r^n f_0(\mathbf{x},t)\|+r^{n-1}\|f_0(\mathbf{x},t)\|+\cdots+r^{k+1}\|f_0(\mathbf{x},t)\| \\
\leq& r^{k+1}\|f_0(\mathbf{x},t)\|(r^{n-k-1}+r^{n-k-2}+\cdots+r+1) \\
\implies \|S_n(\mathbf{x},t)-S_k(\mathbf{x},t)\| \leq& \left(\frac{1-r^{n-k}}{1-r}\right) r^{k+1}\|f_0(\mathbf{x},t)\|
\end{aligned} \tag{3.3.15}$$

Using the concept of limit in geometric series together with the term (3.3.15) for $0 < r < 1$, the partial sum $(S_n(\mathbf{x},t))$ satisfying Cauchy sequence can be verified as follows:

$$\begin{aligned}
&\lim_{k,n\to\infty}\|S_n(\mathbf{x},t)-S_k(\mathbf{x},t)\| \leq \lim_{k,n\to\infty}\left(\frac{1-r^{n-k}}{1-r}\right) r^{k+1}\|f_0(\mathbf{x},t)\| \\
&\lim_{k,n\to\infty}\left(\frac{1-r^{n-k}}{1-r}\right) r^{k+1}\|f_0(\mathbf{x},t)\| = 0 \implies \|S_n(\mathbf{x},t)-S_k(\mathbf{x},t)\| = 0.
\end{aligned} \tag{3.3.16}$$

Equation (3.3.16) indicates, $S_n(\mathbf{x},t)$ is a Cauchy sequence in the Banach space A. It is proved that every Cauchy sequence is convergent. Hence, the series solution in equation (3.3.12) is convergent. This completes the proof. □

Theorem 3.3.2. *As far as the infinite series in equation (3.3.12) converges, where $f_m(\boldsymbol{x},t)$ is governed by the m^{th}-order deformation equations (3.3.8), it must be the accurate solution of the original problem.*

Proof. Given that the series $f(\mathbf{x},t) = f_0(\mathbf{x},t)+\sum_{m=1}^{\infty} f_m(\mathbf{x},t) = \sum_{m=0}^{\infty} f_m(\mathbf{x},t)$ is convergent. This has an implication which can be explained as

$$S(\mathbf{x},t) = \sum_{m=0}^{\infty} f_m(\mathbf{x},t) \implies \lim_{m\to\infty} f_m(\mathbf{x},t) = 0 \text{ by convergent series law.}$$

Then, applying the concept of convergent series law, and step function (χ_m), the following result is obtained.

$$\begin{aligned}
&\sum_{m=1}^{n}[f_m(\mathbf{x},t)-\chi_m f_{m-1}(\mathbf{x},t)] = f_1(\mathbf{x},t)+(f_2(\mathbf{x},t)-f_1(\mathbf{x},t))\\
&+(f_3(\mathbf{x},t)-f_2(\mathbf{x},t))+\cdots(f_n(\mathbf{x},t)-f_{n-1}(\mathbf{x},t)) = f_n(\mathbf{x},t)\\
&\implies \sum_{m=1}^{\infty}[f_m(\mathbf{x},t)-\chi_m f_{m-1}(\mathbf{x},t)] = \lim_{n\to\infty} f_n(\mathbf{x},t) = 0\\
&\sum_{m=1}^{\infty}\mathcal{L}[f_m(\mathbf{x},t)-\chi_m f_{m-1}(\mathbf{x},t)] = \mathcal{L}\sum_{m=1}^{\infty}[f_m(\mathbf{x},t)-\chi_m f_{m-1}(\mathbf{x},t)] = 0.
\end{aligned} \tag{3.3.17}$$

Thus, based on equations (3.3.17) and (3.3.8), the next result is obtained.

$$\begin{aligned}
&\sum_{m=1}^{\infty}\mathcal{L}[f_m(\mathbf{x},t)-\chi_m f_{m-1}(\mathbf{x},t)] = c_0\mathcal{H}(\mathbf{x},t)\sum_{m=1}^{\infty}\mathcal{R}_m[f_{m-1}(\mathbf{x},t)]\\
&\implies 0 = c_0\mathcal{H}(\mathbf{x},t)\sum_{m=1}^{\infty}\mathcal{R}_m[f_{m-1}(\mathbf{x},t)]\ c_0\neq 0,\ \mathcal{H}(\mathbf{x},t)\neq 0\\
&\sum_{m=1}^{\infty}\mathcal{R}_m[f_{m-1}(\mathbf{x},t)] = 0 \implies \mathcal{R}_m[f_{m-1}(\mathbf{x},t)] = 0.
\end{aligned} \tag{3.3.18}$$

Hence, according to equation (3.3.18), it can be concluded that, $S(\mathbf{x},t)=\sum_{m=0}^{\infty} f_m(\mathbf{x},t)$ must be an exact solution of the original problem. □

Theorem 3.3.3. *Assume that the series solution defined in (3.3.12) is convergent to the solution $f(\boldsymbol{x},t)$ for a selected value of c_0. If the truncated series $f_M(\boldsymbol{x},t)$ expressed in (3.3.13) is used as an approximation to the solution $f(\boldsymbol{x},t)$ of the original problem, then an upper bound for the error, $Err_M(\boldsymbol{x},t)$, is estimated as*

$$Err_M(\boldsymbol{x},t) = \left(\frac{r^{M+1}}{1-r}\right)\|f_0(\boldsymbol{x},t)\|. \tag{3.3.19}$$

Proof. From this theorem, equation (3.3.19) can be referred as an upper bound for error. Thus, with the help of equation (3.3.14), the upper bound error can be expressed by equation (3.3.19). This verification is derived in the following manner.

$$
\begin{aligned}
\|f(\mathbf{x},t)-f_M(\mathbf{x},t)\| =& \|\sum_{m=M+1}^{\infty} f_m(\mathbf{x},t)\| \leq \sum_{m=M+1}^{\infty} r^m \|f_0(\mathbf{x},t)\| \\
\leq& \|f_0(\mathbf{x},t)\|(r^{M+1}+r^{M+2}+r^{M+3}+\cdots) \\
\leq& \|f_0(\mathbf{x},t)\| r^{M+1}(1+r+r^2+\cdots) \text{ for geometric series} \\
\leq& \|f_0(\mathbf{x},t)\| r^{M+1}\left(\lim_{M\to\infty}\frac{1-r^M}{1-r}\right) \text{ since } 0<r<1 \\
\leq& \frac{r^{M+1}}{1-r}\|f_0(\mathbf{x},t)\| \\
\implies \|f(\mathbf{x},t)-f_M(\mathbf{x},t)\| \leq& \frac{r^{M+1}}{1-r}\|f_0(\mathbf{x},t)\| = Err_M(\mathbf{x},t).
\end{aligned}
$$

□

Selecting the appropriate initial guess, control convergent constant, auxiliary function and linear operator has a role in getting a better approximation by truncating the solution in HAM with the minimum error. In this dissertation, the first four problems (Chapter FOUR-SEVEN) are solved by using HAM. However, due to the importance of the numerical method in solving fluid problems, the fifth problem (Chapter EIGHT) is computed numerically, which needs discretization. In the next section, the main points of the numerical methods are discussed.

3.4 Numerical Method

Another method of solving non-linear higher order set of coupled ODEs in boundary value problem is numerical approach. Some of the common and well known kinds of numerical methods are finite difference, finite element and finite volume methods. These are categorized under discretization scheme since they work by approximating the derivatives of function using forward, backward and central differences (Makanda, 2015). The finite difference method is used to approximate the given equations at a limited number of points and applicable on different problems. It takes less memory and computational time. But, the challenge is optimizing the three properties of a numerical method namely: stability, solution accuracy and algorithm efficiency at the same time (Poochinapan et al., 2014). Historically, finite element method is derived from structural mechanics (Veress and Rohács, 2012) and it is highly applicable in engineering fields like thermodynamics, electromagnetism, solid and fluid mechanics (Alves et al., 2013). As Makanda (2015) stated, the finite element method depends on a mesh elements where the polynomial function is used for approximation purpose. Finite volume method is used to avoid the observed discontinuous solution, particularly in vortex sheets, contact discontinuities or shock waves.

Taylor series expansion is used to approximate the differential equation to apply numerical methods. The Taylor expansion of $f(x+\Delta x)$ about x is defined as

$$\begin{aligned} f(x+\Delta x) &= f(x)+\Delta x\frac{df(x)}{dx}+\frac{(\Delta x)^2}{2!}\frac{d^2f(x)}{dx^2}+\frac{(\Delta x)^3}{3!}\frac{d^2f(x)}{dx^3}+\cdots \\ f(x-\Delta x) &= f(x)-\Delta x\frac{df(x)}{dx}+\frac{(\Delta x)^2}{2!}\frac{d^2f(x)}{dx^2}-\frac{(\Delta x)^3}{3!}\frac{d^2f(x)}{dx^3}+\cdots \end{aligned} \tag{3.4.1}$$

From (3.4.1), it can be approximated the first and second derivatives of $f(x)$ in terms of forward and central difference with some order of accuracy. The appearance of higher order derivative in Taylor series expansion makes this approximation tedious. Thus, Runge-Kutta scheme is used to achieve the accuracy of Taylor series method of approximation without computing higher order derivatives. It is derived from the Taylor series expansion by taking suitable values. Currently, single and a system of differential equations has been solved by Runge-Kutta method (Makanda, 2015). Actually, it can be incorporated another numerical approaches like shooting and Newton-Raphson methods which are used to convert the boundary value problem to initial value problem.

According to Makanda (2015), the Runge-Kutta method evaluates in terms of computer code called bvp4c solver on MATLAB software. Basically, this computer program is highly applicable for solving two-point boundary value problems (Shampine and Muir, 2004) and uses Lobatto IIIA collocation method. It can control the residual error by managing the step size. As Budd et al. (2006) explained, the higher order system of ODEs should be converted in to a first order explicit ODEs for using MATLAB bvp4c solver. The details of this procedure can be seen in the specific problem (Chapter EIGHT). Therefore, in this dissertation, the last problem (Chapter EIGHT) is solved by the bvp4c solver on MATLAB. The following chapters deal with the formulation, solving and discussing the results of different problems regarding heat and mass transfer by the boundary layer flow of nanofluids over a stretchable surface.

CHAPTER FOUR

Convective Heat Exchanger from Renewable Sun Radiation by Nanofluid Flow in DASC with Entropy

4.1 Introduction

The problems of non-renewable energy sources are reduced by using renewable power source which has no significant negative effect to the environment (Dincer, 2000) and also satisfy high demand of energy that come from rapid economical growth (Lei et al., 2022). For example, from renewable energy sources, solar is suitable for the environment, sustainable and obtained everyplace in abundant (Bayrak et al., 2017). Recently, Flilihi et al. (2022) declared that, solar energy is used for sundry industrial operations, such as indirect solar dryer, plus warming homes and generating local hot water. Sathyamurthy et al. (2014) also underlined the financial benefits of solar stills. Thus, the energy from the Sun radiation is essential for using the modern technology. As a result, collecting solar radiation adequately satisfies the demand of energy. Many scientists focused their attention towards upgrading the efficiency of collecting solar radiation (Sabiha et al., 2015; Pandey and Chaurasiya, 2017; Rasih et al., 2019).

Heat exchanger plays a key role in engineering by transferring heat among two or more fluids, and it is applicable in refrigeration, direct solar collectors, automobile radiators and managing the central processing units in electronic systems (Qureshi, 2022). In this process, utilizing nanofluid as working fluid is preferable in many industrial manufacturing processes. Nanofluid is constructed by mixing nanosized metallic or nonmetallic or nanofiber particles into a base fluid that increases its thermal properties (Gupta et al., 2018). Thus, most scientists aspired towards the application of nanofluids with respect to heat transfer in solar collector and they remarked that the effectiveness of solar collectors are upgraded by using nanofluid (Bhalla and Tyagi, 2017; Subramani et al., 2018). Considering different kinds of nanofluids flowing on solar collectors, the heat transfer of renewable solar energy was studied by various researchers such as Azam et al., 2019; Jamshed et al., 2021a; Alkathiri et al., 2022.

Bejan (1996) started the concept of entropy which is used to measure energy loss due to irreversible processes. Achievement of collecting energy from solar collector needs enhancement by adopting the second law of analysis-based scheme (Smit and Kessels, 2015). Different studies explained the generation of entropy based on heat irreversibility or conduction impact, friction flow of fluid, hydromagnetic effect, mass, porosity irreversibility, dissipation irreversibility and Joule heat on various kinds of nanofluids Daniel et al. (2017); Aziz et al. (2018); Hayat et al. (2019).

Based on the latest research work, there is a limited information on the Mathematical analysis of convective heat exchanger from solar thermal radiation through nanofluid in DASC with entropy procreation, and solving by semi-analytic approach called HAM. According to the researchers knowledge, such problem has not yet noted. Thus, the researchers aspired to examine the heat and mass transfer by unsteady flow of nanofluid as a transporting medium during sunlight and analyzing the entropy generation. Equations of flow, temperature and concentration of the nanoparticles are derived from laws of conservation. The reduced ODEs are solved by HAM on Mathematica software, employing the package BVPh2.0.

4.2 Mathematical Model Formulation

In this problem, the rectangular coordinate system has been supposed and the surface begin stretching at $t > 0$ (Hussain et al., 2015). Then, the plate elongated horizontally with non uniform velocity, temperature and concentration having the following formulae at the sheet wall during the stretching process (Aziz et al., 2021).

$$U_w = \frac{\hat{b}x}{1-\varsigma t}, \bar{T}_w = \bar{T}_\infty + \frac{\bar{T}_0 \bar{c} x}{\nu(1-\varsigma t)} \quad \text{and} \quad \bar{C}_w = \bar{C}_\infty + \frac{\bar{C}_0 \bar{c} x}{\nu(1-\varsigma t)} \tag{4.2.1}$$

Thus, $\bar{T}_0$ and $\bar{C}_0$ are constants, $\hat{b}$ and $\hat{b}/(1-\varsigma t)$ are the starting and effective extending rates of the plate, respectively where $\hat{b}$ and ς are non negative constants with $1/s$ unit; $\bar{c}$ and $\bar{c}/(1-\varsigma t)$ are initial and effective extending distance rate of the plate with m/s unit. The assumptions are listed below for this specific problem.

- Two dimensional incompresssible unsteady flows.
- Applying Boundary-layer approximations for simplifying governed PDEs.
- Mixing nanoparticles on a base fluid to construct nanofluid.
- The unsteady flow of nanofluid includes the viscous dissipation properties.

- Considering Buongiorno's model (2006) where the impact of Brownian motion and thermophoresis are taken into account on unsteady flow of nanofluid.
- Effect of solar radiation is considered directly on flow of nanofluid using DASC.
- Induced magnetic field is insignificant due to low Reynolds number.

The flow of this model can be set out on Figure 4.2.1.

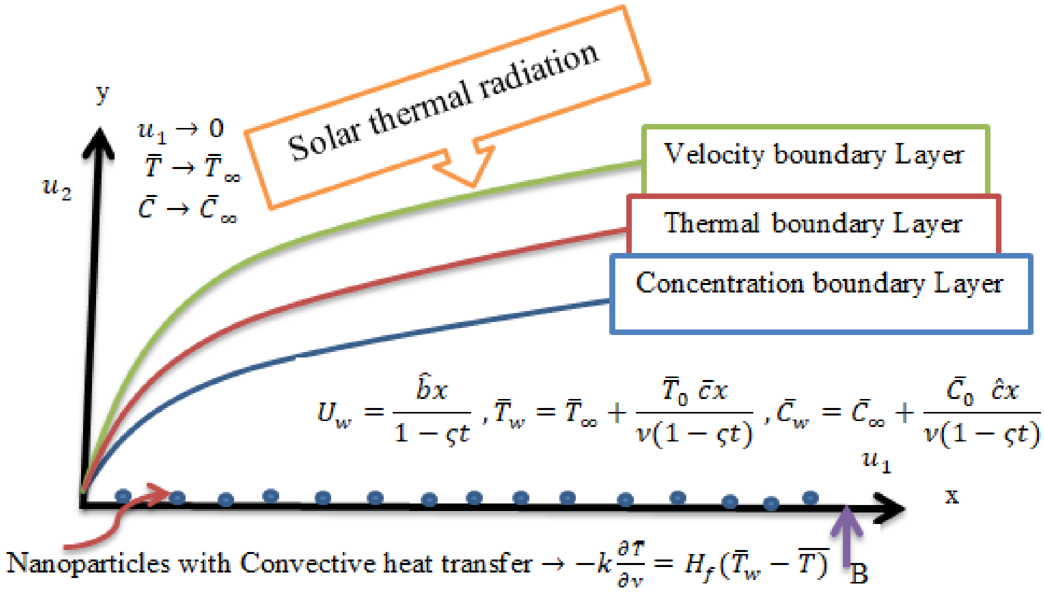

Figure 4.2.1: The physical schematic flow diagram

4.2.1 The Governing Equations of the Problem

In the boundary layer region, there is a standard boundary-layer approximation which is explained in section 3.1.6. With this, the continuity equation in 2D has been taken from equation (3.1.9) as it is. However, the momentum equation which can be referred as the Navier-Stokes modified by adding the impact of magnetic field on equation (3.1.69). In this problem, the magnetic field interaction in the form of Lorentz force $(\mathbf{J}\times\mathbf{B})$ is considered as body force. With $\mathbf{v} = (u_1, u_2, 0)$, $\mathbf{B} = (0, \frac{B_0}{\sqrt{1-\varsigma t}}, 0))$, $\mathbf{J} = \sigma_e(E + \mathbf{v}\times\mathbf{B})$ and $E = 0$, it can be expressed as follows:

$$\mathbf{J} = \sigma_e \begin{vmatrix} i & j & k \\ u_1 & u_2 & 0 \\ 0 & \frac{B_0}{\sqrt{1-\varsigma t}} & 0 \end{vmatrix} = \frac{\sigma_e B_0 u_1}{\sqrt{1-\varsigma t}} k, \Longrightarrow \mathbf{J}\times\mathbf{B} = \sigma_e \begin{vmatrix} i & j & k \\ 0 & 0 & \frac{\sigma_e B_0 u_1}{\sqrt{1-\varsigma t}} \\ 0 & \frac{B_0}{\sqrt{1-\varsigma t}} & 0 \end{vmatrix} = -\frac{\sigma_e B_0^2 u_1}{1-\varsigma t} i.$$

Thus, the momentum equation (3.1.69) becomes

$$\rho \frac{Du_1}{Dt} = \mu \left(\frac{\partial^2 u_1}{\partial y^2} \right) + \mathbf{J} \times \mathbf{B} = \mu \left(\frac{\partial^2 u_1}{\partial y^2} \right) - \frac{\sigma_e B_0^2 u_1}{1 - \varsigma t}.$$

The energy equation (3.1.70) can be modified by the impact of solar radiation which is approximated by Rosseland-approximation (Mukhtar and Gul, 2023) and heat source per volume due to nanoparticles mass flux. Thus, $\bar{q} = -\nabla q_r + c_p \rho_p (\nabla \bar{T}) \left(D_B \nabla \bar{C} + \frac{D_T}{\bar{T}_\infty} \nabla \bar{T} \right)$. Applying boundary layer approximation in 2D, the energy equation is expressed as

$$\rho c_p \frac{D\bar{T}}{Dt} = k \left(\frac{\partial^2 \bar{T}}{\partial y^2} \right) + \mu \left(\frac{\partial u_1}{\partial y} \right)^2 + \bar{q} = k \frac{\partial^2 \bar{T}}{\partial y^2} + \mu \left(\frac{\partial u_1}{\partial y} \right)^2 - \frac{\partial q_r}{\partial y} + \tau_h \frac{\partial \bar{T}}{\partial y} \left(D_B \frac{\partial \bar{C}}{\partial y} + \frac{D_T}{T_\infty} \frac{\partial \bar{T}}{\partial y} \right).$$

Equation of concentration is the same with expression (3.1.71). Following these, the governing equations based on conservation of mass, momentum, energy, and concentration can be summarized (Hussain et al., 2015; Kebede et al., 2020; Hussain, 2022).

$$\frac{\partial u_1}{\partial x} + \frac{\partial u_2}{\partial y} = 0, \tag{4.2.2}$$

$$\frac{\partial u_1}{\partial t} + u_1 \frac{\partial u_1}{\partial x} + u_2 \frac{\partial u_1}{\partial y} = \nu \frac{\partial^2 u_1}{\partial y^2} - \frac{\sigma_e B_0^2 u_1}{\rho (1 - \varsigma t)}, \tag{4.2.3}$$

$$\frac{\partial \bar{T}}{\partial t} + u_1 \frac{\partial \bar{T}}{\partial x} + u_2 \frac{\partial \bar{T}}{\partial y} = \frac{k}{\rho c_p} \frac{\partial^2 \bar{T}}{\partial y^2} + \frac{\mu}{\rho c_p} (\frac{\partial u_1}{\partial y})^2 - \frac{1}{\rho c_p} \frac{\partial q_r}{\partial y} + \tau_h \left(D_B \frac{\partial \bar{C}}{\partial y} \frac{\partial \bar{T}}{\partial y} + \frac{D_T}{T_\infty} (\frac{\partial \bar{T}}{\partial y})^2 \right) \tag{4.2.4}$$

$$\frac{\partial \bar{C}}{\partial t} + u_1 \frac{\partial \bar{C}}{\partial x} + u_2 \frac{\partial \bar{C}}{\partial y} = D_B \frac{\partial^2 \bar{C}}{\partial y^2} + \frac{D_T}{T_\infty} \frac{\partial^2 \bar{T}}{\partial y^2} \tag{4.2.5}$$

The boundary conditions for this model become (Ullah et al., 2017; Aziz et al., 2021)

$$\begin{cases} \text{For } \ y = 0, \ u_2 = 0, u_1 = U_w, -k \dfrac{\partial \bar{T}}{\partial y} = H_f (\bar{T}_w - \bar{T}), \bar{C} = \bar{C}_w \\ \text{and as } \ y \to \infty, \ u_1 \to 0, \bar{T} \to \bar{T}_\infty, \bar{C} \to \bar{C}_\infty \end{cases} \tag{4.2.6}$$

For minor difference in temperature between the sheet and around the nanofluid, the Rosseland-approximation can be applied to describe the radiative term in equation

(4.2.4). Thus, q_r becomes (Brewster, 1992; Kebede et al., 2020; Alkathiri et al., 2022);

$$q_r = -\frac{4\sigma^*}{k^*}\frac{\partial(\bar{T}^4)}{\partial y}. \tag{4.2.7}$$

Applying Taylor series expansion of $\bar{T}^4$ about $\bar{T}_\infty$, then $\bar{T}^4$ is expanded as

$$\bar{T}^4 = \bar{T}_\infty^4 + 4(\bar{T}-\bar{T}_\infty)\bar{T}_\infty^3 + 6(\bar{T}-\bar{T}_\infty)^2\bar{T}_\infty^2 + 4(\bar{T}-\bar{T}_\infty)^3\bar{T}_\infty + (\bar{T}-\bar{T}_\infty)^4 + \ldots \tag{4.2.8}$$

Ignoring the higher order terms of $\bar{T}-\bar{T}_\infty$ of equation (4.2.8), $\bar{T}^4$ can be approximated as $\bar{T}^4 = 4\bar{T}_\infty^3\bar{T} - 3\bar{T}_\infty^4$. Then the radiative flux term becomes

$$q_r = -\frac{4\sigma^*}{k^*}\frac{\partial(\bar{T}^4)}{\partial y} \approx -\frac{4\sigma^*}{3k^*}\frac{\partial(4\bar{T}_\infty^3\bar{T} - 3\bar{T}_\infty^4)}{\partial y} = -\frac{16\bar{T}_\infty^3\sigma^*}{3k^*}\frac{\partial \bar{T}}{\partial y}. \tag{4.2.9}$$

Thus, equation (4.2.4) is reduced as

$$\begin{aligned}\frac{\partial \bar{T}}{\partial t} + u_1\frac{\partial \bar{T}}{\partial x} + u_2\frac{\partial \bar{T}}{\partial y} = &\frac{k}{\rho c_p}\left(1 + \frac{16\bar{T}_\infty^3\sigma*}{3k^*k}\right)\frac{\partial^2 \bar{T}}{\partial y^2} + \frac{\mu}{\rho c_p}(\frac{\partial u_1}{\partial y})^2 \\ &+ \tau_h\left(D_B\frac{\partial \bar{C}}{\partial y}\frac{\partial \bar{T}}{\partial y} + \frac{D_T}{T_\infty}(\frac{\partial \bar{T}}{\partial y})^2\right)\end{aligned} \tag{4.2.10}$$

For Mathematical analysis purpose, the non-linear higher-order PDEs (4.2.2), (4.2.3), (4.2.5) and (4.2.10) have been recast into non-linear higher-order ODEs by launching a similarity transformation with stream function ψ and dimensionless independent variable ϵ. These transformation variables and velocity components are defined as

$$\epsilon = y\sqrt{\frac{\hat{b}}{\nu(1-\varsigma t)}}, \psi(x,y,t) = \sqrt{\frac{\hat{b}\nu}{1-\varsigma t}}xV(\epsilon), u_1(\epsilon) = \frac{\partial \psi}{\partial y}, u_2(\epsilon) = -\frac{\partial \psi}{\partial x}. \tag{4.2.11}$$

Using equation (4.2.11), the velocity components u_1 and u_2, temperature $\bar{T}$ and concentration $\bar{C}$ are expressed in dimensionless form as follows:

$$\begin{aligned}&u_1(\epsilon) = \frac{\partial \psi}{\partial y} = \frac{\hat{b}x}{1-\varsigma t}\frac{\partial V}{\partial \epsilon}, \quad u_2(\epsilon) = -\frac{\partial \psi}{\partial x} = -\sqrt{\frac{\hat{b}\nu}{1-\varsigma t}}V(\epsilon) \\ &H(\epsilon) = \frac{\bar{T}-\bar{T}_\infty}{\bar{T}_w - \bar{T}_\infty}, \quad L(\epsilon) = \frac{\bar{C}-\bar{C}_\infty}{\bar{C}_w - \bar{C}_\infty}.\end{aligned} \tag{4.2.12}$$

Using equation (4.2.12) together with similarity transformation variable (4.2.11), the terms in the governing PDEs (4.2.2-4.2.5) can be defined in the following form.

$$
\begin{aligned}
&\frac{\partial u_1}{\partial t}=\frac{\hat{b}x\varsigma V'}{(1-\varsigma t)^2}+\frac{\hat{b}xV''}{1-\varsigma t}\frac{\varsigma}{2(1-\varsigma t)^{3/2}}y\sqrt{\frac{\hat{b}}{\nu}}=\frac{\hat{b}x\varsigma}{(1-\varsigma t)^2}\left(V'+\frac{\epsilon V''}{2}\right)\\
&\frac{\partial u_1}{\partial x}=\frac{\hat{b}V'}{1-\varsigma t},\ \frac{\partial u_1}{\partial y}=\frac{\hat{b}x}{1-\varsigma t}V''\sqrt{\frac{\hat{b}}{\nu(1-\varsigma t)}},\ \frac{\partial^2 u_1}{\partial y^2}=\frac{\hat{b}x}{1-\varsigma t}V'''\frac{\hat{b}}{\nu(1-\varsigma t)}\\
&\frac{\partial u_2}{\partial y}=-\sqrt{\frac{\hat{b}\nu}{1-\varsigma t}}V'\sqrt{\frac{\hat{b}}{\nu(1-\varsigma t)}}=-\frac{\hat{b}}{1-\varsigma t}V',\ \frac{\partial u_2}{\partial x}=0\\
&\frac{\partial \bar{T}}{\partial t}=\frac{\bar{c}x\varsigma H\bar{T}_0}{(1-\varsigma t)^2}+(\bar{T}_w-\bar{T}_\infty)H'\frac{\varsigma}{2(1-\varsigma t)^{3/2}}y\sqrt{\frac{\hat{b}}{\nu}}=\frac{(\bar{T}_w-\bar{T}_\infty)\varsigma}{1-\varsigma t}\left(H+\frac{\epsilon H'}{2}\right)\\
&\frac{\partial \bar{T}}{\partial x}=\frac{\bar{c}H\bar{T}_0}{(1-\varsigma t)},\ \frac{\partial \bar{T}}{\partial y}=(\bar{T}_w-\bar{T}_\infty)H'\sqrt{\frac{\hat{b}}{\nu(1-\varsigma t)}},\ \frac{\partial^2 \bar{T}}{\partial y^2}=\frac{(\bar{T}_w-\bar{T}_\infty)H''\hat{b}}{\nu(1-\varsigma t)}\\
&\frac{\partial \bar{C}}{\partial t}=\frac{\bar{c}x\varsigma L\bar{C}_0}{(1-\varsigma t)^2}+(\bar{C}_w-\bar{C}_\infty)L'\frac{\varsigma}{2(1-\varsigma t)^{3/2}}y\sqrt{\frac{\hat{b}}{\nu}}=\frac{(\bar{C}_w-\bar{C}_\infty)\varsigma}{1-\varsigma t}\left(L+\frac{\epsilon L'}{2}\right)\\
&\frac{\partial \bar{C}}{\partial x}=\frac{\bar{c}L\bar{C}_0}{(1-\varsigma t)},\ \frac{\partial \bar{C}}{\partial y}=(\bar{C}_w-\bar{C}_\infty)L'\sqrt{\frac{\hat{b}}{\nu(1-\varsigma t)}},\ \frac{\partial^2 \bar{C}}{\partial y^2}=\frac{(\bar{C}_w-\bar{C}_\infty)L''\hat{b}}{\nu(1-\varsigma t)}
\end{aligned}
\tag{4.2.13}
$$

Using the expression in (4.2.13), equation (4.2.1) can be verified as follows.

$$
\frac{\partial u_1}{\partial x}+\frac{\partial u_2}{\partial y}=0 \quad \text{as} \quad \frac{\hat{b}V'}{1-\varsigma t}-\frac{\hat{b}V'}{1-\varsigma t}=0. \tag{4.2.14}
$$

Applying similar approach, the PDE (4.2.3) can be rewritten in the following manner.

$$
\begin{aligned}
&\frac{\partial u_1}{\partial t}+u_1\frac{\partial u_1}{\partial x}+u_2\frac{\partial u_1}{\partial y}=\nu\frac{\partial^2 u_1}{\partial y^2}-\frac{\sigma_e B_0^2 u_1}{\rho(1-\varsigma t)}\\
=&\frac{\hat{b}x\varsigma}{(1-\varsigma t)^2}\left(V'+\frac{\epsilon V''}{2}\right)+\frac{\hat{b}x}{1-\varsigma t}V'\frac{\hat{b}V'}{1-\varsigma t}-\sqrt{\frac{\hat{b}\nu}{1-\varsigma t}}V(\epsilon)\frac{\hat{b}x}{1-\varsigma t}V''\sqrt{\frac{\hat{b}}{\nu(1-\varsigma t)}}\\
&=\nu\frac{\hat{b}x}{1-\varsigma t}V'''\frac{\hat{b}}{\nu(1-\varsigma t)}-\frac{\sigma_e B_0^2}{\rho(1-\varsigma t)}\frac{\hat{b}x}{1-\varsigma t}V'\\
&\implies \frac{\hat{b}^2 x}{(1-\varsigma t)^2}\left(\frac{\varsigma}{\hat{b}}\left(V'+\frac{\epsilon V''}{2}\right)+(V')^2-VV''=V'''-\frac{\sigma_e B_0^2 V'}{\rho\hat{b}}\right)\\
&\implies V'''+VV''-A\left(V'+\frac{\epsilon V''}{2}\right)-(V')^2-MaV'=0,
\end{aligned}
\tag{4.2.15}
$$

where $A=\dfrac{\varsigma}{\hat{b}}$ is non-dimensional unsteadiness parameter and $Ma=\dfrac{\sigma_e B_0^2}{\rho\hat{b}}$ is non-dimensional magnetic field interaction parameter. Following similar approaches, the

PDE in (4.2.10) can be rewritten, based on (4.2.13) which produces non-linear ODE.

$$
\begin{aligned}
&\frac{\partial \bar{T}}{\partial t}+u_1\frac{\partial \bar{T}}{\partial x}+u_2\frac{\partial \bar{T}}{\partial y}=\frac{k}{\rho c_p}\left(1+\frac{16\bar{T}_\infty^3\sigma*}{3k*k}\right)\frac{\partial^2\bar{T}}{\partial y^2}+\frac{\mu}{\rho c_p}(\frac{\partial u_1}{\partial y})^2+\tau_h\left(D_B\frac{\partial \bar{C}}{\partial y}\frac{\partial \bar{T}}{\partial y}+\frac{D_T}{T_\infty}(\frac{\partial \bar{T}}{\partial y})^2\right)\\
&\implies \frac{(\bar{T}_w-\bar{T}_\infty)\varsigma}{1-\varsigma t}\left(H+\frac{\epsilon H'}{2}\right)+\frac{\hat{b}x}{1-\varsigma t}V'\frac{\bar{c}H\bar{T}_0}{\nu(1-\varsigma t)}-\sqrt{\frac{\hat{b}\nu}{1-\varsigma t}}V(\epsilon)(\bar{T}_w-\bar{T}_\infty)H'\sqrt{\frac{\hat{b}}{\nu(1-\varsigma t)}}\\
&=\frac{k}{\rho c_p}\left(1+\frac{16\bar{T}_\infty^3\sigma*}{3k*k}\right)\frac{(\bar{T}_w-\bar{T}_\infty)H''\hat{b}}{\nu(1-\varsigma t)}+\frac{\mu}{\rho c_p}\left(\frac{\hat{b}x}{1-\varsigma t}V''\sqrt{\frac{\hat{b}}{\nu(1-\varsigma t)}}\right)^2+\\
&\tau_h\left(D_B(\bar{C}_w-\bar{C}_\infty)L'\sqrt{\frac{\hat{b}}{\nu(1-\varsigma t)}}(\bar{T}_w-\bar{T}_\infty)H'\sqrt{\frac{\hat{b}}{\nu(1-\varsigma t)}}+\frac{D_T}{T_\infty}\left[(\bar{T}_w-\bar{T}_\infty)H'\sqrt{\frac{\hat{b}}{\nu(1-\varsigma t)}}\right]^2\right)\\
&\implies \frac{(\bar{T}_w-\bar{T}_\infty)\hat{b}}{1-\varsigma t}\left(\frac{\varsigma}{\hat{b}}(H+\frac{\epsilon H'}{2})+V'H-VH'=\frac{k}{\rho c_p\nu}\left(1+\frac{16\bar{T}_\infty^3\sigma*}{3k*k}\right)H''+\frac{(U_wV'')^2}{(\bar{T}_w-\bar{T}_\infty)c_p}\right)\\
&\frac{(\bar{T}_w-\bar{T}_\infty)\hat{b}}{1-\varsigma t}\left(\tau_hD_B\frac{(\bar{C}_w-\bar{C}_\infty)}{\nu}L'H'+\tau D_T\frac{(\bar{T}_w-\bar{T}_\infty)}{T_\infty\nu}(H')^2\right)\\
&\implies \frac{1}{Pr}(1+Rn)H''-A(H+\frac{\epsilon H'}{2})+H'V-V'H+Ec(V'')^2+Nt(H')^2+NbH'L'=0,
\end{aligned}
\tag{4.2.16}
$$

where $P_r=\dfrac{\nu\rho c_p}{k}\to$ Prandtl number; $Rn=\dfrac{16\sigma^*\bar{T}_\infty^3}{3kk^*}\to$ thermal radiation parameter; $Nb=\dfrac{D_B\tau_h(\bar{C}_w-\bar{C}_\infty)}{\nu}\to$ Brownian motion; $Nt=\dfrac{D_T\tau_h(\bar{T}_w-\bar{T}_\infty)}{\bar{T}_\infty\nu}\to$ thermophoresis diffusion; $E_c=\dfrac{(U_w)^2}{(T_w-T_\infty)c_p}\to$ Eckert number. Similarly, the PDE in (4.2.5), can be simplified in non-linear ODE as

$$
\begin{aligned}
&\frac{\partial \bar{C}}{\partial t}+u_1\frac{\partial \bar{C}}{\partial x}+u_2\frac{\partial \bar{C}}{\partial y}=D_B\frac{\partial^2\bar{C}}{\partial y^2}+\frac{D_T}{T_\infty}\frac{\partial^2\bar{T}}{\partial y^2}\\
&=\frac{(\bar{C}_w-\bar{C}_\infty)\varsigma}{1-\varsigma t}\left(L+\frac{\epsilon L'}{2}\right)-\sqrt{\frac{\hat{b}\nu}{1-\varsigma t}}V(\epsilon)(\bar{C}_w-\bar{C}_\infty)L'\sqrt{\frac{\hat{b}}{\nu(1-\varsigma t)}}\\
&+\frac{\hat{b}x}{1-\varsigma t}V'\frac{\bar{c}L\bar{C}_0}{\nu(1-\varsigma t)}=D_B\frac{(\bar{C}_w-\bar{C}_\infty)L''\hat{b}}{\nu(1-\varsigma t)}+\frac{D_T}{T_\infty}\frac{(\bar{T}_w-\bar{T}_\infty)H''\hat{b}}{\nu(1-\varsigma t)}\\
&=\frac{(\bar{C}_w-\bar{C}_\infty)\hat{b}}{1-\varsigma t}\left(\frac{\varsigma}{\hat{b}}(L+\frac{\epsilon L'}{2})+V'L-VL'=\frac{D_B}{\nu}L''+\frac{D_T}{\bar{T}_\infty}\frac{(\bar{T}_w-\bar{T}_\infty)}{\nu(\bar{C}_w-\bar{C}_\infty)}H''\right)\\
&\implies L''-ScA\left(L+\frac{\epsilon L'}{2}\right)+Sc\left(VL'-LV'\right)+\frac{Nt}{Nb}H''=0,
\end{aligned}
\tag{4.2.17}
$$

where $Sc=\dfrac{\nu}{D_B}\to$ Schmidt number.

The boundary conditions in equation (4.2.6) can be remodeled according to the expression in equation (4.2.13)

$$
\begin{aligned}
&u_2(0)=0 \implies -\sqrt{\frac{\hat{b}\nu}{1-\varsigma t}}V(\epsilon)|_{\epsilon=0}=0 \implies V(0)=0\\
&u_1(0)=U_w|_{y=0} \implies \frac{\hat{b}x}{1-\varsigma t}\frac{\partial V}{\partial \epsilon}|_{\epsilon=0}=U_w \implies U_wV'(0)=U_w \implies V'(0)=1,\\
&-k\frac{\partial \bar{T}}{\partial y}|_{y=0}=H_f(\bar{T}_w-\bar{T})|_{y=0} \implies -k(\bar{T}_w-\bar{T}_\infty)\sqrt{\frac{\hat{b}}{\nu(1-\varsigma t)}}H'(\epsilon)|_{\epsilon=0}=H_f(\bar{T}_w-\bar{T})|_{y=0}\\
&\implies H'(0)=-\frac{H_f(\bar{T}_w-\bar{T})}{k(\bar{T}_w-\bar{T}_\infty)}\sqrt{\frac{\nu(1-\varsigma t)}{\hat{b}}}=-\sqrt{\frac{\nu(1-\varsigma t)}{\hat{b}}}\frac{H_f(\bar{T}_w-(\bar{T}_w-T_\infty)H(0)-T_\infty)}{k(\bar{T}_w-\bar{T}_\infty)}\\
&=-\sqrt{\frac{\nu(1-\varsigma t)}{\hat{b}}}\frac{H_f(\bar{T}_w-\bar{T}_\infty)(1-H(0))}{k(\bar{T}_w-\bar{T}_\infty)}=-\sqrt{\frac{\nu(1-\varsigma t)}{\hat{b}}}\frac{H_f(1-H(0))}{k}=-\Upsilon(1-H(0))\\
&\bar{C}|_{y=0}=\bar{C}_w \implies L(\epsilon)(\bar{C}_w-\bar{C}_\infty)|_{\epsilon=0}=\bar{C}_w-\bar{C}_\infty \implies L(0)=\frac{\bar{C}_w-\bar{C}_\infty}{\bar{C}_w-\bar{C}_\infty}=1\\
&u_1(y)|_{y\to\infty}\to 0 \implies \frac{\hat{b}x}{1-\varsigma t}\frac{\partial V}{\partial \epsilon}|_{\epsilon\to\infty}\to 0 \implies V'=\frac{\partial V(\epsilon)}{\partial \epsilon}\to 0 \text{ as } \epsilon\to\infty\\
&\bar{T}|_{y\to\infty}\to\bar{T}_\infty \implies H(\epsilon)(\bar{T}_w-\bar{T}_\infty)|_{\epsilon\to\infty}+\bar{T}_\infty\to\bar{T}_\infty \implies H(\epsilon\to\infty)\to\frac{\bar{T}_\infty-\bar{T}_\infty}{\bar{T}_w-\bar{T}_\infty}=0\\
&\bar{C}|_{y\to\infty}\to\bar{C}_\infty \implies L(\epsilon)(\bar{C}_w-\bar{C}_\infty)|_{\epsilon\to\infty}+\bar{C}_\infty\to\bar{C}_\infty \implies L(\epsilon\to\infty)\to\frac{\bar{C}_\infty-\bar{C}_\infty}{\bar{C}_w-\bar{C}_\infty}=0,
\end{aligned}
\tag{4.2.18}
$$

where $\Upsilon=\frac{H_f}{k}\sqrt{\frac{\nu(1-\varsigma t)}{\hat{b}}}$ represents Biot number. As a result of the procedural simplification of the expressions in (4.2.15) to (4.2.18), the PDEs (4.2.3, 4.2.10, 4.2.5) are transformed in the following non linear higher order ODEs,

$$V'''+VV''-A\left(V'+\frac{\epsilon}{2}V''\right)-(V')^2-MaV'=0, \tag{4.2.19}$$

$$\frac{(1+Rn)}{Pr}H''+NbH'L'+Nt(H')^2-A\left(H+\frac{\epsilon}{2}H'\right)+VH'-HV'+Ec(V'')^2=0, \tag{4.2.20}$$

$$L''-Sc\left[A\left(L+\frac{\epsilon}{2}L'\right)-VL'+LV'\right]+\frac{Nt}{Nb}H''=0. \tag{4.2.21}$$

The boundary conditions in equation (4.2.6), are converted using the expression in equation (4.2.18) as:

$$\begin{cases} V(0)=0,\ V'(0)=1,\ H'(0)=-\Upsilon(1-H(0)), L(0)=1 \\ V'(\epsilon\to\infty)=0,\ H(\epsilon\to\infty)=0,\ L(\epsilon\to\infty)=0 \end{cases} \tag{4.2.22}$$

4.2.2 Physical Quantities in Engineering Perspective

In this portion, the three valuable physical quantities in the sight of engineering have been clarified depending on the supposed nanofluids.

1. Local skin friction coefficient or the rate of momentum transfer (Cf_x) which interfere the flow of fluid over the surface, and based on Rafique et al. (2019)

$$\begin{aligned} Cf_x &= \frac{\tau_w}{\rho U_w^2} = \frac{\mu(\frac{\partial u_1}{\partial y})_{y=0}}{\rho U_w^2} = \frac{\mu(\frac{\hat{b}x}{1-\varsigma t}V''\sqrt{\frac{\hat{b}}{\nu(1-\varsigma t)}})_{y=0}}{\rho U_w^2} \\ \Longrightarrow Cf_x &= \frac{\mu U_w}{\rho U_w^2}V''(0)\sqrt{\frac{\hat{b}}{\nu(1-\varsigma t)}} = \sqrt{\frac{\hat{b}x\nu^2}{U_w^2 x\nu(1-\varsigma t)}}V''(0) = \sqrt{\frac{U_w\nu}{U_w^2 x}}V''(0) \\ \Longrightarrow Cf_x &= \sqrt{\frac{\nu}{U_w x}}V''(0) = Re_x^{-0.5}V''(0) \Longrightarrow V''(0) = Cf_x Re_x^{0.5}, \end{aligned} \tag{4.2.23}$$

where $Re_x = \dfrac{U_w x}{\nu}$ represents the local Reynolds number and $\tau_w = \mu(\dfrac{\partial u_1}{\partial y})_{y=0}$.

2. Local Nusselt number or the rate of heat transfer (Nu_x) measure's the rate of heat transfer and is defined as Kebede et al. (2020)

$$\begin{aligned} Nu_x &= -\frac{xk(\frac{\partial \bar{T}}{\partial y})_{y=0}}{k(\bar{T}-\bar{T}_\infty)} + \frac{q_r x}{k(\bar{T}-\bar{T}_\infty)} = -x\left(\frac{k(\frac{\partial \bar{T}}{\partial y} + \frac{16\bar{T}_\infty^3\sigma^*}{3k^*}\frac{\partial \bar{T}}{\partial y})|_{y=0}}{k(\bar{T}-\bar{T}_\infty)}\right) \\ &= \left[\frac{-3k^*k-16\bar{T}_\infty^3\sigma^*}{3k^*k(\bar{T}-\bar{T}_\infty)}\right]x\frac{\partial \bar{T}}{\partial y}|_{y=0} = \left[\frac{-3k*k-16\bar{T}_\infty^3\sigma*}{3k*k(\bar{T}_w-\bar{T}_\infty)}\right]x(\bar{T}_w-\bar{T}_\infty)H'(0)\sqrt{\frac{\hat{b}}{\nu(1-\varsigma t)}} \\ \Longrightarrow Nu_x &= -\left[1+\frac{16\bar{T}_\infty^3\sigma^*}{3k^*k}\right]H'(0)\sqrt{\frac{\hat{b}x^2}{\nu(1-\varsigma t)}} = -\left[1+Rn\right]H'(0)\sqrt{\frac{U_w x}{\nu}} \\ \Longrightarrow Nu_x &= -(1+Rn)H'(0)\sqrt{Re_x} \Longrightarrow H'(0) = -\frac{Nu_x}{(1+Rn)\sqrt{Re_x}} \end{aligned} \tag{4.2.24}$$

Since $\bar{T}-\bar{T}_\infty = \bar{T}_w - \bar{T}_\infty$ at the surface $(y=0)$ which is given in equation (4.2.1).

3. Local Sherwood number or mass transfer rate (Sh_x) is non-dimensional quantity applied on the mass transfer. According to Rafique et al. (2019), the equation of local Sherwood number becomes

$$
\begin{aligned}
Sh_x =& \frac{xJ_m}{D_B(\bar{C}_w-\bar{C}_\infty)} = -\frac{xD_B(\frac{\partial \bar{C}}{\partial y})_{y=0}}{D_B(\bar{C}_w-\bar{C}_\infty)} \\
=& -\frac{(\bar{C}_w-\bar{C}_\infty)L'(0)\sqrt{\frac{\hat{b}x^2}{\nu(1-\varsigma t)}}}{(\bar{C}_w-\bar{C}_\infty)} = -L'(0)\sqrt{\frac{\hat{b}x^2}{\nu(1-\varsigma t)}} \\
\Longrightarrow Sh_x =& -L'(0)\sqrt{\frac{U_w x}{\nu}} = -L'(0)\sqrt{Re_x} \Longrightarrow L'(0) = -\frac{Sh_x}{\sqrt{Re_x}},
\end{aligned}
\tag{4.2.25}
$$

where $J_m = -D_B(\frac{\partial \bar{C}}{\partial y})_{y=0}$ assign for mass flux at $y=0$ of the plane.

4.2.3 Generation of Entropy

To analyze and apply the energy properly, the concept of the first and second laws of thermodynamics are essential. As Loganathan and Rajan (2020) stated, entropy is the disturbance of regular system and enclosing it which measures for irreversibility. In this work, researchers accounted for the entropy formation triggered by heat transition, friction between nanofluids, and mass transmission. Based on Hussain (2022) and Loganathan et al. (2020), the entropy rate per volume formula has been modified as:

$$
\begin{aligned}
E_{pr} =& \left\{\frac{k}{\bar{T}_\infty^2}\left[1+\frac{16\sigma^*\bar{T}_\infty^3}{3kk^*}\right]\left(\frac{\partial \bar{T}}{\partial y}\right)^2\right\} + \left\{\frac{\mu}{\bar{T}_\infty}\left(\frac{\partial u_1}{\partial y}\right)^2\right\} \\
&+ \left\{\frac{RD}{\bar{C}_\infty}\left(\frac{\partial \bar{C}}{\partial y}\right)^2 + \frac{RD}{\bar{T}_\infty}\left(\frac{\partial \bar{C}}{\partial y}\right)\left(\frac{\partial \bar{T}}{\partial y}\right)\right\}.
\end{aligned}
\tag{4.2.26}
$$

The Bejan number (Be) is defined as the ratio of entropy acquired by heat and mass transfer to the total entropy (Loganathan et al., 2020). That is

$$
Be = \frac{\text{Entropy generated by heat and mass transfer}}{\text{Total entropy generation}}.
$$

The non dimensional form of the local rate of entropy per volume (NG) can be done by multiplying the expression (4.2.26), by $E_0 = \dfrac{\bar{T}_\infty^2 \mathbb{L}^2}{k(\bar{T}_w - \bar{T}_\infty)^2}$. Thus, the dimensionless entropy ($NG = E_0 E_{pr}$) can be simplified by using (4.2.12) and (4.2.13) as follows.

$$
\begin{aligned}
NG =& E_0 E_{pr} = \frac{\bar{T}_\infty^2 \mathbb{L}^2}{k(\bar{T}_w - \bar{T}_\infty)^2} \left(\frac{k}{\bar{T}_\infty^2} \left[1 + \frac{16\sigma^* \bar{T}_\infty^3}{3kk^*} \right] \left(\frac{\partial \bar{T}}{\partial y} \right)^2 + \frac{\mu}{\bar{T}_\infty} \left(\frac{\partial u_1}{\partial y} \right)^2 \right) \\
& + \frac{\bar{T}_\infty^2 \mathbb{L}^2}{k(\bar{T}_w - \bar{T}_\infty)^2} \left(\frac{RD}{\bar{C}_\infty} \left(\frac{\partial \bar{C}}{\partial y} \right)^2 + \frac{RD}{\bar{T}_\infty} \left(\frac{\partial \bar{C}}{\partial y} \right) \left(\frac{\partial \bar{T}}{\partial y} \right) \right) \\
\implies & \frac{\mathbb{L}^2 \hat{b}}{\nu(1-\varsigma t)} \left((1+Rn)(H')^2 + \frac{\bar{T}_\infty \mu \mathbb{L}^2 x^2}{k(\bar{T}_w - \bar{T}_\infty)^2 (1-\varsigma t)^2} (V'')^2 \right) + \\
& \frac{\mathbb{L}^2 \hat{b}}{\nu(1-\varsigma t)} \frac{RD\bar{C}_\infty}{k} \left(\left(\frac{(\bar{C}_w - \bar{C}_\infty)\bar{T}_\infty}{\bar{C}_\infty (\bar{T}_w - \bar{T}_\infty)} L' \right)^2 + \frac{(\bar{C}_w - \bar{C}_\infty)\bar{T}_\infty}{\bar{C}_\infty (\bar{T}_w - \bar{T}_\infty)} H' L' \right) \\
& = Re \left((1+Rn)(H')^2 + \frac{\mu U_w^2}{k(\bar{T}_w - \bar{T}_\infty)} \frac{\bar{T}_\infty}{\bar{T}_w - \bar{T}_\infty} (V'')^2 \right) + \\
& Re\Delta_3 \left(\frac{\Delta_2}{\Delta_1} \right)^2 (L')^2 + Re\Delta_3 \frac{\Delta_2}{\Delta_1} L'H' \\
\implies & NG = Re(1+Rn)(H')^2 + \frac{ReB_r}{\Delta_1}(V'')^2 + Re\Delta_3 \frac{\Delta_2}{\Delta_1} \left(\frac{\Delta_2}{\Delta_1} (L')^2 + L'H' \right),
\end{aligned}
\tag{4.2.27}
$$

where $Re = \dfrac{\mathbb{L}^2 \hat{b}}{\nu(1-\varsigma t)}, B_r = \dfrac{\mu U_w^2}{k(\bar{T}_w - \bar{T}_\infty)}, \Delta_1 = \dfrac{\bar{T}_w - \bar{T}_\infty}{\bar{T}_\infty}, \Delta_2 = \dfrac{\bar{C}_w - \bar{C}_\infty}{\bar{C}_\infty}$ and $\Delta_3 = \dfrac{RD\bar{C}_\infty}{k}$, Global Reynolds number, Brinkman number, temperature variation, concentration difference and diffusive variable, respectively. Similarly, the dimensionless form of Bejan number (Be) becomes:

$$
Be = \frac{Re\Delta_1^2(1+Rn)(H')^2 + Re\Delta_3\Delta_2 \left(\Delta_2 (L')^2 + \Delta_1 L'H' \right)}{\Delta_1^2 NG}. \tag{4.2.28}
$$

4.3 Method of Solving the Problem (HAM)

Currently, HAM is one of the strategies that is used to solve boundary value problems in nonlinear higher-order system of ODEs. It was first forwarded by Liao in his PhD thesis (Liao, 1992). The solutions using HAM are close to the exact one. That is why most scholars including Bano et al. (2018); Kebede et al. (2020); Loganathan et al. (2021); Hayat et al. (2021); Saeed et al. (2022) used it. HAM has a freedom to select linear operators ($\mathcal{L}_V, \mathcal{L}_H, \mathcal{L}_L$), initial guesses ($V_0, H_0, L_0$), auxiliary functions ($\mathcal{H}_V, \mathcal{H}_H, \mathcal{H}_L$) and convergence control parameters ($\hbar_V, \hbar_H, \hbar_L$) to obtain convergent solutions.

4.3.1 Linear Operators, Initial Guesses and Auxiliary Functions

The solution of equations (4.2.19-4.2.22) likely to the exact answer by applying HAM.

- Suitable auxiliary linear operators have been selected (Kebede et al., 2020).

$$\mathcal{L}_V = V''' - V', \quad \mathcal{L}_H = H'' - H \quad \text{and} \quad \mathcal{L}_L = L'' - L \tag{4.3.1}$$

  In this the linear operators meet the following relations.

$$\mathcal{L}_V(C_1 + C_2 e^{\epsilon} + C_3 e^{-\epsilon}) = \mathcal{L}_H(C_4 e^{\epsilon} + C_5 e^{-\epsilon}) = \mathcal{L}_L(C_6 e^{\epsilon} + C_7 e^{-\epsilon}) = 0,$$

  where $C_1 - C_7$ are constants to be determined based on the boundary conditions. Hence, $C_2 = C_4 = C_6 = 0$.

- Then, the initial guesses of this problem are approximated in the following manner (Loganathan et al., 2021).

$$V_0(\epsilon) = 1 - e^{-\epsilon}, \quad H_0(\epsilon) = \frac{\Upsilon e^{-\epsilon}}{1+\Upsilon}, \quad \text{and} \quad L_0(\epsilon) = e^{-\epsilon} \tag{4.3.2}$$

- Constant auxiliary functions are picked for the dimensionless velocity, energy and nanoparticle concentrations which are:

$$\mathcal{H}_V(\epsilon) = \mathcal{H}_H(\epsilon) = \mathcal{H}_L(\epsilon) = 1. \tag{4.3.3}$$

4.3.2 Zero$^{\text{th}}$ and m$^{\text{th}}$ order Deformation Equations

Based on equation (3.3.5), for non-zero convergent control parameter, the zeros order deformation defined like Kebede et al. (2020) as:

$$\begin{aligned}
(1-p)\mathcal{L}_V[V(\epsilon;p) - V_0(\epsilon)] &= p\hbar_V \mathcal{H}_V(\epsilon)\mathcal{N}_V[V(\epsilon;p), H(\epsilon;p), L(\epsilon;p)] \\
(1-p)\mathcal{L}_H[H(\epsilon;p) - H_0(\epsilon)] &= p\hbar_H \mathcal{H}_H(\epsilon)\mathcal{N}_H[V(\epsilon;p), H(\epsilon;p), L(\epsilon;p)] \\
(1-p)\mathcal{L}_L[L(\epsilon;p) - L_0(\epsilon)] &= p\hbar_L \mathcal{H}_L(\epsilon)\mathcal{N}_L[V(\epsilon;p), H(\epsilon;p), L(\epsilon;p)],
\end{aligned} \tag{4.3.4}$$

where $p \in [0,1]$ is the homotopy embedding parameter without physical meaning, $\mathcal{H}_V(\epsilon), \mathcal{H}_H(\epsilon)$ and $\mathcal{H}_L(\epsilon)$ are auxiliary functions given in equation (4.3.3), and the nonlinear operators $\mathcal{N}_V, \mathcal{N}_H$ and $\mathcal{N}_L$ are defined in the next equations (4.3.5), (4.3.6) and (4.3.7) as follows:

$$\begin{aligned} \mathcal{N}_V[V(\epsilon;p)] =& \frac{\partial^3 V(\epsilon;p)}{\partial \epsilon^3} - A\left(\frac{\partial V(\epsilon;p)}{\partial \epsilon} + \frac{\epsilon}{2}\frac{\partial^2 V(\epsilon;p)}{\partial \epsilon^2}\right) \\ &+ V(\epsilon;p)\frac{\partial^2 V(\epsilon;p)}{\partial \epsilon^2} - \left(\frac{\partial V(\epsilon;p)}{\partial \epsilon}\right)^2 - Ma\frac{\partial V(\epsilon;p)}{\partial \epsilon}, \end{aligned} \tag{4.3.5}$$

$$\begin{aligned} &\mathcal{N}_H[V(\epsilon;p), H(\epsilon;p), L(\epsilon;p)] = (\frac{1+Rn}{Pr})\frac{\partial^2 H(\epsilon;p)}{\partial \epsilon^2} + V(\epsilon;p)\frac{\partial H(\xi;p)}{\partial \epsilon} \\ &- H(\epsilon;p)\frac{\partial V(\epsilon;p)}{\partial \epsilon} - A\left(H(\epsilon;p) + \frac{\epsilon}{2}\frac{\partial H(\epsilon;p)}{\partial \epsilon}\right) + Nt\left(\frac{\partial H(\epsilon;p)}{\partial \epsilon}\right)^2 \\ &+ Nb\frac{\partial H(\epsilon;p)}{\partial \epsilon}\frac{\partial L(\epsilon;p)}{\partial \epsilon} + Ec\left(\frac{\partial^2 V(\epsilon;p)}{\partial \epsilon^2}\right)^2, \end{aligned} \tag{4.3.6}$$

$$\begin{aligned} &\mathcal{N}_L[V(\epsilon;p), H(\epsilon;p), L(\epsilon;p)] = \frac{\partial^2 L(\epsilon;p)}{\partial \epsilon^2} + \frac{Nt}{Nb}\frac{\partial^2 H(\epsilon;p)}{\partial \epsilon^2} \\ &+ Sc\left(V(\epsilon;p)\frac{\partial L(\epsilon;p)}{\partial \epsilon} - L(\epsilon;p)\frac{\partial V(\epsilon;p)}{\partial \epsilon}\right) - ScA\left(L(\epsilon;p) + \frac{\epsilon}{2}\frac{\partial L(\epsilon;p)}{\partial \epsilon}\right). \end{aligned} \tag{4.3.7}$$

Next, the boundary conditions have been adjusted to the following manner.

$$\begin{cases} V(0;p) = 0, \ \dfrac{\partial V(\epsilon;p)}{\partial \epsilon}|_{\epsilon=0} = 1, \left[\dfrac{\partial H(\epsilon;p)}{\partial \epsilon}\right]_{\epsilon=0} = \Upsilon(H(0;p) - 1) \\ L(0;p) = 1, \dfrac{\partial V(\epsilon;p)}{\partial \epsilon}|_{\epsilon\to\infty} = H(\epsilon;p)|_{\epsilon\to\infty} = L(\epsilon;p)|_{\epsilon\to\infty} = 0 \end{cases} \tag{4.3.8}$$

It is clear that when $p = 0$, $V(\epsilon,0) = V_0(\epsilon), H(\epsilon,0) = H_0(\epsilon)$, and $L(\epsilon,0) = L_0(\epsilon)$ are solutions for the equations (4.2.19-4.2.22). Likewise, at $p = 1$, the answer of these equations become $V(\epsilon,1) = V(\epsilon), H(\epsilon,1) = H(\epsilon)$, and $L(\epsilon,1) = L(\epsilon)$. Thus, when the value of p changes continuously from 0 to 1, the homotopy solution also runs from initial guesses $V_0(\epsilon), H_0(\epsilon)$, and $L_0(\epsilon)$ (given in equation 4.3.2) to the accurate solutions, $V(\epsilon), H(\epsilon)$, and $L(\epsilon)$ according to Van Gorder (2014). As Rasheed et al. (2021) did, the Taylor series expansion is used to expand $V(\epsilon;p), H(\epsilon;p), L(\epsilon;p)$ about $p = 0$ as in equation (3.3.7).

$$
\begin{aligned}
&V(\epsilon;p) = V_0(\epsilon) + \sum_{m=1}^{\infty} V_m(\epsilon)p^m, H(\epsilon;p) = H_0(\epsilon) + \sum_{m=1}^{\infty} H_m(\epsilon)p^m \\
&\text{Ł}(\epsilon;p) = L_0(\epsilon) + \sum_{m=1}^{\infty} L_m(\epsilon)p^m,
\end{aligned}
\tag{4.3.9}
$$

In equation (4.3.9), $V_m(\epsilon), H_m(\epsilon)$ and $L_m(\epsilon)$ can be defined as follows ($m \geq 1$).

$$
V_m(\epsilon) = \frac{1}{m!}\frac{\partial^m V(\epsilon;p)}{\partial p^m}|_{p=0}, H_m(\epsilon) = \frac{1}{m!}\frac{\partial^m H(\epsilon;p)}{\partial p^m}|_{p=0}, L_m(\epsilon) = \frac{1}{m!}\frac{\partial^m L(\epsilon;p)}{\partial p^m}|_{p=0}.
\tag{4.3.10}
$$

Equation (4.3.10) is called m^{th} order homotopy derivative. The m^{th} order deformation obtained by differentiating the 0^{th} order deformation (4.3.4) m-times with respect to p and substituting $p = 0$, then dividing by m factorial. Thus, similar to equation (3.3.8), the m^{th} order deformation equations become:

$$
\begin{aligned}
&\mathcal{L}_V[V_m(\epsilon) - \chi_m V_{m-1}(\epsilon)] = \hbar_V \mathcal{H}_V(\epsilon)\mathcal{R}^V_{m-1}, \\
&\mathcal{L}_H[H_m(\epsilon) - \chi_m H_{m-1}(\epsilon)] = \hbar_H \mathcal{H}_H(\epsilon)\mathcal{R}^H_{m-1}, \quad \text{and} \\
&\mathcal{L}_L[L_m(\epsilon) - \chi_m L_{m-1}(\epsilon)] = \hbar_L \mathcal{H}_L(\epsilon)\mathcal{R}^L_{m-1}.
\end{aligned}
\tag{4.3.11}
$$

Equation (4.3.11) is called m^{th} order deformation equations, and the boundary conditions in equation (4.3.12) becomes

$$
\begin{aligned}
&V_m(0) = V'_m(0) = \left[H'_m(0) + \Upsilon(1 - H_m(0))\right] = L_m(0) = 0 \\
&V'_m(\epsilon \to \infty) = H_m(\epsilon \to \infty) = L_m(\epsilon \to \infty) = 0.
\end{aligned}
\tag{4.3.12}
$$

From equation (4.3.11), $\chi_m = \begin{cases} 0, & \text{if } \ m \leq 1 \\ 1, & \text{if } \ m > 1 \end{cases}$ denotes a step function. (4.3.13)

In general $\mathcal{R}^V_m, \mathcal{R}^H_m$ and $\mathcal{R}^L_m$ are defined as follows:

$$
\mathcal{R}^V_m = V'''_m + \sum_{l=0}^{m} V_l V''_{m-l} - A\left(V'_m + \frac{\epsilon}{2}V''_m\right) - \sum_{l=0}^{m} V'_l V'_{m-l} - MaV'_m,
\tag{4.3.14}
$$

$$
\begin{aligned}
\mathcal{R}_m^H =&\left(\frac{1+Rn}{Pr}\right)H_m'' - A\left(H_m+\frac{\epsilon}{2}H_m'\right)+Nb\sum_{l=0}^{m}H_l'L_{m-l}' \\
&+Nt\sum_{l=0}^{m}H_l'H_{m-l}'+\sum_{l=0}^{m}V_lH_{m-l}'-\sum_{l=0}^{m}H_lV_{m-l}'+Ec\sum_{l=0}^{m}V_l''V_{m-l}'',
\end{aligned}
\tag{4.3.15}
$$

$$
\mathcal{R}_m^L =L_m'' - Sc\left[A\left(L_m+\frac{\epsilon}{2}L_m'\right)-\sum_{l=0}^{m}V_lL_{m-l}'\right]-Sc\sum_{l=0}^{m}L_lV_{m-l}'+\frac{Nt}{Nb}H_m''. \tag{4.3.16}
$$

To acquire the solutions of ODEs (4.2.19-4.2.22), the inverse linear operators are carried out on both sides of m^{th} order deformation equations in (4.3.11) as follows:

$$
\begin{aligned}
V_m(\epsilon) &= \chi_m V_{m-1}(\epsilon)+\hbar_V\mathcal{L}_V^{-1}\left[\mathcal{H}_V(\epsilon)\mathcal{R}_{m-1}^V\right]\\
H_m(\epsilon) &= \chi_m H_{m-1}(\epsilon)+\hbar_H\mathcal{L}_H^{-1}\left[\mathcal{H}_H(\epsilon)\mathcal{R}_{m-1}^H\right]\\
L_m(\epsilon) &= \chi_m L_{m-1}(\epsilon)+\hbar_L\mathcal{L}_L^{-1}\left[\mathcal{H}_L(\epsilon)\mathcal{R}_{m-1}^L\right].
\end{aligned}
\tag{4.3.17}
$$

In equation (4.3.17), for distinct individual value of $m = 1,2,3,...$, the recurrence solutions are developed. Now, there are auxiliary linear operators from (4.3.1), initial guesses (4.3.2) and auxiliary functions (4.3.3). Still the convergence control parameters ($\hbar_V, \hbar_H$ and $\hbar_L$) are not specified. So, there is an option to take the suitable convergence control parameters from $\hbar$-curves, which is one of the benefits of HAM to get convergent solutions. Accordingly, when $p = 1$, the obtained solutions are convergent, and they are expressed as follows:

$$
\begin{aligned}
V(\epsilon;p) &= V_0(\epsilon)+\sum_{m=1}^{\infty}p^mV_m(\epsilon) \implies V(\epsilon;1)=V_0(\epsilon)+\sum_{m=1}^{\infty}V_m(\epsilon)=V(\epsilon),\\
H(\epsilon;p) &= H_0(\epsilon)+\sum_{m=1}^{\infty}p^mH_m(\epsilon) \implies H(\epsilon;1)=H_0(\epsilon)+\sum_{m=1}^{\infty}H_m(\epsilon)=H(\epsilon),\\
L(\epsilon;p) &= L_0(\epsilon)+\sum_{m=1}^{\infty}p^mL_m(\epsilon) \implies L(\epsilon;1)=L_0(\epsilon)+\sum_{m=1}^{\infty}L_m(\epsilon)=L(\epsilon).
\end{aligned}
\tag{4.3.18}
$$

The expressions in equation (4.3.18) represent the exact solution of this problem. Practically, finding the infinite terms are impossible. So, it is advisable to use the truncated order of approximation whose limit close to the exact one as (3.3.13). This leads to say the HAM is semi-analytic. Thus, selecting appropriate auxiliary linear operators, initial guesses, auxiliary functions and convergence control parameters play a key role to get minimum error with some order of approximation. Except the convergence control parameters, the other three points have been already chosen. Now let us discuss and select the best convergence control parameters for this specific problem.

4.3.3 Analyzing the Convergence of Solutions

In HAM, the convergence of solutions mostly rely on the convergent control parameters. As Van Gorder (2014) discussed, the interval in which $\hbar$-curves are horizontal indicate the possible values of these convergent control parameters to gain a successful solution. Here, $\hbar$-curves have been drawn in Figure 4.3.1a by taking $\hbar_V = \hbar_H = \hbar_L = \hbar$ horizontal axis versus $V''(0), -H'(0)$ and $-L'(0)$. Accordingly, it was chosen for $\hbar_V = -0.75592463, \hbar_H = -0.71300000$ and $\hbar_L = -1.01700000$ by implementing the code from BVPh2.0 package on Mathematica 12.1. Furthermore, from Figure 4.3.1b, it can be seen that, error is reduced in a vertical axis as the order of approximation increases. This result can be assured by Figure 4.3.2a where the magnitude of successive difference values in Table 4.3.1 becoming zero. That is, $|V''(0)_{n+1} - V''(0)_n| \to 0, |H'(0)_{n+1} - H'(0)_n| \to 0$ and $|L'(0)_{n+1} - L'(0)_n| \to 0$, where $n = 1, 2, ..., 9$ is the number of values in Table 4.3.1. Beside, Table 4.3.1 is a testimony on successful accomplishment of convergence for the values of $Ma = 0.5, Sc = Rn = 0.7, Nt = Nb = A = 0.3, Pr = 0.72, Ec = \Upsilon = 0.1$ with residual error on respective order of approximation (m). Pictorial representation of this table is brought by Figures 4.3.2b, 4.3.3a and 4.3.3b for the value of $-V''(0), -H'(0)$ and $-L'(0)$ in that order against the value of n which attest getting the convergent values. Therefore, for this issue, HAM is a guaranteed convergent solution method with acceptable error.

Table 4.3.1: Order of approximation of HAM with residual error

n	m^{th} Order	$-V''(0)$	$-H'(0)$	$-L'(0)$	**Residual Error** $-V''(0)$	$-H'(0)$	$-L'(0)$
1	3	1.30915	0.0830521	0.832144			
2	6	1.31068	0.0824798	0.817938	3.80×10^{-10}	3.16×10^{-6}	9.17×10^{-6}
3	9	1.31070	0.0823044	0.813887			
4	12	1.31070	0.0822521	0.812661	3.68×10^{-17}	8.45×10^{-8}	2.81×10^{-7}
5	15	1.31070	0.082231	0.812166			
6	18	1.31070	0.0822227	0.811969	4.99×10^{-23}	2.90×10^{-9}	1.03×10^{-8}
7	21	1.31070	0.0822191	0.81184			
8	24	1.31070	0.0822176	0.811848	2.27×10^{-29}	1.05×10^{-10}	3.90×10^{-10}
9	27	1.31070	0.0822169	0.811832			
10	30	1.31070	0.08221660	0.811825	2.85×10^{-31}	3.87×10^{-12}	1.49×10^{-11}

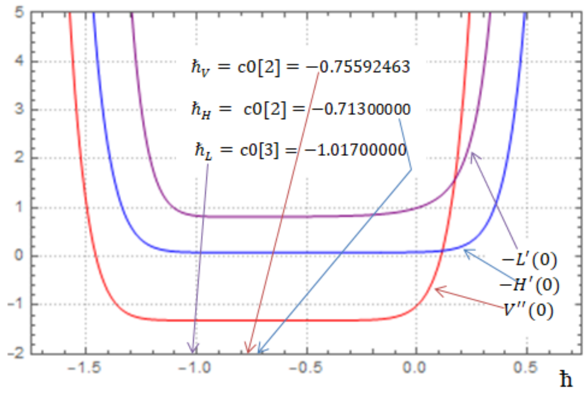

(a) $\hbar$-curves $\hbar_V, \hbar_H$ and $\hbar_L$

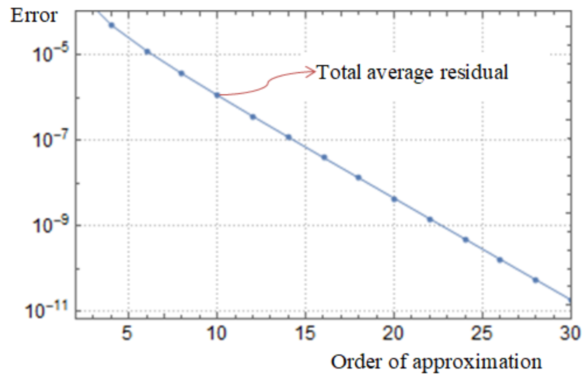

(b) The order of approximation

Figure 4.3.1: $\hbar$-curves and order of approximation

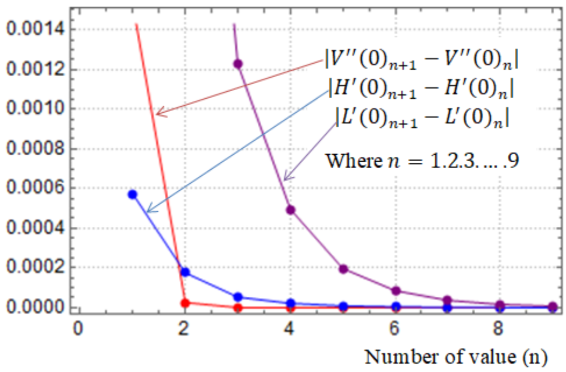

(a) Magnitude of difference values

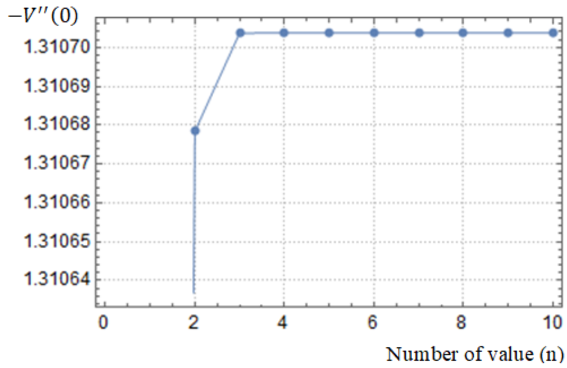

(b) Convergence value of $-V''(0)$

Figure 4.3.2: Differences in absolute value and convergence on the value of $-V''(0)$

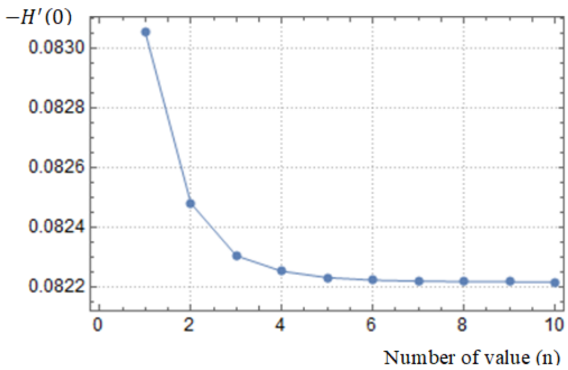

(a) Convergence on the value of $-H'(0)$

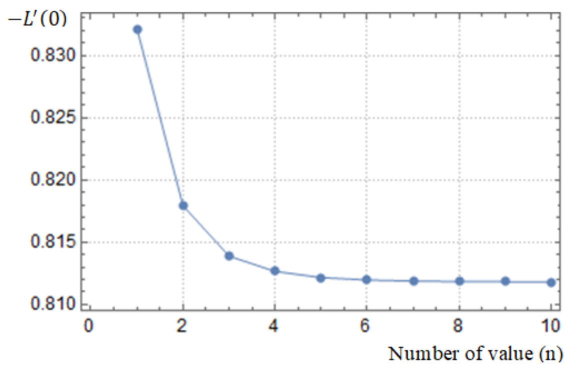

(b) Convergence on the value of $-L'(0)$

Figure 4.3.3: Convergence on the value of $-H'(0)$ and $-L'(0)$

4.4 Computed Outcome and Discussion

The result of semi-analytic computation on this problem offered for velocity, temperature, nanoparticles concentration, entropy, Benjan number, local skin friction coefficient, Nusselt and Sherwood numbers with a brief discussion. Using HAM, the graphical illustrations are given for the influence of physical parameters on ODEs (4.2.19-

4.2.21) with boundary conditions in (4.2.22). The validation of this computation has been justified by comparing the values of $-V''(0)$ depending on A with different published articles as seen from Table 4.4.1. Additionally, Table 4.4.2 also lays out the existence of similar outcomes for distinct values of Pr with another published works.

Table 4.4.1: Comparing the values of $-V''(0)$ for different values of A

A	Ullah et al. (2017)	Bibi et al. (2018)	Kebede et al. (2020)	**Present Result**
0.1	-	-	-	1.034137
0.2	-	1.0685	1.06874	1.068027
0.3	-	-	-	1.101563
0.4	-	1.1349	1.13521	1.134657
0.5	-	-	-	1.167191
0.6	-	1.1992	1.19930	1.199148
0.7	-	-	-	1.230450
0.8	1.2610	-	1.26099	1.261102
1.0	-	-	-	1.320510
1.2	1.3777	-	1.37755	1.377705

Table 4.4.2: Comparing the values of $-H'(0)$ for distinct values of Pr

Pr	Ullah et al. (2017)	Aziz et al. (2021)	Anki Reddy et al. (2018)	**Present Result**
0.72	0.8088	0.8087618	0.80863	0.8086314
1.00	1.0000	1.0000000	1.00000	1.0000000
3.00	1.9237	1.9235740	1.92368	1.9236826
7.00	-	3.0731465	-	3.0722474
10.0	3.7207	3.7205543	3.72060	3.7207112
20.0	-	-	-	5.3639140
30.0	-	-	-	6.6242008
50.0	-	-	-	8.6222647

4.4.1 Velocity and Temperature Profiles

The influence of magnetic field interaction on the movement of nanofluid alluded on Figure 4.4.1a. This outcome admitted with the fact that on stretching surface, the interaction of magnetic field generates Lorentz force which leads to rise up the drag like forces. As a consequence, the flow of the nanofluid is retarded by this force which is realized pictorially in Figure 4.4.1a. Moreover, the velocity boundary layer thickness decreases over the stretching sheet as a result of increasing the values of Ma.

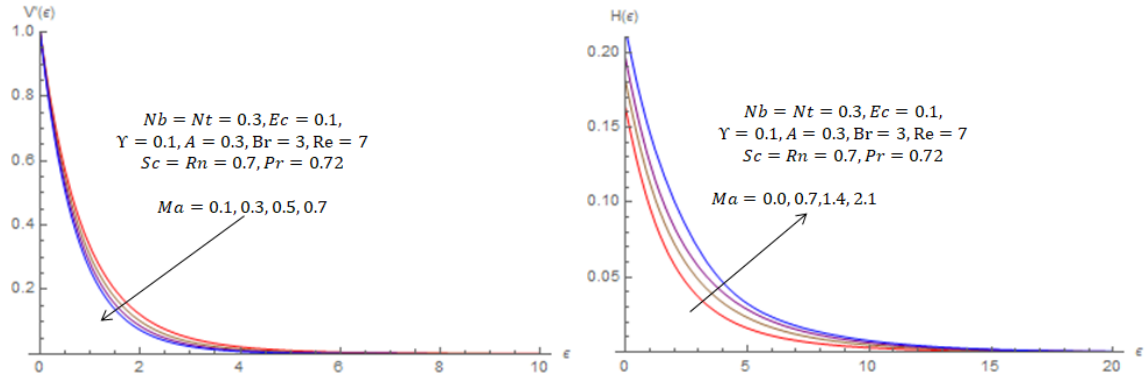

(a) Impact of Ma on $V'(\epsilon)$ (b) Impact of Ma on $H(\epsilon)$

Figure 4.4.1: Impact of magnetic field interaction on velocity and temperature

In energy equation (4.2.20), the parameters which are highly allied with dimensionless temperature are $Ma, Rn, Ec, \Upsilon, Nt, Pr$ and A. The graphical representations from Figures 4.4.1b to 4.4.4 are the results obtained by executing HAM. Generally, the thermal boundary layer thickness on an expandable surface increases due to the parameters that raise the temperature.

Figure 4.4.1b marked that the temperature profile expands as the value of Ma rolls up. This is due to the production of heat as a byproduct of the viscous formation when the magnetic field interaction is increased. The more heat generated by this viscous feature, the warmer the nanofluids as they flow. A byproduct of this circumstance leads to raise the temperature distribution. The impact of thermal radiation (Rn) on dimensionless temperature field has been outlined in Figure 4.4.2a. Accordingly, $H(\epsilon)$ grows up in accordance with (Rn). This takes place due to the presence of more heat transfer from the solar radiations. Like Rn, thermal energy enlarges when Eckert number (Ec) accrues according to Figure 4.4.2b. A dimensionless number Ec represents the ratio of kinetic energy to entalpy variation in the boundary layer. From this point onward, whenever Ec increases, the kinetic energy also goes up, elevating the temperature of the nanofluids. The heat transfer coefficient rises with increasing Biot number (Υ) that enhances the temperature of nanofluid. This is displayed by Figure 4.4.3a, where higher values of Υ propagate the temperature field. Due to the effect of thermophoretic force on nanoparticles, Nt has a tendency to rise the nanofluid's temperature as Figure 4.4.3b shows.

In another way, the distribution of temperature deducted as the Prantdl number (Pr) augments what it is proved on Figure 4.4.4a. Pr and thermal diffusivity are inversely related. This means that as Pr tapers, the temperature of nanofluids rises. At the same time, the thermal boundary layer length diminishes with increasing the values of Pr. As time goes, the unsteady flowing nanofluid becomes cooling and also the thermal boundary layer thickness is reduced. Thus, the unsteadiness parameter (A) and $H(\epsilon)$ have an inverse relation as illustrated in Figure 4.4.4b.

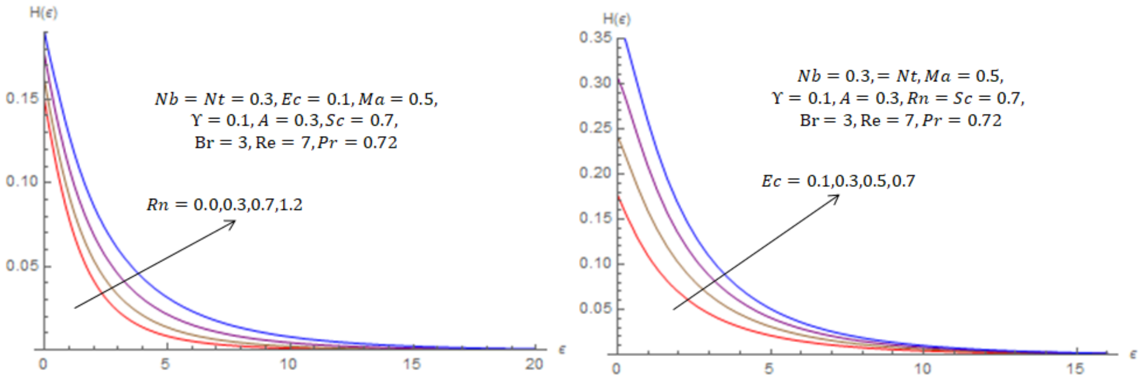

(a) Impact of Rn on $H(\epsilon)$ (b) Impact of Ec on $H(\epsilon)$

Figure 4.4.2: Impact of thermal radiation and Eckert number on temperature

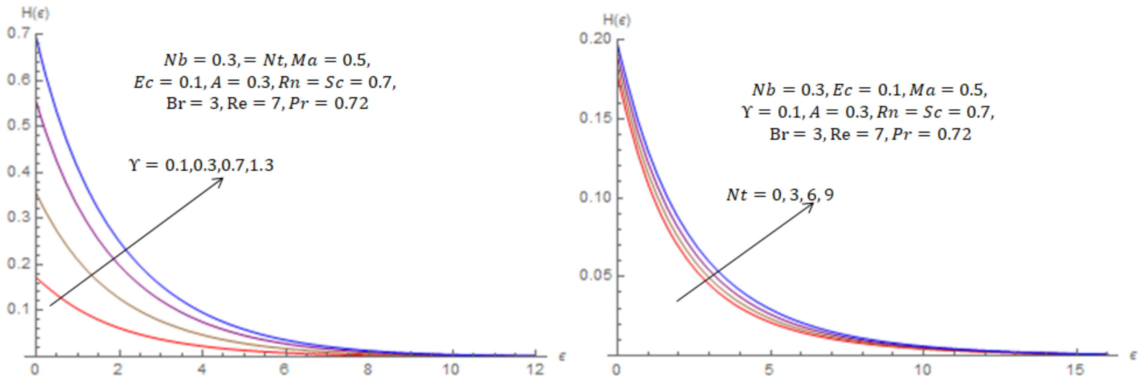

(a) Impact of Υ on $H(\epsilon)$ (b) Impact of Nt on $H(\epsilon)$

Figure 4.4.3: Impact of Biot number and thermophoresis parameter on temperature

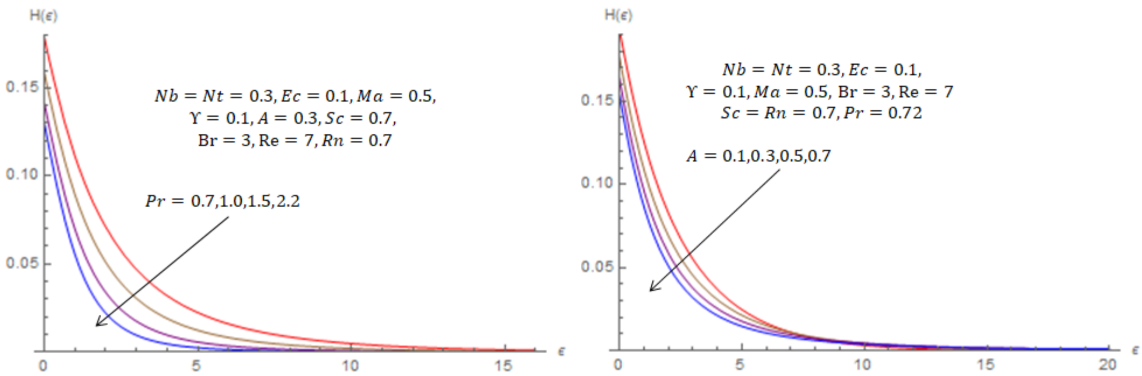

(a) Impact of Pr on $H(\epsilon)$ (b) Impact of A on $H(\epsilon)$

Figure 4.4.4: Impact of Prandtl number and unsteadiness on temperature

4.4.2 The Concentration Profile

The role of micro-sized solid particles concentration on the heat and mass transfer through the flow of nanofluids in DASCs is explicated by the prominent parameters such as Nt, Ma, Υ and Sc using the graphs 4.4.5a to 4.4.6b.

From Figure 4.4.5a, it can be realized that the thermophoresis constant (Nt) increases the micro-sized solid particles concentration. In this case, raising the values of Nt enlarges the amount of $(\bar{T}_w - \bar{T}_\infty)$ which moves the small-sized particles from warm to cold. This results in adding the amount of nanoparticles concentration. The effect of Ma and Υ are similar with Nt on the volume fraction of nanoparticles. Thus, according to Figure 4.4.5b, the magnetic field interaction has a power to increase the concentration of nanoparticles. The Biot number also augments the nanoparticles concentration as Figure 4.4.6a illustrates. This is due to the increment of nanoparticles' motion by the higher temperature distribution.

The constant Schmidt number (Sc) is defined as the ratio of momentum diffusivity to mass diffusivity. The purpose of Sc in convective mass transfer similar to Pr as in case of convective heat transfer.So, for more Sc, the mass diffusivity abates, which causes the dropping of nanoparticles concentration as inspected from Figure 4.4.6b.

4.4.3 Impact of Parameters on Entropy and Bejan Number

In general, entropy has been generated due to irreversible actions, and its concept has been illuminated by the second law of thermodynamics for heat transfer. Based on this problem, the prominent parameters of entropy and also the Bejan number are A, Υ, Ma, Sc and Ec. All problems in this dissertation have fixed values for constants, such as $\Delta_1 = \Delta_2 = \Delta_3 = 1$. Their spheres of influence have been revealed graphically from 4.4.7a to 4.4.9b.

Figure 4.4.7a pointed out that an accretion of A produces more entropy. Biot number has a possibility to raise the temperature which disturb the system order. Thus, the Bejan number (Be) is raised by increasing Υ which observed on Figure 4.4.7b. The parameter Ma promotes the production of entropy and also escalates the Bejan number, which ends up being near one, as it can be see from Figures 4.4.8a and 4.4.8b respectively. Once the nanofluids discharge from the wall, the parameters Υ and Ma exchange extra heat. In light of this, the entropy and Bejan number have gone up

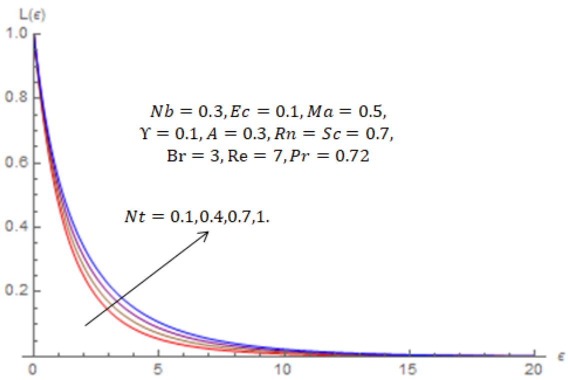

(a) Impact of Nt on $L(\epsilon)$

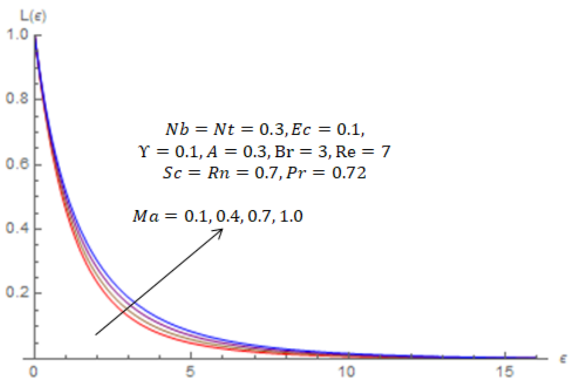

(b) Impact of Ma on $L(\epsilon)$

Figure 4.4.5: Thermophoresis and magnetic field constants impact on concentration

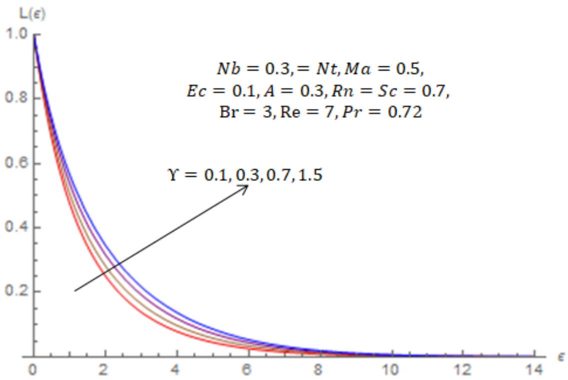

(a) Impact of Υ on $L(\epsilon)$

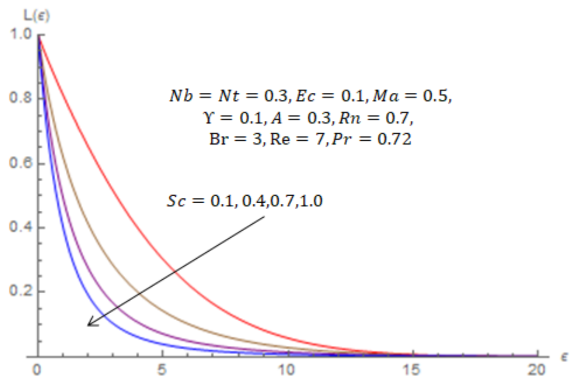

(b) Impact of Sc on $L(\epsilon)$

Figure 4.4.6: Impact of Biot and Schmidt numbers on concentration

in that order. Particularly, Figure 4.4.8b is similar with the published article quoted by Loganathan et al. (2021).

The findings of this research indicates that the parameter Sc has an inverse influence on the formation of volumetric rate of entropy and Bejan number. That is, higher values of Sc add more energy loss, and diminutions the Bejan number. In general, the Bejan number is close to one at a far distance. The impact of Sc and Ec on Bejan number are opposite. For this, Figures 4.4.9a and 4.4.9b can be an evidence in that order. Although, both parameters have a contrary effect on the Bejan number, the final value of Be approaches to 1.

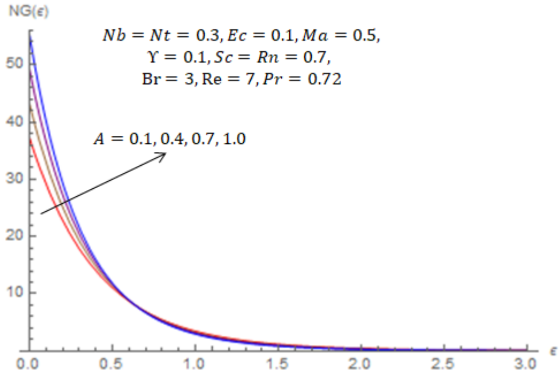

(a) Impacts of A on non-dimensional entropy

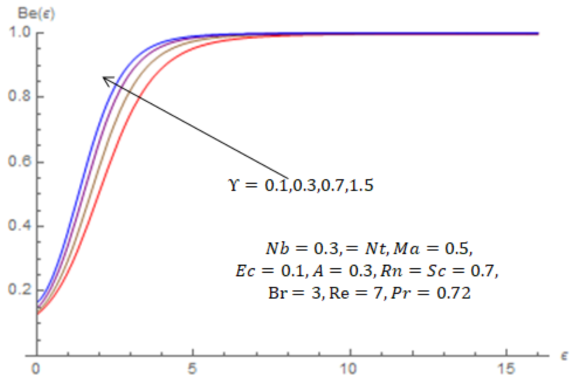

(b) Impacts of Υ on Bejan number

Figure 4.4.7: Impact of Biot number on NG and Be

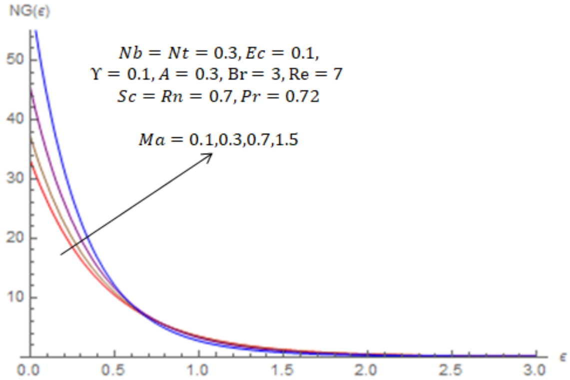

(a) Impacts of Ma on dimensionless entropy

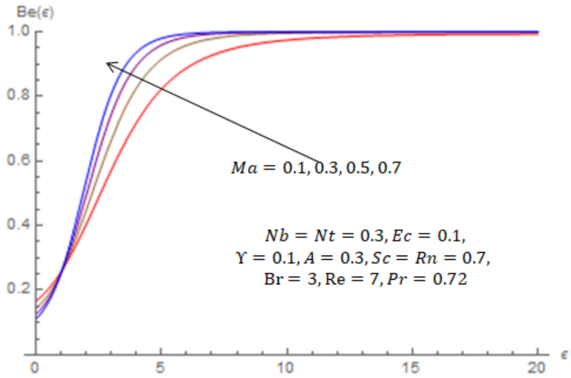

(b) Impacts of Ma on Bejan number

Figure 4.4.8: Impact of magnetic field interaction on NG and Be

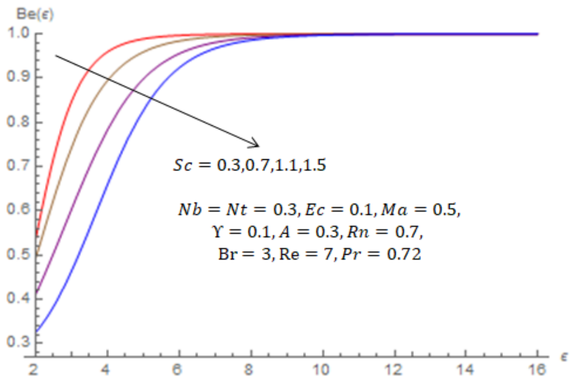

(a) Impacts of Sc on Bejan number

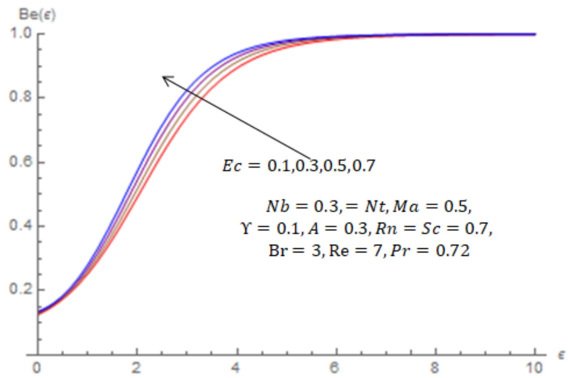

(b) Impacts of Ec on Bejan number

Figure 4.4.9: Impact of Schmidt number and Eckert number on Be

4.4.4 Impact of Parameters on the Physical Quantities

This section explicates the impact of parameters on local skin friction (Cf_x), Nusselt number (Nu_x) and Sherwood number (Sh_x) defined in equations (4.2.23), (4.2.24) and (4.2.25) taking $Re_x = 1$. Accordingly, the graph in Figure 4.4.10a supported more accumulation of the local skin friction coefficient ($-V''(0)$) when the value of Ma is high with a continuous increment of unsteadiness parameter A. Here, that is why this parameter lag the movement of nanofluids in DASCs. The unsteadiness parameter (A) keeps up the Nusselt number, whereas the thermophoresis parameter (Nt) continuously deescalates the heat transfer rate, as it is seen in Figure 4.4.10b. This means that, the heat transfer rate grows with the decreasing of thermophoresis parameter within long time. The impact of Eckert number and Brownian motion constant are opposite on Nusselt and Sherwood numbers. Hence, Figures 4.4.11a and 4.4.11b, tell us, both Ec and Nb have a tendency to decrease the heat transfer rate and increase mass transfer rate in that order. By detracting Ma and Nt without interruption as time goes, the local Sherwood number is intensified, as it is realized from Figures 4.4.12a and 4.4.12b. That means, the magnetic field interaction and the movement of small sized particles due to temperature difference have a possibility to have low mass transfer rate. However, the unsteadiness parameter raises the transmission of mass rate.

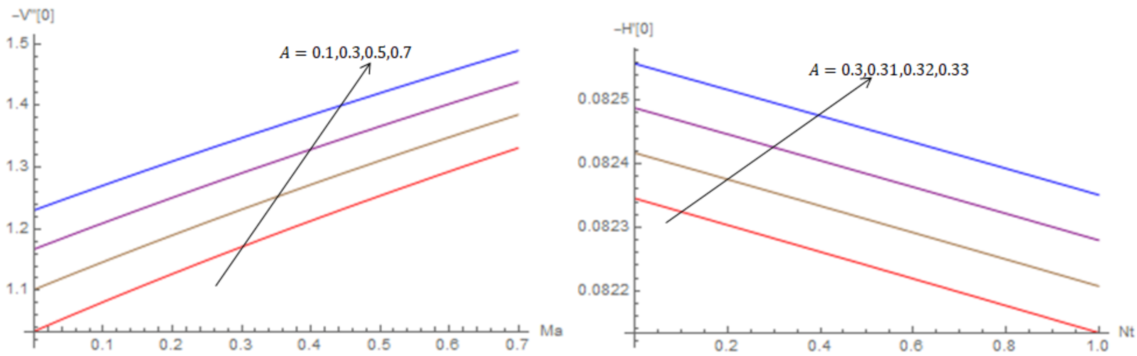

(a) Impact of A on $-V''(0)$ with Ma (b) Impact of A on $-H'(0)$ with Nt

Figure 4.4.10: Impact of A on drag force with Ma and on heat transfer with Nt

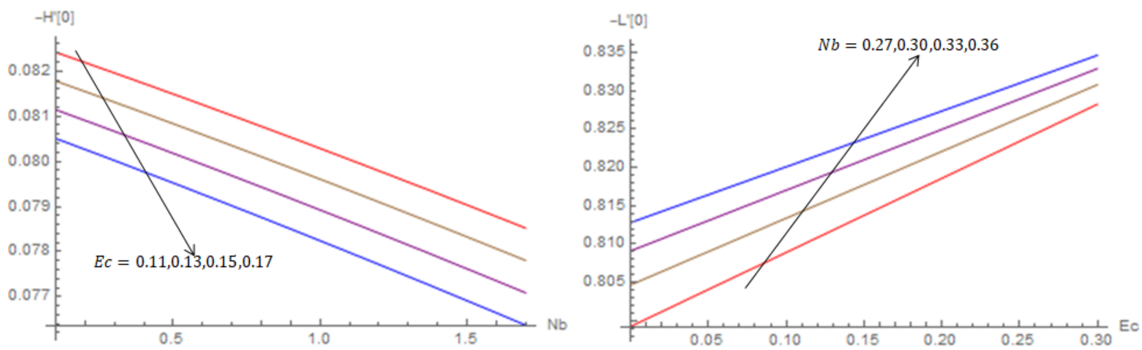

(a) Impact of Ec on $-H'(0)$ with Nb (b) Impact of Nb on $-L'(0)$ with Ec

Figure 4.4.11: Impact of Ec and Nb on heat and mass transfer rate

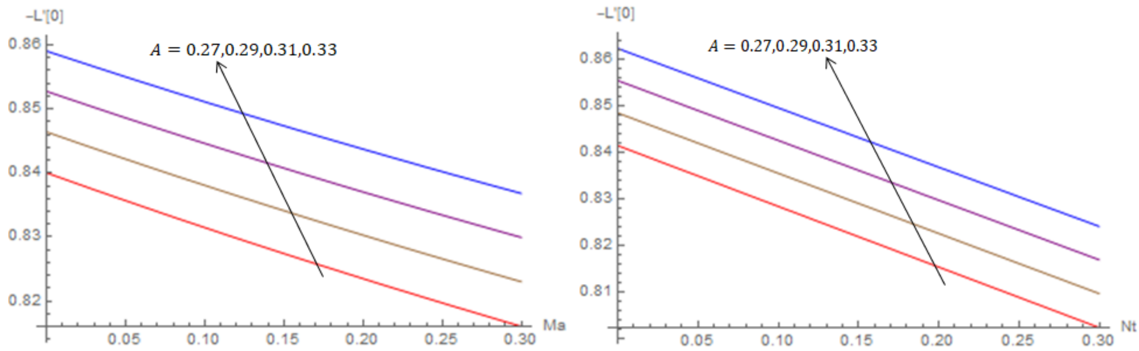

(a) Impact of A on $-L'(0)$ with Ma (b) Impact of A on $-L'(0)$ with Nt

Figure 4.4.12: Impact of A, Ma and Nt on heat and mass transfer rate

4.5 Summary

This research work focuses on the heat and mass transfer of incompressible, 2D, unsteady flowing nanofluid across a stretchable surface as a DASC with the effect of radiation and viscosity. Entropy generation is also addressed in this aspect. The governing PDEs are converted into ODEs by similarity transformation, then it is solved by HAM. There upon, among many parameters that are actualized in this process, the exceedingly influenced ones on $V', H, L, NG, Be, Cf_x, Nu_x$ and Sh_x have been represented graphically. The main findings of this issue are listed below.

- Dimensionless velocity recedes as the value of Ma increases.
- Accretion of Ma, Rn, Ec, Nt and Υ upswings the temperature distribution and thermal boundary layer thickness while it dwindles as Pr and A grow.
- The concentration of micro-sized particles proliferate for higher values of Nt, Ma, Υ and wane away as Sc becomes larger.
- There is a direct relation between the entropy and the values of A and Ma. Bejan number increases with the ascending Υ, Ma, Ec and descending Sc.
- The parameter Ma and A maximize the coefficient of skin friction in magnitude to which they retard the motion of nanofluids.
- Nu_x decreases along with Nt, Ec and Nb, but not A.
- Ec, Nb and A elevate the mass transfer rate (Sh_x) but not Ma and Nt.

CHAPTER FIVE

Heat and Mass Transfer via Flowing Nanofluid through a Porous Medium with the Presence of Radiation and Entropy Generation

5.1 Introduction

At the present time, the world societies are confronted with climate change and shortage of energy due to rising the consumption of non-renewable energy like fuel and coal, in line with economic growth. These challenges initiate scientists to find a workable, free from air pollution and affirming perpetual power source called renewable energy sources. Hence, the sustainability and adequacy of power are assured by renewable energy sources like solar. Specifically, the production of electricity has been increasing by applying solar radiation. It is thermal radiation obtained from hot airs of the Sun by means of radiation. Efficiently, capturing solar thermal radiation ameliorates the energy supply for our everyday activities. Many studies emphasized on advanced collecting solar energy including Sabiha et al. (2015); Pandey and Chaurasiya (2017).

In nanofluid, the nanometric particles are evenly disseminated and stably adjourned in the base fluid. By handling nanofluid as a working fluid, Dugaria et al. (2018) designed the concentric DASCs to collect solar and also Rasih et al. (2019) discerned the possibility of heat transfer on it. Nanofluids are more appropriate for water boilers, solar gathering, cooling systems, absorption refrigeration systems, solar cells, and a combination of various solar devices than the conventional fluids (Elsheikh et al., 2018). Thus, most scientists aspired towards the applications of nanofluids, regarding heat transfer from solar radiation and they noted that, its effectiveness accentuated by applying nanofluids (Bhalla and Tyagi, 2017; Subramani et al., 2018).

A solid region having plenty of pores in which nanofluids can blow over it is called a porous medium. If the inertial forces are not dominating, Darcy's law can be employed. The flow of nanofluids on a porous media rises the heat transfer due to having high dissipation area and choppy motion around the distinct drops (Mahdi et al., 2015). Jamshed et al. (2021a) also utilizes a porous media, viscous dissipation and thermal radiative flow to improve Solar Water Pump (SWP) production. Thus, porosity proliferates the temperature and also entropy. Greater attention is now being paid for designing systems that emit the least amount of entropy, which results in more usable energy. The second law of thermodynamics enlightens the notion of entropy. Entropy formation on many aspects have been mentioned in Daniel et al. (2017); Aziz et al. (2018); Hayat et al. (2019); ur Rahman et al. (2022).

In light of the aforesaid survey, there is a little information about the heat and mass transfer by nanofluid flow on a porous media in DASCs including entropy and solved by HAM. Regarding the records mentioned above, such an issue has not yet been distinguished. Thus, the researchers aspired to look at the heat and mass transfer of nanofluid transporting over a horizontal porous medium with the existence of solar thermal radiation, and analyzing the entropy generation. Equations of flow, temperature and concentration are administered with mass suction, velocity slip and convective boundary conditions. By including these points, the obtained equations are solved by a soundly branded method called HAM on Mathematica software.

5.2 Mathematical Formulation of the Problem

In this problem, the Cartesian coordinate system is imagined and the surface set up is stretching at $t > 0$ (Hussain et al., 2015). Then, the surface elongated horizontally with time-dependent velocity, temperature and concentration where the surface wall is given similar to equation (4.2.1) (Aziz et al., 2021; Hussain, 2022).

$$U_w = \frac{\hat{b}x}{1-\varsigma t},\ \bar{T}_w = \bar{T}_\infty + \frac{\bar{T}_0 \bar{c} x}{\nu(1-\varsigma t)} \text{and}\ \ \bar{C}_w = \bar{C}_\infty + \frac{\bar{C}_0 \bar{c} x}{\nu(1-\varsigma t)} \tag{5.2.1}$$

The physical flow of this problem designated in Figure 5.2.1. The flow model relies on the assumptions in section 4.2 on porous media and adding heat source.

5.2.1 The Governing Equations

Using conservation of mass, momentum, energy and concentration, the governing equations can be derived. This problem is an extension of Chapter FOUR by considering porous medium with velocity slip and mass suction boundary conditions. Therefore, the derivation of governing equations are similar with section 4.2 by adding the effect of porosity on momentum equation, mass suction and velocity slip.

The impact of porosity is modeled by linear Darcy law. This is expressed from the

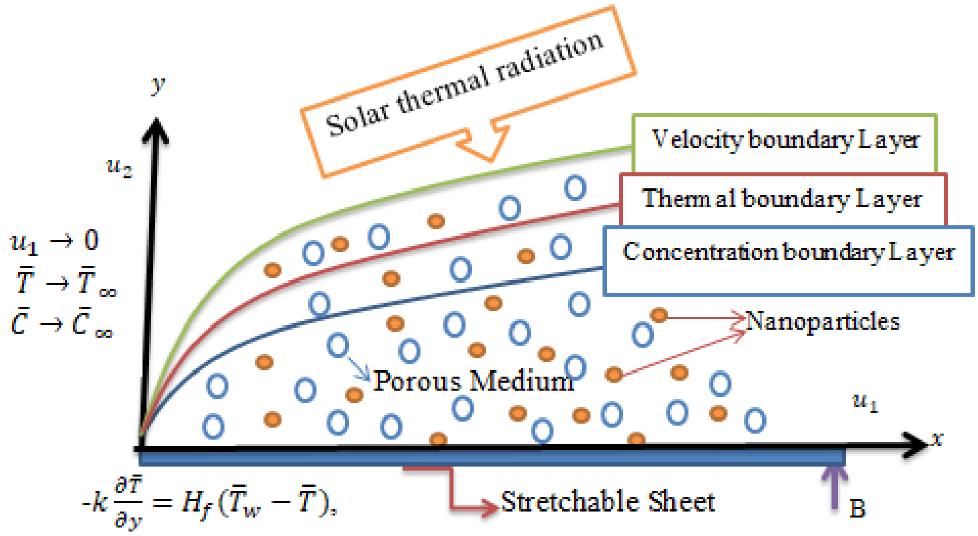

Figure 5.2.1: The conceptual framework for the physical system

equation (1.1.6) on 2D as follows:

$$\nabla P = -\frac{\mu}{k_p}\mathbf{v} \implies (\frac{\partial P}{\partial x}, \frac{\partial P}{\partial y}) = -\frac{\mu}{k_p}(u_1, u_2) \implies \frac{\partial P}{\partial x} = -\frac{\mu}{k_p}u_1, \ \frac{\partial P}{\partial y} - \frac{\mu}{k_p}u_2 = 0.$$

Hence, the momentum equations with the impacts of magnetic field and porous medium can be expressed based on the boundary layer approximations as follows:

$$\rho\frac{D\mathbf{v}}{Dt} = \mu\nabla^2\mathbf{v} + \mathbf{J}\times\mathbf{B} + \nabla P \implies \rho\frac{Du_1}{Dt} = \mu\left(\frac{\partial^2 u_1}{\partial y^2}\right) - \frac{\sigma_e B_0^2 u_1}{1-\varsigma t} - \frac{\mu}{k_p}u_1.$$

In the energy equation (4.2.4), the heat source due temperature difference is added. As a result $\bar{q} = -\nabla q_r + c_p\rho_p(\nabla\bar{T})\left(D_B\nabla\bar{C} + \frac{D_T}{\bar{T}_\infty}\nabla\bar{T}\right) + Q_g(\bar{T}-\bar{T}_\infty)$. The concentration equation taken as it is. Thus, the following simplified PDEs are derived (Kebede et al., 2020; Jamshed et al., 2021a; Hussain, 2022).

$$\frac{\partial u_1}{\partial x} + \frac{\partial u_2}{\partial y} = 0, \tag{5.2.2}$$

$$\frac{\partial u_1}{\partial t} + u_1\frac{\partial u_1}{\partial x} + u_2\frac{\partial u_1}{\partial y} = \nu\frac{\partial^2 u_1}{\partial y^2} - \frac{\sigma_e B_0^2 u_1}{\rho(1-\varsigma t)} - \frac{\mu}{\rho k_p}u_1, \tag{5.2.3}$$

$$\begin{aligned}\frac{\partial \bar{T}}{\partial t} + u_1\frac{\partial \bar{T}}{\partial x} + u_2\frac{\partial \bar{T}}{\partial y} = &\frac{k}{\rho c_p}\frac{\partial^2 \bar{T}}{\partial y^2} + \frac{\mu}{\rho c_p}\left(\frac{\partial u_1}{\partial y}\right)^2 - \frac{1}{\rho c_p}\frac{\partial q_r}{\partial y} + Q_g\frac{\bar{T}-\bar{T}_\infty}{\rho c_p}\\ &+ \tau_h\frac{\partial \bar{T}}{\partial y}\left(D_B\frac{\partial \bar{C}}{\partial y} + \frac{D_T}{T_\infty}\frac{\partial \bar{T}}{\partial y}\right),\end{aligned} \tag{5.2.4}$$

$$\frac{\partial \bar{C}}{\partial t} + u_1 \frac{\partial \bar{C}}{\partial x} + u_2 \frac{\partial \bar{C}}{\partial y} = D_B \frac{\partial^2 \bar{C}}{\partial y^2} + \frac{D_T}{T_\infty} \frac{\partial^2 \bar{T}}{\partial y^2}. \tag{5.2.5}$$

The associated boundary conditions become (Jamshed et al., 2021a; Aziz et al., 2021):

$$\text{For } t > 0 \begin{cases} y = 0; u_1 = U_w + S_l \frac{\partial u_1}{\partial y}, u_2 = V_w, -k\frac{\partial \bar{T}}{\partial y} = H_f(\bar{T}_w - \bar{T}), \bar{C} = \bar{C}_w \\ \text{and} \quad y \to \infty; u_1 \to 0, \bar{T} \to \bar{T}_\infty, \bar{C} \to \bar{C}_\infty \end{cases} \tag{5.2.6}$$

Within an optically thick medium containing small temperature gradients, there is nearly isotropic intensity which is important for diffusion approximation (Howell et al., 2020). Hence, similar to equation (4.2.9), the radiative term in equation (5.2.4) becomes:

$$q_r = -\frac{4\sigma^*}{k^*} \frac{\partial (\bar{T}^4)}{\partial y} \approx -\frac{16\bar{T}_\infty^3 \sigma^*}{3k^*} \frac{\partial \bar{T}}{\partial y}. \tag{5.2.7}$$

Thus, equation (5.2.4) can be rearranged in the following manner.

$$\begin{aligned} \frac{\partial \bar{T}}{\partial t} + u_1 \frac{\partial \bar{T}}{\partial x} + u_2 \frac{\partial \bar{T}}{\partial y} =& \frac{k}{\rho c_p}\left(1 + \frac{16\bar{T}_\infty^3 \sigma^*}{3k^* k}\right)\frac{\partial^2 \bar{T}}{\partial y^2} + \frac{\mu}{\rho c_p}(\frac{\partial u_1}{\partial y})^2 + Q_g \frac{\bar{T} - \bar{T}_\infty}{\rho c_p} \\ &+ \tau_h \left(D_B \frac{\partial \bar{C}}{\partial y}\frac{\partial \bar{T}}{\partial y} + \frac{D_T}{T_\infty}(\frac{\partial \bar{T}}{\partial y})^2\right). \end{aligned} \tag{5.2.8}$$

For computational purpose, the PDEs, in equations (5.2.2), (5.2.3), (5.2.5) and (5.2.8) have been converted into ODEs by means of similarity transformation variables with stream function ψ and dimensionless independent variable ϵ are defined as

$$\epsilon = y\sqrt{\frac{\hat{b}}{\nu(1-\varsigma t)}}, \ \psi(x,y,t) = \sqrt{\frac{\hat{b}\nu}{1-\varsigma t}} xV(\epsilon), u_1(\epsilon) = \frac{\partial \psi}{\partial y}, -u_2(\epsilon) = \frac{\partial \psi}{\partial x}. \tag{5.2.9}$$

Upon equation (5.2.9), the velocity components u_1 and u_2, temperature $\bar{T}$ and concentration $\bar{C}$ have been articulated in non-dimensional form as follows:

$$u_1 = \frac{\hat{b}x}{1-\varsigma t}\frac{\partial V}{\partial \epsilon}, \ u_2 = -\sqrt{\frac{\hat{b}\nu}{1-\varsigma t}} V(\epsilon), \ H(\epsilon) = \frac{\bar{T} - \bar{T}_\infty}{\bar{T}_w - \bar{T}_\infty}, \ L(\epsilon) = \frac{\bar{C} - \bar{C}_\infty}{\bar{C}_w - \bar{C}_\infty}. \tag{5.2.10}$$

Considering the procedural work in equations (4.2.13-4.2.18), the following simplified coupled non linear ODEs are developed for PDEs in equations (5.2.3, 5.2.5 and 5.2.8).

$$V''' + VV'' - A\left(V' + \frac{\epsilon}{2}V''\right) - (V' + Ma + ka)V' = 0 \tag{5.2.11}$$

$$\frac{(1+Rn)}{Pr}H'' - A\left(H + \frac{\epsilon}{2}H'\right) + Ec(V'')^2 + H'\left(NbL' + NtH' + V\right) - H\left(V' - q\right) = 0 \tag{5.2.12}$$

$$L'' - Sc\left[A\left(L + \frac{\epsilon}{2}L'\right) - VL' + LV'\right] + \frac{Nt}{Nb}H'' = 0 \tag{5.2.13}$$

Likewise, the boundary conditions in equation (5.2.6) are reformed as follows:

$$\begin{cases} V(0) = S, V'(0) = 1 + \varpi V''(0), L(0) = 1, H'(0) = -\Upsilon(1 - H(0)), \\ V'(\epsilon \to \infty) = H(\epsilon \to \infty) = L(\epsilon \to \infty) = 0. \end{cases} \tag{5.2.14}$$

The obtained dimensionless constants are registered underneath in Table 5.2.1.

Table 5.2.1: Non-dimensional symbols with their names

Constants	**Representation**	**Constants**	**Representation**
$A = \frac{\varsigma}{\hat{b}}$	Unsteadiness	$Ma = \frac{\sigma_e B_0^2}{\hat{b}\rho}$	Magnetic field
$P_r = \frac{\nu}{\alpha} = \frac{\nu \rho c_p}{k}$	Prandtl number	$\alpha = \frac{k}{\rho c_p}$	Thermal diffusivity
$N_b = \frac{D_B \tau_h (\bar{C}_w - \bar{C}_\infty)}{\nu}$	Brownian motion	$N_t = \frac{D_T \tau_h (\bar{T}_w - \bar{T}_\infty)}{\bar{T}_\infty \nu}$	Thermophoresis
$Sc = \frac{\nu}{D_B}$	Schmidt number	$E_c = \frac{(U_w)^2}{(T_w - T_\infty)c_p}$	Eckert number
$\Upsilon = \frac{H_f}{k}\sqrt{\frac{\nu(1-\varsigma t)}{\hat{b}}}$	Biot number	$S = -V_w \sqrt{\frac{1-\varsigma t}{\hat{b}\nu}}$	Mass suction
$ka = \frac{\nu(1-\varsigma t)}{\hat{b} k_p}$	Porosity constant	$q = \frac{Q_g(1-\varsigma t)}{\hat{b}\rho c_p}$	Heat generation
$\varpi = \sqrt{\frac{\hat{b}}{\nu(1-\varsigma t)}} S_l$	The velocity slip	$Rn = \frac{16\sigma^* \bar{T}_\infty^3}{3\alpha \rho c_p k^*}$	Thermal radiation

The prime $'$ in (5.2.11-5.2.14), pointed out the differentiation with respect to ϵ.

5.2.2 Physical Quantities

In this part, the three important physical quantities have been summarized from an engineering viewpoint, subject to the assumed nanofluids' properties. The detailed simplifications of the quantities are presented in the equations (4.2.23-4.2.25).

1. Coefficient of local skin friction or the rate of momentum transfer (Cf_x) is the resistance between stirring fluid and solid surface, and is defined as Rafique et al. (2019)

$$Cf_x = \frac{\tau_w}{\rho U_w^2} = \frac{\mu\left(\dfrac{\partial u_1}{\partial y}\right)_{y=0}}{\rho U_w^2} = \frac{\mu\left(\dfrac{\partial^2 \psi}{\partial y^2}\right)_{y=0}}{\rho U_w^2}, \quad \text{where } \tau_w = \mu\left(\frac{\partial u_1}{\partial y}\right)_{y=0}. \tag{5.2.15}$$

Using the dimensionless variable in (5.2.9), equation (5.2.15) becomes

$$Cf_x = \frac{\tau_w}{\rho U_w^2} = Re_x^{-0.5} V''(0) \implies V''(0) = Cf_x Re_x^{0.5}. \tag{5.2.16}$$

2. Local Nusselt number or heat transfer rate (Nu_x) is the ratio of convective heat transfer to conductive heat transfer across a boundary (Jamshed et al., 2021a).

$$Nu_x = -\frac{xk\left(\dfrac{\partial \bar{T}}{\partial y}\right)_{y=0}}{k(\bar{T}-\bar{T}_\infty)} + \frac{q_r x}{k(\bar{T}-\bar{T}_\infty)} = \left[\frac{-3k^*k - 16\bar{T}_\infty^4\sigma^*}{3k^*k(\bar{T}-\bar{T}_\infty)}\right] x \frac{\partial \bar{T}}{\partial y}_{y=0} \tag{5.2.17}$$

Since $\bar{T}-\bar{T}_\infty = \bar{T}_w - \bar{T}_\infty$ at the surface ($y=0$), then equation (5.2.17) becomes:

$$Nu_x = -Re_x^{0.5}(1+Rn)H'(0) \implies H'(0) = -\frac{Re_x^{-0.5} Nu_x}{(1+Rn)}. \tag{5.2.18}$$

3. Sherwood number or the rate of mass transfer (Sh_x) is the ratio of convective mass transfer to diffusion mass transfer. Its equation becomes Rafique et al. (2019):

$$Sh_x = \frac{xJ_m}{D_B(\bar{C}_w - \bar{C}_\infty)} = -Re_x^{0.5} L'(0) \implies L'(0) = -Sh_x Re_x^{-0.5}, \tag{5.2.19}$$

where $Re_x = \dfrac{U_w x}{\nu}$ represents the local Reynolds number, and $J_m = -D_B\left(\dfrac{\partial \bar{C}}{\partial y}\right)_{y=0}$

assign for mass flux at $y=0$ of the plane.

5.2.3 Entropy Generation

In order to put more energy into action properly, the first and second laws of thermodynamics are essential. Entropy is the disturbance of a regular system and measures the irreversible process as stated by Loganathan et al. (2020). In this study, the researchers realized entropy generation by thermal, nanofluid friction, magnetic field, porosity and mass transmission (Loganathan et al., 2020; Hussain, 2022). It is formulated as follows:

$$\begin{aligned} E_{pr} =&\frac{k}{\bar{T}_\infty^2}\left(1+\frac{16\sigma^*\bar{T}_\infty^3}{3kk^*}\right)\left(\frac{\partial \bar{T}}{\partial y}\right)^2+\frac{\mu}{\bar{T}_\infty}\left(\frac{\partial u_1}{\partial y}\right)^2+\frac{RD}{\bar{C}_\infty}\left(\frac{\partial \bar{C}}{\partial y}\right)^2 \\ &+\frac{RD}{\bar{T}_\infty}\left(\frac{\partial \bar{C}}{\partial y}\right)\left(\frac{\partial \bar{T}}{\partial y}\right)+\frac{\sigma_e B_0^2 u_1^2}{\bar{T}_\infty(1-\varsigma t)}+\frac{\mu}{k_p\bar{T}_\infty}u_1^2. \end{aligned} \tag{5.2.20}$$

The non-dimensional form of local entropy (NG) in equation (5.2.20) is acquired by multiplying the expression, $E_0=\dfrac{\bar{T}_\infty^2\mathbb{L}^2}{k(\bar{T}_w-\bar{T}_\infty)^2}$. According to equation (4.2.27), the following reduced form of dimensionless entropy $(NG=E_0E_{pr})$ is developed.

$$\begin{aligned} NG(\epsilon) =&Re\left[(1+Rn)(H')^2+\frac{Br(V'')^2+BrMa(V')^2}{\Delta_1}\right] \\ &+\frac{Re}{\Delta_1}\left[Brka(V')^2+\Delta_3\Delta_2\left(\frac{\Delta_2}{\Delta_1}(L')^2+L'H'\right)\right], \end{aligned} \tag{5.2.21}$$

where the symbols, $Re, Br, \Delta_1, \Delta_2$ and Δ_3 have similar meaning with the notations in (4.2.27). The Bejan number (Be) stands for the ratio of entropy acquired through heat and mass transfer to the total entropy (Loganathan et al., 2020). Mathematically, it can be expressed in a similar manner with equation (4.2.28). Thus, it becomes

$$Be(\epsilon)=\frac{Re\left[\Delta_1(1+Rn)(H')^2+\lambda_1\Delta_2L'\left(\Delta_2L'+H'\right)\right]}{\Delta_1 NG}. \tag{5.2.22}$$

5.3 Homotopy Analysis Method (HAM)

At the moment, HAM is used to work out the boundary value problems of non linear higher-order systems of ODEs. Similar to section 4.3, the linear operators $(\mathcal{L}_V, \mathcal{L}_H, \mathcal{L}_L)$, initial guesses $(V_0(\epsilon), H_0(\epsilon), L_0(\epsilon))$, auxiliary functions $(\mathcal{H}_V(\epsilon), \mathcal{H}_H(\epsilon), \mathcal{H}_L(\epsilon))$ and convergence control parameters $(\hbar_V, \hbar_H, \hbar_L)$ are selected based on the freedom that HAM have for obtaining an acceptable convergent solutions.

5.3.1 Choosing $\mathcal{L}_V, \mathcal{L}_H, \mathcal{L}_L, V_0(\epsilon), H_0(\epsilon), L_0(\epsilon), \mathcal{H}_V(\epsilon), \mathcal{H}_H(\epsilon), \mathcal{H}_L(\epsilon)$

HAM is applied to solve the higher order non-linear coupled ODEs (5.2.11-5.2.14). For this purpose, the following conditions are selecting according to the principles of HAM.

- The appropriate auxiliary linear operators have been taken similar to (4.3.1)

$$\mathcal{L}_V = V''' - V', \quad \mathcal{L}_H = H'' - H, \quad \text{and} \quad \mathcal{L}_L = L'' - L. \tag{5.3.1}$$

- The initial guesses are approximated as follows (Loganathan et al., 2021)

$$V_0(\epsilon) = \frac{1 - e^{-\epsilon}}{1 + \varpi} + S, \quad H_0(\epsilon) = \frac{\Upsilon e^{-\epsilon}}{1 + \Upsilon}, \quad \text{and} \quad L_0(\epsilon) = e^{-\epsilon}. \tag{5.3.2}$$

- Constant auxiliary functions have been picked similar to equation (4.3.3):

$$\mathcal{H}_V(\epsilon) = \mathcal{H}_H(\epsilon) = \mathcal{H}_L(\epsilon) = 1. \tag{5.3.3}$$

5.3.2 Zero$^{\text{th}}$ and m$^{\text{th}}$ order Deformation Equations

For the non zero auxiliary parameters, $\hbar_V, \hbar_H$ and $\hbar_L$, the zeros order deformation equations are defined similar to equation (4.3.4) as follows (Kebede et al., 2020):

$$\begin{aligned}
&(1-p)\mathcal{L}_V[V(\epsilon;p) - V_0(\epsilon)] = p\hbar_V \mathcal{H}_V(\epsilon)\mathcal{N}_V[V(\epsilon;p), H(\epsilon;p), L(\epsilon;p)],\\
&(1-p)\mathcal{L}_H[H(\epsilon;p) - H_0(\epsilon)] = p\hbar_H \mathcal{H}_H(\epsilon)\mathcal{N}_H[V(\epsilon;p), H(\epsilon;p), L(\epsilon;p)],\\
&(1-p)\mathcal{L}_L[L(\epsilon;p) - L_0(\epsilon)] = p\hbar_L \mathcal{H}_L(\epsilon)\mathcal{N}_L[V(\epsilon;p), H(\epsilon;p), L(\epsilon;p)],
\end{aligned} \tag{5.3.4}$$

where $p \in [0,1]$, and the nonlinear operators $\mathcal{N}_V, \mathcal{N}_H$ and $\mathcal{N}_L$ are defined in a similar way with equations (4.3.5, 4.3.6 and 4.3.7). Next, the boundary conditions in equation (5.2.14) have been adjusted to:

$$\begin{cases}
\left[\dfrac{\partial V(\epsilon;p)}{\partial \epsilon} - \varpi \dfrac{\partial^2 V(\epsilon;p)}{\partial \epsilon^2}\right]|_{\epsilon=0} = 1, \left[\dfrac{\partial H(\epsilon;p)}{\partial \epsilon}\right]_{\epsilon=0} = \Upsilon(H(0;p) - 1),\\
V(0;p) = S, \; L(0;p) = 1, \; \dfrac{\partial V(\epsilon;p)}{\partial \epsilon}|_{\epsilon\to\infty} = H(\epsilon;p)|_{\epsilon\to\infty} = L(\epsilon;p)|_{\epsilon\to\infty} = 0
\end{cases} \tag{5.3.5}$$

It is clear that when $p=0$, $V(\epsilon,0)=V_0(\epsilon), H(\epsilon,0)=H_0(\epsilon)$ and $L(\epsilon,0)=L_0(\epsilon)$ and at $p=1$, $V(\epsilon,1)=V(\epsilon), H(\epsilon,1)=H(\epsilon)$ and $L(\epsilon,1)=L(\epsilon)$ are solutions for the equations (5.2.11-5.2.14). Thus, when the value of p changes continuously from 0 to 1, the homotopy solutions also run from the initial guesses to the accurate solutions, $V(\epsilon), H(\epsilon)$, and $L(\epsilon)$ (Van Gorder, 2014). Similar to equation (4.3.9), there is:

$$\begin{aligned}
&V(\epsilon;p)=V_0(\epsilon)+\sum_{m=1}^{\infty}V_m(\epsilon)p^m,\ H(\epsilon;p)=H_0(\epsilon)+\sum_{m=1}^{\infty}H_m(\epsilon)p^m\\
&Ł(\epsilon;p)=L_0(\epsilon)+\sum_{m=1}^{\infty}L_m(\epsilon)p^m.
\end{aligned} \tag{5.3.6}$$

In equation (5.3.6), $V_m(\epsilon), H_m(\epsilon)$ and $L_m(\epsilon)$ have similar definitions with equation (4.3.10) which are known as m^{th} order homotopy derivatives. The m^{th} order deformation can be obtained by differentiating (5.3.4) m-times with respect to p and putting $p=0$, then dividing by $m!$. Like (4.3.11), the m^{th} order deformation equations become:

$$\begin{aligned}
&\mathcal{L}_V[V_m(\epsilon)-\chi_m V_{m-1}(\epsilon)]=\hbar_V\mathcal{H}_V(\epsilon)\mathcal{R}^V_{m-1},\\
&\mathcal{L}_H[H_m(\epsilon)-\chi_m H_{m-1}(\epsilon)]=\hbar_H\mathcal{H}_H(\epsilon)\mathcal{R}^H_{m-1},\quad \text{and}\\
&\mathcal{L}_L[L_m(\epsilon)-\chi_m L_{m-1}(\epsilon)]=\hbar_L\mathcal{H}_L(\epsilon)\mathcal{R}^L_{m-1}.
\end{aligned} \tag{5.3.7}$$

Subject to the boundary conditions

$$\begin{cases}
V_m(0)=V'_m(0)=[H'_m(0)+\Upsilon(1-H_m(0))]=L_m(0)=0\\
V'_m(\epsilon\to\infty)=H_m(\epsilon\to\infty)=L_m(\epsilon\to\infty)=0
\end{cases} \tag{5.3.8}$$

From equation (5.3.7), χ_m denotes a step function and is defined based on equation (4.3.13). In this problem, $\mathcal{R}^V_{m-1}, \mathcal{R}^H_{m-1}$ and $\mathcal{R}^L_{m-1}$ are defined in a similar way with equation (4.3.14). Then, applying the inverse of linear operators on both sides of equation (5.3.7), the following expressions are developed, which have repeating processes.

$$\begin{aligned}
V_m(\epsilon)&=\chi_m V_{m-1}(\epsilon)+\hbar_V\mathcal{L}_V^{-1}\left[\mathcal{H}_V(\epsilon)\mathcal{R}^V_{m-1}\right]\\
H_m(\epsilon)&=\chi_m H_{m-1}(\epsilon)+\hbar_H\mathcal{L}_H^{-1}\left[\mathcal{H}_H(\epsilon)\mathcal{R}^H_{m-1}\right]\\
L_m(\epsilon)&=\chi_m L_{m-1}(\epsilon)+\hbar_L\mathcal{L}_L^{-1}\left[\mathcal{H}_L(\epsilon)\mathcal{R}^L_{m-1}\right]
\end{aligned} \tag{5.3.9}$$

In equation (5.3.9), for distinct individual values of $m=1,2,3,...$, the recurrence solution is derived. Now, the auxiliary linear operators (5.3.1), initial approximation (5.3.2) and auxiliary functions (5.3.3) are selected. Still the convergence control parameters ($\hbar_V, \hbar_H$ and $\hbar_L$) are not specified. So, $\hbar_V, \hbar_H$ and $\hbar_L$ are selected appropriately from the $\hbar$-curves. They aid to achieve convergent solutions when $p=1$. Hence, the resulting solutions can be expressed in the following manner.

$$\begin{aligned} V(\epsilon;p) &= V_0(\epsilon)+\sum_{m=1}^{\infty} p^m V_m(\epsilon) \implies V(\epsilon;1)=V_0(\epsilon)+\sum_{m=1}^{\infty} V_m(\epsilon)=V(\epsilon) \\ H(\epsilon;p) &= H_0(\epsilon)+\sum_{m=1}^{\infty} p^m H_m(\epsilon) \implies H(\epsilon;1)=H_0(\epsilon)+\sum_{m=1}^{\infty} H_m(\epsilon)=H(\epsilon) \\ L(\epsilon;p) &= L_0(\epsilon)+\sum_{m=1}^{\infty} p^m L_m(\epsilon) \implies L(\epsilon;1)=L_0(\epsilon)+\sum_{m=1}^{\infty} L_m(\epsilon)=L(\epsilon). \end{aligned} \tag{5.3.10}$$

The equations in (5.3.10) represent the exact solution of these problems. However, the truncated order of approximation provides a semi-analytic solution whose limit close to the exact one. For this, selecting the best values of $\hbar_V, \hbar_H$ and $\hbar_L$ are essential. Except the convergence control parameters, the other three points have been already chosen. Now, let us select the convergence control parameters for which the error is reduced for the convergent solutions.

5.3.3 Analyzing the Convergence of Solutions

In HAM, the convergent control parameters play a key role in the convergence of solutions. Henceforth, by considering $\hbar_V=\hbar_H=\hbar_L=\hbar$, Figure 5.3.1a has been drawn which is called $\hbar$-curves. The interval where the $\hbar$-curves become horizontal indicate the range of the possible values for the convergent control parameters. Accordingly, $\hbar_V=-0.7120631, \hbar_H=-1.0616537$ and $\hbar_L=-1.13731361$ are chosen by implementing the code from BVPh2.0 package on Mathematica 12.1. Furthermore, from Figure 5.3.1b, the error is reduced (vertical axis) as the order of approximation increased horizontally. Beside, Table 5.3.1 is a testimony on successful accomplishment of convergence for the values of $Ma=0.5, Sc=0.7, Nt=Nb=1, S=ka=Rn=A=0.3, Pr=1.2, q=\varpi=Ec=\Upsilon=0.1$ with residual error on respective order of approximation (m). In addition, Figure 5.3.2a also indicates the difference between consecutive values of local skin friction coefficient, Nusselt and Sherwood numbers are close to zero in magnitude. Pictorial representation of Table 5.3.1 has been brought by using Figures 4.3.2b, 5.3.3a and 5.3.3b for the value of $-V''(0), -H'(0)$ and $-L'(0)$ in that order against the values of n which attest getting the convergent values. Therefore, for this issue, HAM is a guaranteed method to get convergent solution with acceptable error.

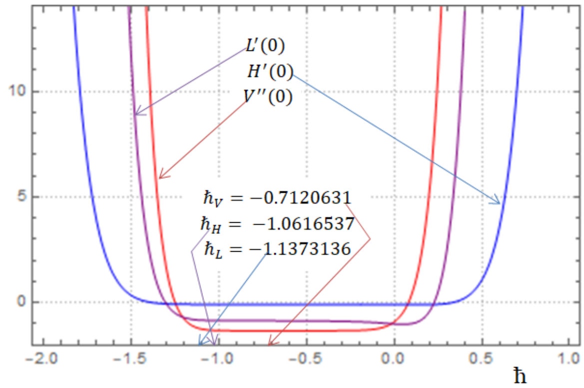

(a) $\hbar$-curves for $\hbar_V, \hbar_H$ and $\hbar_L$

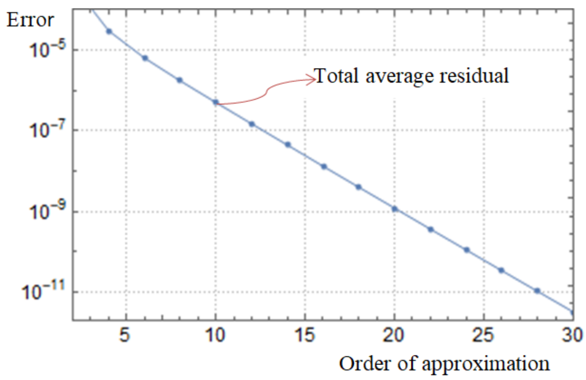

(b) Order of approximation

Figure 5.3.1: $\hbar$-curves for convergence control parameters and order of approximation

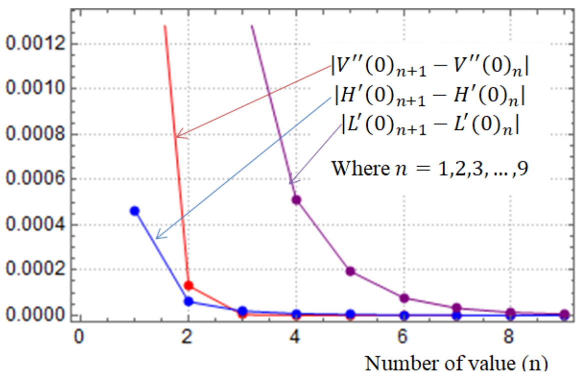

(a) Magnitude difference

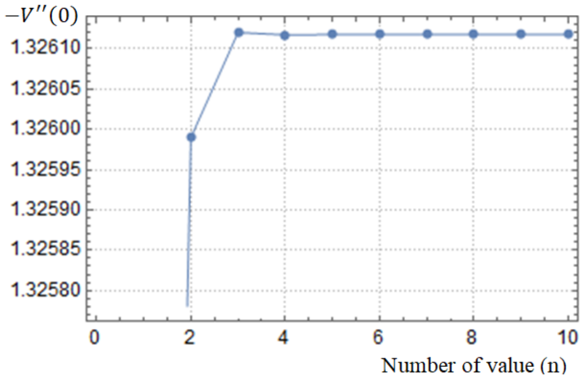

(b) Convergence of the values of $-V''(0)$

Figure 5.3.2: Differences in absolute value and convergence of the values of $-V''(0)$

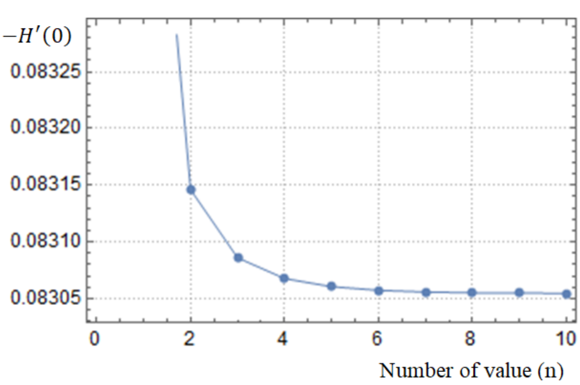

(a) Convergence of the values of $-H'(0)$

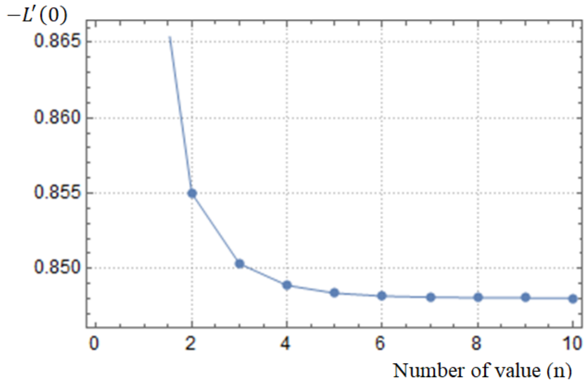

(b) Convergence of the values of $-L'(0)$

Figure 5.3.3: Convergence of the values of $-H'(0)$ and $-L'(0)$

Table 5.3.1: Order of approximation of HAM with residual error

n	m^{th} Order	$-V''(0)$	$-H'(0)$	$-L'(0)$	Residual Error $-V''(0)$	Residual Error $-H'(0)$	Residual Error $-L'(0)$
1	3	1.32326	0.083609	0.877443			
2	6	1.32599	0.083146	0.854996	2.98×10^{-8}	4.52×10^{-7}	5.98×10^{-6}
3	9	1.32612	0.083086	0.850333			
4	12	1.32612	0.083068	0.848890	1.50×10^{-12}	1.55×10^{-8}	1.34×10^{-7}
5	15	1.32612	0.083061	0.848378			
6	18	1.32612	0.083057	0.848182	1.66×10^{-16}	6.57×10^{-10}	3.31×10^{-9}
7	21	1.32612	0.083056	0.848105			
8	24	1.32612	0.083055	0.848074	2.06×10^{-20}	2.65×10^{-11}	8.35×10^{-11}
9	27	1.32612	0.083055	0.848061			
10	30	1.32612	0.083055	0.848056	2.76×10^{-24}	1.07×10^{-12}	2.07×10^{-12}

5.4 Computed Results and Explanation

This semi-analytic computation has provided for velocity, temperature, concentration, entropy generation, Benjan number, local skin friction coefficient, local rate of heat and mass transfer by applying HAM, on Mathematica 12.1 software with BVPh2.0 package (Zhao and Liao, 2014). Graphical explanations are displayed for emerging physical parameters from the ODEs given in (5.2.11 -5.2.14). The validity of this computation is assured by contrasting the values of $-V''(0)$ and $-H'(0)$ taking particular values of ka, A, Ma and Pr with various published articles (see Tables 5.4.1, 5.4.2 and 5.4.3).

Table 5.4.1: Comparing $-V''(0)$ with $Ma = S = \varpi = 0, Pr = 10$ and $\Upsilon \to \infty$

ka	A	Verma et al. (2022)	**Present result**
0.1	0.8	1.30034571	1.3003400
0.3	0.8	1.37549882	1.3755000
0.5	0.8	1.44667143	1.4466707
0.7	0.8	1.51447680	1.5144500
1.0	0.8	1.61070519	1.6107000
1.5	0.8	-	1.7593260
2.0	0.8	-	1.8962000
0.1	0.3	-	1.1466800
0.1	0.4	1.17847442	1.1784800
0.1	0.5	-	1.2097744
0.1	0.6	1.24052331	1.2405200
0.1	0.7	-	1.2707100
0.1	0.8	1.30034571	1.3003400
0.1	1.0	1.35790000	1.3579770
0.1	1.2	1.41356556	1.4135580
0.1	1.4	-	1.4672400

Table 5.4.2: Comparing the values of $-V''(0)$ with $S = \varpi = 0$ and $\Upsilon \to \infty$

Ma	Hayat et al. (2017b)	Ali et al. (2022)	**Present result**
0.00	1.000000	1.000000	1.0000000
0.25	1.118030	1.118034	1.1180340
0.50	-	-	1.2297449
0.75	-	-	1.3228756
1.00	1.414214	1.414214	1.4142127

Table 5.4.3: Values of $-H'(0)$ at $Ma = ka = A = Nt = Ec = Sc = S = \varpi = 0, \Upsilon \to \infty$

Pr	Ullah et al. (2017)	Aziz et al. (2021)	Verma et al. (2022)	**Present result**
0.72	0.8088	0.80876180	0.80883421	0.80872200
1.00	1.0000	1.00000000	1.00000000	1.00000000
3.00	1.9237	1.92357400	1.92367864	1.92377556
7.00	-	3.07314651	-	3.07222000
10.0	3.7207	3.72055429	3.72067117	3.72068000
20.0	-	-	-	5.36392000
30.0	-	-	-	6.62419270
50.0	-	-	-	8.62224320
100	-	-	12.29408513	12.2943660

5.4.1 Velocity Profile

The parameters such as porosity (ka), mass suction (S), velocity slip (ϖ) and magnetic field interaction (Ma) on the flow of nanofluids have been exposed on Figures 5.4.1a and 5.4.2b. The resistance influence of the porous materials on the flow field lingers the nanofluids mobility as they transit over it. Thus, the porosity parameter, ka lagging the velocity of nanofluids as directed in Figure 5.4.1a. The heated nanofluid is drawn toward the wall by the greater mass suction, which makes them more viscous and retards the flow of nanofluid. Thus, Figure 5.4.1b approved that the motion of nanofluids hinder by going up the value of S. Increasing the velocity slip parameters generate results in abating the flow of nanofluid as marked in Figure 5.4.2a. Physically, when the ϖ is increased, the velocity of nanofluid decreases and become zero at distant. As Figure 5.4.2b illustrates, increasing the values of Ma, retards the flow of nanofluid. Thus, the formation of more drag force by magnetic field interaction causes to slow the motion of nanofluid. This phenomena occurred due to Lorentz drag forces generated by the magnetic field interaction that delay the mobility of nanofluids. Hence, the additional values of Ma increases Lorentz forces opposes the motion of nanofluids which disappear at remote as we perceived from figure 5.4.2b.

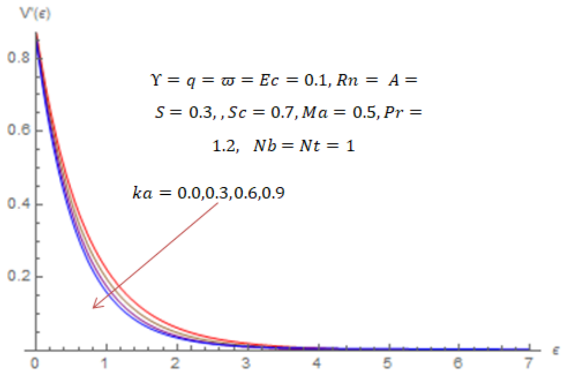

(a) The consequence of ka on $V'(\epsilon)$

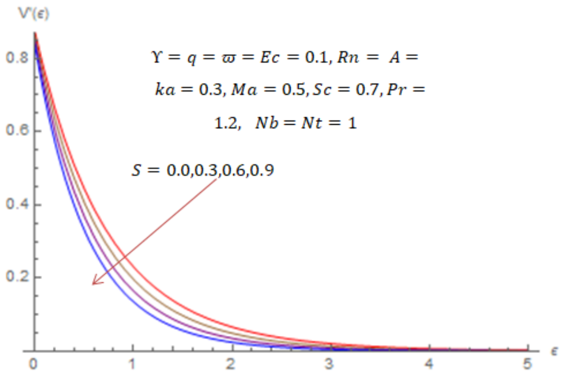

(b) The consequence of S on $V'(\epsilon)$

Figure 5.4.1: Impact of porosity and mass suction parameters on velocity field

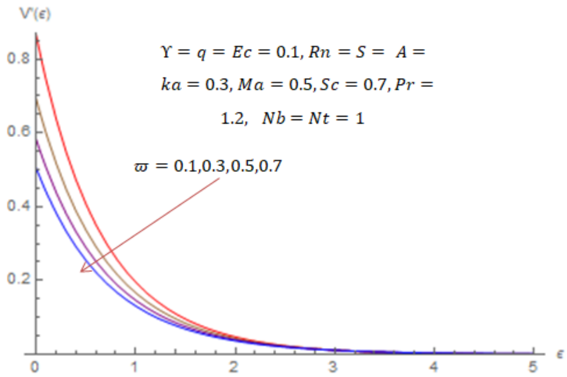

(a) The consequence of ϖ on $V'(\epsilon)$

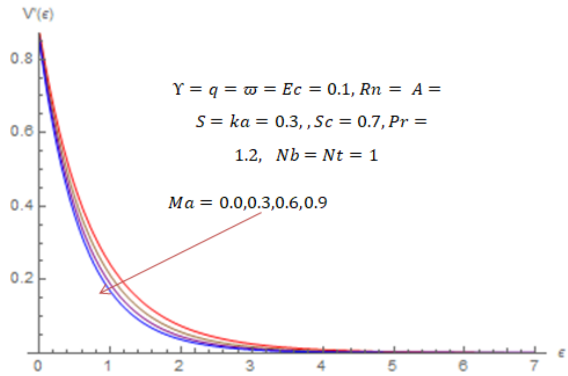

(b) The consequence of Ma on $V'(\epsilon)$

Figure 5.4.2: Impact of slip and magnetic field interaction parameters on velocity field

5.4.2 Temperature Profile

The outcomes on energy equation depicts in Figures 5.4.3a to 5.4.7b by executing HAM with a short briefing on the emerging parameters related to heat. Generally, the markdown velocity will be associated with the bearing of temperature. Figures 5.4.3a and 5.4.3b are epitomize the implication of ka and Ma on the temperature field respectively. These parameters are supersized the distribution of temperature in the unsteady flow of nanofluid. This is because of viscous formation by high resistance to the flow of nanofluid on a porous medium and Lorentz force which yield more heat. As a result of this viscous features, there is a creation of high heat which upswing the temperature distribution. Based on Figures 5.4.4a, 5.4.4b, 5.4.5a, 5.4.5b, 5.4.6a and 5.4.6b, the thermal radiation (Rn), heat source (q), Eckert number (Ec), Biot number (Υ), thermophoresis (Nt) and Brownian motion (Nb) increase the temperature profile as they grow up in that order. This is because of the greater heat transfer induced by the accessibility of solar thermal radiation, heat source, viscous heat dissipation, convective heat transfer, thermophoresis and Brownian motion of nanoparticles that elevate the dimensionless temperature of nanofluids. The sway of mass suction (S) and Prandtl number (Pr) on temperature field illuminated on Figures 5.4.7a and 5.4.7b respectively. Higher value of mass suction cooled the nanofluid's temperature as noted in Figure 5.4.7a. This happened due to the stretchable sheet nearby the atmospheric condition reduces the thermal boundary layer thickness. Similarly, heightening in Pr brings to drop down the temperature profile according to Figure 5.4.7b. Thermal diffusivity has reverse relation with Pr. As a consequence, enormous values of Pr is designated to slight the values of thermal diffusivity which leads to decrease the temperature distribution.

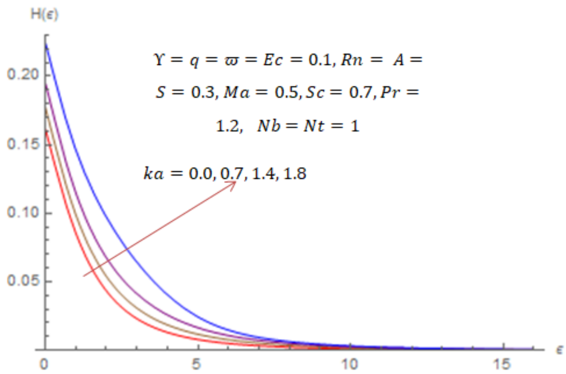

(a) The consequence of ka on $H(\epsilon)$

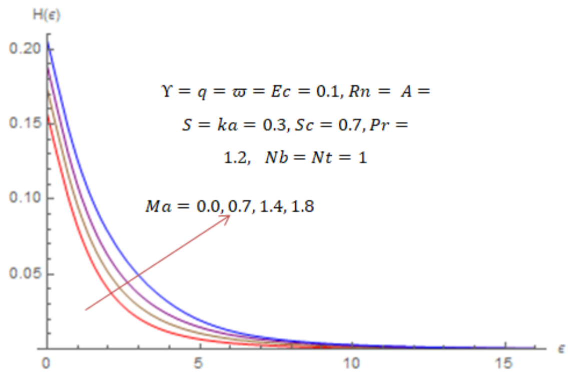

(b) The consequence of Ma on $H(\epsilon)$

Figure 5.4.3: Impact of porosity and magnetic field interaction on temperature field

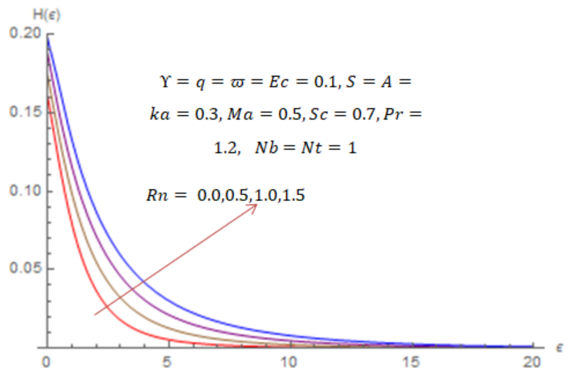

(a) The consequence of Rn on $H(\epsilon)$

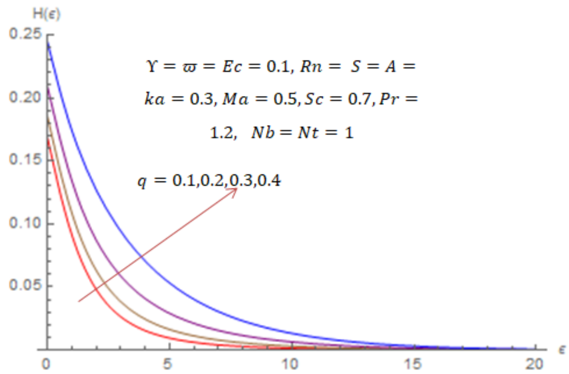

(b) The consequence of q on $H(\epsilon)$

Figure 5.4.4: The thermal radiation and heat generation impact on temperature field

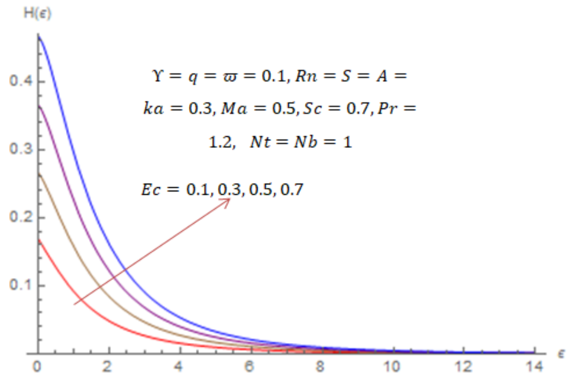

(a) The consequence of Ec on $H(\epsilon)$

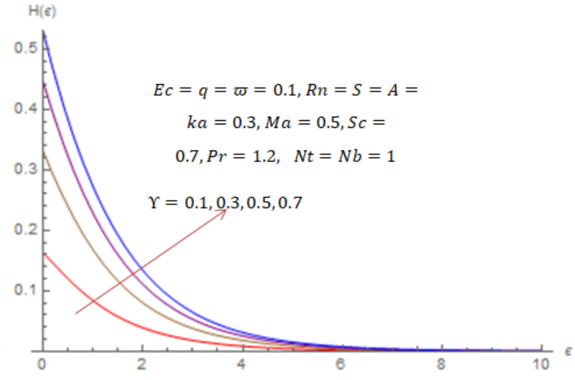

(b) The consequence of Υ on $H(\epsilon)$

Figure 5.4.5: The consequence of Eckert and Biot numbers on temperature field

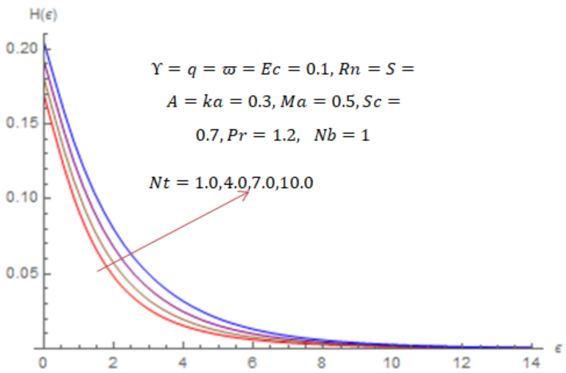

(a) The consequence of Nt on $H(\epsilon)$

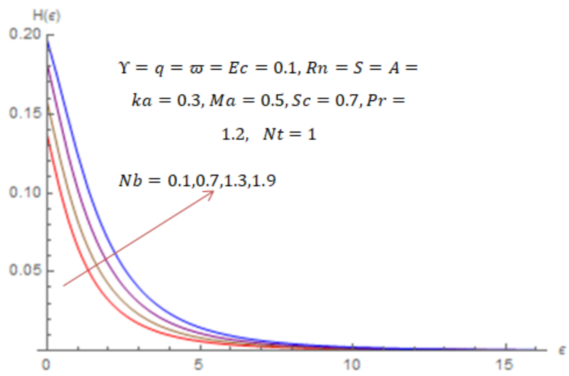

(b) The consequence of Nb on $V'(\epsilon)$

Figure 5.4.6: Thermophoresis and Brownian motion impact on temperature field

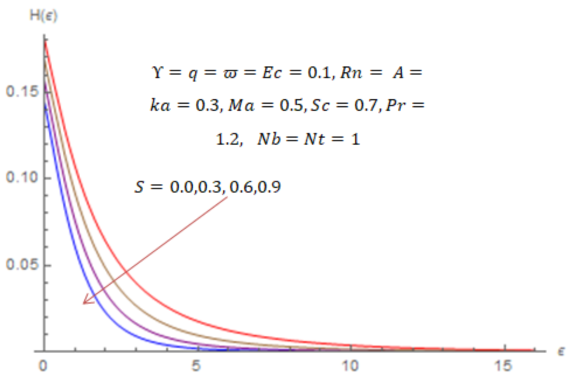

(a) The consequence of S on $H(\epsilon)$

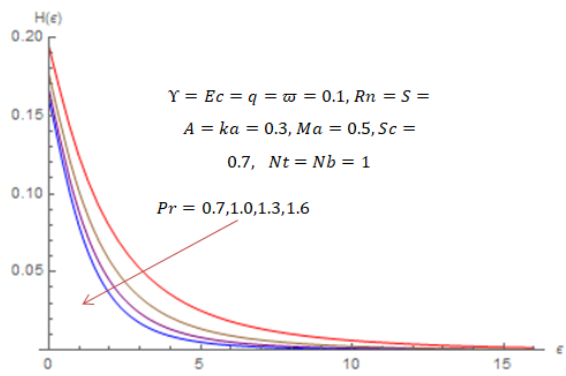

(b) The consequence of Pr on $H(\epsilon)$

Figure 5.4.7: The mass suction and Prantdl number impact on temperature field

5.4.3 Concentration Profile

The graphs from Figure 5.4.8a to 5.4.10b serve to highlight the relevance of prominent parameters, notably ka, Ma, Nt, Ec, S, and Sc on nanoparticles volume fraction. The porosity parameter,(ka) on the stretchable sheet and the interaction of magnetic field (Ma) have been illustrated on Figures 5.4.8a and 5.4.8b. These graphs show that the concentration of nanoparticles directly proportional to ka and Ma. That is the porous media and the magnetic field interaction have a tendency to accumulate more concentration. In addition, the maximum approximated nanoparticles volume fraction obtained for $ka = 2.3$ at $\epsilon = 2.117$ as $L(2.117) = 1.65409$ in Figure 5.4.8a, and for $Ma = 2.4$ at $\epsilon = 1.97392$ as $L(1.97392) = 1.2604$ in Figure 5.4.8b. As flaunted in Figure 5.4.9a, the concentration of nano-sized particles proliferates due to the more value of thermophoresis parameter (Nt). Similar results observed for Eckert number (Ec) on concentrations of nano-sized particles. There up on, Ec appendage the nanoparticles concentration as seen in Figure 5.4.9b. However, the mass suction (S) and Schmidt number (Sc) decline the concentration as we inspected from Figures 5.4.10a and 5.4.10b, respectively. The purpose of Sc in convective mass transfer resembles the role of Prandtl number in case of convective heat transfer. Hence, the existence of reverse relation between Schmidt number and mass diffusivity implies, a greater Sc invokes lower mass diffusivity which is the root for dropping nanoparticles concentration.

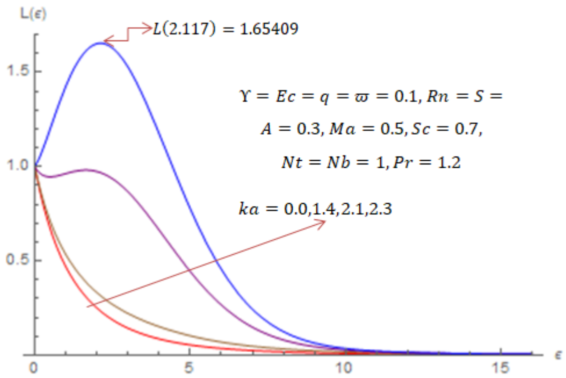

(a) The consequence of ka on $L(\epsilon)$

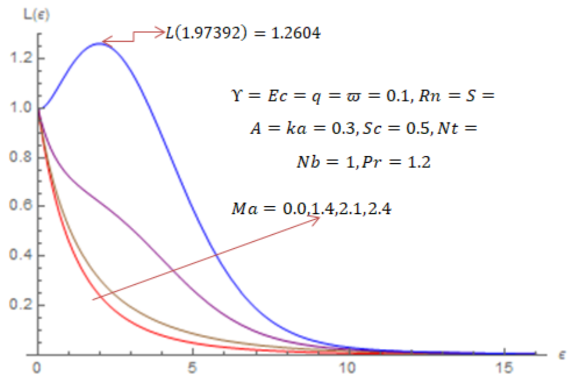

(b) The consequence of Ma on $L(\epsilon)$

Figure 5.4.8: Impact of porosity and magnetic field interaction on concentration

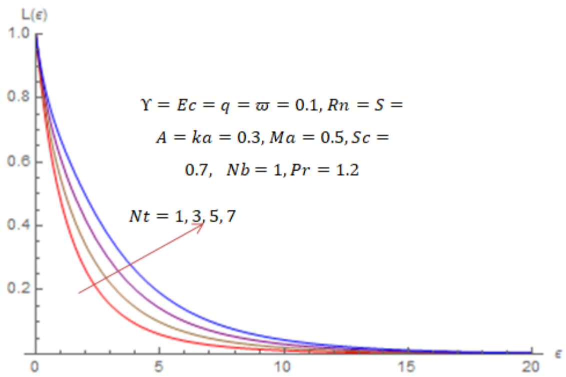

(a) The consequence of Nt on $L(\epsilon)$

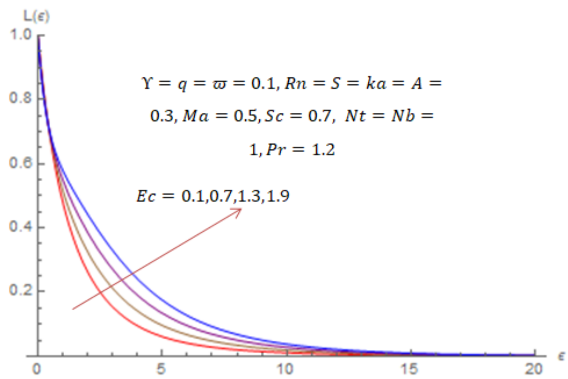

(b) The consequence of Ec on $L(\epsilon)$

Figure 5.4.9: The thermopheresis and Eckert number impact on concentration

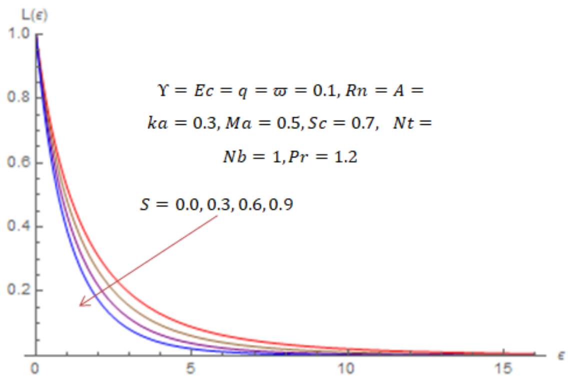

(a) The consequence of S on $L(\epsilon)$

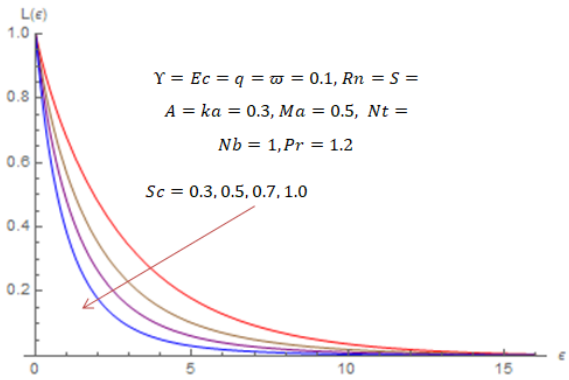

(b) The consequence of Sc on $L(\epsilon)$

Figure 5.4.10: Impact of mass suction and Schmidt number on concentration

5.4.4 Entropy and Bejan Number

Entropy is typically produced by the process of irreversible activities, and the second rule of thermodynamics for heat transport helps to illuminate it. In accordance with the issues under consideration, the parameters $A, \varpi, Ec, Re, Br, ka, Ma$ and S have a direct relation to the entropy generation and also on the Bejan number. Their spheres of influence are outlined graphically from Figure 5.4.11a to Figure 5.4.15b.

The rate of entropy formation per volume (NG) diminutions as a result of increasing the parameters A and ϖ as it is observed in the Figures 5.4.11a and 5.4.11b, respectively due to decreasing the temperature of nanofluid.

It is widely known that extra heat transfer is the primary root for the irreversible process that upsurges entropy generation. Thus, unusable energy is directly proportional to thermal transmission. In line with this, the strength of entropy enlarged with outstanding values of the parameters namely Ec, Re, and Br as Figures 5.4.12a, 5.4.12b and 5.4.13a pointed out, respectively.

Be decreases when Br increases as it is observed from Figure 5.4.13b. Besides, the Bejen number increases with the incremental values of ka, Ma, S and ϖ as it is perceived on Figures 5.4.14a, 5.4.14b,5.4.15a and 5.4.15b, respectively. Be and NG have similar properties on most parameters that exist in this study except for some like Br and ϖ.

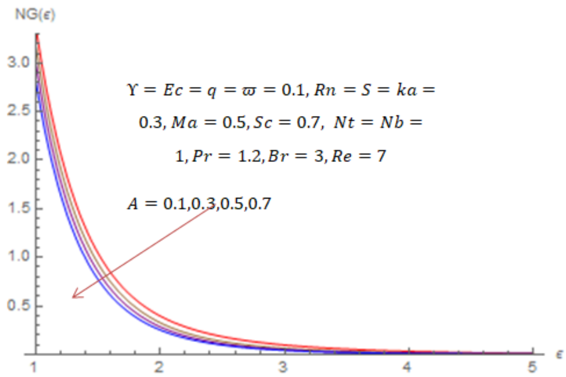

(a) The consequence of A on $NG(\epsilon)$

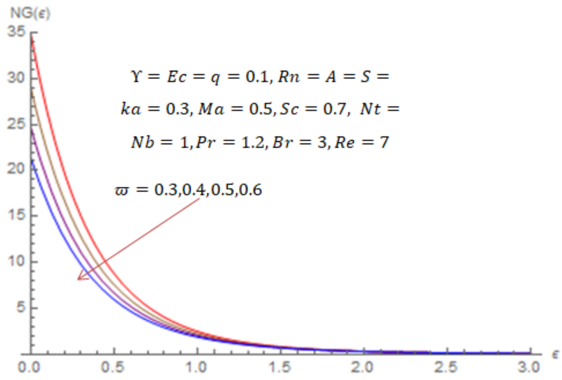

(b) The consequence of ϖ on $NG(\epsilon)$

Figure 5.4.11: Impact of unsteady and magnetic field interaction parameters on entropy

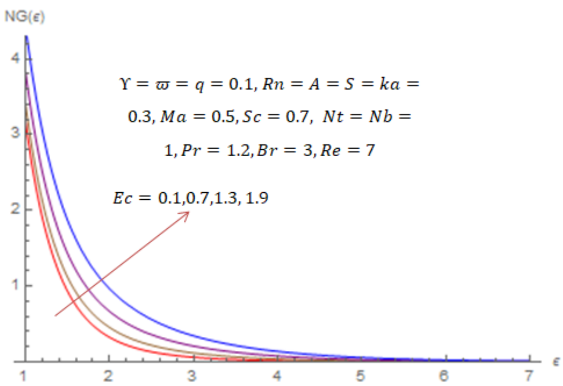

(a) The consequence of Ec on $NG(\epsilon)$

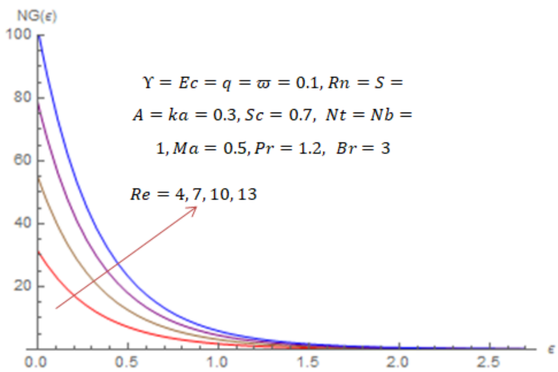

(b) The consequence of Re on $NG(\epsilon)$

Figure 5.4.12: The Eckert number and global Reynolds number impact on entropy

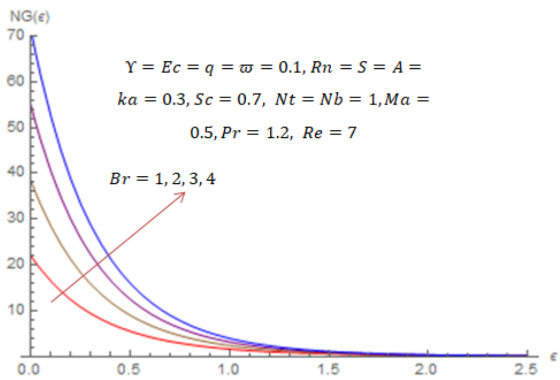

(a) The consequence of Br on $NG(\epsilon)$

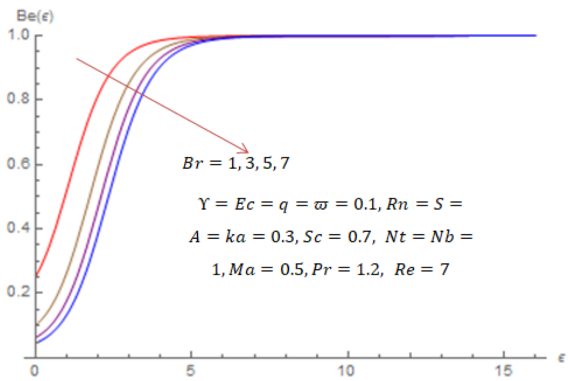

(b) The consequence of Br on $Be(\epsilon)$

Figure 5.4.13: The consequence of Brinkman number on entropy and Bejan number

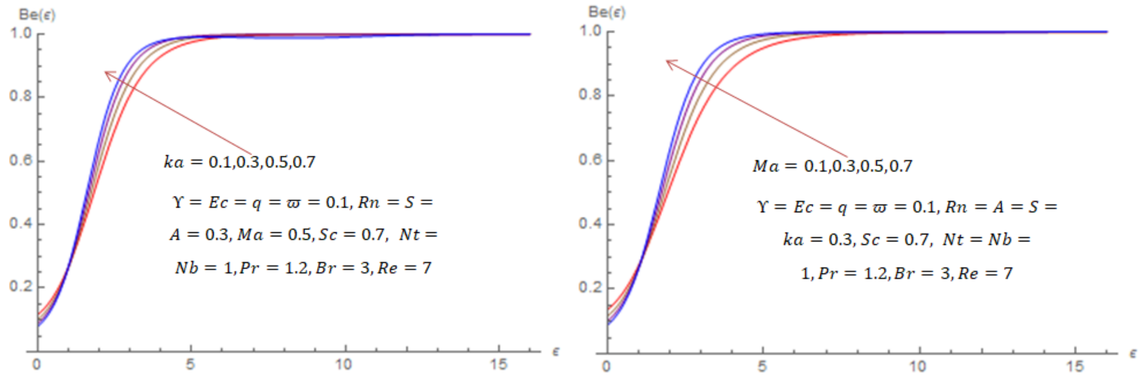

(a) The consequence of ka on $Be(\epsilon)$ (b) The consequence of Ma on $Be(\epsilon)$

Figure 5.4.14: The consequence of porosity and magnetic field on Bejan number

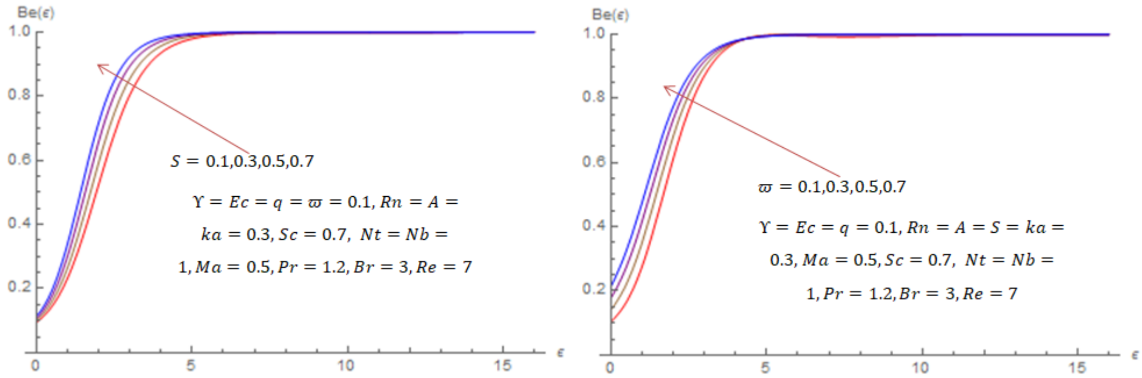

(a) The consequence of S on $Be(\epsilon)$ (b) The consequence of ϖ on $Be(\epsilon)$

Figure 5.4.15: Impact of mass suction and velocity slip on Bejan number

5.4.5 Impact of Parameters on Physical Quantities

This section assesses the outgrowth of possible factors on the local skin friction coefficient (Cf_x), Nusselt number (Nu_x), and Sherwood number (Sh_x) in terms of 3D surface plots in Figures 5.4.16a to 5.4.18b. They are based on equations (5.2.16, 5.2.18 and 5.2.19) with $Re_x = 1$. The 3D plot 5.4.16a and 5.4.16b pointed out, the absolute value of Cf_x ascends for higher values of A, ka and Ma. Since, as time goes the speed of flowing nanofluid is retarded due to the formation of more drag forces which are also supported by porous media and magnetic field interaction. According to the 3D plot 5.4.17a the parameters Sc have a role in resisting the heat transfer rate where as Pr supports the rate of heat transfer with decreasing the temperature of flowing nanofluid. Detracting ka and adding the values of S, intensify the Nusselt number (heat transfer rate) and Sherwood number (mass transfer rate), as it is looked on the surface plot 5.4.17b and 5.4.18a, respectively. The increments of q and the decreases of ka keep to increase the mass transfer rate (Sherwood number) as it is realized from 3D plot

5.4.18a. It follows that when the values of ka deescalate, the rate of convective mass transfer surpasses the rate of diffusive mass transport. As well, the surface plot 5.4.18b shows that when the heat source (q) improved, Sh_x or the values $-L'(0)$ raised which is the opposite of ka.

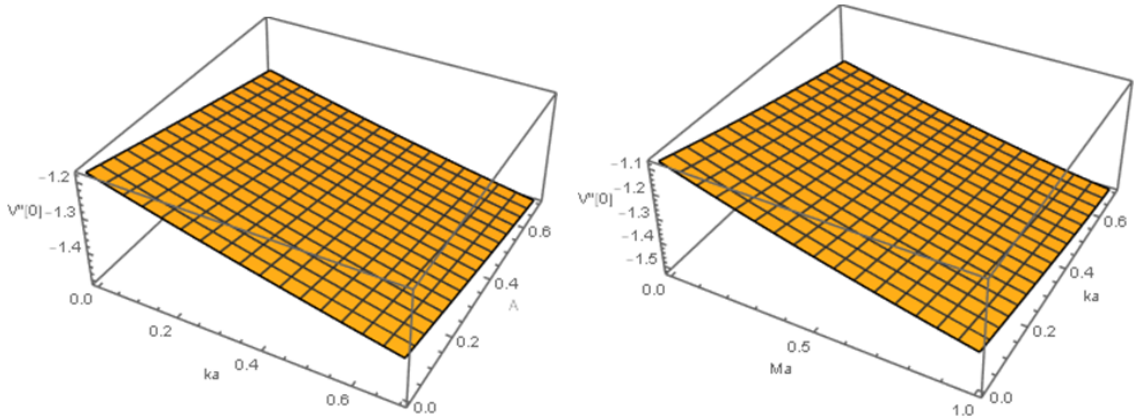

(a) Impact of A and ka on Cf_x

(b) Impact of ka and Ma on Cf_x

Figure 5.4.16: Consequence of A, ka and Ma on local skin friction coefficient

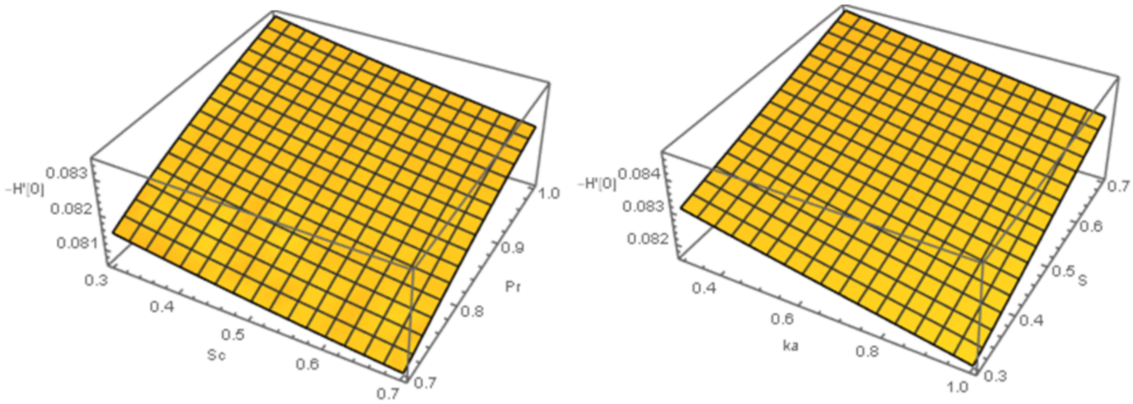

(a) Impact of Sc and Pr on Nu_x

(b) Impact of ka and S on Nu_x

Figure 5.4.17: Impact of Sc, Pr, ka and S on heat transfer rate

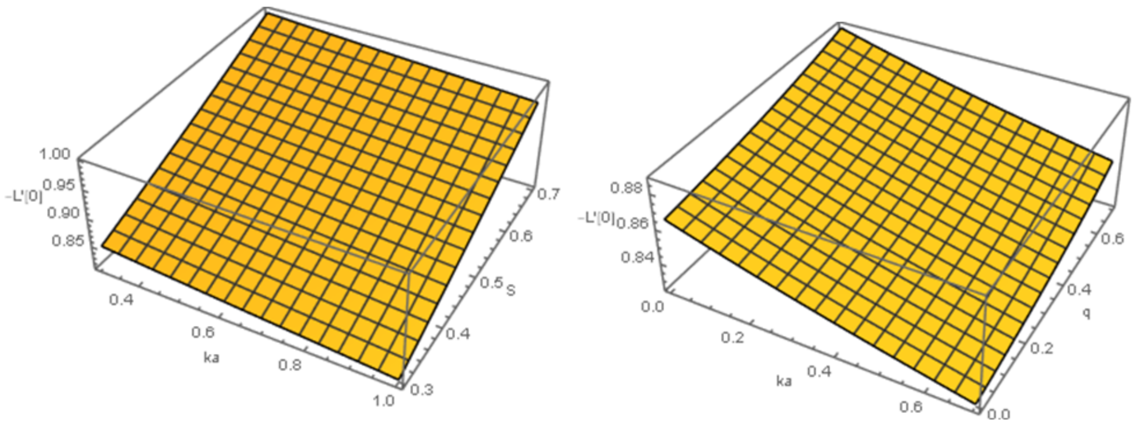

(a) Impact of ka and S on Sh_x

(b) Impact of ka and q on Sh_x

Figure 5.4.18: The consequence of ka, S and q on mass transfer rate

5.5 Summary

This chapter explores the heat and mass transfer of viscous nanofluids flowing over a horizontally stretched porous medium with entropy. The influence of a porous media combined with solar radiation, heat source, viscous dissipation and magnetic field on dimensionless velocity, temperature, concentration and entropy fields are investigated by taking velocity slip, convective heat transfer and mass suction boundary conditions into account. The obtained equations are solved by HAM using Mathematica 12.1 software. The conclusion of this problem is summarized as:

- The flow of nanofluid is retarded for raising the values of ka, S, ϖ and Ma.
- The temperature increases with $ka, Ma, Rn, q, Ec, \Upsilon, Nt$ and Nb. Conversely, it decreases whenever there is an enlargement on parameters S and Pr.
- The impact of ka, Ma, Nt and Ec have direct relation with the concentration of nanofluids, whereas the parameters S and Sc are inversely proportionate with it.
- Entropy production rises with Ec, Re and Br but not for A and ϖ.
- The magnitude of local skin friction coefficient is raised by Ma, ka and A.
- Nusselt number rises for more values of Pr, S and with lower values of Sc, ka.
- Sherwood number increases due to the values of S and q but not for ka.

CHAPTER SIX

Heat and Mass Transfer by Stirring Nanofluid with the Presence of Renewable Solar Rays, Joule Heating and Entropy Procreation

6.1 Introduction

The flow of heat from a warmer object to a cooler body is characterized as heat transfer. Direct solar, geothermal, and biomass sources all rely heavily on this form of heat transmission (Twidell, 2021). The heat transfer from solar energy increases the water's temperature, which is applicable in our real lives. This has a wide range of practical applications in the industrial sector (Jamshed et al., 2022). Plenty of researchers spent time in studying heat transfer under a number of circumstances, such as constant flow of an electrically conducting fluid on a stretchable permeable surface (Daniel, 2015), flow of nanofluid across porous medium with convective heat transfer (Daniel, 2016), including partial sliding situation (Daniel, 2017).

The dispersion of tiny particles in a base fluid are essential in absorbing the Sun's radiation in the form of solar energy. Thus, in gathering solar radiation by direct solar collectors, the role of nanofluid is incredibly essential due to the occurrence of tiny particles that are dispersed in convectional fluids (Afzal and Aziz, 2016). Consequently, employing nanofluid as the conveying fluid optimizes the heat transfer. That is why numerous scientists have adopted nanofluids as heat-transfer fluids, such as Daniel et al. (2019); Shahzad et al. (2022a,b); Jaddoa et al. (2023).

The conceptual frameworks for the characteristics of nanofluids are modeled in two forms: homogeneous flow and disbandment of nanoparticles in a separate manner (Malvandi et al., 2014). But, this declaration has been reformed by Buongiorno (2006) which archetype to neglect the scattering effect of small-sized solid particles in convectional fluids and he set a preference to construe the extraordinary appearance of nanofluids regarding heat transfer. Furthermore, Buongiorno focused on the two vital slip mechanisms that subsist in nanofluids: Brownian and thermophoresis diffusion, out of seven. Several researchers reflected the Buongiorno's model which quoted in Rawat et al. (2020); Rana et al. (2021); Shahzad et al. (2022a).

The practical applications of MHD are mentioned by Khan et al. (2022b); Reddy et al. (2022). Thus, solar radiation can be magnified by moving nanofluids with MHD on permeable surfaces. In light of this, sundry academics apply the Joule heating on a porous medium for consolidating the heat transfer from solar thermal radiation as quoted in (Eid and Makinde, 2018; Swain et al., 2020; Khan et al., 2022a). Moreover, there is also a formation of entropy and it is analyzed by the second law of thermodynamic which is used to assess the energy lost due to its irreversiblty. In this problem, the entropy production is occurred by nanofluid friction, Joule heating, heat, mass, and porosity dissipation irreversibility which are considered by Daniel et al. (2017); Aziz et al. (2018); Hayat et al. (2019).

In light of the aforesaid survey, there is a limited information about the heat and mass transfer via nanofluids flow on an inclined porous media in the presence of sunlight and Joule heating with the analysis of entropy formation. With the records mentioned above, such an issue has not yet been noted. Thus, the researchers aspired to look at the heat and mass transfer of unsteady, electrically conducting nanofluids flowing over an inclined porous medium in the presence of sunlight. In this study, the entropy formation is also deliberated. Here, the equations of flow, temperature and concentration are administered with mass suction, velocity slip and convective boundary conditions. By incorporating these points, the outcomes of governing equations are displayed graphically using HAM, on Mathematica 12.1 software.

6.2 Mathematical formulation of the problem

In this problem, the Cartesian coordinate system is imagined and the surface set up stretching at $t > 0$ (Kebede et al., 2020). The inclined plate acquires non-uniform velocity, temperature and concentration having surface wall similar to equation 5.2.1. The physical flow of this problem is designated in Figure 6.2.1. To figure out this issue, the flow model relies on the assumptions in section 4.2 and the following.

- Unsteady flowing nanofluid over an inclined porous medium.
- Considering Joule heating, viscous dissipation and Darcy model for porosity.
- The velocity slip and mass suction/injection boundary conditions are assumed.

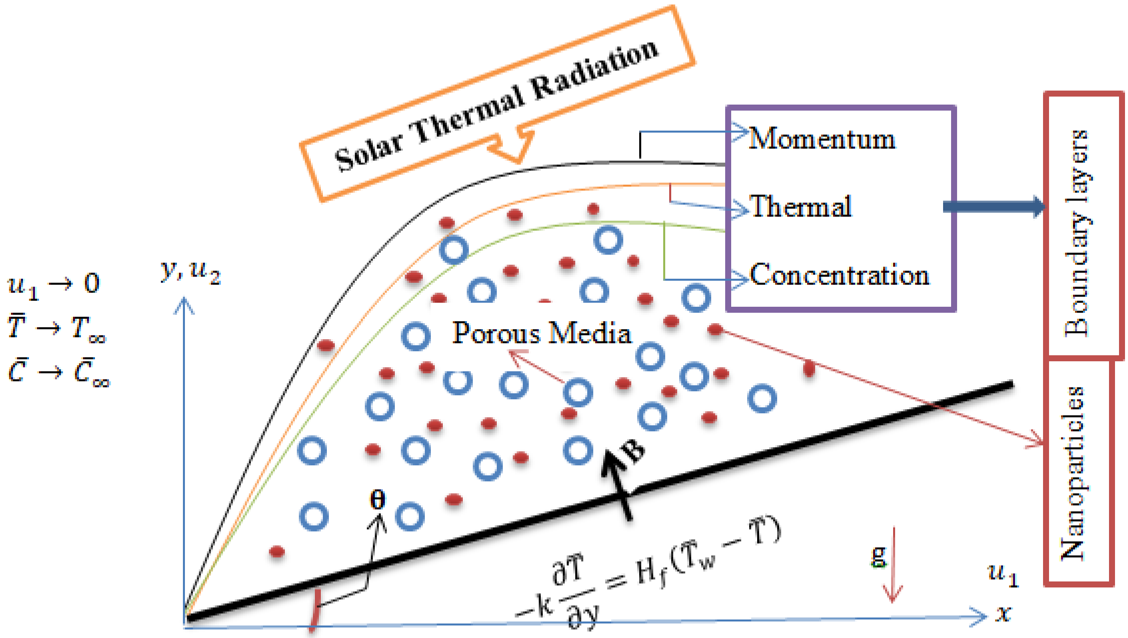

Figure 6.2.1: Physical representation for the boundary layer of the condition

6.2.1 Governing Equations

Underlying the above assumptions, the primary guiding equations based on the conservation of mass, momentum, energy and concentration can be derived. They are simplified using the concept of boundary layer approximation that was discussed in section 3.1.6. Due to the consideration of the inclined surface, there is a body force which can be formulated by Oberbeck-Boussinesq approximation (Daniel et al., 2020). Consequently, the momentum equation is derived from the impact of magnetic field, porous medium, and body force as a result of an inclined surface with an angle of θ from the horizontal. It is expressed as follows:

$$\rho\frac{D\mathbf{V}}{Dt} = \mu\nabla^2\mathbf{V} + \mathbf{J}\times\mathbf{B} + \nabla P + \rho\mathbf{g} \implies \rho\frac{Du_1}{Dt} = \mu\left(\frac{\partial^2 u_1}{\partial y^2}\right) - \frac{\sigma_e B_0^2 u_1}{1-\varsigma t} - \frac{\mu}{k_p}u_1 + \rho g\sin\theta.$$

According to Boussinesq approximation, the difference in density due to temperature and concentration variations are essential for body force term. Thus, using Taylor series for $\rho = \rho(\bar{T},\bar{C})$, with $\rho_0 = \rho(\bar{T}_\infty,\bar{C}_\infty)$ becomes

$$\rho = \rho_0 + \frac{\partial\rho}{\partial\bar{T}}(\bar{T}-\bar{T}_\infty) + \frac{\partial\rho}{\partial\bar{C}}(\bar{C}-\bar{C}_\infty) + \frac{\partial^2\rho}{\partial\bar{T}^2}(\bar{T}-\bar{T}_\infty)^2 + \frac{\partial^2\rho}{\partial\bar{C}^2}(\bar{C}-\bar{C}_\infty)^2 + \cdots$$

Avoiding the higher order derivatives with $\rho_0 = 0,\ \rho = \frac{\partial \rho}{\partial \bar{T}}(\bar{T}-\bar{T}_\infty) + \frac{\partial \rho}{\partial \bar{C}}(\bar{C}-\bar{C}_\infty)$. Then, applying boundary layer approximation, the momentum equation becomes

$$\begin{aligned}
\rho\frac{Du_1}{Dt} &= \mu\left(\frac{\partial^2 u_1}{\partial y^2}\right) - \frac{\sigma_e B_0^2 u_1}{1-\varsigma t} - \frac{\mu}{k_p}u_1 + \left(\frac{\partial \rho}{\partial \bar{T}}(\bar{T}-\bar{T}_\infty) + \frac{\partial \rho}{\partial \bar{C}}(\bar{C}-\bar{C}_\infty)\right) g\sin\theta \\
\implies \frac{Du_1}{Dt} &= \frac{\mu}{\rho}\left(\frac{\partial^2 u_1}{\partial y^2}\right) - \frac{\sigma_e B_0^2 u_1}{\rho(1-\varsigma t)} - \frac{\mu}{\rho k_p}u_1 + \left(\frac{1}{\rho}\frac{\partial \rho}{\partial \bar{T}}(\bar{T}-\bar{T}_\infty) + \frac{1}{\rho}\frac{\partial \rho}{\partial \bar{C}}(\bar{C}-\bar{C}_\infty)\right) g\sin\theta
\end{aligned}.$$

The expansion coefficient of thermal and concentration can be denoted by $\beta_t = \frac{1}{\rho}\frac{\partial \rho}{\partial \bar{T}}$ and $\beta_c = \frac{1}{\rho}\frac{\partial \rho}{\partial \bar{C}}$, respectively. In this problem, the impacts of magnetic field and porosity are added on the energy equation (4.2.4). From equation (3.1.55), $\bar{q}$ is defined as

$$\bar{q} = -\nabla q_r + c_p\rho_p(\nabla\bar{T})\left(D_B\nabla\bar{C} + \frac{D_T}{\bar{T}_\infty}\nabla\bar{T}\right) - \mathbf{v}\cdot\nabla P - \mathbf{v}\cdot(\mathbf{J}\times\mathbf{v}),$$

where $\mathbf{v}\cdot\nabla P = (u_1,u_2)\cdot(\frac{\partial P}{\partial x},\frac{\partial P}{\partial y}) = u_1\frac{\partial P}{\partial x} = -\frac{\mu}{\rho k_p}u_1^2$ and $\mathbf{v}\cdot(\mathbf{J}\times\mathbf{v}) = (u_1,u_2)\cdot(-\frac{\sigma_e B_0^2 u_1}{1-\varsigma t},0) = -\frac{\sigma_e B_0^2 u_1^2}{1-\varsigma t}$. By applying boundary layer approximation, $\bar{q}$ becomes

$$\bar{q} = -\frac{\partial q_r}{\partial y} + c_p\rho_p\frac{\partial \bar{T}}{\partial y}\left(D_B\frac{\partial \bar{C}}{\partial y} + \frac{D_T}{T_\infty}\frac{\partial \bar{T}}{\partial y}\right) + \frac{\sigma_e B_0^2}{1-\varsigma t}u_1^2 + \frac{\mu}{k_p}u_1^2.$$

With out changing the concentration equation, the governing PDEs can be summarized as follows (Daniel et al., 2020; Nandi et al., 2022; Rehman et al., 2022b).

$$\frac{\partial u_1}{\partial x} + \frac{\partial u_2}{\partial y} = 0, \tag{6.2.1}$$

$$\begin{aligned}
&\frac{\partial u_1}{\partial t} + u_1\frac{\partial u_1}{\partial x} + u_2\frac{\partial u_1}{\partial y} = \nu\frac{\partial^2 u_1}{\partial y^2} - \frac{\sigma_e B_0^2 u_1}{\rho(1-\varsigma t)} - \frac{\mu}{\rho k_p}u_1 \\
&+ \Big(\beta_c(\bar{C}-\bar{C}_\infty) + \beta_t(\bar{T}-\bar{T}_\infty)\Big) g\sin\theta,
\end{aligned} \tag{6.2.2}$$

$$\begin{aligned}
\frac{\partial \bar{T}}{\partial t} + u_1\frac{\partial \bar{T}}{\partial x} + u_2\frac{\partial \bar{T}}{\partial y} =& \frac{k}{\rho c_p}\left(1 + \frac{16\bar{T}_\infty^3\sigma^*}{3k^*k}\right)\frac{\partial^2 \bar{T}}{\partial y^2} + \frac{\mu}{\rho c_p}\left(\frac{\partial u_1}{\partial y}\right)^2 \\
&+ \left(\frac{\sigma_e B_0^2}{1-\varsigma t} + \frac{\mu}{k_p}\right)\frac{u_1^2}{\rho c_p} + \tau_h\left(D_B\frac{\partial \bar{C}}{\partial y}\frac{\partial \bar{T}}{\partial y} + \frac{D_T}{T_\infty}\left(\frac{\partial \bar{T}}{\partial y}\right)^2\right),
\end{aligned} \tag{6.2.3}$$

$$\frac{\partial \bar{C}}{\partial t} + u_1\frac{\partial \bar{C}}{\partial x} + u_2\frac{\partial \bar{C}}{\partial y} = D_B\frac{\partial^2 \bar{C}}{\partial y^2} + \frac{D_T}{T_\infty}\frac{\partial^2 \bar{T}}{\partial y^2}. \tag{6.2.4}$$

The associated boundary conditions are (Kebede et al., 2020; Jamshed et al., 2021c).

$$\begin{cases} \text{For } y=0; & u_1 - U_w = S_l \dfrac{\partial u_1}{\partial y}, u_2 = V_w, k\dfrac{\partial \bar{T}}{\partial y} = H_f(\bar{T}-\bar{T}_w), \bar{C} = \bar{C}_w \\ y \to \infty; & u_1 \to 0, \bar{T} \to \bar{T}_\infty, \bar{C} \to \bar{C}_\infty \end{cases} \tag{6.2.5}$$

To figure out this issue, the PDEs, (6.2.1, 6.2.2 and 6.2.3) have been converted into a system of ODEs by means of similarity transformation variables which are stream function ψ and dimensionless independent variable ϵ. They are defined in equation (5.2.9). Then, the velocity components u_1 and u_2, temperature $\bar{T}$ and concentration $\bar{C}$ are written in terms of ψ and ϵ as non-dimensional forms similar to equation (5.2.10).

Because of the continuous stream function ψ, equation (6.2.1) has been well-adjusted. As well, the PDEs (6.2.2, 6.2.3, and 6.2.4) have been transformed into ODEs as follows by applying similar approach as in equations (4.2.14-4.2.16).

$$V''' + VV'' - A\left(V' + \frac{\epsilon}{2}V''\right) - (V' + Ma + ka)V' + GpL + GtH = 0, \tag{6.2.6}$$

$$\begin{aligned} \frac{(1+Rn)}{Pr}H'' - A\left(H + \frac{\epsilon}{2}H'\right) + Ec(V'')^2 + H'\left(NbL' + NtH' + V\right) - HV' \\ + Ec(Ma+ka)(V')^2 = 0, \end{aligned} \tag{6.2.7}$$

$$L'' - Sc\left[A\left(L + \frac{\epsilon}{2}L'\right) - VL' + LV'\right] + \frac{Nt}{Nb}H'' = 0. \tag{6.2.8}$$

Likewise, the boundary conditions in equation (6.2.5) are recast as follows

$$\begin{cases} V(0) = S, V'(0) - \varpi V''(0) = L(0) = 1, H'(0) = \Upsilon(H(0)-1), \\ V'(\epsilon) = H(\epsilon) = L(\epsilon) = 0 \text{ at } \epsilon \to \infty \end{cases} \tag{6.2.9}$$

The dimensionless constants originated during this process are defined as $g \to$ gravitational acceleration; $Gt = \dfrac{\beta_t \nu(\bar{T}_w - \bar{T}_\infty)Re_x g \sin\theta}{U_w^3}$ and $Gp = \dfrac{\beta_c \nu(\bar{C}_w - \bar{C}_\infty)Re_x g \sin\theta}{U_w^3}$ $\to$ thermal and concentration Grashof number, respectively. and on Table 5.2.1. The prime $'$ in equations (6.2.6-6.2.9) denotes the differentiation with respect to ϵ.

6.2.2 Physical Quantities

The explanation and formula of local skin friction coefficient (Cf_x), Nusselt number (Nu_x) and Sherwood number (Sh_x) are similar to section 5.2.2. They are the three essential physical quantities from an engineering viewpoint. Moreover their simplified formulas are directly related to equations (5.2.16, 5.2.18 and 5.2.19). For recalling them, their formula can be written in the following summarized form.

$$\begin{aligned}
&Cf_x = \frac{\mu\left(\frac{\partial u_1}{\partial y}\right)_{y=0}}{\rho U_w^2} = \frac{\mu\left(\frac{\partial^2 \psi}{\partial y^2}\right)_{y=0}}{\rho U_w^2} = Re_x^{-0.5} V''(0) \\
&Nu_x = -Re_x^{0.5}\left[1 + Rn\right] H'(0), \quad Sh_x = \frac{x J_m}{D_B(\bar{C}_w - \bar{C}_\infty)} = -Re_x^{0.5} L'(0).
\end{aligned} \tag{6.2.10}$$

6.2.3 Entropy Generation

Entropy is the disturbance of a regular system and measures the irreversible process (Loganathan et al., 2020). The existence of irreversibility reduces the total work done. So, in this study, the researchers noted the entropy formation by the irreversible transmission of heat, mass, friction, Joule heating and porosity dissipation. The rate of entropy per volume (E_{pr}) and its dimensionless (NG) form are similar to equations (5.2.20) and (5.2.21), respectively.

6.3 Homotopy Analysis Method (HAM)

At the moment, HAM is the superlative practice to work out the boundary value problems of non-linear higher-order systems of ODEs. It is proposed by Shi-Jun Liao in his Ph.D. dissertation (Liao, 1992). The series solutions using HAM are highly close to the exact one, that is why most scholars put it into action to deal with their problems including Hayat et al. (2021); Loganathan et al. (2021); Saeed et al. (2022). Like the previous problems in this dissertation, the linear operators, initial guesses, auxiliary functions and convergence control parameters are selected to implement HAM for attaining an acceptable convergent solutions.

6.3.1 Selecting $\mathcal{L}$, Initial Guesses and $\mathcal{H}(\epsilon)$

The auxiliary linear operators $(\mathcal{L}_V, \mathcal{L}_H, \mathcal{L}_L)$, initial guesses $(V_0(\epsilon), H_0(\epsilon), L_0(\epsilon))$ and auxiliary functions $(\mathcal{H}_V(\epsilon) = \mathcal{H}_H(\epsilon) = \mathcal{H}_L(\epsilon) = 1)$ are selected according to equations (5.3.1), (5.3.2) and (5.3.3) respectively. These selections have an impact on getting convergent solutions for the problem in equations (6.2.6-6.2.8) by applying HAM.

6.3.2 Zero$^{\text{th}}$ and m$^{\text{th}}$ order Deformation Equations

The Zero$^{\text{th}}$ order deformation defined as follows like Kebede et al. (2020)

$$\begin{aligned}
&(1-p)\mathcal{L}_V[V(\epsilon;p) - V_0(\epsilon)] = p\hbar_V \mathcal{H}_V(\epsilon)\mathcal{N}_V[V(\epsilon;p), H(\epsilon;p), L(\epsilon;p)] \\
&(1-p)\mathcal{L}_H[H(\epsilon;p) - H_0(\epsilon)] = p\hbar_H \mathcal{H}_H(\epsilon)\mathcal{N}_H[V(\epsilon;p), H(\epsilon;p), L(\epsilon;p)] \\
&(1-p)\mathcal{L}_L[L(\epsilon;p) - L_0(\epsilon)] = p\hbar_L \mathcal{H}_L(\epsilon)\mathcal{N}_L[V(\epsilon;p), H(\epsilon;p), L(\epsilon;p)],
\end{aligned} \tag{6.3.1}$$

where $\hbar_V$, $\hbar_H$, and $\hbar_L$ are non-zero convergent control parameters, $0 \leq p \leq 1$ is homotopy embedding parameter without any physical interpretation, and the nonlinear operators $\mathcal{N}_V$, $\mathcal{N}_H$ and $\mathcal{N}_L$ are defined in similar fashion with equations (4.3.5, 4.3.6 and 4.3.7). In the same way, the boundary conditions also similar with equation (5.3.5).

It is clear that when $p = 0$, $V(\epsilon, 0) = V_0(\epsilon)$, $H(\epsilon, 0) = H_0(\epsilon)$, and $L(\epsilon, 0) = L_0(\epsilon)$ are solutions for the equations (6.2.6-6.2.8). Furthermore, at $p = 1$, the answer for equations (6.2.6-6.2.8) are given by $V(\epsilon, 1) = V(\epsilon), H(\epsilon, 1) = H(\epsilon)$, and $L(\epsilon, 1) = L(\epsilon)$. Thus, when the value of p changes continuously from 0 to 1, the homotopy solution also runs from initial estimation, $V_0(\epsilon), H_0(\epsilon)$ and $L_0(\epsilon)$ to the accurate solution, $V(\epsilon), H(\epsilon)$, and $L(\epsilon)$ (Van Gorder, 2014). By exerting the Taylor series expansion rule about $p = 0$ like Rasheed et al. (2021), similar equations are developed with equations (5.3.6). It follows that, for $m \geq 1$, the m$^{\text{th}}$ order homotopy derivatives are formulated for $V_m(\epsilon), H_m(\epsilon)$ and $L_m(\epsilon)$ with the same as equation (4.3.10).

The m^{th} order deformation equations which is similar with equation (5.3.7), obtained by differentiating the 0^{th} order on equation (6.3.1) m-times with respect to p and putting $p = 0$, then dividing by m factorial. Right now, the linear operators, initial guesses and auxiliary functions are selected. The convergence control parameters, $\hbar_V$, $\hbar_H$ and $\hbar_L$ are still unknown. After selecting the convergence control parameters, the equation (5.3.9) can be solved. Then, for $p = 1$, equation (5.3.10) delivers an exact solution for the ODEs (6.2.6-6.2.8) with a boundary conditions (6.2.9).

6.3.3 Investigating the Convergence of Solutions

In HAM, the convergent control parameters play a key role to secure the doubtfulness concerning solutions' convergence. Henceforth, by considering $\hbar_V = \hbar_H = \hbar_L = \hbar$, Figure 6.3.1a is sketched for $V''(0)$, $H'(0)$ and $L'(0)$ versus $\hbar$. The range where this graph becomes horizontal proposes the potential values of $\hbar_V$, $\hbar_H$ and $\hbar_L$ to ensure the convergence of HAM (Van Gorder, 2014). Accordingly, the values of convergent control parameters $\hbar_V = -0.768772, \hbar_H = \hbar_L = 1.343359$ are selected for this issue. Additionally, it is inferred that from Figure 6.3.1b the inaccuracy decreases with increasing order of approximation (m). The performance of convergence is further attested by Table 6.3.1 for $Ma = Sc = 0.5, Pr = 0.72, Nt = Nb = S = \varpi = A = ka = Gt = Gp = 0.3, Ec = \Upsilon = 0.1, Rn = 0.7, Re = 7,\ \Delta_1 = \Delta_2 = \Delta_3 = 1$ and $Br = 3$ with residual error on the respective order of approximation (m). Figure 6.3.2a shows that the absolute value of the differences in consecutive values of the local skin friction coefficient, Nusselt and Sherwood numbers in Table 6.3.1 are approaching zero, which is the justification for obtaining a convergent solutions. These values are based on equation (6.2.10). That is, $|V''(0)_{n+1} - V''(0)_n| \to 0, |H'(0)_{n+1} - H'(0)_n| \to 0$ and $|L'(0)_{n+1} - L'(0)_n| \to 0$, with number of values $n = 1, 2, ..., 9$. Moreover, their tabular values in Table 6.3.1 have also been elaborated pictorially by Figures 6.3.2b, 6.3.3a and 6.3.3b for the values of $-V''(0)$, $-H'(0)$ and $-L'(0)$ on the y-axis, respectively, against the consecutive number of their values denoted by n as in Table 6.3.1. For this issue, a guaranteed convergent solutions are established by using HAM.

Table 6.3.1: Order of approximation of HAM with residual error

n	m^{th} Order	$-V''(0)$	$-H'(0)$	$-L'(0)$	Residual Error $-V''(0)$	Residual Error $-H'(0)$	Residual Error $-L'(0)$
1	3	0.893894	0.0842103	0.672462			
2	6	0.887287	0.0836247	0.668208	6.85×10^{-7}	1.78×10^{-7}	1.08×10^{-6}
3	9	0.886869	0.0835067	0.667764			
4	12	0.886762	0.0834751	0.667707	3.12×10^{-9}	1.90×10^{-9}	2.99×10^{-9}
5	15	0.886730	0.0834645	0.667693			
6	18	0.886718	0.0834605	0.667693	5.79×10^{-11}	1.101×10^{-10}	1.68×10^{-11}
7	21	0.886713	0.0834588	0.667690			
8	24	0.886711	0.0834580	0.667691	1.22×10^{-12}	5.75×10^{-12}	2.98×10^{-13}
9	27	0.886710	0.0834576	0.667691			
10	30	0.886710	0.0834574	0.667691	3.15×10^{-14}	3.45×10^{-13}	6.79×10^{-14}

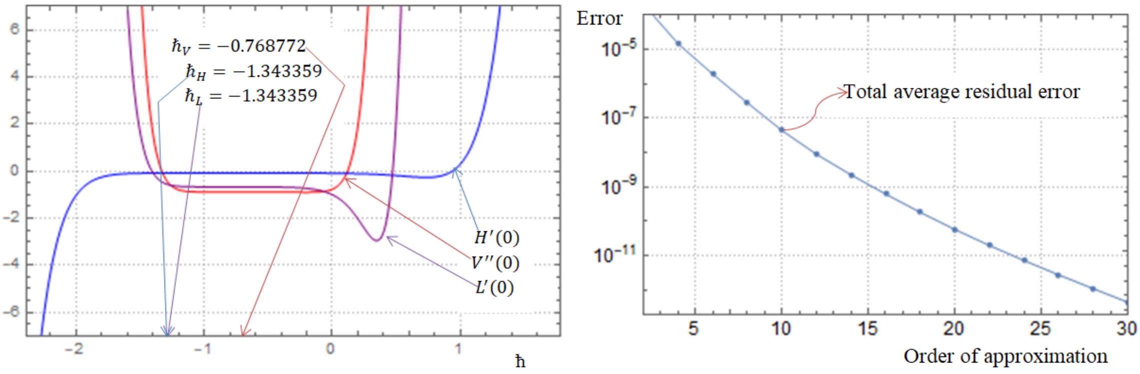

(a) $\hbar$-curves for $\hbar_V, \hbar_H$ and $\hbar_L$ (b) Error with order of approximation (m)

Figure 6.3.1: $\hbar$-curves for $\hbar_V, \hbar_H$ and $\hbar_L$ and order of approximation

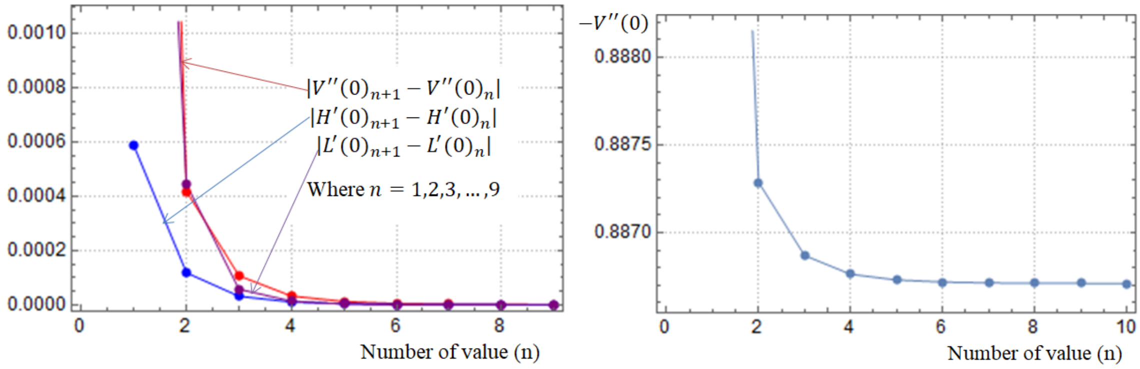

(a) Differences in magnitude (b) Convergence of the values of $-V''(0)$

Figure 6.3.2: Differences in absolute value and convergence of the values of $-V''(0)$

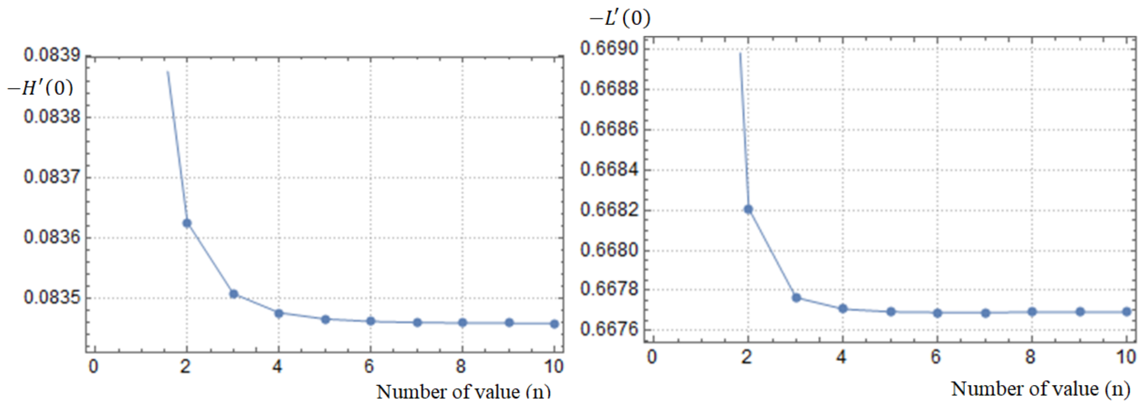

(a) Convergence of the values of $-H'(0)$ (b) Convergence of the values of $-L'(0)$

Figure 6.3.3: Convergence of the values of $-H'(0)$ and $-L'(0)$

6.4 Computed Results and Discussions

The semi-analytic computation on nanofluid's flow, temperature, concentration, entropy generation, local skin friction, Nusselt and Sherwood numbers are outlined by HAM depending on potential parameters. Graphical representations are delivered for the physical sway of stand-in coefficients. HAM is employed on Mathematica 12.1

software with the BVPh2.0 package. The validity of this calculation is approved by contrasting the values of $-V''(0)$ for distinct values of Ma, ϖ and S as it is observed in Table 6.4.1. For a range of Pr values, the values of $-H'(0)$ highly related with scholars' result, which also approved the validity of this approach (see Table 6.4.2).

Table 6.4.1: $-V''(0)$ values when $ka = Nt = Gp = Gt = Ec = A = 0$ and $\Upsilon \to \infty$

Ma	ϖ	S	Daniel et al. (2020)	Ali et al. (2022)	Nandi et al. (2022)	**Present result**
0.00	0.0	0.0	-	1.000000	1.000000	1.000000
0.25	0.0	0.0	-	1.118034	-	1.118030
0.50	0.0	0.0	-	-	-	1.224740
0.75	0.0	0.0	-	-	-	1.322880
1.00	0.0	0.0	1.414214	1.414214	-	1.414210
0.00	0.5	0.0	-	0.591195	0.591211	0.591195
0.00	1.0	0.0	-	0.430160	-	0.430160
0.00	3.0	0.0	-	-	-	0.214055
0.00	5.0	0.0	-	-	0.144870	0.144840
0.00	7.0	0.0	-	-	-	0.110050
0.00	10	0.0	-	-	-	0.081242
1.00	0.0	0.2	1.517745	-	-	1.517740
1.00	0.0	0.5	1.686141	-	-	1.686141
1.00	0.0	0.7	-	-	-	1.806888
1.00	0.0	1.0	2.000000	-	-	2.000000

Table 6.4.2: $-H'(0)$ value at $Ma = ka = A = Nt = Ec = Rn = Sc = S = \varpi = 0, \Upsilon \to \infty$

Pr	Reddy et al. (2022)	Bouslimi et al. (2022)	Naqvi et al. (2022)	**Present result**
0.50	-	-	-	0.630978
0.72	0.808629	0.8087618	0.8087618	0.808632
1.00	1.000000	1.0000000	1.0000000	1.000000
1.50	-	-	-	-1.284040
3.00	1.923681	1.9235742	1.9235742	1.923620
7.00	-	-	3.0731465	3.072220

6.4.1 Velocity Profile

The parameters such as thermal Grashof number (Gt), concentration Grashof number (Gp), Brownian diffusivity constant (Nb), Eckert number (Ec), mass suction (S) and Schemed number (Sc) on the movement of nanofluids have been divulged on Figures 6.4.1a to 6.4.3b. Generally speaking, the buoyant to viscous force ratio is represented by the Grashof number. Consequently, higher values of Gt and Gp have an impact in lowering the formation of viscous which increase the speed of nanofluid as Figures 6.4.1a and 6.4.1b, accredited, respectively. Figures 6.4.2a and 6.4.2b pointed out, Ec

and Nb speed up the motion of nanofluid on an inclined porous media. Physically, more active nanofluids disperse as a result of Ec and Brownian random motion of nanoparticles. Consequently, the small-sized solid particles of nanofluids collide and spread out quickly. In the contrary of the above four parameters, S and Sc have an inverse relation with $V'(\epsilon)$. Thus, S and Sc increase the viscous formation which hinder the flow of nanofluid as seen in Figures 6.4.3a and 6.4.3b, respectively.

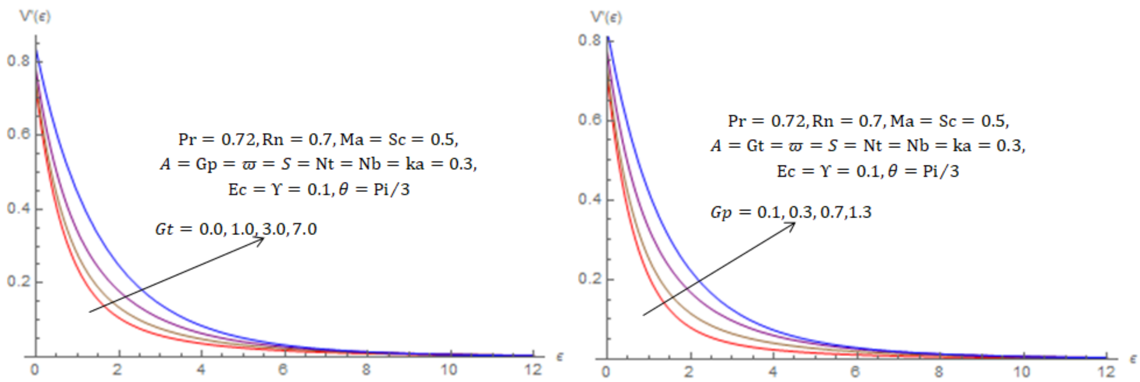

(a) The consequence of Gt on $V'(\epsilon)$ (b) The consequence of Gp on $V'(\epsilon)$

Figure 6.4.1: Consequence of thermal and mass Grashof number on velocity

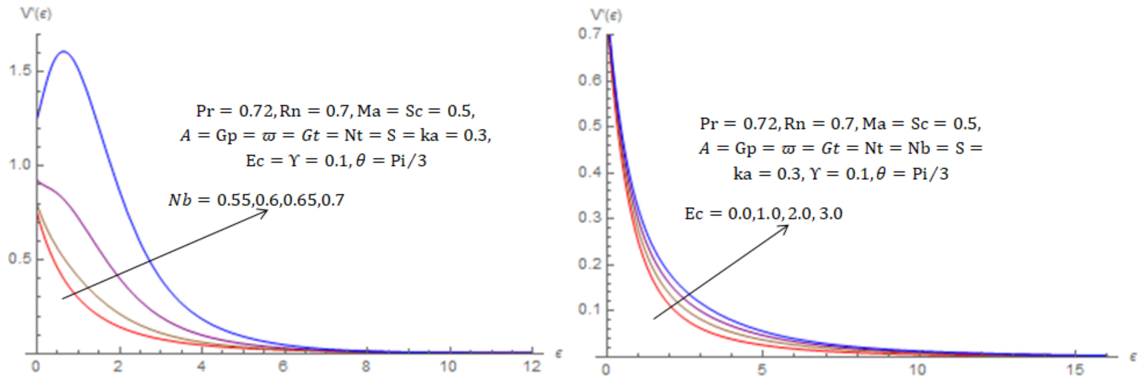

(a) The consequence of Nb on $V'(\epsilon)$ (b) The consequence of Ec on $V'(\epsilon)$

Figure 6.4.2: Impact of Brownian motion and Eckert number on velocity field

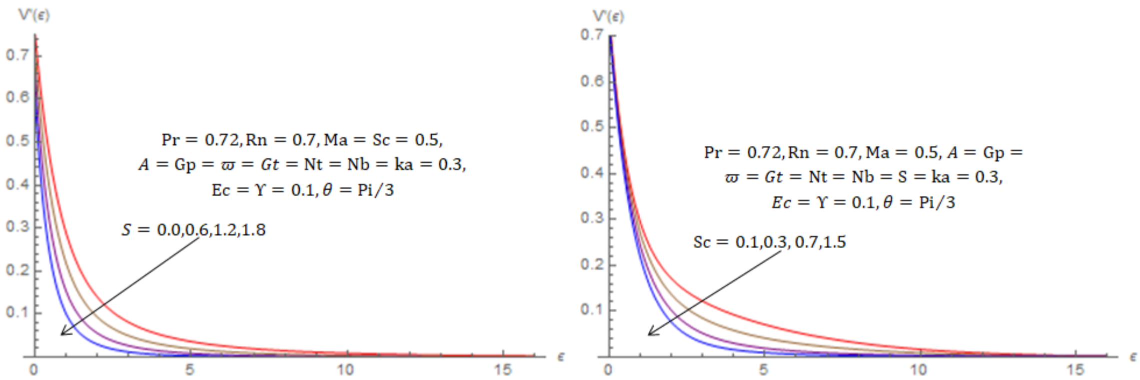

(a) The consequence of S on $V'(\epsilon)$ (b) The consequence of Sc on $V'(\epsilon)$

Figure 6.4.3: The consequence of mass suction and Schmidt number on velocity field

6.4.2 Temperature Profile

The outcome of energy equation is set out in Figures 6.4.4a to 6.4.7a by executing HAM with a short briefing on the selected parameters like $Rn, Ec, \Upsilon, Pr, Gt, Gp$ and S. Overall, Rn, Ec and Υ supersize the distribution of temperature on nanofluid flow since they supplement the rate of heat transmission. Conversely, Pr, Gt, Gp and S minimize the distribution of temperature in the nanofluid.

The Sun's rays deliver an amazing amount of heat, particularly when the radiative thermal energy emissions become higher. Normally, the ratio of heat transfer through thermal radiation to conduction is boosted by the thermal radiation parameter, Rn. In accordance with this, ascending Rn by sunlight upgrades the temperature of nanofluids. Henceforth, Figure 6.4.4a asserted how Rn drastically heightened the temperature distribution in the nanofluids. A dimensionless Eckert number (Ec) denotes the ratio of kinetic energy in the nanofluid to enthalpy. As the value of Ec rises, the variation between the wall and ambient temperature $(\bar{T}_w - \bar{T}_\infty)$ is lessened at a constant pressure. The consequence of this is that, it adds to the quantity of kinetic energy striking the nanofluid flow and wanes the total heat offered in the thermodynamics system called enthalpy. Thus, the temperature profile ascends for immense values of Ec as Figure 6.4.4b divulges. Biot number Υ and $H(\epsilon)$ is directly proportional. In accordance with physical law, elevating Υ, expands the distribution of temperature. Figure 6.4.5a confirms this claim.

Heightening Pr brings down the temperature profile according to Figure 6.4.5b. Here, thermal diffusivity has an adverse relation with Pr. Thus, numerous values of Pr are designated to slight the thermal diffusivity, which lead to waning the temperature of nanofluids. Actually, in the process of heat transmission, Pr is applicable for controlling the thickness of the thermal boundary layer. The temperature of nanofluid decreases for advanced values of Gt and Gp as Figures 6.4.6a and 6.4.6b indicate. This phenomena occurs due to the lowering of viscous formation with more values of Gt and Gp. A higher value of S cooled the nanofluids' temperature, as noted in Figure 6.4.7a. This happened as a result of the stretchable sheet nearby the atmospheric condition, which reduces the thermal boundary layer thickness.

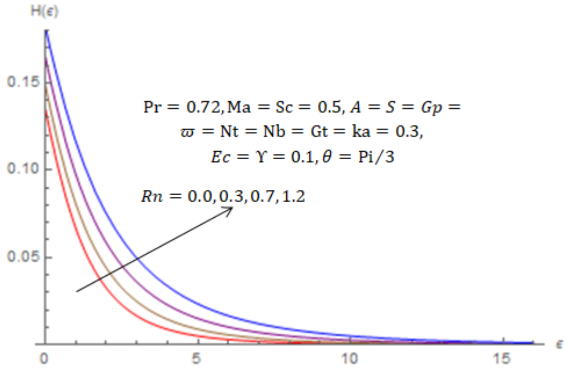

(a) The consequence of Rn on $H(\epsilon)$

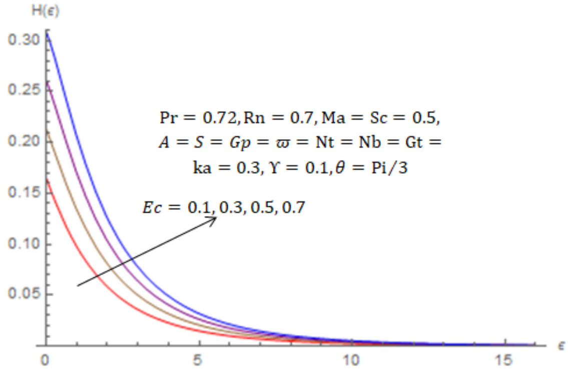

(b) The consequence of Ec on $H(\epsilon)$

Figure 6.4.4: The consequences of thermal radiation and Eckert number on temperature

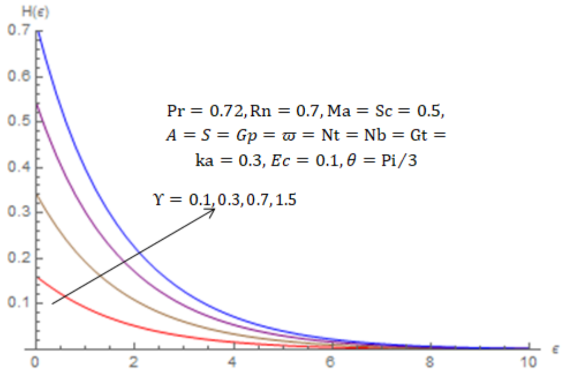

(a) The consequence of Υ on $H(\epsilon)$

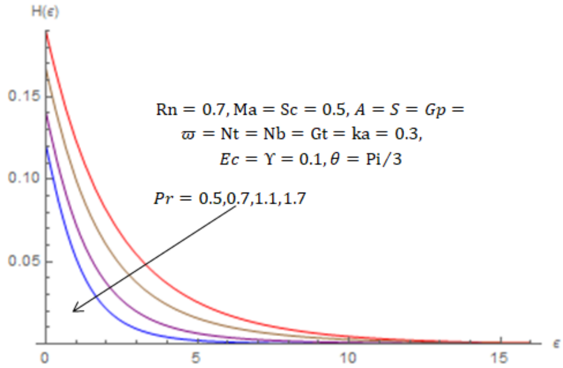

(b) The consequence of Pr on $H(\epsilon)$

Figure 6.4.5: The consequences of Biot and Prandtl numbers on temperature field

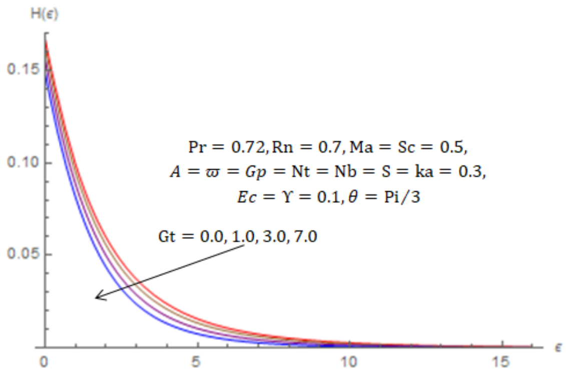

(a) The consequence of Gt on $H(\epsilon)$

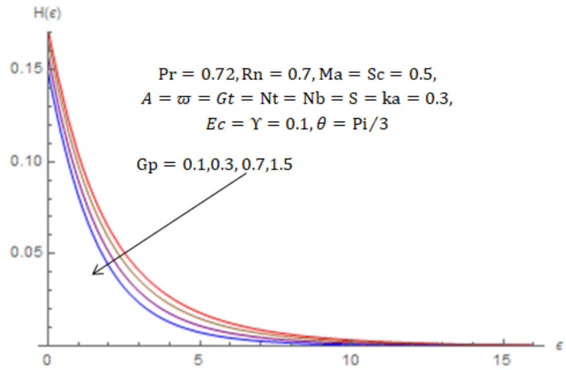

(b) The consequence of Gp on $H(\epsilon)$

Figure 6.4.6: Consequences of thermal and mass Grashof numbers on temperature

6.4.3 Concentration Profile

The graphs sketched from Figure 6.4.7b to Figure 6.4.9b serve for highlighting the attributions of prominent parameters, notably the mass suction (S), mass Grashof number (Gp), thermal Grashof number (Gt), Schmidt number (Sc) and thermophoresis parameters (Nt) on nanoparticles volume fraction. The non dimensional constants,

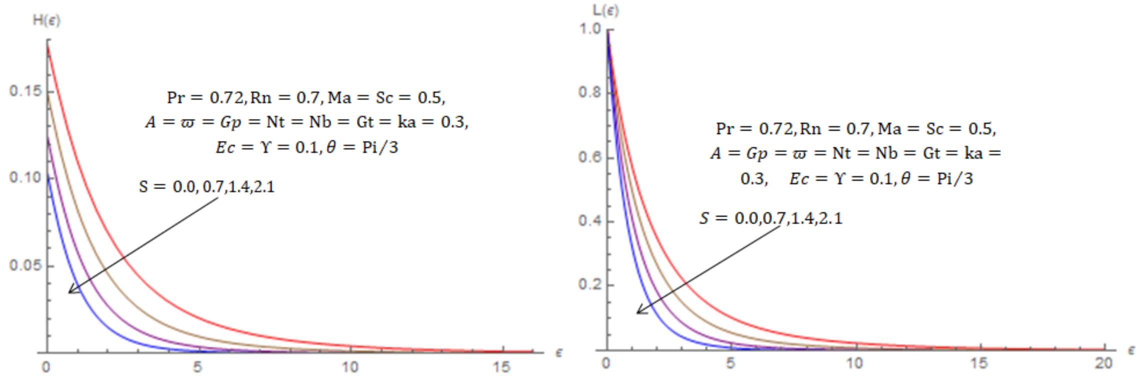

(a) The consequence of S on $H(\epsilon)$ (b) The consequence of S on $L(\epsilon)$

Figure 6.4.7: The consequences of mass suction on temperature and concentration field

S, Gp, Gt, and Sc decrease the concentrations of nanofluids as they are inspected from Figures 6.4.7b, 6.4.8a, 6.4.8b and 6.4.9a in that order. Specifically, for the case of S, the findings of this scenario is displayed in Figure 6.4.7b. Here, $L(\epsilon)$ is associated oppositely to S. The underlying root of this is that, the heated nanofluids are drawn towards the wall by rising S. Enlarging the values of Gp and Gt impute the flow of nanofluid, which in turn decline the concentrations of small-sized solid particles as viewed in Figures 6.4.8a and 6.4.8b. The existence of a reciprocal relationship between Schmidt number and mass diffusivity implies that a larger Sc prompts lower mass diffusivity, which is the root of dropping in nanoparticles concentration as we foresee in Figure 6.4.9a. As flaunted in Figure 6.4.9b, Nt supplements the concentration profile. Since progressive values of Nt, expand the amount of $(\bar{T}_w - \bar{T}_\infty)$ which moves the small-sized particles from warm to cold. This results in a augmenting of micro-sized solid particles concentrations.

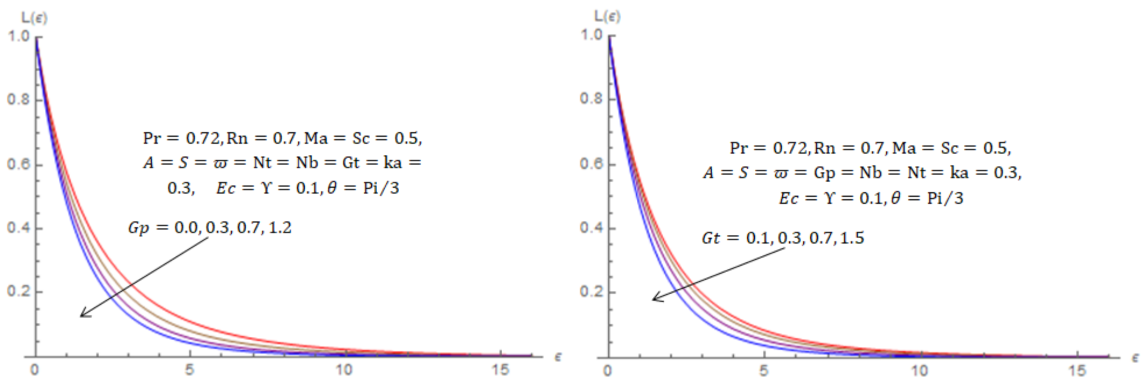

(a) The consequence of Gp on $L(\epsilon)$ (b) The consequence of Gt on $L(\epsilon)$

Figure 6.4.8: Consequences of mass and thermal Grashof numbers on concentration

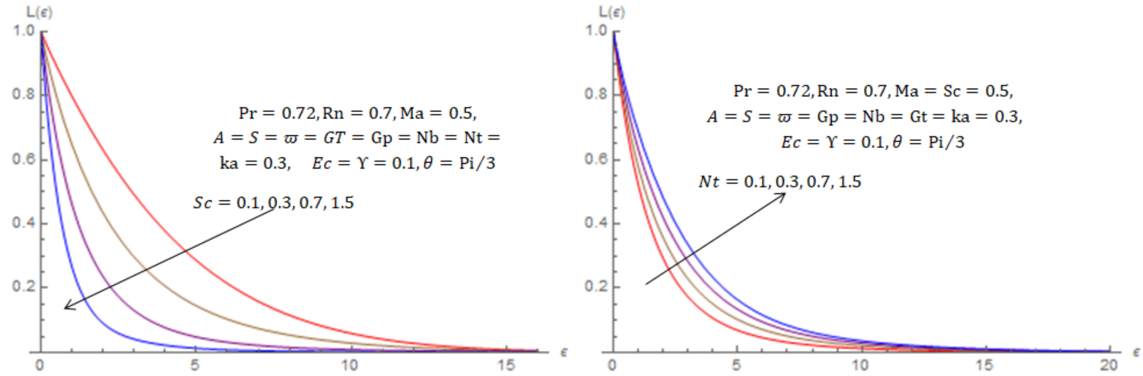

(a) The consequence of Sc on $L(\epsilon)$ (b) The consequence of Nt on $L(\epsilon)$

Figure 6.4.9: Consequences of Schmidt number and thermophoresis on concentration

6.4.4 Impact of Parameters on Entropy

Entropy is typically generated by the process of irreversible activities, and the second law of thermodynamics for heat transport aids in illuminating it. In accordance with this issue, the parameters Rn, Ec, Re, Br, Pr and ϖ have an immediate impacts on the formation of entropy. Their spheres of influence are epitomized graphically from Figure 6.4.10a to 6.4.12b through the aid of equation (5.2.21). The dimensionless entropy $NG(\epsilon)$ is elevated with outstanding values of the thermal radiation constant (Rn). Figure 6.4.10a constitutes proof for the development of entropy through the rising value of Rn. On this graph, it can be identified the approximated maximum establishment of entropy for $Rn = 2.25$, which is 59.42137 at $\epsilon = 0.24488$. The impact of Ec towards the generation of entropy is analogous to Rn. Physically, increasing Ec implies rising the nanofluids' kinetic energy, leading to a high rate of irreversibility in the system. Consequently, Ec develops the formation of entropy, which is exposed in Figure 6.4.10b. Figures 6.4.11a and 6.4.11b tell us, the existence of more energy loss due to the incremental values of Re and Br respectively. From this study, it is acquired an equivalent upshot with Aziz et al. (2021) and Loganathan et al. (2020) regarding the relation between Br and total non-dimensional entropy. Naturally, Brinkman number (Br) has an impact on the viscous materials towards heat and mass transfer. This produces a large amount of heat by growing the rate of irreversibility. Hence, the entropy is generated more by Br as we foresee in Figure 6.4.11b. Pr has also an impact on the formation entropy. Hence, Figure 6.4.12a indicates that, there is high formation of entropy by raising the values of Pr. Particularly, it is obtained the optimal formation of entropy when $Pr = 4.7$, which is approximated as $NG(1.4869567) = 51.9223$. On the reverse side, the velocity slip parameter (ϖ) subsides the formation of entropy as it is looked at Figure 6.4.12b which is equivalent with the result of Aziz et al. (2021). Thus, ϖ has a role in cooling down the temperature. This results in minimizing the generation of entropy in a system, as publicized on Figure 6.4.12b.

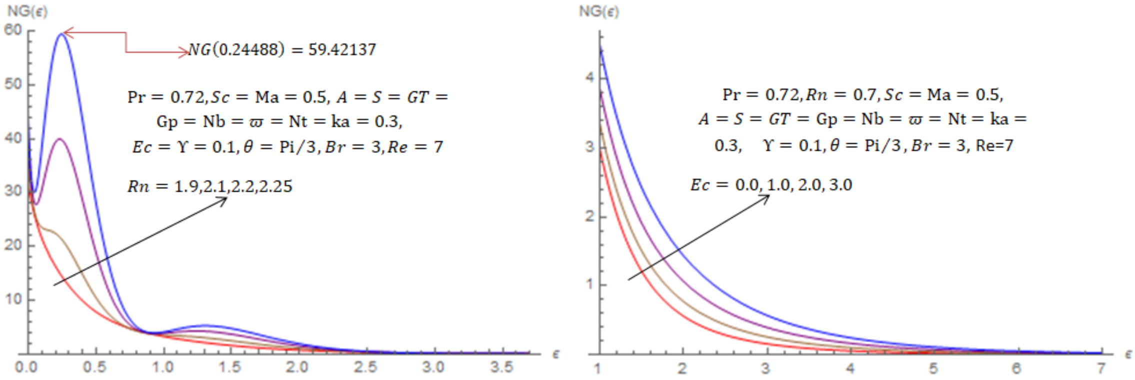

(a) The consequence of Rn on $NG(\epsilon)$ (b) The consequence of Ec on $NG(\epsilon)$

Figure 6.4.10: Impact of thermal radiation and Eckert number on entropy formation

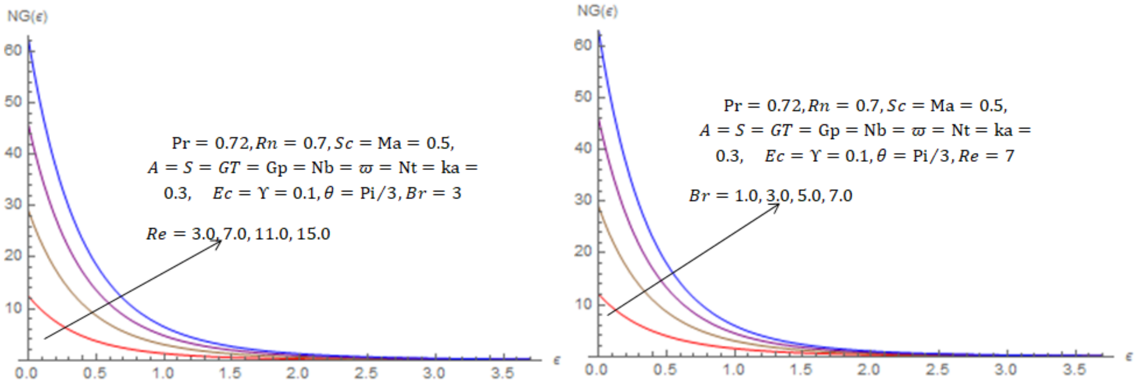

(a) The consequence of Re on $NG(\epsilon)$ (b) The consequence of Br on $NG(\epsilon)$

Figure 6.4.11: Consequences of Reynolds and Brinkman numbers on entropy formation

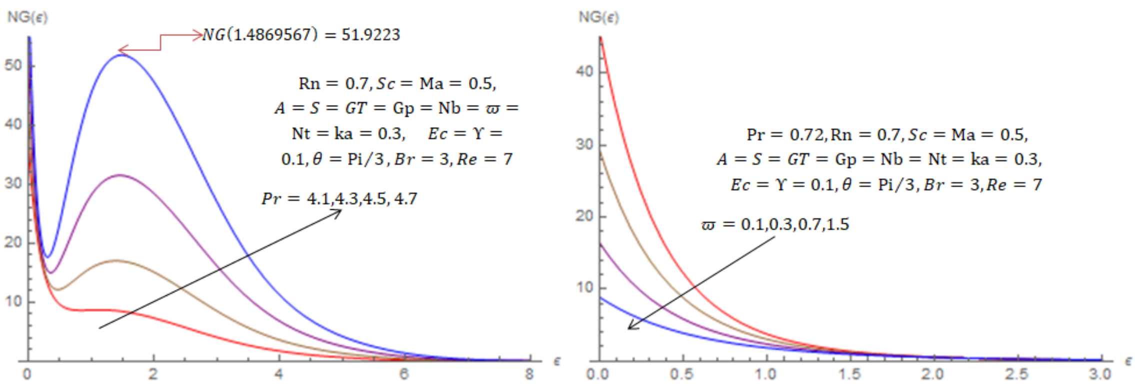

(a) The consequence of Pr on $NG(\epsilon)$ (b) The consequence of ϖ on $NG(\epsilon)$

Figure 6.4.12: Impact of Prandtl number and slip velocity on entropy formation

6.4.5 Physical Quantities

This portion assesses the outgrowth of possible factors on the local skin friction coefficient (Cf_x), Nusselt number (Nu_x) and Sherwood number (Sh_x) in terms of $V''(0)$, $-H'(0)$ and $-L'(0)$ respectively. Given that $Re_x = 1$, equations (6.2.10) implies $Cf_x = V''(0), Nu_x/(1+Rn) = -H'(0)$ and $Sh_x = -L'(0)$. Thus, the 3D surface plots are used to elaborate these physical quantity with respect to prominent parameters in terms of $V''(0)$, $-H'(0)$ and $-L'(0)$.

As the 3D plot 6.4.13a and 6.4.13b pointed out, the magnitude of local skin friction coefficient ($|Cf_x| = |V''(0)|$) decreases when the values of both Gt and Ec ascend while Ma and Sc descend. Physically, Gt and Ec have a tendency to set up the flow of nanofluids quickly, having less impact on impeding force. However, Ma and Sc retard the motion of nanofluids being that they discharge a high drag force. The effect of unsteadiness, A initiates the rate of heat transfer while ka limits it as exposed in Figure 6.4.14a. Diminishing the values of Ma and raising Gt improve the heat transfer rate as exhibited in Figure 6.4.14b. These imply that convective heat transfer exceeds conductive heat transfer at the boundary layer for parameters A and Gt but not for ka and Ma. The Sherwood and Nusselt numbers have similar result using Ma and Gt parameters. This is justified by looking Figures 6.4.14b and 6.4.15a. The Grashof number is inversely related to viscous formation, which increases the rate of mass transfer. Thus, decreasing Ma and increasing Gt, speed up the mass transfer rate as viewed in 3D surface plot in Figure 6.4.15a. Both Ec and S are initiated mass transfer rate as seen in Figure 6.4.15b. It follows that when the values of Ec, S and Gt escalate while Ma deescalates, the rate of convective mass transfer more than the rate of diffusive mass transport.

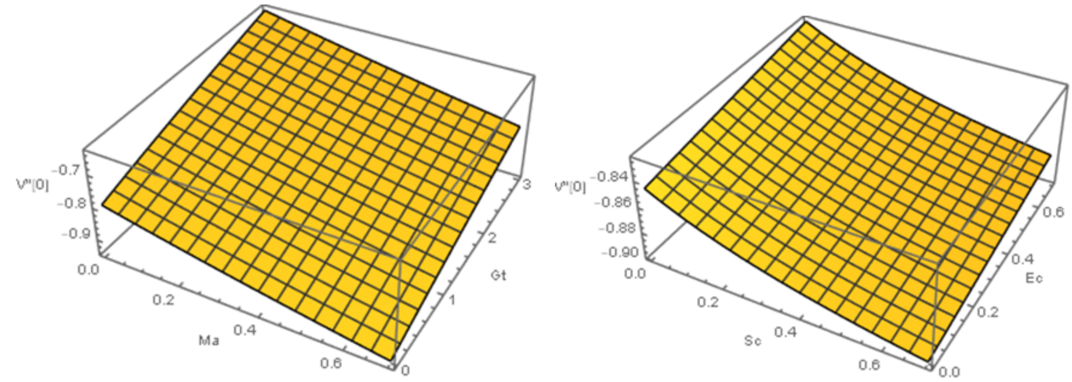

(a) Impactof Ma and Gt on $-V''(0)$ (b) Impact of Sc and Ec on $-V''(0)$

Figure 6.4.13: The consequences of Ma, Gt, Sc and Ec on local skin friction coefficient

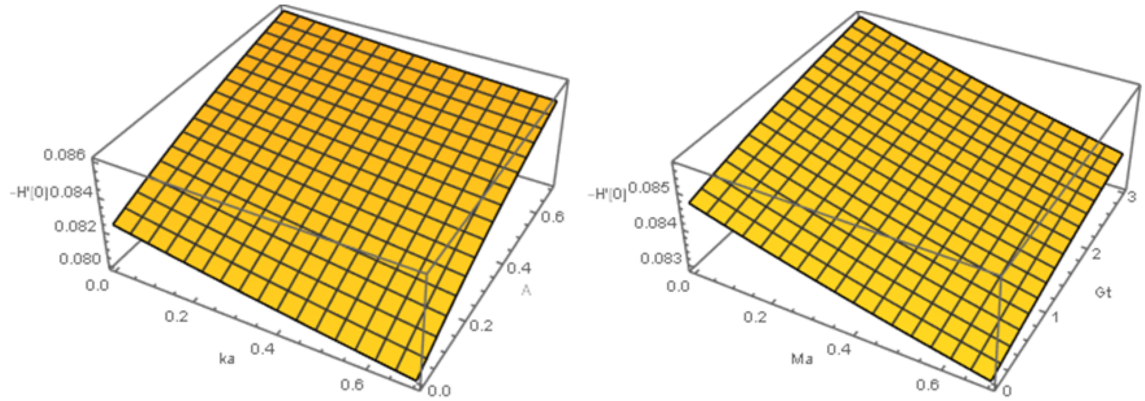

(a) Impact of ka and A on $-H'(0)$ (b) Impact of Ma and Gt on $-H'(0)$

Figure 6.4.14: The consequences of ka, A, Mg and Gt on heat transfer rate

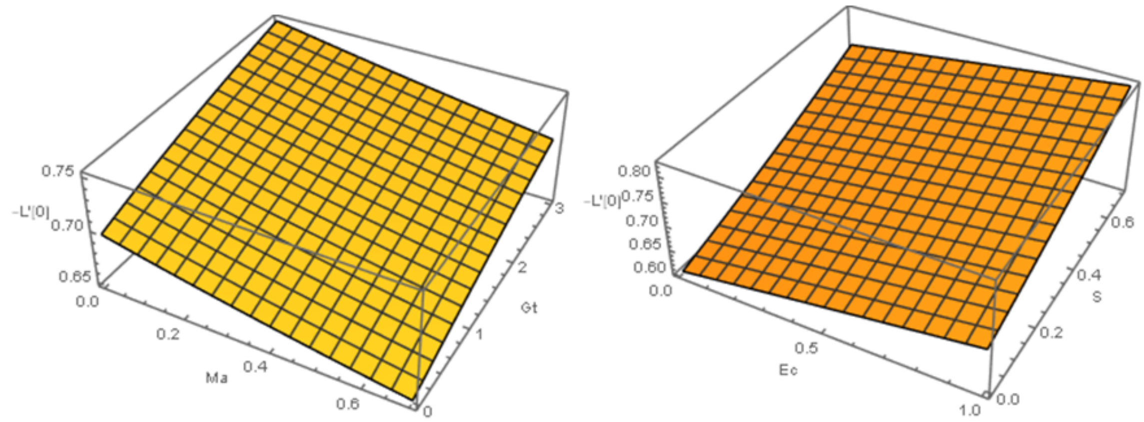

(a) Impact of Ma and Gt on $-L'(0)$ (b) Impact of Ec and S on $-L'(0)$

Figure 6.4.15: The consequences of Ma, Gt, Ec and S on mass transfer rate

6.5 Summary

In this problem, heat and mass transfer behaviors have been clarified for 2D incompressible, viscous nanofluids flowing unsteadily over an inclined stretchable permeable surface with the presence of Joule heating and solar thermal radiation. Here, the velocity slip, convective heat transfer and entropy generation are considered. The transformed set of non-linear ODEs from the governing PDEs have been solved by HAM implementing BVPh 2.0 package on Mathematica 12.1. The main findings are listed as follows:

- Nanofluid motion is retarded by S rise but it is moved rapidly for the increment of Gt, Gp, Ec and Nb.
- Rn, Ec and Υ increase the spread of temperature in the nanofluids. Conversely, it decreases whenever there is an enlargement of Gt, Gp, S and Pr.
- Nt is directly related to the concentration of nanofluids, whereas Gt, Gp, S and Sc are inversely proportional to the concentration profile.
- Entropy formation is intensified by increasing the values of Rn, Ec, Re, Br and Pr but not for ϖ.
- The drag forces reduces by the raise of Gt and Ec but not for Ma and S.
- Nu_x decreases for raising Ma and ka whereas enlarge with A and Gt.
- Sh_x increases for Gt, Ec and S while Ma reduces.

CHAPTER SEVEN

Convective Heat Transfer via Slip Moving Nanofluids through a Permeable Surface with Thermal Radiation and Entropy Generation

This chapter is an extension of Chapter SIX, in which it focuses on the convective heat transfer and velocity slip effect over an inclined permeable surface.

7.1 Introduction

Convective heat transfer is the process in which overheated particles migrate from one location to the next for transferring heat. It is the transmission of energy that is prompted by fluid wave. Numerous experts adopt convective heat transfer as one of the boundary conditions in their inquiries. For example on an expanding plate, Makinde and Aziz (2011); Azam et al. (2019); Shafiq et al. (2023) considered the convective heat transfer as a boundary condition. Based on their findings, temperature distribution is raised by the progressive values of convective heat transfer parameter.

Thermal radiation has a function in managing the heat transfer process and producing a tactical result having suitable features (Pandey et al., 2023). It is produced by the conversion of heat through the motion of charged particles (electron and proton) into an electromagnetic radiation. The heat transfer process takes place via fluids, even from the Sun radiation over absorbing surface (Alzahrani et al., 2021). However, nanofluid can improve the heat transport mechanism (Mukhopadhyay et al., 2022). It is applicable in various fields as stated by Zaib et al. (2015); Ahmmed et al. (2018), even in heat transfer from thermal radiation. For instance, Hussain et al. (2021) utilized nanofluid to improve the heat transfer from thermal radiation in the airplane fin.

Academicians such as Wang et al. (2023), Pasha et al. (2023) and Anjum et al. (2023) considered the Brownian motions and thermophoresis properties of nanoparticles where Buongiorno's model included, and it is used by many researchers which quoted in (Shahzad et al., 2022a; Hussain et al., 2023; Nasir et al., 2023).

In the flow of nanofluids, there is a situation where the borderline between solid and nanofluid is not smooth. Such boundary conditions expressed in terms of velocity slip (Mukhopadhyay, 2011). Hence, sundry researchers imagined the slip effect such as Li et al. (2016), Afzal and Aziz (2016) and Aziz et al. (2018). In heat transfer process, the presence of slip situations together with Joule and viscous dissipation have a significant impact (Hussain et al., 2022). Particularly, the presence of modicum viscous dissipation has an essential influence in the flow of fluid viscosity (Zaib et al., 2016). Numerous academics consider the inclined porous medium such as Ahmmed et al. (2018); Reddy and Sreedevi (2020); Rasel et al. (2022); Nandi et al. (2022).

Following the aforementioned survey, the issue of slip-flowing viscous nanofluid across an inclined permeable surface in the presence of thermal radiation, Joule heating and convective heat transfer with entropy has not yet been delved by employing the HAM. Thereby, the researchers intended to explore the heat and mass transfer of unsteady nanofluid slipping over an inclined porous media by considering the thermal radiation, Joule heating and entropy generation. Equations of flow, temperature and concentration are administered with mass suction, velocity slip and convective boundary conditions. Thus, the outcome of this problem displayed graphically using HAM by BVPh2.0 package on Mathematica 12.1.

7.2 Mathematical Model Formulation

The Cartesian coordinate system is assumed for the stretching inclined sheet at $t > 0$, and acquires non-uniform velocity, temperature and concentration on the surface wall similar to equation (5.2.1). The physical flow is given in Figure 7.2.1. Nanofluid has similar assumptions in chapter SIX in section 6.2.

7.2.1 Governing Equations

The governing equations have been expressed according to the conservation of mass, momentum, energy and concentration. Simplified PDEs of this problem taken from section 6.2.1 by focusing the angle of inclination, convective heat transfer and velocity slip. They are stated as follow.

$$\frac{\partial u_1}{\partial x} + \frac{\partial u_2}{\partial y} = 0 \tag{7.2.1}$$

$$\frac{Du_1}{Dt} = \nu \frac{\partial^2 u_1}{\partial y^2} - \left(\frac{\sigma_e B_0^2}{\rho(1-\varsigma t)} + \frac{\nu}{k_p} \right) u_1 + \Big(\beta_c(\bar{C} - \bar{C}_\infty) + \beta_t(\bar{T} - \bar{T}_\infty) \Big) g \sin\theta \tag{7.2.2}$$

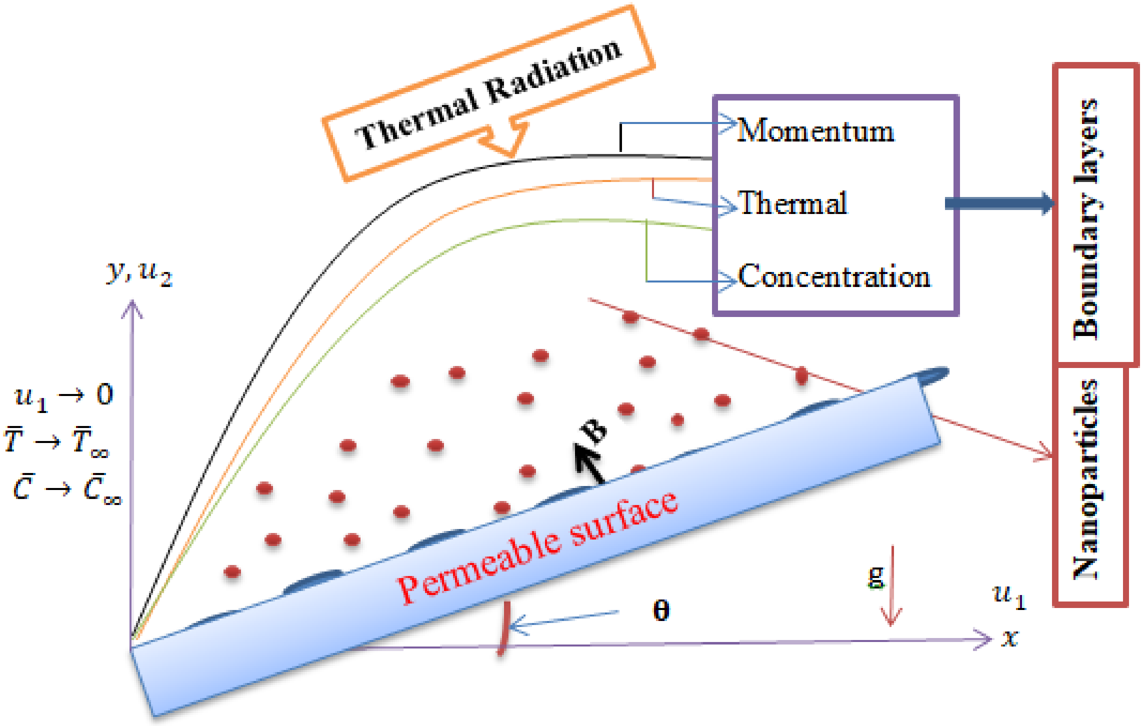

Figure 7.2.1: Physical set up for the flow pattern

$$\begin{aligned}\frac{D\bar{T}}{Dt} = &\left(\frac{\sigma_e B_0^2}{1-\varsigma t}+\frac{\mu}{k_p}\right)\frac{u_1^2}{\rho c_p}+\frac{\mu}{\rho c_p}(\frac{\partial u_1}{\partial y})^2+\frac{k}{\rho c_p}\left(1+\frac{16\bar{T}_\infty^3\sigma^*}{3k^*k}\right)\frac{\partial^2 \bar{T}}{\partial y^2}\\ &+\tau_h\frac{\partial \bar{T}}{\partial y}\left(D_B\frac{\partial \bar{C}}{\partial y}+\frac{D_T}{T_\infty}\frac{\partial \bar{T}}{\partial y}\right)\end{aligned} \tag{7.2.3}$$

$$\frac{D\bar{C}}{Dt} = D_B\frac{\partial^2 \bar{C}}{\partial y^2}+\frac{D_T}{T_\infty}\frac{\partial^2 \bar{T}}{\partial y^2} \tag{7.2.4}$$

The associated boundary conditions are formulated in the following manner (Kebede et al., 2020; Jamshed et al., 2021c).

$$\begin{cases}\text{For } y=0; & u_1-U_w=S_l\dfrac{\partial u_1}{\partial y}, u_2=V_w, k\dfrac{\partial \bar{T}}{\partial y}=H_f(\bar{T}-\bar{T}_w), \bar{C}=\bar{C}_w\\ y\to\infty; & u_1\to 0, \bar{T}\to\bar{T}_\infty, \bar{C}\to\bar{C}_\infty\end{cases} \tag{7.2.5}$$

To work out this problem, the PDEs (7.2.1), (7.2.2), (7.2.3) and (7.2.4) are transformed into a system of ODEs by fitting similarity transformation variables with stream function ψ and dimensionless independent variable ϵ. They are defined similar to equation (5.2.9). The non-dimensional forms of velocity components u_1 and u_2, temperature $\bar{T}$ and concentration $\bar{C}$ have been expressed in terms ψ and ϵ the same as equation (5.2.10). Due to the continuous stream function ψ, equation (7.2.1) isn well-balanced.

As well, PDEs (7.2.2), (7.2.3) and (7.2.4) are remodeled as follow.

$$V''' = (V' + Ma + ka)V' - GpL\sin\theta - GtH\sin\theta + A\left(V' + \frac{\epsilon}{2}V''\right) - VV'' \tag{7.2.6}$$

$$\begin{aligned}(1+Rn)H'' =& Pr\left(H(A+V') - Ec\,(Ma+ka)\,(V')^2 - Ec(V'')^2\right)\\ & - PrH'(-\frac{A\epsilon}{2} + NbL' + NtH' + V)\end{aligned} \tag{7.2.7}$$

$$L'' = Sc\left[L'(A\epsilon/2 - V) + L(A+V')\right] + \frac{Nt}{Nb}H'' \tag{7.2.8}$$

Here, prime $'$ pointed out the differentiation with respect to ϵ. In a similar step, the boundary conditions in equation (7.2.5) are re-formed as follows:

$$\begin{cases} V'(0) - \varpi V''(0) = L(0) = 1, H'(0) = \Upsilon(H(0)-1) \\ V(0) = S, V'(\epsilon) = H(\epsilon) = L(\epsilon) = 0 \text{ at } \epsilon \to \infty \end{cases} \tag{7.2.9}$$

In non-dimension process, the parameters are defined according to Table 5.2.1, $Gt = \frac{\beta_t \bar{T}_0 x(1-\varsigma t)g}{\nu \hat{b}}$ and $Gp = \frac{\beta_c \bar{C}_0 x(1-\varsigma t)g}{\nu \hat{b}}$ are thermal and mass Grashof number.

7.2.2 Physical Quantities

This section contains the three established physical quantities namely, local skin friction coefficient (Cf_x), local Nusselt number (Nu_x) and Sherwood number (Sh_x) toward an engineering standpoint. They are summarized based on equation (6.2.10) as follows:

$$\begin{aligned} &Cf_x = Re_x^{-0.5}V''(0) \implies V''(0) = Re_x^{0.5}Cf_x \\ &Nu_x = -Re_x^{0.5}\,[1+Rn]\,H'(0) \implies -H'(0) = \frac{Re_x^{-0.5}}{1+Rn}Nu_x \\ &Sh_x = -Re_x^{0.5}L'(0) \implies -L'(0) = Re_x^{-0.5}Sh_x. \end{aligned} \tag{7.2.10}$$

.

7.2.3 Expressing Entropy Generation

The irreversible process measured by entropy which is the stir of scheduled system (Loganathan et al., 2020). With the presence of energy loss, it is tough to exchange the total thermal radiation into heat and electric energy. So, in this study, researchers realized the formation of entropy by heat and mass transmission, fluid friction, Joule heating and porosity dissipation. Here of, the entropy formation rate per unit volume has been recast from Loganathan et al. (2020) and Nandi et al. (2022). Thus, the equation of E_{pr} and NG are similar to equations (5.2.20) and (5.2.21) in that order.

7.3 Homotopy Analysis Method (HAM)

Similar to section 6.3, this part put the highlight concept on the HAM regarding this specific problem. HAM is an analytic technique addressing the nonlinear higher-order systems of ODEs, boundary value problem type. Shi-Jun Liao set up the HAM in his Ph.D. dissertation (Liao, 1992). HAM's series solutions are nearer to the accurate one. As a result, many academicians adopt HAM, as cited in (Hayat et al., 2021; Loganathan et al., 2021; Saeed et al., 2022; Wang et al., 2023; Nasir et al., 2023). HAM has an interesting freedom to select linear operators $(\mathcal{L}_V, \mathcal{L}_H, \mathcal{L}_L)$, initial guesses $(V_0(\epsilon), H_0(\epsilon), L_0(\epsilon))$, auxiliary functions $(\mathcal{H}_V(\epsilon), \mathcal{H}_H(\epsilon), \mathcal{H}_L(\epsilon))$ and convergence control parameters $(\hbar_V, \hbar_H, \hbar_L)$ for getting an acceptable convergent solution. Thus, the complete character of this issue is brought in semi-analytical form by HAM's rule.

For this specific problem, the linear operators, initial guesses and auxiliary function are taken similar to equations (5.3.1), (5.3.2) and (5.3.3) respectively.

7.3.1 Zero$^{\text{th}}$ and m$^{\text{th}}$ order Deformation Equations

These are defined in a similar fashion with section 6.3.2.

Employing the inverse linear operator on both sides of m^{th} order deformation equations, a recurrence forms are obtained. As usual, the auxiliary linear operators, initial guesses and auxiliary functions are selected according to the previous procedures. However, $\hbar_V$, $\hbar_H$ and $\hbar_L$ are questionable. Once, these values are fixed, then at $p=1$ the following expressions represent the exact solution of this problem.

$$\begin{aligned}
V(\epsilon;1) &= V_0(\epsilon) + \sum_{m=1}^{\infty} V_m(\epsilon) = V(\epsilon),\\
H(\epsilon;1) &= H_0(\epsilon) + \sum_{m=1}^{\infty} H_m(\epsilon) = H(\epsilon),\\
L(\epsilon;1) &= L_0(\epsilon) + \sum_{m=1}^{\infty} L_m(\epsilon) = L(\epsilon).
\end{aligned} \tag{7.3.1}$$

Hence, equation (7.3.1) represents the exact solution to this problem. Practically, computing equation (7.3.1) is impossible due to having infinite term. So, it is necessary to truncate the series solution to have the minimum error. This is done by choosing the possible convergent control parameters that reduce the error in acceptable way on a limited order of approximation. Further, the solutions obtained in this way should be convergent. The next section explains the convergence of the solutions.

7.3.2 Exploring the Convergence of Solutions

Through HAM, there is an opportunity to prefer convergent control parameters to get convergence solutions. For this, Figure 7.3.1a is sketched by considering $\hbar_V = \hbar_H = \hbar_L = \hbar$ on horizontal axis, along with $V''(0), H'(0)$ and $L'(0)$ on vertical axis. There up on, for this issue, approximately $\hbar_V = -0.791679, \hbar_H = -1.324926$ and $\hbar_L = -1.149782$ are elected. As a result of these values, the inaccuracy decreases when the order of approximation (m) rolls up, as Figure 7.3.1b infers. Furthermore, the convergence of HAM is assured by tending the values of $-V''(0), -H'(0)$ and $-L'(0)$ toward a single value, for $Ma=0.5, Sc=1, Pr=0.72, Nt=Nb=S=\varpi=A=ka=Gt=Gp=0.3, Ec=\Upsilon=0.1, Rn=0.7$ and $\theta=\pi/6$ with residual error designated on Table 7.3.1. Moreover, the values $|V''(0)_{n+1}-V''(0)_n| \to 0, |H'(0)_{n+1}-H'(0)_n| \to 0$ and $|L'(0)_{n+1}-L'(0)_n| \to 0$, with number of values $n=1,2,...,9$ are the justification for obtaining a convergent solution (see on Figure 7.3.2a). The pictorial representation shown in Figures 7.3.2b, 7.3.3a and 7.3.3b for the value of $-V''(0)$, $-H'(0)$ and $-L'(0)$ against the number of values (n) in Table 7.3.1 are attest for the convergent solution. Therefore, HAM has a guaranteed convergent solutions for this specific problem.

Table 7.3.1: Order of approximation of HAM with residual error

n	m^{th} Order	$-V''(0)$	$-H'(0)$	$-L'(0)$	Residual Error $-V''(0)$	Residual Error $-H'(0)$	Residual Error $-L'(0)$
1	3	0.964628	0.0838811	1.047380			
2	6	0.960889	0.0829446	1.044210	7.41×10^{-8}	8.99×10^{-7}	2.70×10^{-7}
3	9	0.960594	0.0826672	1.044800			
4	12	0.960450	0.0825648	1.045010	2.02×10^{-9}	3.99×10^{-8}	2.93×10^{-9}
5	15	0.960400	0.0825218	1.045111			
6	18	0.960376	0.0825024	1.045150	1.12×10^{-10}	2.52×10^{-9}	1.76×10^{-10}
7	21	0.960365	0.0824932	1.045170			
8	24	0.960360	0.0824887	1.045180	8.59×10^{-12}	1.74×10^{-10}	8.16×10^{-12}
9	27	0.960357	0.0824864	1.045180			
10	30	0.960356	0.0824853	1.045180	6.47×10^{-13}	1.24×10^{-11}	4.30×10^{-13}

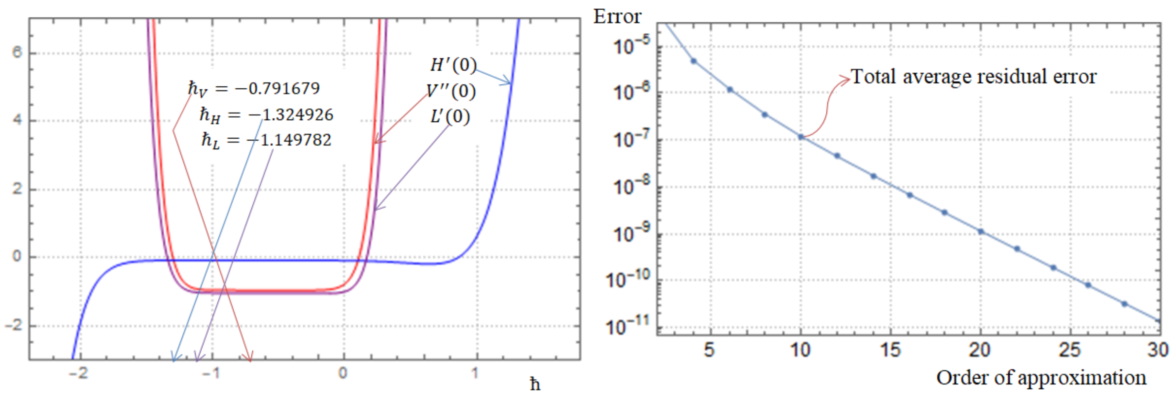

(a) $\hbar$-curves of $\hbar_V, \hbar_H$ and $\hbar_L$ (b) Total average residual error

Figure 7.3.1: $\hbar$-curves of the convergence control parameters and order approximation

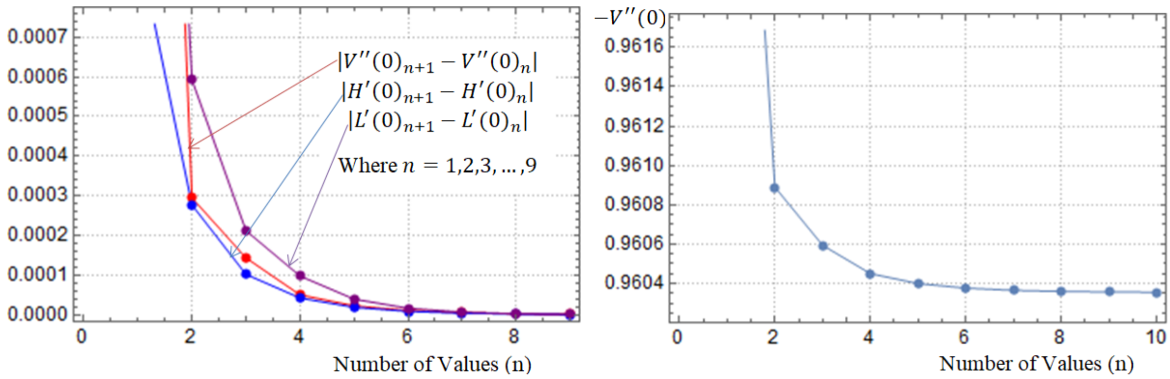

(a) Magnitude difference (b) Convergence of the values of $-V''(0)$

Figure 7.3.2: Differences in absolute value and convergence of the values of $-V''(0)$

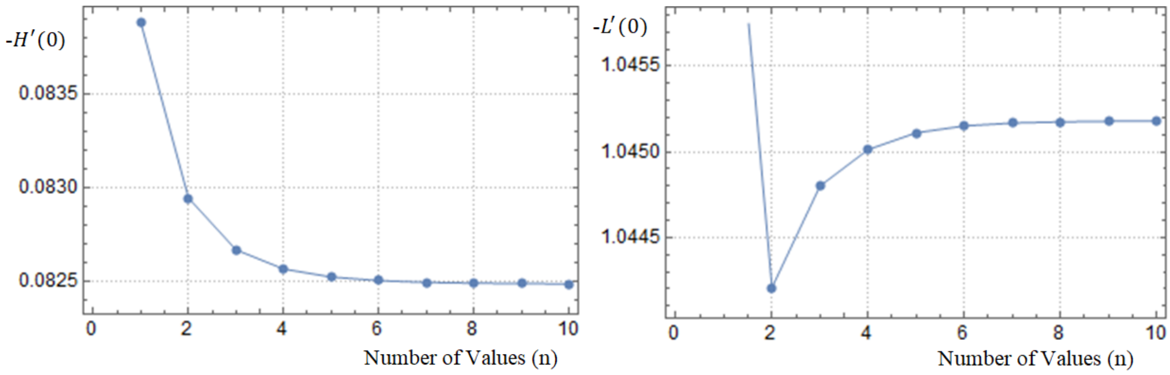

(a) Convergence of the values of $-H'(0)$ (b) Convergence of the values of $-L'(0)$

Figure 7.3.3: Convergence of the values of $-H'(0)$ and $-L'(0)$

7.4 Computed Result and Explanation

Non-linear higher order systems of ODEs (7.2.6 -7.2.8) with boundary conditions (7.2.9) have been solved for the nanofluid flow, temperature, concentration, entropy procreation, local skin friction coefficient, Nusselt and Sherwood numbers by realizing HAM. It is implemented on Mathematica 12.1 software with BVPh2.0 package developed by

Zhao and Liao (2014). This computation was asserted by comparing the values of $-V''(0)$ for distinct values of Ma and ϖ with various published articles (as seen in Table 7.4.1). Likewise, the comparison of $-H'(0)$ in Table 7.4.2, for a range of Pr values supports the validity of this method.

Table 7.4.1: $-V''(0)$ value at $\Upsilon \to \infty$, all parameters are zero except Ma, Pr and ϖ

Ma	ϖ	Ahmed et al. (2017)	Wang et al. (2023)	**Present result**
0.00	0.0	-	1.0000	1.000000
0.25	0.0	-	1.1180	1.118030
0.50	0.0	-	-	1.500000
0.00	0.5	0.591195	-	0.591195
0.00	1.0	0.430160	-	0.430160
0.00	3.0	-	-	0.214055
0.00	5.0	0.144842	-	0.144840
0.00	7.0	-	-	0.110050
0.00	10	0.081200	-	0.081242

Table 7.4.2: $-H'(0)$ value at $\Upsilon \to \infty$ and all other parameters are zero except Pr

Pr	Shahzad et al. (2022a)	Hussain et al. (2021)	**Present Result**
0.50	-	-	0.630978
0.72	0.80876181	0.8087618	0.808632
1.00	1.00000000	1.0000000	1.000000
1.50	-	-	1.284040
3.00	1.9235742	1.92357420	1.923682

7.4.1 Velocity Profile

From this problem, the role of parameters like angle of inclination (θ), mass Grashof number (Gp), the velocity slip (ϖ) and mass suction/injection (S) parameters on nanofluid motion have been exposed pictorially on Figures 7.4.1a and 7.4.2b. When θ runs anticlockwise from 0^0 to 90^0, the motion of nanofluid rapids as directed in Figure 7.4.1a as long as the sheet changes from horizontal to vertical gradually. Naturally, this shift speeds up the flow of nanofluid. In the same way, Figure 7.4.1b also enunciates the direct relation between $V'(\epsilon)$ and Gp. Dissimilar result obtained as ϖ rises according to Figure 7.4.2a. In fact, the velocity slip parameter initiates the formation of sliding friction between the nanofluid and the surface. This opposing force delays the motion of nanofluid. Similar to the parameter ϖ, there is an opposite relation between $V'(\epsilon)$ and S as Figure 7.4.2b manifested. The underlying root of this is that, the heated nanofluids are drawn toward the wall by mounting S. This engenders more viscosity which retards the flow of nanofluids. There up on, Figure 7.4.2b accredited that the motion of nanofluid is hindered by going up the value of S.

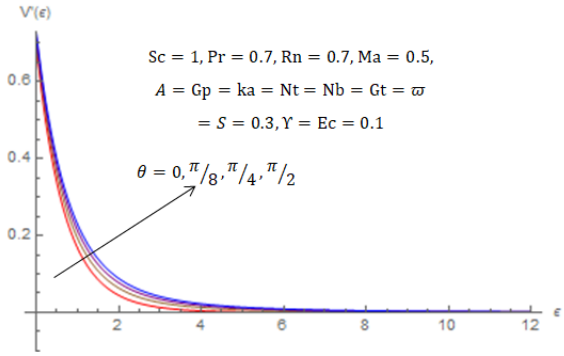

(a) Consequence of θ over $V'(\epsilon)$

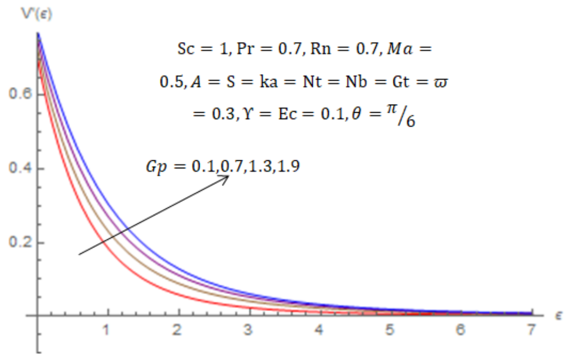

(b) Consequence of Gp over $V'(\epsilon)$

Figure 7.4.1: The impact of θ and Gp on velocity field

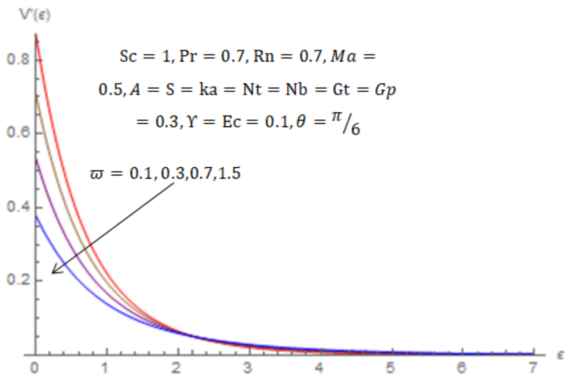

(a) Consequence of ϖ over $V'(\epsilon)$

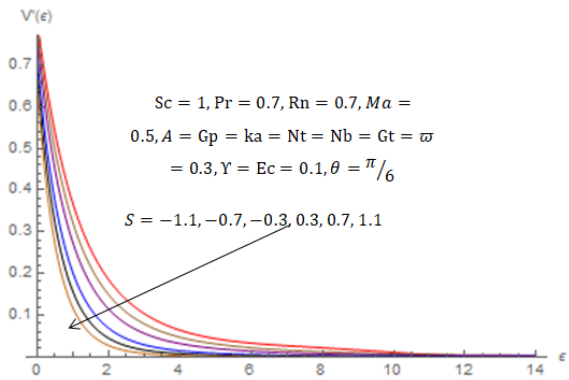

(b) Consequence of S over $V'(\epsilon)$

Figure 7.4.2: The impact of ϖ and S on velocity field

7.4.2 Temperature Profile

Figures from 7.4.3a to 7.4.6a set out the result of heat equation by exercising HAM with a brief discussion on the prominent emerging parameters such as $Gp, A, S, \Upsilon, Rn, Ec$ and Nb. The Gp has an impact in reducing the temperature distribution of the unsteady flowing nanofluid as proofed in Figure 7.4.3a. Likewise, the unsteadiness constant (A) and mass suction/injection (S) have a role in cooling the nanofluid's temperature, as observed in Figures 7.4.3b and 7.4.4a, respectively. Thus, immense values of Gp, A and S have been designated to reduce the thermal diffusivity which restricts the temperature distribution in the flowing nanofluid over a stretchable permeable surface.

Without doubt, ascending Υ is triggered the elevation of heat transmission coefficient where the dispersion of temperature in nanofluid flow expands more. This is publicized by Figure 7.4.4b. Physically, the Biot number resists more the internal heat transfer of nanofluid by conduction than convective at the surface which rises the temperature distribution. Thermal radiations deliver a high amount of heat when their radiative thermal energy emissions become higher. Henceforth, Figure 7.4.5a indicates that Rn heightened the temperature distribution in the flowing nanofluid. Similar to the other inquires, here the viscous dissipation has been described by Eckert number (Ec). Higher values of Ec increases the dispersal of temperature during the unsteady motion of nanofluid that has been shown by Figure 7.4.5b. In fact, Ec has a tendency to improve the kinetic energy, which elevates the nanofluid's temperature. Ascending the Brownian motion (Nb) of the nanoparticles yields more heat in the nanofluid due to the collision occur by random motion. As a result, raising the values of Nb brings more temperature in the nanofluid. This is assured by seeing the Figure 7.4.6a.

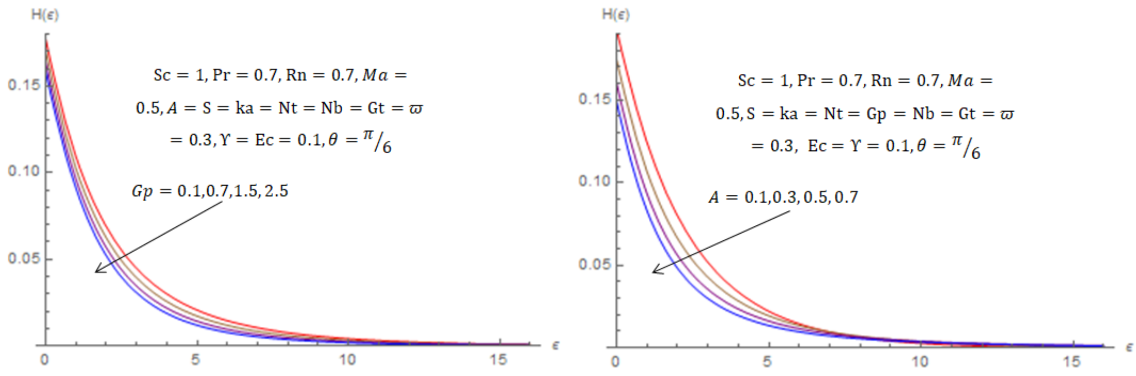

(a) Consequence of Gp over $H(\epsilon)$ (b) Consequence of A over $H(\epsilon)$

Figure 7.4.3: The impact of Gp and A on temperature field

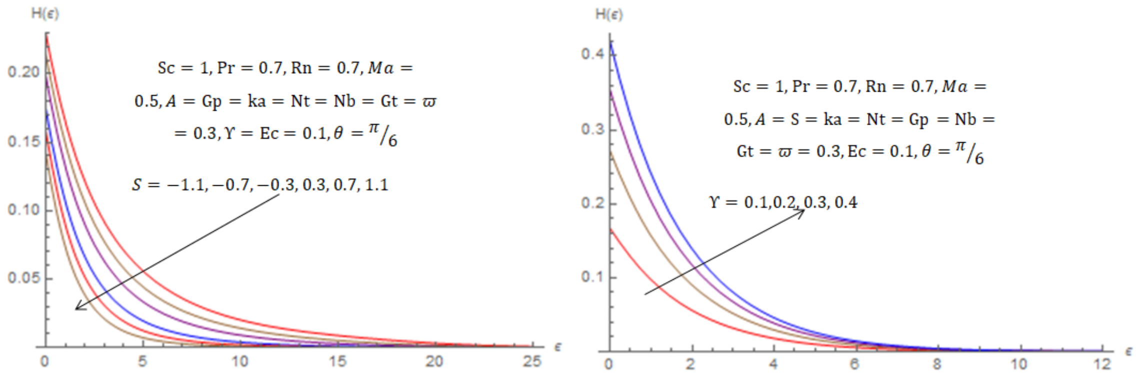

(a) Consequence of S over $H(\epsilon)$ (b) Consequence of Υ over $H(\epsilon)$

Figure 7.4.4: The impact of S and Υ on temperature field

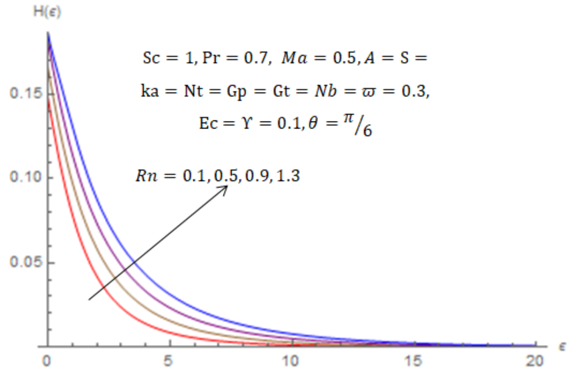

(a) Consequence of Rn over $H(\epsilon)$

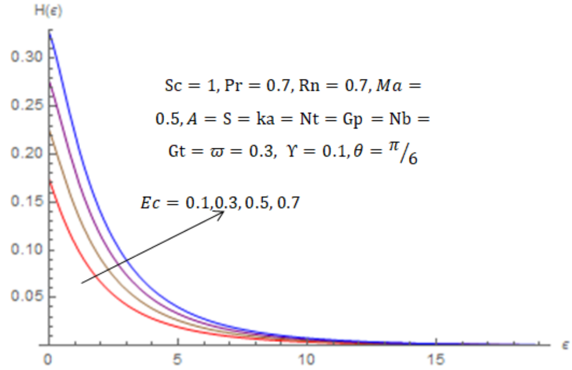

(b) Consequence of Ec over $H(\epsilon)$

Figure 7.4.5: The impact of Rn and Ec on temperature field

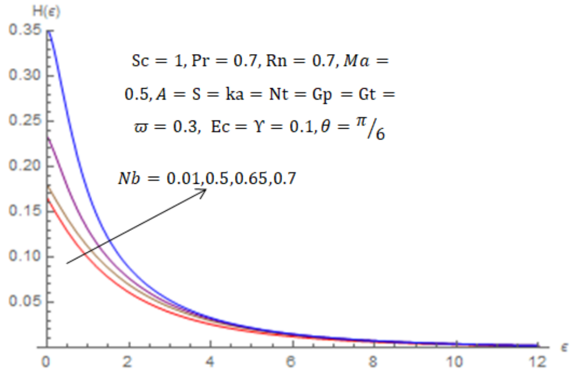

(a) Consequence of Nb over $H(\epsilon)$

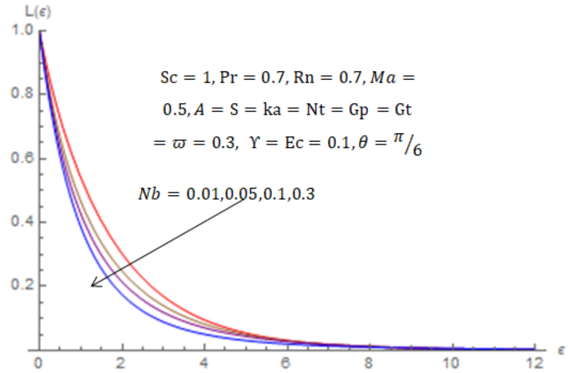

(b) Consequence of Nb over $L(\epsilon)$

Figure 7.4.6: The impact of Nb over temperature and concentration fields

7.4.3 Concentration Profile

The graphs from Figure 7.4.6b to 7.4.8b serve to highlight the relevance of prominent parameters, notably Nb, Sc, Nt, Υ, and ϖ on nanoparticles volume fraction. The random motion of micro sized solid particles produces low concentrations in the nanofluid. This declaration is supported by Figure 7.4.6b, where increasing the values of Nb reduces the concentrations of nanofluids. The roles of Sc on concentration and Pr on heat are similar. Thus, the existence of a reverse relation between Schmidt number and mass diffusivity implies that a larger Sc leads to lower the mass diffusivity. This is the root cause of dropping nanoparticles concentration in the base fluid. It is manifested by Figure 7.4.7a. As flaunted in Figure 7.4.7b, the concentration of nano-sized particles proliferates along with the values of Nt. Physically, the thermophoresis diffusion drives nanoparticles in base fluid with the help of temperature variation. This leads to rise the concentration of nanofluid. The parameters ϖ and Υ have also a tendency to increase the concentrations as seen in Figures 7.4.8a and 7.4.8b, respectively.

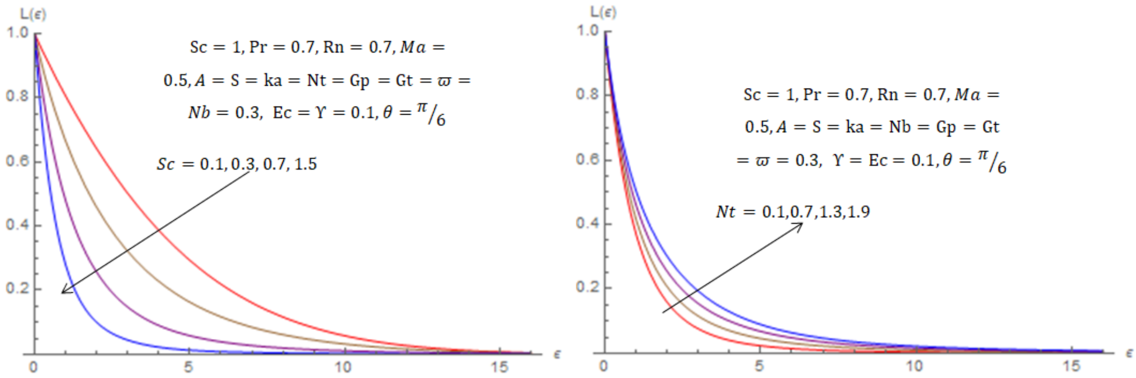

(a) Consequence of Sc over $L(\epsilon)$ (b) Consequence of Nt over $L(\epsilon)$

Figure 7.4.7: The impact of Sc and Nt on concentration field

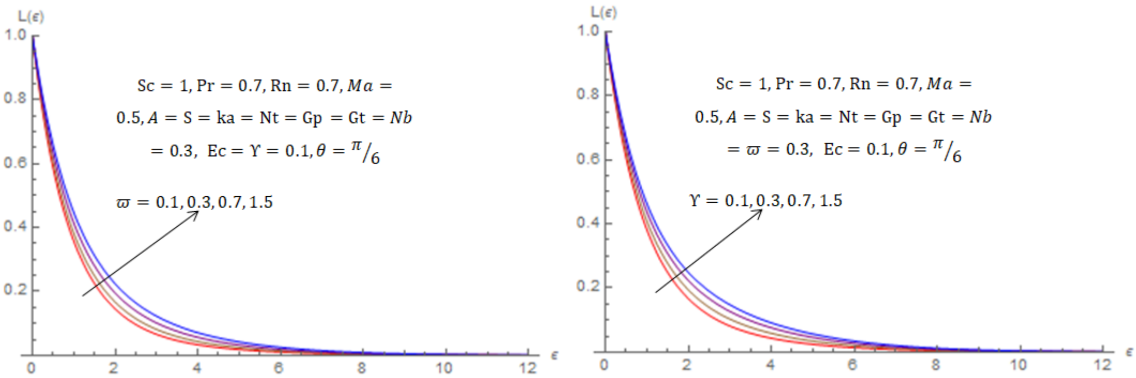

(a) Consequence of ϖ over $L(\epsilon)$ (b) Consequence of Υ over $L(\epsilon)$

Figure 7.4.8: The impact of ϖ and Υ over concentration field

7.4.4 Impact of Parameters on Entropy Generation

The second law of thermodynamics for heat transport helps to explain the entropy generation. Naturally, the energy loss is inevitable throughout the energy conversion process, although it can be mitigated by monitoring how distinct factors regulate the workflow. Accordingly, the influences of ϖ, Sc, Re and Br on $NG(\epsilon)$ are epitomized pictorially from Figure 7.4.9a to 7.4.10b, experiencing fixed values of $\Delta_3 = \Delta_2 = \Delta_1 = 1$. The parameter, ϖ descends the rate volumetric formation of entropy as it is publicized in the Figure 7.4.9a. Since, ϖ is lessened the heat transfer. However, Sc has a the tendency to increase the $NG(\epsilon)$ as it is observed in Figure 7.4.9b. Similarly, the global Reynolds number (Re) maximizes the formation of entropy near $\epsilon = 0$ while no influence for $\epsilon \to \infty$, as seen in Figure 7.4.10a. Brinkman number (Br) is assigned for the ratio of heat generation by viscous dissipation to heat transfer by molecular conduction. As Figure 7.4.10b illuminates, Br aids the entropy formation. Here, our findings on

Re, Br and ϖ are analogous to those of Shahzad et al. (2022a).

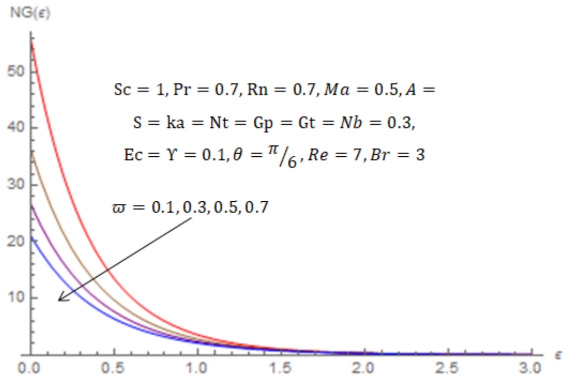

(a) Consequence of ϖ over $NG(\epsilon)$

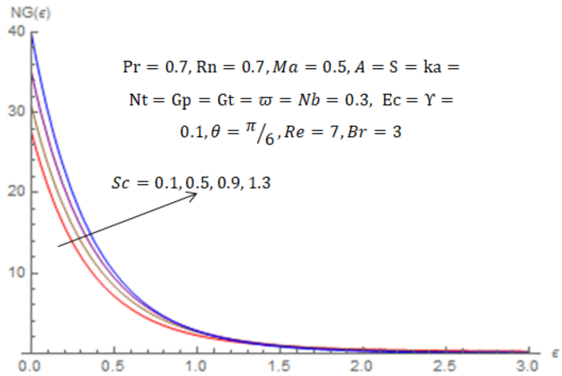

(b) Consequence of Sc over $NG(\epsilon)$

Figure 7.4.9: The impact of ϖ and Sc on entropy production

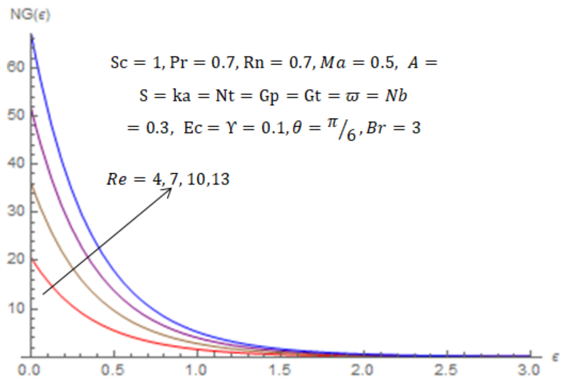

(a) Consequence of Re over $NG(\epsilon)$

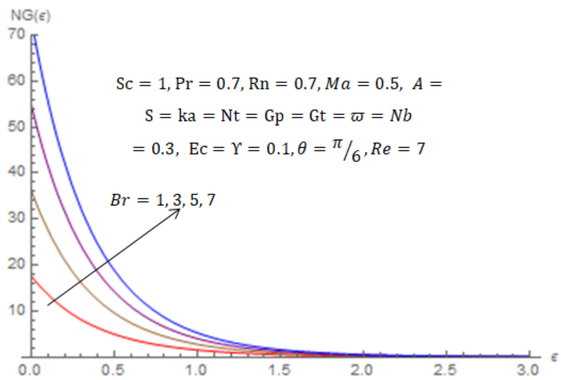

(b) Consequence of Br over $NG(\epsilon)$

Figure 7.4.10: The impact of Re and Br over entropy production

7.4.5 Physical Quantities

Under this part, the Cf_x, Nu_x and Sh_x are attempted based on an engineering viewpoint in terms of $V''(0) = Cf_x, -H'(0) = Nu_x/1.7$ and $-L'(0) = Sh_x$ according to equation (7.2.10) with $Re_x = 1$. The outcome of different parameters on these quantities are displayed using 3D surface plots, from Figure 7.4.11a to 7.4.13b. As the 3D plot 7.4.11a and 7.4.11b pointed out, the magnitude of Cf_x is increased for additional values of Ma and ka with decreasing the value θ. In fact, the incremental values of Ma and ka retard the flow of nanofluid where as θ quick up the speed of nanofluid. Based on the 3D surface plots 7.4.12a and 7.4.12b, $-H'(0$ is increased when lowering the values of ka and Ma as we go from horizontal to vertical in anticlockwise direction. This means, the rate of heat transfer is propagated by shifting the inclined sheet towards vertical. Thus, the heat transfer in conductive surpass convective for parameters

ka and Ma although θ has an opposite tendency. $-L'(0)$ is increased by shifting the inclined sheet to the vertical direction with decreasing Nt which divulged in the 3D plot 7.4.13a. Likewise, the 3D plot 7.4.13b pointed out decreasing Ma with rising θ, produces more Sh_x. Hence, appending the values of θ, quick up the mass transfer rate.

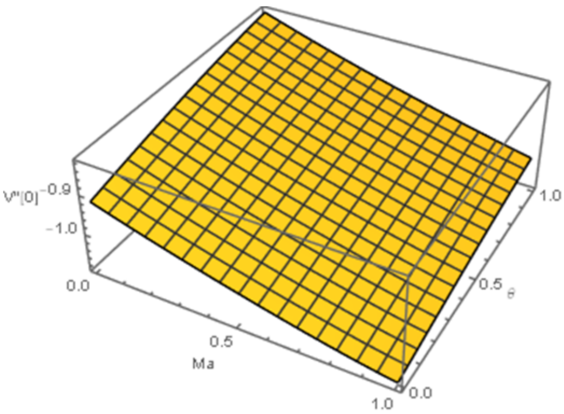

(a) Consequence of Ma and θ over Cf_x

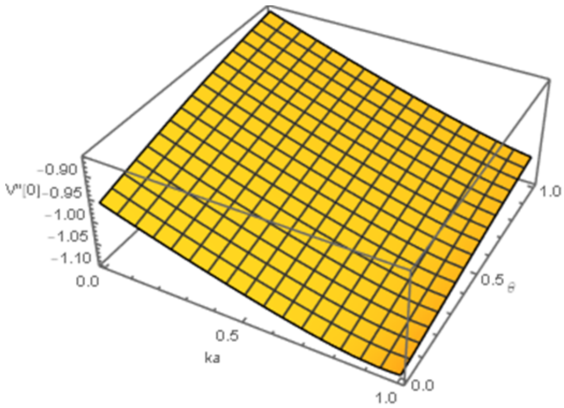

(b) Consequence of ka and θ over Cf_x

Figure 7.4.11: The impact of Ma, ka and θ on formation of drag force

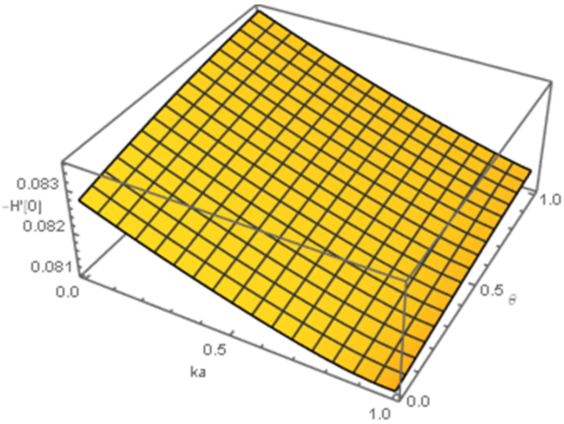

(a) Consequence of ka and θ over Nu_x

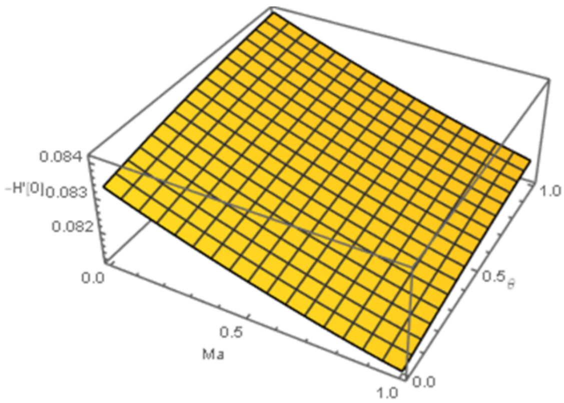

(b) Consequence of Ma and θ over Nu_x

Figure 7.4.12: The impact of Ma, ka and θ on the rate of heat transfer

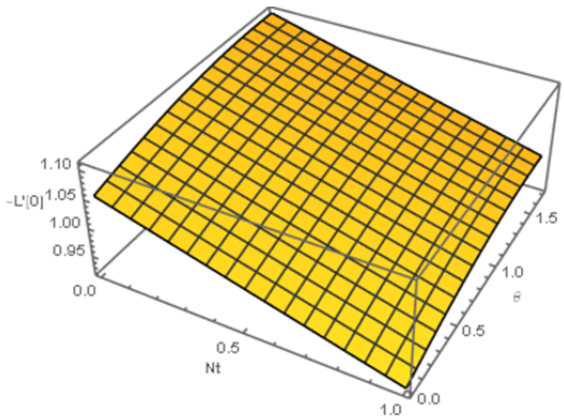

(a) Consequence of Nt and θ over Sh_x

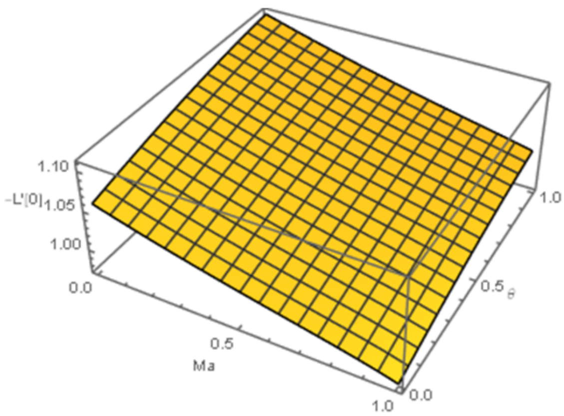

(b) Consequence of Ma and θ over Sh_x

Figure 7.4.13: The impact of Nt, Ma and θ on the rate of mass transfer

7.5 Summary

The heat and mass transfer features of 2D incompressible viscous nanofluid slip moving over an inclined expandable permeable surface with Joule heating and thermal radiation are expatiated in this chapter. HAM has been accomplished in Mathematica 12.1 to solve the obtained controlling equations. From these computations, the dominant findings are summarized as follows:

- θ and Gp speed up the transport of nanofluid. But, not as ascending as that of ϖ and S.
- The temperature of nanofluid expands more by enlarging Υ, Rn, Ec and Nb, and subtracting Gp, A and S.
- As Nt, ϖ and Υ rise, so does the nanofluid concentration, but not Nb and Sc.
- The entropy is magnified by higher values of Sc, Re and Br. Contrasting these, the rolling up of ϖ abates the formation unworkable energy.
- The frictional drag is accumulated more by amplifying ka, Ma, and minifying by θ. This statement bear out for slowing the flow of nanofluid.
- Nu_x is raised by lowering Ma and Ka as well as shifting θ from 0^0 to 90^0.
- Sh_x is maximized by gradual shifting θ from 0 to $\Pi/2$ and minimizing Nt, ka, Ma.

CHAPTER EIGHT

Heat and Mass Transfer within Unsteady Nanofluid Flow in the Presence of Sustained Solar Radiation

8.1 Introduction

The main cause of global warming and power shortages are human activities intended to accommodate their energy needs. Following this, plenty of scientists give attention to renewable energy sources, knowing that they fulfill the power requirements of many people around the world without introducing air pollution (Dincer, 2000; Lei et al., 2022; Al-Askaree and Al-Muhsen, 2023). Thereby, the most accessible, persistent, and peaceful source of renewable energy is solar, which can be transformed into electric and heat energy (Shehzad et al., 2016; Mukhtar and Gul, 2023). Solar radiation can be expressed by employing Beer's law formula for the sake of analyzing Dorsey's data (Fathalah and Elsayed, 1980; Ahmed et al., 2019). Precisely, the power from solar has a promising future as a sustainable application in various industries and domestics (Priyam and Chand, 2019).

Through the installation of solar collectors, sunlight has been trapped and processed into various forms of energy using working fluid. However, the poor performance attributes in thermal conductivity of convectional fluids can be fixed by supplanting the new technology named nanofluids (Mukhtar and Gul, 2023). Naturally, the stability of micro-sized particles improve the thermal conductivity, viscosity, and convective heat transfer. Thereby, nanofluids drastically boost the efficiency of a solar collectors due to containing nanoparticles. That is why, Hameed and Saha (2023) used nanofluid in solar power applications. The properties of nanofluids can be studied using the Tiwari and Das (2007) model. It is used for the analysis of heat transfer through nanofluid flow and implemented by different scholars, such as Dinarvand and Pop (2017); Aghamajidi et al. (2018); Asif Ali Shah et al. (2023).

Moreover, the porous medium with nanofluid, yields a high heat transformation due to the expansion of nanoparticles that enhance thermal conductivity (Siavashi et al., 2021). Particularly, the heat transfer from solar radiation can be maximized by a permeable solar collector surface since the incident solar radiation is absorbed more by a solid high permeable sheet. Noghrehabadi et al. (2013) explained the two drag forces that exist under the permeable surface in which the Darcy-Forchheimer model considered them in the non-linear form. Right now, a number of scientists adopt the Darcy-Forchheimer model, Charreh et al. (2023); Hameed and Saha (2023); Nagaraja et al. (2023). In the real world, the applications of nanofluid flow over a stretchable surface might not be handled adequately by a time-independent case. Mainly, the interaction of solar energy is time-dependent even with steady external conditions, which leads to irregular heat distribution (Mathie et al., 2014). Numerous scholars considered the unsteady flow, as quoted in (Hussanan et al., 2018; Sreedevi et al., 2020; Reddy and Reddy, 2022).

The authors' inspection points out that there is inadequate knowledge regarding the heat transfer from solar radiation through the unsteady flowing nanofluid over an inclined permeable expandable surface by integrating the Beer's law, Darcy-Forchheimer and Tiwari-Das models. As long as the writers are aware, such a problem still has not been worked out. Thereby, researchers analyze the properties of unsteady flowing nanofluids with respect to the heat transfer process in the presence of solar radiation using a single-phase model. Here, velocity and heat equations are solved by a numerical and semi-analytic approach used for verifying the approximated outcomes.

8.2 Mathematical Formulation

The following three points are the main differences between this problem and the previous four problems in chapters (FOUR, FIVE, SIX and SEVEN).

1. Considering Tiwari-Das model for analyzing the impact of nanofluid flow towards heat transfer, particularly from solar radiation that is expressed by Beer's law.

2. Darcy-Forchheimer model is used for the impact of permeable surface.

3. The problem is solved by using both numerical method (bvp4c on MATLAB) and semi-analytic technique (HAM on Mathematica 12.1 software).

Thus, at $t > 0$, the Cartesian coordinate system is assumed for a sliding slanted surface encompassing non-uniform velocity and temperature at the wall as:

$$V_w = \frac{V_o}{1-\varsigma t},\ U_w = \frac{\hat{b}x}{1-\varsigma t},\ \bar{T}_w = \bar{T}_\infty + \frac{\bar{T}_0 \bar{c} x}{\nu(1-\varsigma t)}, \tag{8.2.1}$$

where V_o is constant velocity value and the other symbols have similar meaning with previous chapters. The physical flow path is displayed in Figure 8.2.1.

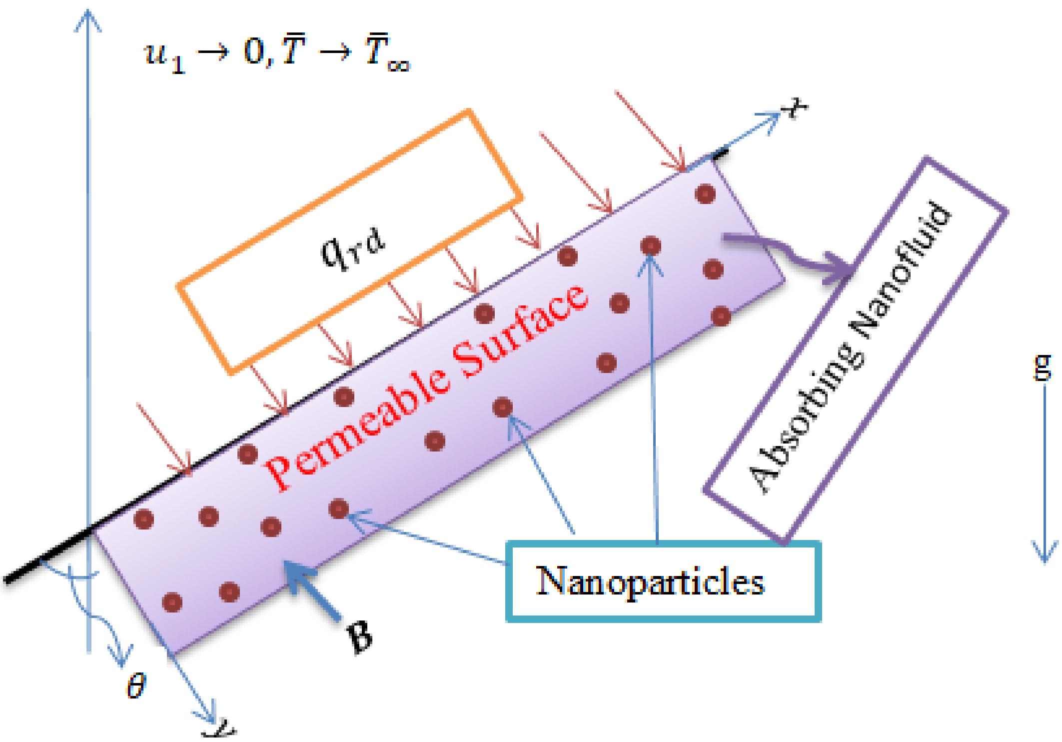

Figure 8.2.1: The physical description of the problem

8.2.1 Governing Equations

The basic equations for this problem are derived from mass, momentum and energy conservation by considering a magnetic field perpendicular to a stretchable surface. The governing equations are considered from section 6.2.1 with out the impact of nanoparticles flux. Moreover, taking the Darcy-Forchheimer law from equation (1.1.7), the gradient pressure can be simplified by boundary layer approximations as follows:

$$\nabla P = -\frac{\mu \mathbf{V}}{k_p} - \frac{F_d}{\sqrt{k_p}}\rho_l|\mathbf{V}|\mathbf{V} \implies (\frac{\partial P}{\partial x}, \frac{\partial P}{\partial y}) = -\frac{\mu}{k_p}(u_1, u_2) - \frac{F_d}{\sqrt{k_p}}\rho_l\sqrt{u_1^2 + u_2^2}(u_1, u_2)$$
$$\implies \frac{\partial P}{\partial x} = -\frac{\mu}{k_p}u_1 - \frac{F_d}{\sqrt{k_p}}\rho_l u_1^2$$

The energy equation considered only the incident radiation flux. Then, the following PDEs are obtained (Chamkha et al., 2002; Dehsara et al., 2014).

$$\frac{\partial u_1}{\partial x} + \frac{\partial u_2}{\partial y} = 0 \tag{8.2.2}$$

$$
\begin{aligned}
\frac{\partial u_1}{\partial t}+u_1\frac{\partial u_1}{\partial x}+u_2\frac{\partial u_1}{\partial y}=&\nu_n\frac{\partial^2 u_1}{\partial y^2}+\frac{(\beta_t\rho)_n}{\rho_n}(\bar{T}-\bar{T}_\infty)g\cos\theta\\
&-\frac{\sigma_n B_0^2 u_1}{\rho_n(1-\varsigma t)}-\frac{\nu_n u_1}{k_p}-\frac{F_d u_1^2}{\sqrt{k_p}}
\end{aligned}
\tag{8.2.3}
$$

$$
\frac{\partial \bar{T}}{\partial t}+u_1\frac{\partial \bar{T}}{\partial x}+u_2\frac{\partial \bar{T}}{\partial y}=\alpha_n\frac{\partial^2 \bar{T}}{\partial y^2}+\frac{1}{(c_p\rho)_n}\left(\mu_n(\frac{\partial u_1}{\partial y})^2+\frac{\partial q_{rd}}{\partial y}\right)
\tag{8.2.4}
$$

The boundary conditions are convective heat transfer and mass suction/injection.

$$
\begin{cases}
\text{At } y=0;\ u_1=U_w=\dfrac{\hat{b}x}{1-\varsigma t},\ u_2=V_w,\ k\dfrac{\partial \bar{T}}{\partial y}=H_f(\bar{T}-\bar{T}_w),\\
\text{and as } y\to\infty;\ u_1\to 0,\quad \bar{T}\to\bar{T}_\infty
\end{cases}
\tag{8.2.5}
$$

In accordance with Fathalah and Elsayed (1980) and Chamkha (1997), the investigators execute Beer's law for solar radiation term in heat equation (8.2.4) rather than the Rosseland approximation. Since Beer's law considers the ability of fluid to absorb solar radiation. In addition, Dorsey's data incorporated the Beer's law for the absorption of radiation in water layers of different thicknesses. This is expressed as follows:

$$
q_{rd}=q_{ir}(1-e^{-\tilde{a}y}),\ \text{and}\ \frac{\partial q_r}{\partial y}=q_{ir}\tilde{a}e^{-\tilde{a}y}.
\tag{8.2.6}
$$

In equation (8.2.6), q_{ir} and $\tilde{a}$ are the incident radiation flux and the fluid absorption coefficient in which both are fixed. Thus, equation (8.2.4) rewritten as follows.

$$
\frac{\partial \bar{T}}{\partial t}+u_1\frac{\partial \bar{T}}{\partial x}+u_2\frac{\partial \bar{T}}{\partial y}=\alpha_n\frac{\partial^2 \bar{T}}{\partial y^2}+\frac{1}{(c_p\rho)_n}\left(\mu_n(\frac{\partial u_1}{\partial y})^2+q_{ir}\tilde{a}e^{-\tilde{a}y}\right)
\tag{8.2.7}
$$

The thermophysical characters of nanofluid can be summarized in Table 8.2.1. Here, the subscript n, s and l represent nanofluid, nanoparticle and base fluids respectively.

To work out this problem, the PDEs (8.2.2, 8.2.3, 8.2.7) have been redefined into systems of non-linear higher order ODEs. This is done by using suitable similarity transformation variables in terms of stream function ψ and dimensionless independent variable ϵ. They are defined based on Dehsara et al. (2014) where $m=1$.

$$
\epsilon=y\sqrt{\frac{\hat{b}}{\nu(1-\varsigma t)}},\ \psi(x,y,t)=\sqrt{\frac{\hat{b}\nu}{1-\varsigma t}}xV(\epsilon)
\tag{8.2.8}
$$

Upon (8.2.8), the non-dimensional forms of velocity components u_1 and u_2, and tem-

Table 8.2.1: Thermophysical characters of nanofluids from Ahmed et al. (2019), Jamshed et al. (2021b) and Alkathiri et al. (2022)

Dynamic viscousity	$\mu_n = \frac{\mu_l}{(1-\phi)^{2.5}} \implies \frac{\mu_l}{\mu_n} = (1-\phi)^{2.5} = p_1$
Density	$\rho_n = \phi\rho_s + (1-\phi)\rho_l \implies \frac{\rho_n}{\rho_l} = 1-\phi+\frac{\rho_s}{\rho_l}\phi = p_2$
Electrical conductivity	$\sigma_n = \sigma_l\left[1+\frac{3\left(\frac{\sigma_s}{\sigma_l}-1\right)\phi}{\left(\frac{\sigma_s}{\sigma_l}+2\right)-\left(\frac{\sigma_s}{\sigma_l}-1\right)\phi}\right] \implies$ $\frac{\sigma_n}{\sigma_l} = \left[1+\frac{3\left(\frac{\sigma_s}{\sigma_l}-1\right)\phi}{\left(\frac{\sigma_s}{\sigma_l}+2\right)-\left(\frac{\sigma_s}{\sigma_l}-1\right)\phi}\right] = p_3$
Thermal diffusivity	$\alpha_n = \frac{k_n}{(c_p\rho)_n}$
Thermal Conductivity	$k_n = k_l\left(\frac{k_s+2k_l-2\phi(k_l-k_s)}{k_s+2k_l+\phi(k_l-k_s)}\right) \implies$ $\frac{k_n}{k_l} = \left(\frac{k_s+2k_l-2\phi(k_l-k_s)}{k_s+2k_l+\phi(k_l-k_s)}\right) = p_4$
Heat capacity	$(c_p\rho)_n = \phi(c_p\rho)_s + (1-\phi)(c_p\rho)_l \implies$ $\frac{(c_p\rho)_n}{(c_p\rho)_l} = 1-(1-\frac{(c_p\rho)_s}{(c_p\rho)_l})\phi = p_5$
Thermal expansion	$(\beta_t\rho)_n = \phi(\beta_t\rho)_s + (1-\phi)(\beta_t\rho)_l \implies$ $\frac{(\beta_t\rho)_n}{(\beta_t\rho)_l} = 1-(1-\frac{(\beta_t\rho)_s}{(\beta_t\rho)_l})\phi = p_6$

perature $\bar{T}$ have been expressed in the next formulas.

$$u_1 = \frac{\hat{b}x}{1-\varsigma t}\frac{\partial V}{\partial \epsilon},\ u_2 = -\sqrt{\frac{\hat{b}\nu}{1-\varsigma t}}V(\epsilon) \text{ and } \bar{T} = H(\epsilon)(\bar{T}_w - \bar{T}_\infty) + \bar{T}_\infty \tag{8.2.9}$$

Then, using equation (8.2.1) and (8.2.9), the PDEs are converted into ODEs based on the procedures in equations (4.2.13-4.2.16). Hence, equation (8.2.2) is balanced by the continuous stream function ψ. Then, (8.2.3) and (8.2.7) are redesigned as follows.

$$\begin{aligned} &V''' + p_1p_2\left[(V - A\frac{\epsilon}{2})V'' - ((F_h+1)V' + A)V'\right] + p_1p_6GtH\cos\theta \\ &- (Map_1p_3 + ka)V' = 0 \end{aligned} \tag{8.2.10}$$

$$H'' + \frac{p_5Pr}{p_4}\left(VH' - HV' - AH - \frac{A\epsilon}{2}H'\right) + \frac{Pr}{p_4}S_oe^{-\Gamma\epsilon} + \frac{PrEc}{p_1p_4}(V'')^2 = 0 \tag{8.2.11}$$

Here, prime ($\prime$) denotes the differentiation with regard to ϵ. Correspondingly, boundary conditions (8.2.5) are adjusted according to (4.2.18), thereby:

$$V'(0) = 1, H'(0) = \Upsilon(H(0)-1),\ V(0) = S, V'(\epsilon) = H(\xi) = 0 \text{ at } \epsilon \to \infty \tag{8.2.12}$$

The consequent constants in the non-dimension procedure are taken from Table 5.2.1, $Gt = \dfrac{\beta_t \bar{T}_0 x(1-\varsigma t)g}{\nu \hat{b}} \to$ thermal Grashof number; $Fh = \dfrac{F_d x}{\sqrt{k_p}} = \dfrac{F_d}{Da}$, $Da = \dfrac{\sqrt{k_p}}{x} \to$ Darcy number; $S_o = \dfrac{q_{ir}\tilde{a}(1-\varsigma t)}{\hat{b}(\bar{T}_w - \bar{T}_\infty)(c_p\rho)_l} \to$ incident solar radiation parameter, $\Gamma = \tilde{a}\sqrt{\dfrac{\nu(1-\varsigma t)}{\hat{b}}}$ $\to$ absorption constant of nanofluid, and $p_i, i = 1,2,3,4,5,6$ are stated in Table 8.2.1.

8.2.2 Nanofluid Thermophysical Values

The following information is used about the thermophysical values of liquids and nanoparticles that form the nanofluid for this problem to probe the heat transfer in the presence of solar radiation (see Table 8.2.2). Two distinct kinds of liquids have been selected for comparison: water (H_2O) and propylene glycol ($C_3H_8O_2$). Like water, propylene glycol is colorless and nearly odorless. Further, it has also weakly sweet taste. At the end, formation of drag force and rate of heat transfer ae compared between these two kinds of conventional fluids to construct nanofluid.

Table 8.2.2: Thermophysical properties of two host fluids and nanoparticles from Ahmed et al. (2019) and Mukhtar and Gul (2023)

Material	ρ in Kg/m^3	c_p in J/KgK	k in W/mK	σ in s^3A^2/kgm	β_t in K^{-1}
H_2O	997.1	4179	0.613	0.05	21×10^{-5}
$C_3H_8O_2$	5060	4338	34.5	5.0×10^5	62×10^{-5}
Cu	8933	385	400	5.96×10^7	1.67×10^{-5}

8.2.3 Concerned Physical Quantities

With respect to an engineering viewpoint, the two physical quantities: the local skin friction coefficient (Cf_x) and Nusselt number (Nu_x) are explored in this subsection.

- The coefficient of Local skin friction (Cf_x) can be expressed as :

$$Cf_x = \frac{\mu_n \left(\dfrac{\partial u_1}{\partial y}\right)_{y=0}}{\rho_l U_w^2} = \frac{1}{p_1 Re_x^{0.5}} V''(0) \implies V''(0) = p_1 Re_x^{0.5} Cf_x \tag{8.2.13}$$

- Nu_x controls the rate of heat transfer and expressed Dehsara et al. (2014):

$$
\begin{aligned}
Nu_x = -\frac{xk_n\left(\frac{\partial \bar{T}}{\partial y}\right)_{y=0}}{k_l(\bar{T}-\bar{T}_\infty)} = -xp_4H'(0)\sqrt{\frac{\hat{b}}{\nu(1-\varsigma t)}} = \\
-p_4H'(0)\sqrt{\frac{\hat{b}x^2}{\nu(1-\varsigma t)}} \implies -H'(0) = Re_x^{-0.5}Nu_x/p_4
\end{aligned}
\tag{8.2.14}
$$

8.3 Method of Solution

This problem is handled in terms of a numerical method by implementing bvp4c code on Matlab software and a semi-analytic approach called the Homotopy Analysis Method (HAM). Both methods have been carried out to this particular boundary value problem type for the sake of comparing our findings from both side perspectives.

8.3.1 Numerical Approach

In this numerical technique, the set of coupled non-linear higher-order ODEs (8.2.10 and 8.2.11) with boundary conditions (8.2.12) are converted in a system of first order ODEs, boundary value problem types. In order to accomplish this, the new functions are established. These are $V = Y_1, V' = Y_2, V'' = Y_3, V''' = Y_3', H = Y_4, H' = Y_5$ and $H'' = Y_5'$. Then, a system of the first order ODEs is developed as follows.

$$
\begin{cases}
Y_1' = Y_2 \\
Y_2' = Y_3 \\
Y_3' = -p_1p_2\left[(Y_1 - A\frac{\epsilon}{2})Y_3 - ((F_h+1)Y_2 + A)Y_2\right] - p_1p_6GtY_4\cos\alpha + (Map_1p_3 + ka)Y_2 \\
Y_4' = Y_5 \\
Y_5' = -\frac{p_5Pr}{p_4}\left(Y_1Y_5 - Y_4Y_2 - AY_4 - \frac{A\epsilon}{2}Y_5\right) - \frac{Pr}{p_4}S_oe^{-\Gamma\epsilon} - \frac{PrEc}{p_1p_4}(Y_3)^2
\end{cases}
\tag{8.3.1}
$$

The boundary conditions are expressed in the following manner.

$$
Y_1(0) = S, Y_2(0) = 1, Y_5(0) = \Upsilon(Y_4(0)-1), Y_2(\epsilon) = Y_4(\epsilon) = 0 \text{ at } \epsilon \to \infty \tag{8.3.2}
$$

Afterward, MATLAB's built-in code, bvp4c, has been put into practice. The basic idea behind the code bvp4c, is a finite difference that employs the 3-stage Lobatto

IIIa formula with fourth-order accuracy (Chu et al., 2021). It uses the first derivative continuous polynomial for the collocation formula, and error can be controlled by the concept of residual. In general, it is one of the methods used to solve non linear higher order ODEs by discretizing the domain into different points. Thus, a number of academicians adopt it, including Khan et al. (2022c) and Alqahtani et al. (2023).

8.3.2 Homotopy Analysis Method (HAM)

To the contrary of the numerical method, HAM eliminates the necessity for domain discretization. The HAM's series solutions are at any point in the domain. This implies that the obtained result using HAM is continuous, not at a discrete point. Consequently, HAM is implemented by a number of academicians (see Dinarvand et al. (2016); Dinarvand and Pop (2017); Rehman et al. (2022a)). It has a freedom to prefer linear operators $(\mathcal{L}_V, \mathcal{L}_H)$, initial guesses $(V_0(\epsilon), H_0(\epsilon))$, auxiliary function $(\mathcal{H}_V(\epsilon), \mathcal{H}_H(\epsilon))$ and convergence control parameters $(\hbar_V, \hbar_H)$ to get an acceptable convergent solutions. Similar to the previous problems, here the linear operators, initial guesses and auxiliary functions are selected as follows:

- The suitable linear operators are from Hayat et al. (2016b); Khan et al. (2022d)

$$\mathcal{L}_V = V''' - V', \text{ and } \mathcal{L}_H = H'' - H \tag{8.3.3}$$

  $\mathcal{L}$ satisfy the relations $\mathcal{L}_V(C_1 + C_2 e^{\epsilon} + C_3 e^{-\epsilon}) = 0$, and $\mathcal{L}_H(C_4 e^{\epsilon} + C_5 e^{-\epsilon}) = 0$.

- The starting approximations, that meet the boundary (Hayat et al., 2016b).

$$V_0(\epsilon) = 1 - e^{-\epsilon} + S, \text{ and } H_0(\xi) = \frac{\Upsilon e^{-\epsilon}}{1+\Upsilon} \tag{8.3.4}$$

- Taking constant auxiliary function for dimensionless velocity and temperature as

$$\mathcal{H}_V(\epsilon) = \mathcal{H}_H(\epsilon) = 1 \tag{8.3.5}$$

8.3.3 Exploring the Convergence of HAM and Validity

It is well known that divergent solutions have no tangible meaning. Consequently, HAM allows for selecting the right convergent control parameters, which play a key role in obtaining convergent solutions. In connection with this, the h-curves in Figure 8.3.1a has been attained through putting $\hbar_V = \hbar_H = \hbar$ on horizontal axes, alongside $V''(0)$ and $H'(0)$ on vertical axes. Then, according to Van Gorder (2014), $\hbar_V = -0.70139847$ and $\hbar_H = -1.76962216$ have been choosen. By using these values of convergent control parameters and constants such as $ka = S = A = Gt = 0.3, Ma = \phi = 0.2, Pr = 0.72, \theta = \pi/12, So = Ec = \Upsilon = 0.1, Fd = \Gamma = 1, Da = 3,$ the error gets down at higher orders of approximation (m) (see Figure 8.3.1b). These values of the parameters are fixed throughout this chapter (EIGHT) unless specified. Thus, the existence of convergent solutions have been ensured by HAM.

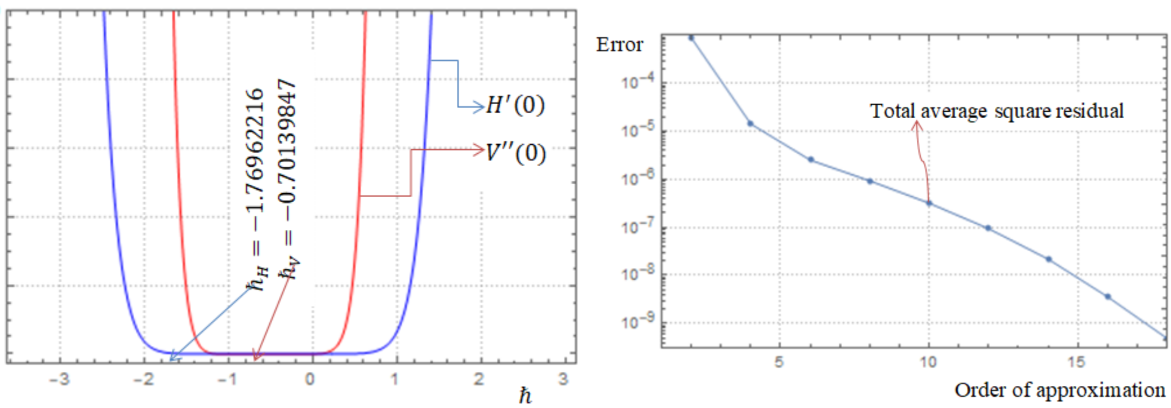

(a) $\hbar$-curves of $\hbar_V$ and $\hbar_H$

(b) Total average error

Figure 8.3.1: $\hbar$-curves of convergence control parameters and residual error

8.4 Findings and Discussion

Under this issue, the nanofluid's velocity, temperature, local skin friction and Nusselt number are briefly discussed by taking the most prominent parameters that have a linkage to the study objective. In this problem, researchers examine heat transfer via the unsteady motion of $Cu - H_2O$ nanofluid across a slanted permeable stretchable surface in the presence of solar radiation and viscous dissipation. Here, the convective heat transfer and mass suction/injection are included as the boundary conditions. Then, the problem is figured out by solving ODEs (8.2.10) and (8.2.11), with the boundary conditions in equation (8.2.12) numerically, employing the builtin code bvp4c in the MATLAB mathematical language. Moreover, this approach is strengthened by implementing a semi-analytic method called HAM on Mathematica 12.1 software. The validity of these two approaches are justified by comparing the values of $-V''(0)$ for distinct values of Ma and A, and also the values of $-H'(0)$ for distinct values of Pr (see Table 8.4.1, 8.4.2 and 8.4.3). For convenience, the comparison made on these tables are within the standard numerical methods such as Keller Box Method (KBM) and Runge-Kutta-Fehlberg (RK-Fehlberg). Hence, the outcomes obtained by implementing bvp4c code and HAM are highly related to the results of published articles.

Table 8.4.1: Values of $-V''(0)$ with $ka = So = Gt = Ec = \alpha = Fh = 0$, $Da \to \infty$.

		bvp4c		**Present Result**	
Ma	A	Khan and Azam (2017)	Hussain and Sheremet (2023)	bvp4c	HAM
0.00	0.0	1.00000	-	1.0002	1.00000
0.25	0.0	-	-	1.1181	1.11803
0.50	0.0	-	1.2247	1.2248	1.22474
0.75	0.0	-	-	1.3229	1.32288
1.00	0.0	-	1.4142	1.4142	1.41421
1.25	0.0	-	-	1.5000	1.50000
1.50	0.0	-	1.5811	1.5811	1.58114
0.00	0.1	-	-	1.0343	1.03411
0.00	0.4	1.13469	-	1.1347	1.13469
0.00	0.7	-	-	1.2304	1.23039
0.00	1.0	-	-	1.3205	1.32051
0.00	1.2	1.37772	-	1.3777	1.37772
0.00	1.4	1.43284	-	1.4328	1.43286

Table 8.4.2: $-H'(0)$ value at $Ma = Gt = Fh = ka = A = Ec = So = S = 0, Da\&\Upsilon \to \infty$.

	KBM	HAM	**bvp4c**
Pr	Aziz et al. (2021)	Abolbashari et al. (2014)	**Present Result**
0.72	0.80876181	0.80863135	0.8103
1.00	1.00000000	1.00000000	1.0002
3.00	1.92357420	1.92368259	1.9236
7.00	3.07314651	3.07225021	3.0722
10.0	3.72055429	3.72067390	3.7206

Table 8.4.3: $-H'(0)$ value at $Ma = Gt = Fh = ka = A = Ec = So = S = 0, Da\&\Upsilon \to \infty$.

	bvp4c	RK-Fehlberg	**HAM**
Pr	Das et al. (2015)	Naqvi et al. (2022)	**Present Result**
0.72	0.80876122	0.80876181	0.808632
1.00	1.00000000	1.00000000	1.000000
3.00	1.92357431	1.92357420	1.923790
7.00	3.07314679	3.07314651	3.072220
10.0	3.72055436	-	3.720930

8.4.1 Velocity Profile

In this scenario, the flow of nanofluid can be influenced by mass suction/injection (S), incident solar radiation parameter (S_o) and Darcy number (Da). The contribution of these parameters can be visualized pictorially. In Figure 8.4.1a, the parameter S declines the flow of nanofluid. Physically, S attracts the hot nanofluid from the atmosphere towards the surface, which delays the speed of nanofluid. Due to the incredible Sun's radiation, the S_o releases enormous solar energy, which in turn disturbs the nanofluid's motion. As a result, S_o moves the nanofluid rapidly and vanish at far away from the wall, as appeared in Figure 8.4.1b. The graph in Figure 8.4.2a tells us, Da hastens the flow of nanofluid. Darcy number express as the ratio of permeability to the cross sectional area. Physically, when Da enlarges, the cross sectional area narrows which speed up the flow of nanofluid.

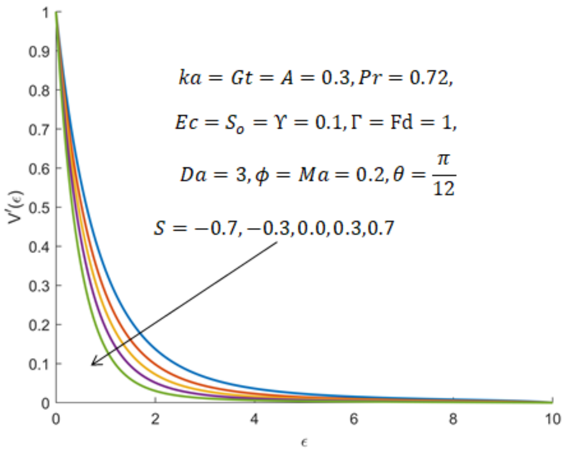

(a) The influence of S on $V'(\epsilon)$

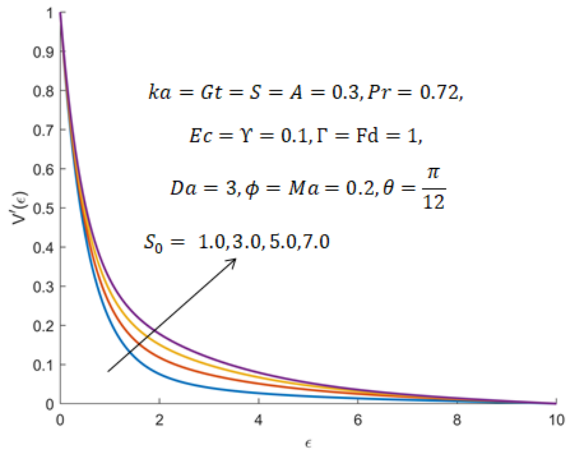

(b) The influence of So on $V'(\epsilon)$

Figure 8.4.1: The influence of S and So on velocity profile

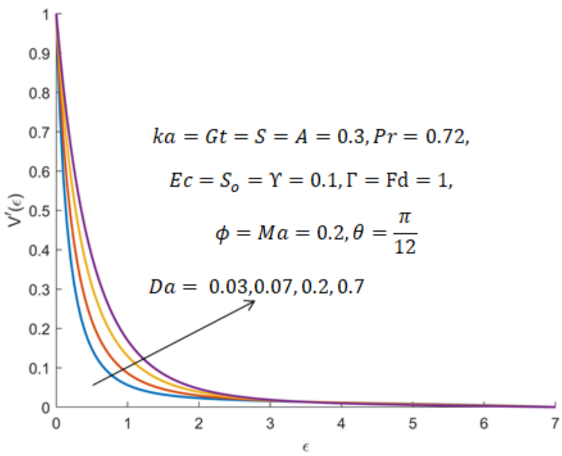

(a) The influence of Da on $V'(\epsilon)$

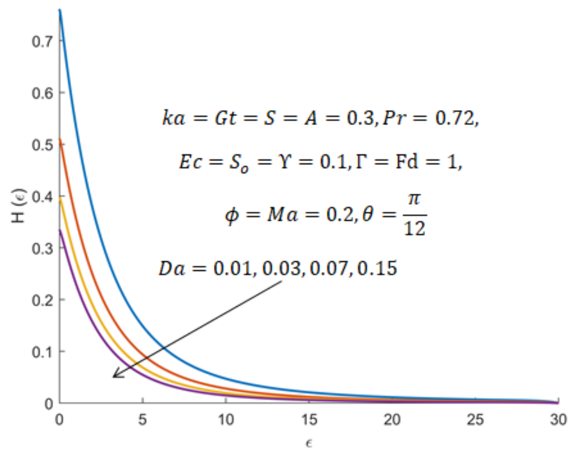

(b) The influence of Da on $H(\epsilon)$

Figure 8.4.2: The influence of Da on velocity and temperature profiles

8.4.2 Temperature Profile

Mainly, the heat of time-dependent flowing nanofluid is regulated by Darcy number (Da), absorption parameter (Γ), unsteady parameter (A), incident solar radiation parameter (S_o), Eckert number (Ec), Biot number (Υ) and concentration of nanoparticles (ϕ) in the context of this issue. The nanofluid's temperature declines when the Da increases, as recognized in Figure 8.4.2b. In light of this problem, Da directly relates to the flow of nanofluid. In contrast, it is inversely related to the temperature of nanofluid, which is similar to the outcomes of Hussain and Sheremet (2023). As it is detected from Figures 8.4.3a and 8.4.3b, the temperature of nanofluid diminishes because of increasing values of Γ and A, respectively. Physically, the existence of more absorptions of the Sun's radiation leads to the transfer of more heat from high temperatures toward lower temperatures during the motion of nanofluid, which is the cause of heat loss. This implies that the temperature of the nanofluid is cooled down by adding the values of Γ as Figure 8.4.3a illustrates. Naturally, as time goes on, the temperature of nanofluid gets lower owing to the loss of heat to the environment over time. This is well-founded by Figure 8.4.3b as it is illustrated below.

The Figures from 8.4.4a to 8.4.5b show that the temperature of unsteady flowing nanofluid is promoted by the parameters S_o, Ec, Υ and ϕ respectively. Naturally, during the daytime, there may be high solar rays that increase the amount of solar energy. Consequently, the heat of the nanofluid rises, as foreseen in Figure 8.4.4a due to increasing the values of S_o. Ec has the power to accelerate the kinetic energy and subtract enthalpy. This insinuates that the distribution of temperature in the unsteady flowing nanofluid is becoming higher, as Figure 8.4.4b revealed. Figure 8.4.5a tells us that Υ has a role in distributing more temperature in the unsteady flowing nanofluid on an inclined surface. Physically, the Biot number optimizes convective heat transfer, which increases the nanofluid's temperature. Increasing the concentration of nanoparticles (ϕ) produces more heat in the nanofluid as they have high heat conductivity. As a consequence, the nanofluid's temperature is upgraded with increasing ϕ to some amount, as we observed in Figure 8.4.5b.

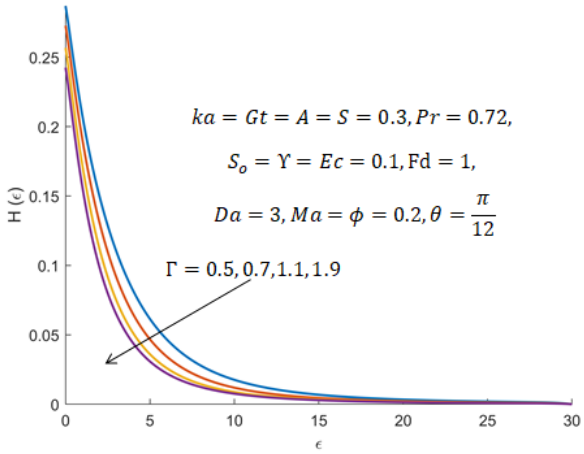

(a) The influence of Γ on $H(\epsilon)$

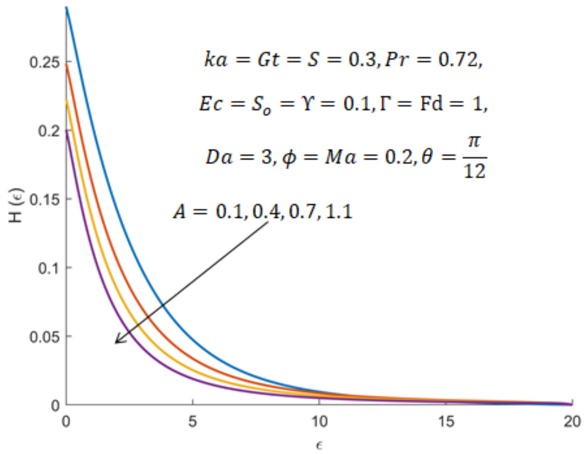

(b) The influence of A on $H(\epsilon)$

Figure 8.4.3: The influence of Γ and A on temperature profiles

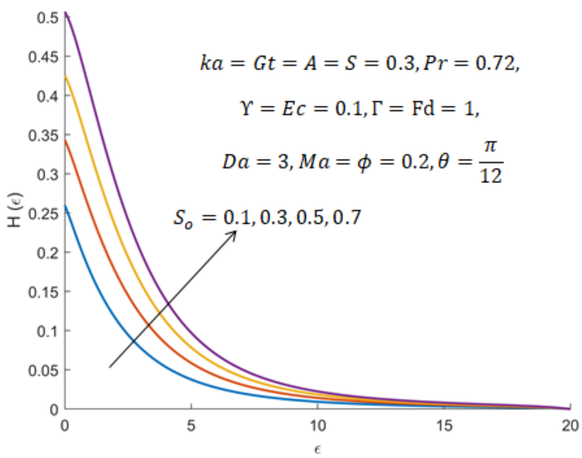

(a) The influence of So on $H(\epsilon)$

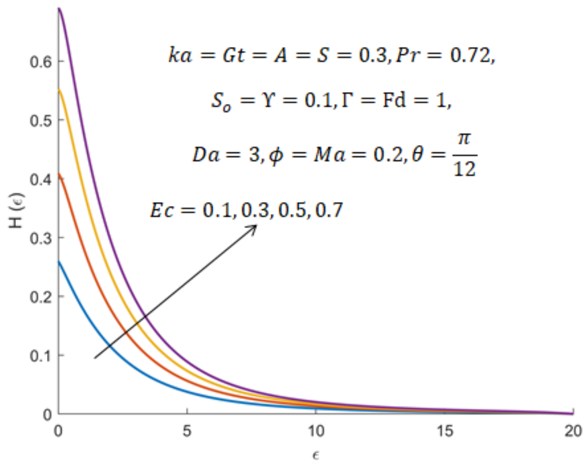

(b) The influence of Ec on $H(\epsilon)$

Figure 8.4.4: The influence of S_o and Ec on temperature profiles

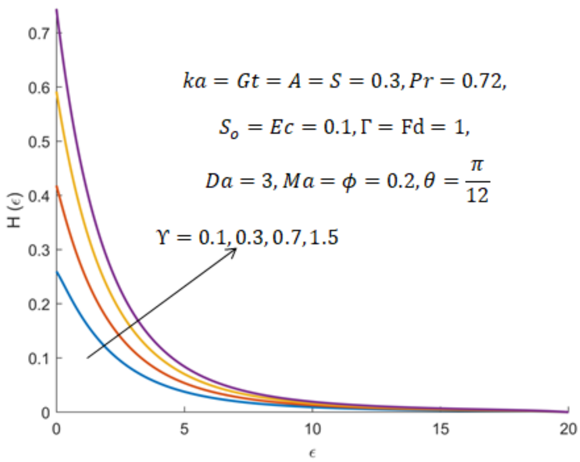

(a) The influence of Υ on $H(\epsilon)$

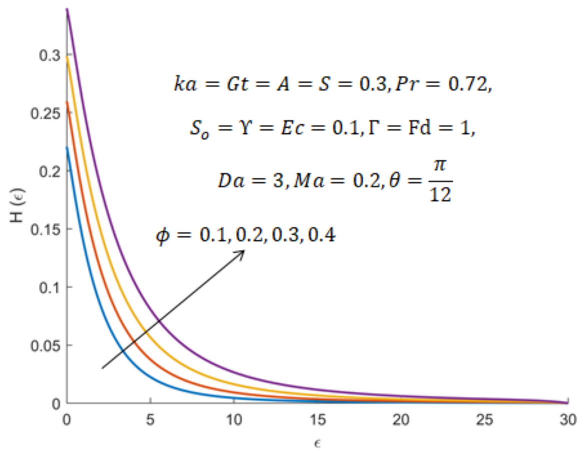

(b) The influence of ϕ on $H(\epsilon)$

Figure 8.4.5: The influence of Υ and ϕ on temperature profiles

8.4.3 Concerned Physical Quantities

In the context of this issue, the physical quantities are Cf_x and Nu_x based on an engineering perspectives. These quantities can be expressed in terms of $V''(0) = p_1 Cf_x$ and $-H'(0) = Nu_x/p_4$ given that $Re_x = 1$ according to equations (8.2.13) and (8.2.14). The numerical values of $-V''(0)$ and $-H'(0)$ are shown in tabular form for the nanofluids, which are constructed by using water (H_2O) and propylene glycol ($C_3H_8O_2$) as the base fluids and Copper (Cu) as nanoparticles (see Table 8.4.4). Thus, the influences of constants such as ϕ, Ma, ka, A, S_o, S and Gt on local skin friction coefficient and local rate of heat transfer in terms of the values of $-V''(0)$ and $-H'(0)$, respectively, are exhibited in Table 8.4.4.

Hence, the obtained numerical results indicate that the nanofluid constructed by water, as the host fluid has an ability to form more drag force than propylene glycol for those selected parameters. However, the reverse trend is observed in the case of heat transfer rate. The magnitude of the skin friction coefficient rises with the values of ϕ, Ma, kaA and S. Physically, the formation of drag forces maximizes due to these constants, which retard the flow of nanofluid. But, this phenomenon is reversed when So and Gt are increased since they can speed up the flow of nanofluid. The rate of heat transfer is degraded by ϕ, Ma, ka and S_o whereas it ascends due to the constants A, S and Gt. Particularly, when S_o added by 0.2, the values of local skin friction coefficient $(-V''(0))$ and local Nusselt number Nu_x are reduced approximately by 0.01 for both H_2O and $C_3H_8O_2$ base fluids. Similarly, as Gt increases by 0.2, the local Nusselt number $(-H'(0))$ rises approximately by 0.0003 for both conventional fluids.

Table 8.4.4: Values of $-V''(0)$ and $-H'(0)$ at $Da = 3, Fh = \Gamma = 1, Pr = 0.72, \theta = \pi/12, Ec = 0.2, \Upsilon = 0.1$.

							$-V''(0)$		$-H'(0)$	
ϕ	Ma	ka	A	So	S	Gt	$Cu-H_2O$	$Cu-C_3H_8O_2$	$Cu-H_2O$	$Cu-C_3H_8O_2$
0.0	0.2	0.3	0.3	0.1	0.3	0.3	1.5134	1.5134	0.0821	0.0821
0.1							1.7598	1.4009	0.0779	0.0797
0.2							1.8242	1.2820	0.0740	0.0768
	0.3						1.8859	1.3234	0.0737	0.0764
	0.4						1.8860	1.3633	0.0734	0.0760
	0.5						1.9160	1.4021	0.0731	0.0756
	0.2	0.5					1.8859	1.3632	0.0734	0.0760
		0.7					1.9533	1.4394	0.0729	0.0752
		0.9					2.0025	1.5116	0.0723	0.0745
		0.3	0.5				1.8928	1.3242	0.0762	0.0785
			0.7				1.9585	1.3649	0.0777	0.0798
			0.9				2.0220	1.4043	0.0790	0.0809
			0.3	0.3			1.8141	1.2719	0.0657	0.0681
				0.5			1.8042	1.2621	0.0575	0.0596
				0.7			1.7945	1.2524	0.0493	0.0511
				0.1	0.5		1.9918	1.3530	0.0743	0.0775
					0.7		2.1730	1.4278	0.0745	0.0781
					0.9		2.3672	1.5063	0.0749	0.0788
					0.3	0.5	1.8081	1.2682	0.0743	0.0770
						0.7	1.7925	1.2549	0.0746	0.0773
						0.9	1.7774	1.2418	0.0749	0.0775

8.5 Summary

This chapter focuses on the theoretical investigation of heat transfer through an unsteady flowing nanofluid over a slanted, permeable surface. 2D, incompressible, laminar flow with mass suction/injection and convective heat transfer are thought out. The Tiwari-Das and Darcy-Forchheimer models are applied. The governing PDEs are converted into a system of coupled non-linear higher-order ODEs using the proper similarity transformation. Then, they were solved numerically using the built-in package bvp4c in MATLAB and a semi-analytic approach called HAM. The obtained result was compared with the published articles for specific values, and strong agreement was detected. The mobility of nanofluid is enhanced by Da, S_o and Gt but not by ka and S. The constants ka, S_o, Ec and Υ expand the temperature of nanofluid, whereas Γ, Da, A and Pr have an opposite trend. Cf_x is mounted by the parameters ϕ, Ma, ka, A and S but not by Ec, S_o and Gt. Nu_x increases for Gt, S, A but not for Ma, ϕ, ka, S_o.

Conclusion and Recommendation

Conclusions

In this dissertation work, the heat and mass transfer characteristics were explored through a 2D, unsteady flowing incompressible viscous nanofluid over a stretchable surface. Here, solar thermal radiation and entropy generation are also considered. The Biot number, porosity, magnetic field interaction, Eckert number, and heat source increase the temperature of the nanofluid where the thickness of the thermal boundary is wider and produces more entropy formation. The mass suction/injection parameter decreases the nanofluids' flow, temperature, and concentrations. The velocity slip and mass suction parameters tend to decrease the generation of entropy. From this study, it can be concluded that there is a parameter that is used for heating or cooling purposes by the unsteady-flowing nanofluid. Thus, the heat transfer process can be managed by using nanofluid flow in terms of various constants. In general, the main findings of this dissertation are listed below as a conclusion.

1. The flow of nanofluid is retarded due to the parameters ka, S, Ma and ϖ. This implies that the velocity boundary layer thickness diminishes due to these parameters. The parameters such as Ec, Gt, Gp, Nb, Da and θ speed up the nanofluid's motion and increase the velocity boundary layer thickness.

2. The temperature distribution inside the unsteady moving nanofluid and thermal boundary layer thickness can be enhanced by parameters $Rn, Ma, Ec, Nt, ka, Nb, \varpi, So$ and Υ. Conversely, the temperature of nanofluid is cooled down by rising S, Gt, Gp, A, Da, Γ and Pr, which lead to decreased thermal boundary layer thickness.

3. Ma, ka, Ec, Nt, ϖ and Υ have been directly related to the concentration of nanofluids, whereas Gp, S, Nb and Sc are inversely proportional to it.

4. The entropy production intensifies for ascending values of $Ma, ka, \Upsilon, Re, Pr, Rn, Ec, Br$ and Sc. Contrary to these, the parameters ϖ and S make it wane.

5. The constants that increase the speed of nanofluid have a chance to reduce the formation drag force, and vice versa. Thus, the magnitude of the local skin friction coefficient is increased by amplifying the parameters Sc, Ma, ka and S. The drag force is reduced by raising the values of Ec, Gt, θ and Gp.

6. Based on the value of the parameter, we can compare the convective heat transfer with conductive heat transfer by the value of Nusselt number. This is very essential to choose the method of heat transfer according to the need for heat. Thus, Nu_x enlarges for Nb, Ma, Sc, S, Pr and S but not for rising ka, Gt and Gp parameters.

7. The rate of mass transfer by convective is higher than the diffusive as the values of Nb, Ec, θ, Gt and A increase, while Ma, Nt, ka decrease.

Recommendations

The outcomes of this study together with experimental investigations are highly recommended for engineering and industrial processes that need the application of heat and mass transfer. This is because the presented study explores the role of nanofluid in transferring heat from renewable energy sources like solar radiation and other heat sources. In addition, the parameters that affect usable energy by raising the development of entropy during heat transmission are also identified which helps for concerned body to reduce the energy loss during heat transform processes. Hence, it can improve usable energy by reducing entropy generation. Thus, the numerical result of this dissertation, combined with another practical work, yields a fruitful outcome by providing an alternative method of solving the problem of power demand and climate change.

Suggestions for Future Research

In the future, this study can be extended in a more applicable manner by taking into account on the different characteristics of nanofluid. These are listed as follows:

- Considering the cylindrical surface geometry where the nanofluid flow.
- Applying hybrid nanofluids and non-Fourier heat conduction law.
- Constructing nanofluid using tiny solid particles and non-Newtonian fluid as a base fluid which is applicable in various industries.

REFERENCES

Abbas, A., Khan, A., Abdeljawad, T., and Aslam, M. (2023). Numerical simulation of variable density and magnetohydrodynamics effects on heat generating and dissipating williamson sakiadis flow in a porous space: Impact of solar radiation and joule heating. *Heliyon*, 9(11).

Abolbashari, M. H., Freidoonimehr, N., Nazari, F., and Rashidi, M. M. (2014). Entropy analysis for an unsteady mhd flow past a stretching permeable surface in nano-fluid. *Powder Technology*, 267:256–267.

Afzal, K. and Aziz, A. (2016). Transport and heat transfer of time dependent mhd slip flow of nanofluids in solar collectors with variable thermal conductivity and thermal radiation. *Results in physics*, 6:746–753.

Aghamajidi, M., Yazdi, M., Dinarvand, S., and Pop, I. (2018). Tiwari-das nanofluid model for magnetohydrodynamics (mhd) natural-convective flow of a nanofluid adjacent to a spinning down-pointing vertical cone. *Propulsion and Power Research*, 7(1):78–90.

Ahmed, S. E., Aly, A. M., and Raizah, Z. (2019). Heat transfer enhancement from an inclined plate through a heat generating and variable porosity porous medium using nanofluids due to solar radiation. *SN Applied Sciences*, 1:1–13.

Ahmed, S. E., Mansour, M., Mahdy, A., and Mohamed, S. S. (2017). Entropy generation due to double diffusive convective flow of casson fluids over nonlinearity stretching sheets with slip conditions. *Engineering Science and Technology, an International Journal*, 20(6):1553–1562.

Ahmmed, S., Biswas, R., and Afikuzzaman, M. (2018). Unsteady magnetohydrodynamic free convection flow of nanofluid through an exponentially accelerated inclined plate embedded in a porous medium with variable thermal conductivity in the presence of radiation. *Journal of Nanofluids*, 7(5):891–901.

Al-Askaree, E. H. and Al-Muhsen, N. F. (2023). Experimental investigation on thermal performance of solar water heater equipped with serpentine fin core heat exchanger. *Cleaner Engineering and Technology*, 12:100593.

Al-Waeli, A. H., Sopian, K., Kazem, H. A., and Chaichan, M. T. (2017). Photovoltaic/thermal (pv/t) systems: Status and future prospects. *Renewable and Sustainable Energy Reviews*, 77:109–130.

Ali, F., Loganathan, K., Eswaramoorthi, S., Faizan, M., Prabu, E., and Zaib, A. (2022). Bioconvective applications of unsteady slip flow over a tangent hyperbolic nanoliquid with surface heating: Improving energy system performance. *International Journal of Applied and Computational Mathematics*, 8(6):1–22.

Alkathiri, A. A., Jamshed, W., Eid, M. R., Bouazizi, M. L., et al. (2022). Galerkin finite element inspection of thermal distribution of renewable solar energy in presence of binary nanofluid in parabolic trough solar collector. *Alexandria Engineering Journal*, 61(12):11063–11076.

Alqahtani, S., Rehman, S., Alshehery, S., Bibi, S., et al. (2023). Computational investigation of magnetized hybrid nanofluids heat transport and flow through elongational surface with thermal radiation and wall slip. *Heliyon*, 9(10).

Alves, P. D., Pitangueira, R. L., et al. (2013). An object-oriented approach to the generalized finite element method. *Advances in Engineering Software*, 59:1–18.

Alzahrani, A. K., Ullah, M. Z., Alshomrani, A. S., and Gul, T. (2021). Hybrid nanofluid flow in a darcy-forchheimer permeable medium over a flat plate due to solar radiation. *Case Studies in Thermal Engineering*, 26:100955.

Anjum, N., Khan, W., Ali, M., Hussain, I., Waqas, M., and Irfan, M. (2023). Thermal performance analysis of sutterby nanoliquid subject to melting heat transportation. *International Journal of Modern Physics B*, 37(19):2350185.

Anki Reddy, P. B., Reddy, S., and Suneetha, S. (2018). Magnetohydro dynamic flow of blood in a permeable inclined stretching surface with viscous dissipation, non-uniform heat source/sink and chemical reaction. *Frontiers in Heat and Mass Transfer (FHMT)*, 10.

Arpaci, V. S. (1987). Radiative entropy productionâ€"lost heat into entropy. *International journal of heat and mass transfer*, 30(10):2115–2123.

Arpaci, V. S. (1991). Radiative entropy production-heat lost to entropy. In *Advances in Heat transfer*, volume 21, pages 239–276. Elsevier.

Asif Ali Shah, S., Kanwal, S., Idrees, M., Mahmood, A., Mahmood, I., Akgul, A., and Bariq, A. (2023). Significance of heat transfer rate in water-based nanoparticles with magnetic and shape factors effects: Tiwari and das model. *Scientific Reports*, 13(1):15507.

Azam, M., Shakoor, A., Rasool, H., and Khan, M. (2019). Numerical simulation for solar energy aspects on unsteady convective flow of mhd cross nanofluid: A revised approach. *International Journal of Heat and Mass Transfer*, 131:495–505.

Aziz, A., Jamshed, W., and Aziz, T. (2018). Mathematical model for thermal and entropy analysis of thermal solar collectors by using maxwell nanofluids with slip conditions, thermal radiation and variable thermal conductivity. *Open Physics*, 16(1):123–136.

Aziz, A., Jamshed, W., Aziz, T., Bahaidarah, H., and Ur Rehman, K. (2021). Entropy analysis of powell–eyring hybrid nanofluid including effect of linear thermal radiation and viscous dissipation. *Journal of Thermal Analysis and Calorimetry*, 143(2):1331–1343.

Baehr, H. D. and Stephan, K. (2011). Convective heat and mass transfer. single phase flow. In *Heat and Mass Transfer*, pages 275–441. Springer.

Bano, N., Singh, B., and Sayyed, S. (2018). Homotopy analysis for mhd hiemenz flow in a porous medium with thermal radiation, velocity and thermal slips effects. *Frontiers in Heat and Mass Transfer (FHMT)*, 10::http://dx.doi.org/10.5098/hmt.10.14.

Bayrak, F., Abu-Hamdeh, N., Alnefaie, K. A., and Öztop, H. F. (2017). A review on exergy analysis of solar electricity production. *Renewable and Sustainable Energy Reviews*, 74:755–770.

Bejan, A. (1979). A study of entropy generation in fundamental convective heat transfer.

Bejan, A. (1996). Entropy generation minimization: The new thermodynamics of finite-size devices and finite-time processes. *Journal of Applied Physics*, 79(3):1191–1218.

Bejan, A. (2013). *Entropy generation minimization: the method of thermodynamic optimization of finite-size systems and finite-time processes*. CRC press.

Bhalla, V. and Tyagi, H. (2017). Solar energy harvesting by cobalt oxide nanoparticles, a nanofluid absorption based system. *Sustainable Energy Technologies and Assessments*, 24:45–54.

Bhalla, V. and Tyagi, H. (2018). Parameters influencing the performance of nanoparticles-laden fluid-based solar thermal collectors: a review on optical properties. *Renewable and Sustainable Energy Reviews*, 84:12–42.

Bibi, M., Malik, M., Tahir, M., et al. (2018). Numerical study of unsteady williamson fluid flow and heat transfer in the presence of mhd through a permeable stretching surface. *The European Physical Journal Plus*, 133(4):1–15, :https://doi.org/10.1140/epjp/i2018–11991–2.

Biswal, P. and Basak, T. (2017). Entropy generation vs energy efficiency for natural convection based energy flow in enclosures and various applications: a review. *Renewable and Sustainable Energy Reviews*, 80:1412–1457.

Boujelbene, M., Albouchi, F., Ullah, Z., Aldhabani, M. S., Alsulami, S. H., and Hassan, A. M. (2023). Solar radiation and lower gravitational effects on wave oscillations in heat transfer along magnetic-driven porous cone in the presence of joule heating. *Case Studies in Thermal Engineering*, page 103782.

Bouslimi, J., Alkathiri, A. A., Althagafi, T. M., Jamshed, W., and Eid, M. R. (2022). Thermal properties, flow and comparison between cu and ag nanoparticles suspended in sodium alginate as sutterby nanofluids in solar collector. *Case Studies in Thermal Engineering*, 39:102358.

Brewster, M. Q. (1992). *Thermal radiative transfer and properties.* John Wiley & Sons.

Budd, C., Koch, O., and Weinmüller, E. (2006). From nonlinear pdes to singular odes. *Applied numerical mathematics*, 56(3-4):413–422.

Buongiorno, J. (2006). Convective transport in nanofluids. *J. Heat Tran.*, 128:240–250.

Can, A., Selimefendigil, F., and Öztop, H. F. (2022). A review on soft computing and nanofluid applications for battery thermal management. *Journal of Energy Storage*, 53:105214.

Chamkha, A. (1997). Solar radiation assisted natural convection in uniform porous medium supported by a vertical flat plate.

Chamkha, A. J., Issa, C., and Khanafer, K. (2002). Natural convection from an inclined plate embedded in a variable porosity porous medium due to solar radiation. *International Journal of Thermal Sciences*, 41(1):73–81.

Chanie, A. G., Shankar, B., and Nandeppanavar, M. M. (2018). Mhd flow of nanofluids through a porous media due to a permeable stretching sheet. *Journal of Nanofluids*, 7(3):488–498.

Charreh, D., Saleem, M., et al. (2023). Entropy generation and natural convection analyses in a non-darcy porous square cavity with thermal radiation and viscous dissipation. *Results in Physics*, 52:106874.

Choi, S. U. and Eastman, J. A. (1995). Enhancing thermal conductivity of fluids with nanoparticles. Technical report, Argonne National Lab., IL (United States).

Chu, Y.-M., Khan, U., Shafiq, A., and Zaib, A. (2021). Numerical simulations of time-dependent micro-rotation blood flow induced by a curved moving surface through conduction of gold particles with non-uniform heat sink/source. *Arabian Journal for Science and Engineering*, 46:2413–2427.

Daniel, Y. S. (2015). Steady mhd laminar flows and heat transfer adjacent to porous stretching sheets using ham. *American journal of heat and mass transfer*, 2(3):146–159.

Daniel, Y. S. (2016). Steady mhd boundary-layer slip flow and heat transfer of nanofluid over a convectively heated of a non-linear permeable sheet. *Journal of Advanced Mechanical Engineering*, 3(1):1–14.

Daniel, Y. S. (2017). Mhd laminar flows and heat transfer adjacent to permeable stretching sheets with partial slip condition. *Journal of Advanced Mechanical Engineering*, 4(1):1–15.

Daniel, Y. S., Aziz, Z. A., Ismail, Z., Bahar, A., and Salah, F. (2020). Slip role for unsteady mhd mixed convection of nanofluid over stretching sheet with thermal radiation and electric field. *Indian Journal of Physics*, 94:195–207.

Daniel, Y. S., Aziz, Z. A., Ismail, Z., and Salah, F. (2017). Entropy analysis in electrical magnetohydrodynamic (mhd) flow of nanofluid with effects of thermal radiation, viscous dissipation, and chemical reaction. *Theoretical and Applied Mechanics Letters*, 7(4):235–242.

Daniel, Y. S., Aziz, Z. A., Ismail, Z., and Salah, F. (2019). Thermal radiation on unsteady electrical mhd flow of nanofluid over stretching sheet with chemical reaction. *Journal of King Saud University-Science*, 31(4):804–812.

Das, S., Chakraborty, S., Jana, R., and Makinde, O. (2015). Entropy analysis of unsteady magneto-nanofluid flow past accelerating stretching sheet with convective boundary condition. *Applied Mathematics and Mechanics*, 36:1593–1610.

Dehsara, M., Dalir, N., and Nobari, M. R. H. (2014). Numerical analysis of entropy generation in nanofluid flow over a transparent plate in porous medium in presence of solar radiation, viscous dissipation and variable magnetic field. *Journal of Mechanical Science and Technology*, 28(5):1819–1831.

Dinarvand, S., Hosseini, R., and Pop, I. (2016). Homotopy analysis method for unsteady mixed convective stagnation-point flow of a nanofluid using tiwari-das nanofluid model. *International Journal of Numerical Methods for Heat & Fluid Flow*, 26(1):40–62.

Dinarvand, S. and Pop, I. (2017). Free-convective flow of copper/water nanofluid about a rotating down-pointing cone using tiwari-das nanofluid scheme. *Advanced Powder Technology*, 28(3):900–909.

Dincer, I. (2000). Renewable energy and sustainable development: a crucial review. *Renewable and sustainable energy reviews*, 4(2):157–175.

Dugaria, S., Bortolato, M., and Del Col, D. (2018). Modelling of a direct absorption solar receiver using carbon based nanofluids under concentrated solar radiation. *Renewable Energy*, 128:495–508.

Eid, M. R. and Makinde, O. (2018). Solar radiation effect on a magneto nanofluid flow in a porous medium with chemically reactive species. *International Journal of Chemical Reactor Engineering*, 16(9):20170212.

Elsheikh, A., Sharshir, S., Mostafa, M. E., Essa, F., and Ali, M. K. A. (2018). Applications of nanofluids in solar energy: a review of recent advances. *Renewable and Sustainable Energy Reviews*, 82:3483–3502.

Enjavi, Y., Sedghamiz, M. A., and Rahimpour, M. R. (2022). Application of nanofluids in drug delivery and disease treatment. In *Nanofluids and Mass Transfer*, pages 449–465. Elsevier.

Esfe, M. H. and Toghraie, D. (2022). Numerical study on the effect of solar radiation intensity on the fresh water productivity of solar still equipped with thermoelectric cooling system (tec) for hot and dry areas of semnan. *Case Studies in Thermal Engineering*, 32:101848.

Everett, R., Boyle, G., Peake, S., and Ramage, J. (2012). *Energy systems and sustainability: power for a sustainable future.* Oxford Univerity Press.

Fathalah, K. and Elsayed, M. (1980). Natural convection due to solar radiation over a non-absorbing plate with and without heat losses. *International Journal of Heat and Fluid Flow*, 2(1):41–45.

Flilihi, E., Sebbar, E., Achemlal, D., EL Rhafiki, T., Sriti, M., and Chaabelasri, E. (2022). Effect of absorber design on convective heat transfer in a flat plate solar collector: A cfd modeling. *Frontiers in Heat and Mass Transfer (FHMT)*, 18.

Gorji, T. B. and Ranjbar, A. (2017). A review on optical properties and application of nanofluids in direct absorption solar collectors (dascs). *Renewable and Sustainable Energy Reviews*, 72:10–32.

Gupta, M., Singh, V., and Katyal, P. (2018). Synthesis and structural characterization of al2o3 nanofluids. *Materials Today: Proceedings*, 5(14):27989–27997.

Haile, E. and Shankar, B. (2014). Heat and mass transfer in the boundary layer of unsteady viscous nanofluid along a vertical stretching sheet. *Journal of Computational Engineering*, 2014:1–17.

Hameed, S. and Saha, S. (2023). Analysis of mixed convecto-magnetic buongiorno nanofluid flow in a non-darcy porous medium. *Journal of Taibah University for Science*, 17(1):2233755.

Hamzat, A. K., Omisanya, M. I., Sahin, A. Z., Oyetunji, O. R., and Olaitan, N. A. (2022). Application of nanofluid in solar energy harvesting devices: A comprehensive review. *Energy Conversion and Management*, 266:115790.

Hayat, T., Haider, F., Muhammad, T., and Alsaedi, A. (2017a). Darcy-forchheimer flow due to a curved stretching surface with cattaneo-christov double diffusion: A numerical study. *Results in physics*, 7:2663–2670.

Hayat, T., Khan, M. I., Waqas, M., and Alsaedi, A. (2017b). Stagnation point flow of hyperbolic tangent fluid with soret-dufour effects. *Results in physics*, 7:2711–2717.

Hayat, T., Muhammad, T., Al-Mezal, S., and Liao, S. (2016a). Darcy-forchheimer flow with variable thermal conductivity and cattaneo-christov heat flux. *International Journal of Numerical Methods for Heat & Fluid Flow*.

Hayat, T., Riaz, R., Aziz, A., and Alsaedi, A. (2019). Analysis of entropy generation for mhd flow of third grade nanofluid over a nonlinear stretching surface embedded in a porous medium. *Physica Scripta*, 94(12):125703.

Hayat, T., Ullah, I., Muhammad, K., and Alsaedi, A. (2021). Gyrotactic microorganism and bio-convection during flow of prandtl-eyring nanomaterial. *Nonlinear Engineering*, 10(1):201–212.

Hayat, T., Waqas, M., Shehzad, S., and Alsaedi, A. (2016b). A model of solar radiation and joule heating in magnetohydrodynamic (mhd) convective flow of thixotropic nanofluid. *Journal of Molecular Liquids*, 215:704–710.

Howell, J. R., Mengüç, M. P., Daun, K., and Siegel, R. (2020). *Thermal radiation heat transfer*. CRC press.

Hussain, M. and Sheremet, M. (2023). Convection analysis of the radiative nanofluid flow through porous media over a stretching surface with inclined magnetic field. *International Communications in Heat and Mass Transfer*, 140:106559.

Hussain, S. M. (2022). Dynamics of radiative williamson hybrid nanofluid with entropy generation: significance in solar aircraft. *Scientific Reports*, 12(1):1–23.

Hussain, S. M., Jamshed, W., Akgül, E. K., and Mohd Nasir, N. A. A. (2021). Mechanical improvement in solar aircraft by using tangent hyperbolic single-phase nanofluid. *Proceedings of the Institution of Mechanical Engineers, Part E: Journal of Process Mechanical Engineering*, page 09544089211059377.

Hussain, S. M., Jamshed, W., Safdar, R., Shahzad, F., Mohd Nasir, N. A. A., and Ullah, I. (2023). Chemical reaction and thermal characteristiecs of maxwell nanofluid flow-through solar collector as a potential solar energy cooling application: A modified buongiorno's model. *Energy & Environment*, 34(5):1409–1432.

Hussain, S. M., Sharma, R., and Chamkha, A. J. (2022). Numerical and statistical explorations on the dynamics of water conveying cu-al2o3 hybrid nanofluid flow over an exponentially stretchable sheet with navier's partial slip and thermal jump conditions. *Chinese Journal of Physics*, 75:120–138.

Hussain, T., Hayat, T., Shehzad, S. A., Alsaedi, A., and Chen, B. (2015). A model of solar radiation and joule heating in flow of third grade nanofluid. *Zeitschrift für Naturforschung A*, 70(3):177–184.

Hussanan, A., Aman, S., Ismail, Z., Salleh, M. Z., and Widodo, B. (2018). Unsteady natural convection of sodium alginate viscoplastic casson based based nanofluid flow over a vertical plate with leading edge accretion/ablation. *Journal of Advanced Research in Fluid Mechanics and Thermal Sciences*, 45(1):92–98.

Ikram, M. (2021). Models for predicting non-renewable energy competing with renewable source for sustainable energy development: case of asia and oceania region. *Global Journal of Flexible Systems Management*, 22(2):133–160.

Irfan, M., Hamid, A., Khan, M., Nadeem, A., Khan, W., and Nasir, N. (2023). Enhancement of heat transfer considering joule heating and variable conductivity in magneto maxwell nanofluid. *International Journal of Modern Physics B*, 37(08):2350076.

Jaddoa, A., Hamad, K., and Hameed, A. (2023). Fluid inflow and heat transfer enhancement: an experimental analysis of nanofluids in minchannel. *Frontiers in Heat and Mass Transfer (FHMT)*, 20.

Jalili, B., Emad, M., Jalili, P., Ganji, D. D., Saleem, S., and Tag-eldin, E. M. (2023). Thermal analysis of boundary layer nanofluid flow over the movable plate with internal heat generation, radiation, and viscous dissipation. *Case Studies in Thermal Engineering*, page 103203.

Jameel, M., Shah, Z., Rooman, M., Alshehri, M. H., and Vrinceanu, N. (2023). Entropy generation analysis on darcy-forchheimer maxwell nanofluid flow past a porous stretching sheet with threshold non-fourier heat flux model and joule heating. *Case Studies in Thermal Engineering*, page 103738.

Jamshed, W., Alanazi, A. K., Isa, S. S. P. M., Banerjee, R., Eid, M. R., Nisar, K. S., Alshahrei, H., and Goodarzi, M. (2022). Thermal efficiency enhancement of solar aircraft by utilizing unsteady hybrid nanofluid: A single-phase optimized entropy analysis. *Sustainable Energy Technologies and Assessments*, 52:101898.

Jamshed, W., Eid, M. R., Nasir, N. A. A. M., Nisar, K. S., Aziz, A., Shahzad, F., Saleel, C. A., and Shukla, A. (2021a). Thermal examination of renewable solar energy in parabolic trough solar collector utilizing maxwell nanofluid: A noble case study. *Case Studies in Thermal Engineering*, 27:101258.

Jamshed, W., Mishra, S., Pattnaik, P., Nisar, K. S., Devi, S. S. U., Prakash, M., Shahzad, F., Hussain, M., and Vijayakumar, V. (2021b). Features of entropy optimization on viscous second grade nanofluid streamed with thermal radiation: A tiwari and das model. *Case Studies in Thermal Engineering*, 27:101291.

Jamshed, W., Nasir, N. A. A. M., Isa, S. S. P. M., Safdar, R., Shahzad, F., Nisar, K. S., Eid, M. R., Abdel-Aty, A.-H., and Yahia, I. (2021c). Thermal growth in solar water pump using prandtl–eyring hybrid nanofluid: a solar energy application. *Scientific reports*, 11(1):1–21.

Jan, S. U., Haq, S. U., Shah, S. I. A., and Khan, I. (2019). Heat and mass transfer of free convection flow over a vertical plate with chemical reaction under wall–slip effect. *Arabian Journal for Science and Engineering*, 44(12):9869–9887.

Jyothi, N. and Avula Golla, V. K. (2023). Study of radiative heat and mass intensification with magnetic field for casson and williamson nanofluid flow model over a porous stretching sheet with higher-order chemical reaction: application of solar energy. *Journal of Thermal Analysis and Calorimetry*, pages 1–14.

Kandasamy, R., Muhaimin, I., and Mohamad, R. (2013). Thermophoresis and brownian motion effects on mhd boundary-layer flow of a nanofluid in the presence of thermal stratification due to solar radiation. *International Journal of Mechanical Sciences*, 70:146–154.

Kebede, T., Haile, E., Awgichew, G., and Walelign, T. (2020). Heat and mass transfer in unsteady boundary layer flow of williamson nanofluids. *Journal of Applied Mathematics*, 2020.

Khan, M. and Azam, M. (2017). Unsteady heat and mass transfer mechanisms in mhd carreau nanofluid flow. *Journal of Molecular Liquids*, 225:554–562.

Khan, M. I., Khan, M. I., and Al-Ghamdi, S. G. (2022a). Computational analysis of solar thermal system with prandtl nanofluid. *Scientific Reports*, 12(1):1–12.

Khan, S. A., Hayat, T., Alsaedi, A., and Alhodaly, M. (2022b). Thermal analysis for radiative flow of darcy-forchheimer nanomaterials subject to entropy generation. *Journal of Computational Design and Engineering*.

Khan, U., Zaib, A., Pop, I., Waini, I., and Ishak, A. (2022c). Mhd flow of a nanofluid due to a nonlinear stretching/shrinking sheet with a convective boundary condition: Tiwari–das nanofluid model. *International Journal of Numerical Methods for Heat & Fluid Flow*, 32(10):3233–3258.

Khan, Z., Jawad, M., Bonyah, E., Khan, N., and Jan, R. (2022d). Magnetohydrodynamic thin film flow through a porous stretching sheet with the impact of thermal radiation and viscous dissipation. *Mathematical Problems in Engineering*, 2022:1–10.

Kumar, A., Tripathi, R., Singh, R., and Chaurasiya, V. (2020). Simultaneous effects of nonlinear thermal radiation and joule heating on the flow of williamson nanofluid with entropy generation. *Physica A: Statistical Mechanics and its Applications*, 551:123972.

Lai, W. M., Rubin, D. H., Rubin, D., and Krempl, E. (2009). *Introduction to continuum mechanics*. Butterworth-Heinemann.

Lei, W., Ozturk, I., Muhammad, H., and Ullah, S. (2022). On the asymmetric effects of financial deepening on renewable and non-renewable energy consumption: insights from china. *Economic Research-Ekonomska Istraživanja*, 35(1):3961–3978.

Li, J., Zheng, L., and Liu, L. (2016). Mhd viscoelastic flow and heat transfer over a vertical stretching sheet with cattaneo-christov heat flux effects. *Journal of Molecular Liquids*, 221:19–25.

Li, Y.-X., Alshbool, M. H., Lv, Y.-P., Khan, I., Khan, M. R., and Issakhov, A. (2021). Heat and mass transfer in mhd williamson nanofluid flow over an exponentially porous stretching surface. *Case Studies in Thermal Engineering*, 26:100975.

Liao, S. (2003). *Beyond perturbation: introduction to the homotopy analysis method*. CRC press.

Liao, S. (2012). *Homotopy analysis method in nonlinear differential equations*. Springer.

Liao, S. (2013). *Advances in the homotopy analysis method*. World Scientific.

Liao, S.-J. (1992). *The proposed homotopy analysis technique for the solution of nonlinear problems*. PhD thesis, PhD thesis, Shanghai Jiao Tong University.

Liao, S.-j. (1997). A kind of approximate solution technique which does not depend upon small parametersâ€”ii. an application in fluid mechanics. *International Journal of Non-Linear Mechanics*, 32(5):815–822.

Loganathan, K., Mohana, K., Mohanraj, M., Sakthivel, P., and Rajan, S. (2021). Impact of third-grade nanofluid flow across a convective surface in the presence of inclined lorentz force: an approach to entropy optimization. *Journal of Thermal Analysis and Calorimetry*, 144(5):1935–1947. :https://doi.org/10.1007/s10973–020–09751–3.

Loganathan, K., Muhiuddin, G., Alanazi, A., Alshammari, F. S., Alqurashi, B. M., and Rajan, S. (2020). Entropy optimization of third-grade nanofluid slip flow embedded in a porous sheet with zero mass flux and a non-fourier heat flux model. *Frontiers in Physics*, 8:250.

Loganathan, K. and Rajan, S. (2020). An entropy approach of williamson nanofluid flow with joule heating and zero nanoparticle mass flux. *Journal of Thermal Analysis and Calorimetry*, 141(6):2599–2612.

Ma, T., Guo, Z., Lin, M., and Wang, Q. (2021). Recent trends on nanofluid heat transfer machine learning research applied to renewable energy. *Renewable and Sustainable Energy Reviews*, 138:110494.

Mahdi, R. A., Mohammed, H., Munisamy, K., and Saeid, N. (2015). Review of convection heat transfer and fluid flow in porous media with nanofluid. *Renewable and Sustainable Energy Reviews*, 41:715–734.

Mahian, O., Kianifar, A., Kalogirou, S. A., Pop, I., and Wongwises, S. (2013). A review of the applications of nanofluids in solar energy. *International Journal of Heat and Mass Transfer*, 57(2):582–594.

Makanda, G. (2015). *Numerical study of convective fluid flow in porous and non-porous media*. PhD thesis.

Makinde, O. D. and Aziz, A. (2011). Boundary layer flow of a nanofluid past a stretching sheet with a convective boundary condition. *International Journal of Thermal Sciences*, 50(7):1326–1332.

Malvandi, A., Moshizi, S., Soltani, E. G., and Ganji, D. (2014). Modified buongiornoâ€™s model for fully developed mixed convection flow of nanofluids in a vertical annular pipe. *Computers & Fluids*, 89:124–132.

Mathie, R., Markides, C. N., and White, A. J. (2014). A framework for the analysis of thermal losses in reciprocating compressors and expanders. *Heat Transfer Engineering*, 35(16-17):1435–1449.

Mechael, S. S., Wu, Y., Schlingman, K., and Carmichael, T. B. (2018). Stretchable metal films. *Flexible and Printed Electronics*, 3(4):043001.

Mukhopadhyay, S. (2011). Effects of slip on unsteady mixed convective flow and heat transfer past a porous stretching surface. *Nuclear Engineering and Design*, 241(8):2660–2665.

Mukhopadhyay, S., Mandal, M. S., and Vajravelu, K. (2022). Cu–water nanofluid flow with arbitrarily shaped nanoparticles over a porous plate in a porous medium in the presence of slip. *Pramana*, 96(4):196.

Mukhtar, S. and Gul, T. (2023). Solar radiation and thermal convection of hybrid nanofluids for the optimization of solar collector. *Mathematics*, 11(5):1175.

Nagaraja, B., Ajaykumar, A., Felicita, A., Kumar, P., and Ng, R. (2023). Non-darcy-forchheimer flow of casson-williamson nanofluid on melting curved stretching sheet influenced by magnetic dipole. *ZAMM-ZEITSCHRIFT FUR ANGEWANDTE MATHEMATIK UND MECHANIK*.

Nandi, S., Das, M., and Kumbhakar, B. (2022). Entropy generation in magneto-casson nanofluid flow along an inclined stretching sheet under porous medium with activation energy and variable heat source/sink. *Journal of Nanofluids*, 11(1):17–30.

Naqvi, S. M. R. S., Waqas, H., Yasmin, S., Liu, D., Muhammad, T., Eldin, S. M., and Khan, S. A. (2022). Numerical simulations of hybrid nanofluid flow with thermal radiation and entropy generation effects. *Case Studies in Thermal Engineering*, 40:102479.

Nasir, M., Waqas, M., Bég, O. A., Znaidia, S., Khan, W., and Zamri, N. (2023). Functional magnetic maxwell viscoelastic nanofluids for tribological coatings-a model for stretching flow using the generalized theory of heat-mass fluxes, darcy-forchheimer formulation and dual convection. *Tribology International*, 187:108610.

Noghrehabadi, A., Behseresht, A., Ghalambaz, M., and Behseresht, J. (2013). Natural-convection flow of nanofluids over vertical cone embedded in non-darcy porous media. *Journal of thermophysics and heat transfer*, 27(2):334–341.

Pandey, A. K., Bhattacharyya, K., Gautam, A. K., Rajput, S., Mandal, M. S., Chamkha, A. J., and Yadav, D. (2023). Insight into the relationship between non-linear mixed convection and thermal radiation: The case of newtonian fluid flow due to non-linear stretching. *Propulsion and Power Research*, 12(1):153–165.

Pandey, K. M. and Chaurasiya, R. (2017). A review on analysis and development of solar flat plate collector. *Renewable and Sustainable Energy Reviews*, 67:641–650.

Pang, C., Lee, J. W., and Kang, Y. T. (2015). Review on combined heat and mass transfer characteristics in nanofluids. *International Journal of Thermal Sciences*, 87:49–67.

Pasha, A. A., Hussain, Z., Alam, M. M., Kasim, N., Irshad, K., Ali, M., Waqas, M., and Khan, W. A. (2023). Impact of magnetized non-linear radiative flow on 3d chemically reactive sutterby nanofluid capturing heat sink/source aspects. *Case Studies in Thermal Engineering*, 41:102610.

Poochinapan, K., Wongsaijai, B., Disyadej, T., et al. (2014). Efficiency of high-order accurate difference schemes for the korteweg-de vries equation. *Mathematical Problems in Engineering*, 2014.

Priyam, A. and Chand, P. (2019). Experimental investigations on thermal performance of solar air heater with wavy fin absorbers. *Heat and Mass Transfer*, 55:2651–2666.

Qasim, M., Khan, Z., Lopez, R., and Khan, W. (2016). Heat and mass transfer in nanofluid thin film over an unsteady stretching sheet using buongiornoâ€™s model. *The European Physical Journal Plus*, 131:1–11.

Qureshi, M. A. (2022). Thermal capability and entropy optimization for prandtl-eyring hybrid nanofluid flow in solar aircraft implementation. *Alexandria Engineering Journal*, 61(7):5295–5307.

Rafique, K., Anwar, M. I., Misiran, M., Khan, I., Alharbi, S., Thounthong, P., and Nisar, K. (2019). Numerical solution of casson nanofluid flow over a non-linear inclined surface with soret and dufour effects by keller-box method. *Frontiers in Physics*, 7:139.

Rana, P., Srikantha, N., Muhammad, T., and Gupta, G. (2021). Computational study of three-dimensional flow and heat transfer of 25 nm cu–h2o nanoliquid with convective thermal condition and radiative heat flux using modified buongiorno model. *Case Studies in Thermal Engineering*, 27:101340.

Rasel, M. M. H., Reza-E-Rabbi, S., and Ahmmed, S. F. (2022). Heat and mass transfer simulation of mhd radiative convective flow of nanofluid through an inclined porous surface. *Khulna University Studies*, pages 610–624.

Rasheed, H. U., Islam, S., Helmi, M. M., Alsallami, S. A., Khan, Z., and Khan, I. (2021). An analytical study of internal heating and chemical reaction effects on mhd flow of nanofluid with convective conditions. *Crystals*, 11(12):1523. :https://doi.org/10.3390/cryst1112152.

Rasih, R. A., Sidik, N. A. C., and Samion, S. (2019). Recent progress on concentrating direct absorption solar collector using nanofluids. *Journal of Thermal Analysis and Calorimetry*, 137(3):903–922.

Rawat, S. K., Upreti, H., and Kumar, M. (2020). Comparative study of mixed convective mhd cu-water nanofluid flow over a cone and wedge using modified buongiornoâ€™s model in presence of thermal radiation and chemical reaction via cattaneo-christov double diffusion model. *Journal of Applied and Computational Mechanics*.

Reddy, P. S. and Sreedevi, P. (2020). Mhd boundary layer heat and mass transfer flow of nanofluid through porous media over inclined plate with chemical reaction. *Multidiscipline Modeling in Materials and Structures*.

Reddy, S. and Reddy, P. B. A. (2022). Thermal radiation effect on unsteady three-dimensional mhd flow of micropolar fluid over a horizontal surface of a parabola of revolution. *Propulsion and Power Research*, 11(1):129–142.

Reddy, Y. D., Mebarek-Oudina, F., Goud, B. S., and Ismail, A. (2022). Radiation, velocity and thermal slips effect toward mhd boundary layer flow through heat and mass transport of williamson nanofluid with porous medium. *Arabian Journal for Science and Engineering*, 47(12):16355–16369.

Rehman, A., Khan, W., Abdelrahman, A., Jan, R., Khan, M. S., and Galal, A. M. (2022a). Influence of marangoni convection, solar radiation, and viscous dissipation on the bioconvection couple stress flow of the hybrid nanofluid over a shrinking surface. *Frontiers in Materials*, 9:964543.

Rehman, M. I. U., Chen, H., Jamshed, W., Eid, M. R., Guedri, K., and El Din, S. M. (2022b). Thermal radiative flux and energy of arrhenius evaluation on stagnating point flowing of carreau nanofluid: a thermal case study. *Case Studies in Thermal Engineering*, 40:102583.

Sabiha, M., Saidur, R., Mekhilef, S., and Mahian, O. (2015). Progress and latest developments of evacuated tube solar collectors. *Renewable and Sustainable Energy Reviews*, 51:1038–1054.

Saeed, A., Algehyne, E. A., Aldhabani, M. S., Dawar, A., Kumam, P., and Kumam, W. (2022). Mixed convective flow of a magnetohydrodynamic casson fluid through a permeable stretching sheet with first-order chemical reaction. *Plos one*, 17(4):e0265238.

San, J., Worek, W., and Lavan, Z. (1987). Entropy generation in combined heat and mass transfer. *International journal of heat and mass transfer*, 30(7):1359–1369.

Sathe, T. M. and Dhoble, A. (2017). A review on recent advancements in photovoltaic thermal techniques. *Renewable and Sustainable Energy Reviews*, 76:645–672.

Sathyamurthy, R., Nagarajan, P., Kennady, H., Ravikumar, T., Paulson, V., and Ahsan, A. (2014). Enhancing the heat transfer of triangular pyramid solar still using phase change material as storage material. *Frontiers in Heat and Mass Transfer (FHMT)*, 5(1).

Schlichting, H. and Gersten, K. (2000). Fundamentals of boundary-layer theory. In *Boundary-Layer Theory*, pages 29–49. Springer.

Seethamahalakshmi, V., Babitha, Rao, T., and Reddy, G. (2023). Computational study of mhd nanofluid flow with effects of variable viscosity and non-uniform heat generation. *International Journal of Applied and Computational Mathematics*, 9(6):124.

Sehra, Haq, S. U., Shah, S. I. A., Nisar, K. S., Jan, S. U., and Khan, I. (2021). Convection heat mass transfer and mhd flow over a vertical plate with chemical reaction, arbitrary shear stress and exponential heating. *Scientific Reports*, 11(1):4265.

Seth, G. S. and Mandal, P. K. (2018). Hydromagnetic rotating flow of casson fluid in darcy-forchheimer porous medium. In *MATEC Web of Conferences*, volume 192, page 02059. EDP Sciences.

Shafiq, A., Çolak, A. B., and Sindhu, T. N. (2023). Modeling of soret and dufourâ€™s convective heat transfer in nanofluid flow through a moving needle with artificial neural network. *Arabian Journal for Science and Engineering*, 48(3):2807–2820.

Shahzad, F., Jamshed, W., Eid, M. R., Safdar, R., Putri Mohamed Isa, S. S., El Din, S. M., Mohd Nasir, N. A. A., and Iqbal, A. (2022a). Thermal cooling efficacy of a solar water pump using oldroyd-b (aluminum alloy-titanium alloy/engine oil) hybrid nanofluid by applying new version for the model of buongiorno. *Scientific Reports*, 12(1):19817.

Shahzad, F., Jamshed, W., Safdar, R., Hussain, S. M., Nasir, N. A. A. M., Dhange, M., Nisar, K. S., Eid, M. R., Sohail, M., Alsehli, M., et al. (2022b). Thermal analysis characterisation of solar-powered ship using oldroyd hybrid nanofluids in parabolic trough solar collector: An optimal thermal application. *Nanotechnology Reviews*, 11(1):2015–2037.

Shampine, L. F. and Muir, P. H. (2004). Estimating conditioning of bvps for odes. *Mathematical and Computer Modelling*, 40(11-12):1309–1321.

Sharma, B. K., Kumar, A., Gandhi, R., Bhatti, M. M., and Mishra, N. K. (2023). Entropy generation and thermal radiation analysis of emhd jeffrey nanofluid flow: Applications in solar energy. *Nanomaterials*, 13(3):544.

Shehzad, S., Hayat, T., Alsaedi, A., and Chen, B. (2016). A useful model for solar radiation. *Energy, Ecology and Environment*, 1:30–38.

Sheremet, M. A. (2021). Applications of nanofluids.

Siavashi, M., Bozorg, M. V., and Toosi, M. H. (2021). A numerical analysis of the effects of nanofluid and porous media utilization on the performance of parabolic trough solar collectors. *Sustainable Energy Technologies and Assessments*, 45:101179.

Smit, S. and Kessels, W. (2015). Variational method for the minimization of entropy generation in solar cells. *Journal of Applied Physics*, 117(13):134504.

Souza, R. R., Gonçalves, I. M., Rodrigues, R. O., Minas, G., Miranda, J., Moreira, A. L., Lima, R., Coutinho, G., Pereira, J., and Moita, A. S. (2022). Recent advances on the thermal properties and applications of nanofluids: From nanomedicine to renewable energies. *Applied Thermal Engineering*, 201:117725.

Sreedevi, P., Sudarsana Reddy, P., and Chamkha, A. (2020). Heat and mass transfer analysis of unsteady hybrid nanofluid flow over a stretching sheet with thermal radiation. *SN Applied Sciences*, 2(7):1222.

Statistics, E. (2016). Ministry of statistics and programme implementation government of india.

Subramani, J., Nagarajan, P., Mahian, O., and Sathyamurthy, R. (2018). Efficiency and heat transfer improvements in a parabolic trough solar collector using tio2 nanofluids under turbulent flow regime. *Renewable energy*, 119:19–31.

Swain, B., Parida, B., Kar, S., and Senapati, N. (2020). Viscous dissipation and joule heating effect on mhd flow and heat transfer past a stretching sheet embedded in a porous medium. *Heliyon*, 6(10):e05338.

Szulejko, J. E., Kumar, P., Deep, A., and Kim, K.-H. (2017). Global warming projections to 2100 using simple co2 greenhouse gas modeling and comments on co2 climate sensitivity factor. *Atmospheric Pollution Research*, 8(1):136–140.

Tabarhoseini, S. M. and Sheikholeslami, M. (2022). Entropy generation and thermal analysis of nanofluid flow inside the evacuated tube solar collector. *Scientific Reports*, 12(1):1–16.

Takhanov, D. (2011). Forchheimer model for non-darcy flow in porous media and fractures.

Tiwari, G. N. and Mishra, R. K. (2012). *Advanced renewable energy sources.* Royal Society of Chemistry.

Tiwari, R. K. and Das, M. K. (2007). Heat transfer augmentation in a two-sided lid-driven differentially heated square cavity utilizing nanofluids. *International Journal of heat and Mass transfer*, 50(9-10):2002–2018.

Twidell, J. (2021). *Renewable energy resources.* Routledge.

Tyagi, S., Wang, S., Singhal, M., Kaushik, S., and Park, S. (2007). Exergy analysis and parametric study of concentrating type solar collectors. *International journal of thermal sciences*, 46(12):1304–1310.

Ullah, I., Khan, I., and Shafie, S. (2017). Soret and dufour effects on unsteady mixed convection slip flow of casson fluid over a nonlinearly stretching sheet with convective boundary condition. *Scientific Reports*, 7(1):1–19.

Ullah, Z., Abbas, A., El-Zahar, E. R., Seddek, L. F., Akgul, A., and Hassan, A. M. (2023). Significance of thermal density and viscous dissipation on heat and mass transfer of chemically reactive nanofluid flow along stretching sheet under magnetic field. *Results in Engineering*, 20:101413.

ur Rahman, M., Haq, F., Khan, M. I., and Nawaz, M. S. (2022). Irreversibility analysis in viscous nanomaterial flow with darcy–forchheimer and activation energy. *International Journal of Applied and Computational Mathematics*, 8(6):270.

Van Gorder, R. A. (2014). Chapter 4: Stability of auxiliary linear operator and convergence-control parameter in the homotopy analysis method. In *Advances in the Homotopy Analysis Method*, pages 123–180. World Scientific.

Veress, Á. and Rohács, J. (2012). Application of finite volume method in fluid dynamics and inverse design based optimization. *Finite Volume Method: Powerful Means of Engineering Design*, 1.

Verma, A. K., Rajput, S., Bhattacharyya, K., and Chamkha, A. J. (2022). Nanoparticle's radius effect on unsteady mixed convective copper-water nanofluid flow over an expanding sheet in porous medium with boundary slip. *Chemical Engineering Journal Advances*, 12:100366.

Wang, F., Waqas, M., Khan, W., Makhdoum, B. M., and Eldin, S. M. (2023). Cattaneo–christov heat-mass transfer rheology in third-grade nanoliquid flow confined by stretchable surface subjected to mixed convection. *Computational Particle Mechanics*, pages 1–13.

Welty, J., Rorrer, G. L., and Foster, D. G. (2014). *Fundamentals of momentum, heat, and mass transfer*. John Wiley & Sons.

Yirga, Y. and Shankar, B. (2015). Mhd flow and heat transfer of nanofluids through a porous media due to a stretching sheet with viscous dissipation and chemical reaction effects. *International Journal for Computational Methods in Engineering Science and Mechanics*, 16(5):275–284.

Yirga, Y. and Tesfay, D. (2015). Heat and mass transfer in mhd flow of nanofluids through a porous media due to a permeable stretching sheet with viscous dissipation and chemical reaction effects. *International Journal of Mechanical, Aerospace, Industrial, Mechatronic and Manufacturing Engineering*, 9(5):1–8.

Yousefi, T., Veysi, F., Shojaeizadeh, E., and Zinadini, S. (2012). An experimental investigation on the effect of al2o3–h2o nanofluid on the efficiency of flat-plate solar collectors. *Renewable Energy*, 39(1):293–298.

Zaib, A., Bhattacharyya, K., and Shafie, S. (2015). Unsteady boundary layer flow and heat transfer over an exponentially shrinking sheet with suction in a copper-water nanofluid. *Journal of Central South University*, 22:4856–4863.

Zaib, A., Bhattacharyya, K., Uddin, M. S., Shafie, S., et al. (2016). Dual solutions of non-newtonian casson fluid flow and heat transfer over an exponentially permeable shrinking sheet with viscous dissipation. *Modelling and simulation in engineering*, 2016.

Zeeshan, A., Majeed, A., Akram, M. J., and Alzahrani, F. (2021). Numerical investigation of mhd radiative heat and mass transfer of nanofluid flow towards a vertical wavy surface with viscous dissipation and joule heating effects using keller-box method. *Mathematics and Computers in Simulation*, 190:1080–1109.

Zhang, X. and Liang, S. (2015). Adomian decomposition method is a special case of lyapunov's artificial small parameter method. *Applied Mathematics Letters*, 48:177–179.

Zhao, Y. and Liao, S. (2014). Chapter 9: Ham-based mathematica package bvph 2.0 for nonlinear boundary value problems. In *Advances in the homotopy analysis method*, pages 361–417. World Scientific.

APPENDICES

In this appendix, essential definitions, theorems and code of solver are included.

A.1 Basic Preliminary Definitions and Theorems

The basic Mathematical facts, theorems and physical definitions which have a key role to understand this dissertation are stated as follows.

Definition 3. The term ”solar radiation” refers to the electromagnetic radiation that the Sun emits. A variety of devices can be used to catch solar radiation and transform it into useful forms of energy, such as heat and electricity.

Definition 4. Viscous dissipation is breaking or spreading the internal resistance of a fluid to motion. It is loss of energy due to the friction caused by the shear viscosity.

Definition 5. Shear force is a force exerted on the fluid element by its surroundings through direct contact which is not in normal direction.

Definition 6. Heat flux (W/m^2) is the rate of thermal energy flow per unit surface area of heat transfer surface.

Definition 7. The volumetric heat capacity of a material is the heat capacity of a sample of the substance divided by the volume of the sample.

Definition 8. Skin friction, or skin friction drag, is the resistance to the laminar flow of an object moving through a fluid. It’s the result of the viscosity of the fluid through which it passes. The skin friction coefficient specifies the fraction of the local dynamic pressure, that is felt as shear stress on the surface.

Definition 9. Nusselt number (Nu_L) is a measure of the ratio of the magnitude of the convective heat transfer rate to the magnitude of the conductive heat transfer rate which expressed as

$$Nu_L = \frac{\text{Convective heat transfer rate}}{\text{Conductive heat transfer}} = \frac{hL}{k},$$

where h is the convective heat transfer coefficient, L is the characteristic length and k is the thermal conductivity of the fluid.

It is the dimensionless temperature gradient at the surface, and it provides a measure of the convection heat transfer occurring at the surface.

Definition 10. The Sherwood number (Sh_L) (mass transfer rate) is a dimensionless constant used in mass-transfer operation. It represents the ratio of convective mass transfer to the rate of diffusive mass transport, and defined as follows

$$Sh_L = \frac{\text{Convective mass transfer rate}}{\text{Diffusive mass transfer rate}} = \frac{h_m}{D/L} = \frac{h_m L}{D}, \tag{8.5.1}$$

where D is mass diffusivity (m^2s^{-1}) and h_m is convective mass transfer coefficient (ms^{-1}).

Definition 11. Mangnetohydrodynamic (MHD): is the study of the interaction between magnetic fields, moving and conducting fluids. It deals the magnetic properties of electrically conducting fluids. Joule heating is the conversion of electrical energy into heat energy by the resistance in a circuit.

Definition 12. Laminar flow, is a type of fluid (gas or liquid) flow in which the fluid travels smoothly or in regular paths. Turbulent flow is occurred when the fluid undergoes irregular fluctuations and mixing.

Definition 13. A fluid is said to be compressible if its density changes with pressure. But, if there is insignificant change in density with pressure, it is called incompressible.

Definition 14. A fluid is said to be viscous when both the normal stress (pressure) and the shearing stress exist but it is said to be inviscid fluid when only the normal stress (pressure) acts between the adjoining layers.

Definition 15. Newtonian fluid is a fluid where the shear stress is linearly related to the rate of strain or velocity gradient (rate of deformation). Here the dynamic viscosity (μ) is a constant of proportionality. Thus, fluids that obey this law is called Newton's law of viscosity, and they are referred as Newtonian fluids. The fluids that do not obey this law are called non Newtonian fluids.

Definition 16. If the fluids properties at every point in the flow depend upon time then they are called unsteady flow otherwise, they are known as steady flow.

Definition 17. Similarity transformation is a transformation by which (n) -independent variables in PDEs changed into ($n-1$) independent variables. For instance in this dissertation work nonlinear PDEs with two independent variables will be converted into PDEs with one independent variable called ODEs.

Definition 18. A porous medium can be defined as a solid, or collection of solid bodies, having an open space in or around the solids to enable a fluid to pass through or around them. Permeability is the surface ability to permit the flow of fluid via its interconnected void space.

Definition 19. Brownian motion is a random motion of particles as a result of collision with surrounding. Where as thermophoresis is a force generated by temperature difference that affecting the particles movement.

Definition 20. Specific heat can be defined as the amount of energy required for a unit mass of a fluid for unit rise in temperature. For a given gas, there are two kinds of specific heat corresponding to the extreme conditions of constant volume (c_v) and constant pressure (c_p).

Definition 21. Energy can be defined as the ability to do work. There are many different forms of energy. For example, heat, light, electrical, chemical, gravitational can be considered as energy forms.

Definition 22. Isotropic refers to the characters of a substance which is independent of the direction. Anisotropic is the opposite of isotropic in which the properties of a material depend on direction.

Definition 23. Thermodynamics in physics is a branch that deals with heat, work and temperature, and their relation to energy, radiation and physical properties of matter.

First law of thermodynamics, also known as the law of conservation of energy. Whereas, the second law of thermodynamics states that the total entropy of a system either increases or remains constant in any spontaneous process.

A.1.1 Reynolds's Transport Theorem(RTT)

Let V be an arbitrary volume with boundary surface S, which moves at the velocity $\mathbf{v}$. The exterior normal to the boundary is denoted by n. Then

$$\frac{d}{dt}\int_{V(t)} \boldsymbol{R}(x,t)dV = \int_{V(t)} \frac{\partial \boldsymbol{R}(x,t)}{\partial t}dV + \int_{S(t)} \boldsymbol{R}(x,t)\mathbf{v}\cdot ndS.,$$

where $\boldsymbol{R}(x,t)$ is any quantity to be conserved. It may be fluid element.

An important concept in the process of developing governing equations is the idea of **continuum hypothesis**. It says that instead of a discontinuous molecular medium, a fluid can be better defined as an aggregate or macroscopic continuum, or that a fluid is at the macroscopic scale of the flow in continuum mechanics. Because of this, fluid properties like mass, density, volume, viscosity, pressure, body and surface forces, linear or angular momentum, and so on are considered to have continuum properties and are therefore seen to be (piece-wise) continuous functions in space and time. In the flow-governing equations, the continuum hypothesis leads to applying the RTT.

A.1.2 Gauss's Divergence Theorem

Let T be a closed bounded region in space whose boundary is a piece wise smooth orient-able surface S. Let $F(x,y,z)$ be a vector function that is continuous and has continuous first partial derivatives in some domain containing T, then

$$\iiint_T div(\vec{\mathbf{F}})dV = \iiint_T \nabla\cdot\vec{\mathbf{F}}dV = \iint_S \vec{\mathbf{F}}\cdot\mathbf{n}dS. \tag{8.5.2}$$

The divergence of $\vec{\mathbf{F}}$ $(\nabla\cdot\vec{\mathbf{F}})$ is defined in component form as follows:

$$\nabla\cdot\vec{\mathbf{F}} = \frac{\partial F_1}{\partial x} + \frac{\partial F_2}{\partial y} + \frac{\partial F_3}{\partial z}, \quad \text{where } \nabla = (\frac{\partial}{\partial x},\frac{\partial}{\partial y},\frac{\partial}{\partial z}) \text{ and } \vec{\mathbf{F}} = (F_1,F_2,F_3). \tag{8.5.3}$$

Appendix B

B.1 BVPh2.0 Codes for Problems from Chapter 4 to 7

This code solves basically velocity, temperature and concentration of unsteady flowing nanofluid on the Mathematica 12.1 software. The code for problems in chapter FOUR can be expressed in the following manner in general.

```
(* Filename: ConcePro1.m     *)
Print["The input file ",$InputFileName," is loaded !"];
(* Modify  control parameters in BVPh if necessary *)
ErrReq=10^-30;
(*           Define the governing equation           *)
TypeEQ = 1;
NumEQ = 3;
f[1,z_,{f_,g_,s_},sigma_] := D[f,{z,3}]+f*D[f,{z,2}]-(D[f,z])^2
-A*(D[f,z]+0.5*z*D[f,{z,2}])-Ma*D[f,z];
f[2,z_,{f_,g_,s_},sigma_] := ((1+Rn)/Pr)*D[g,{z,2}]-A*(g+0.5*z*D[g,z])
+f*D[g,z]-D[f,z]*g+Nb*D[g,z]*D[s,z]+Nt*(D[g,z])^2+Ec*(D[f,{z,2}])^2;
f[3,z_,{f_,g_,s_},sigma_] := Nb*(D[s,{z,2}]-Sc*A*(s+0.5*z*D[s,z])
+Sc*(f*D[s,z]-D[f,z]*s))+Nt*D[g,{z,2}];
(*            Define boundary conditions             *)
NumBC = 7;
BC[1,z_,{f_,g_,s_}] :=f/.z-> 0;
BC[2,z_,{f_,g_,s_}] :=(D[f,z]-1)/.z-> 0;
BC[3,z_,{f_,g_,s_}] :=(D[g,z]+\Upsilon*(1-g))/.z-> 0;
BC[4,z_,{f_,g_,s_}] :=(s-1)/.z-> 0;
BC[5,z_,{f_,g_,s_}] :=D[f,z]/.z-> infinity;
BC[6,z_,{f_,g_,s_}] :=g/.z-> infinity;
BC[7,z_,{f_,g_,s_}] :=s/.z-> infinity;
(*   Defined intial and end points  *)
zL[1] = 0;
zR[1] = infinity;
zL[2] = 0;
zR[2] = infinity;
zL[3] = 0;
zR[3] = infinity;
zRintegral[1] = 10;
zRintegral[2] = 10;
zRintegral[3] = 10;
(*      Defines the auxiliary linear operator      *)
L[1, u_] := D[u,{z, 3}]-D[u,z];
```

```
L[2, u_] := D[u,{z, 2}]-u;
L[3, u_] := D[u,{z, 2}]-u;
H[1,z]=H[2,z]= H[3,z]=1;
(*    Assumed values of the parameters   *)
Ma=0.5; Sc=0.7;Pr=0.72;  A=Nb=Nt=0.3; \Upsilon=Ec=0.1;
c0[1]=-0.866927905681793;c0[2]=-0.72660679068499;
c0[3]=-4.315261695854243;
(*      Defines the initial guess     *)
U[1,0]= 1-Exp[-z];
U[2,0]=\Upsilon*Exp[-z]/(1+\Upsilon);
U[3,0]=Exp[-z];
(*                Print input data                  *)
PrintInput[{f[z], g[z], s[z]}];
(*    Get optimal convergence-control parameters    *)
(*c0[1]=c0[2]=c0[3]=h;
GetOptiVar[5, {}, {c0[1], c0[2], c0[3]}];*)
BVPh[1, 10];
```

The procedure and codes of BVPh2.0 for the problems in chapters FIVE, SIX and SEVEN are similar as stated below except the difference in function and values of constants.

```
(*           Filename: Concepro2.m                    *)
Print["The input file ",$InputFileName," is loaded !"];
(* Modify   control parameters in BVPh if necessary *)
ErrReq=10^-30;
(*           Define the governing equation           *)
TypeEQ = 1;
NumEQ = 3;
f[1,z_,{f_,g_,s_},sigma_] := D[f,{z,3}]+f*D[f,{z,2}]-(D[f,z])^2
-A*(D[f,z]+0.5*z*D[f,{z,2}])-(Ma+ka)*D[f,z];
f[2,z_,{f_,g_,s_},sigma_] := ((1+Rn)/Pr)*D[g,{z,2}]-A*(g+0.5*z*D[g,z])+q*g
+f*D[g,z]-D[f,z]*g+Nb*D[g,z]*D[s,z]+Nt*(D[g,z])^2+Ec*(D[f,{z,2}])^2;
f[3,z_,{f_,g_,s_},sigma_] := D[s,{z,2}]-Sc*A*(s+0.5*z*D[s,z])
+Sc*(f*D[s,z]-D[f,z]*s)+Nt*D[g,{z,2}]/Nb;
(*            Define boundary conditions       *)
NumBC = 7;
BC[1,z_,{f_,g_,s_}] :=(f-S)/.z-> 0;
BC[2,z_,{f_,g_,s_}] :=(D[f,z]-1-\varpi*D[f,{z,2}])/.z-> 0;
```

```
BC[3,z_,{f_,g_,s_}] :=(D[g,z]+\Upsilon*(1-g))/.z-> 0;
BC[4,z_,{f_,g_,s_}] :=(s-1)/.z-> 0;
BC[5,z_,{f_,g_,s_}] :=D[f,z]/.z-> infinity;
BC[6,z_,{f_,g_,s_}] :=g/.z-> infinity;
BC[7,z_,{f_,g_,s_}] :=s/.z-> infinity;
(*    Defined the initial and end point   *)
zL[1] = 0;
zR[1] = infinity;
zL[2] = 0;
zR[2] = infinity;
zL[3] = 0;
zR[3] = infinity;
zRintegral[1] = 10;
zRintegral[2] = 10;
zRintegral[3] = 10;
(*      Defines the auxiliary linear operator      *)
L[1, u_] := D[u,{z, 3}]-D[u,z];
L[2, u_] := D[u,{z, 2}]-u;
L[3, u_] := D[u,{z, 2}]-u;
H[1,z]=H[2,z]= H[3,z]=1;
(*    Assumed values of the parameters    *)
$Ma=0.5, Sc=0.7, Nt=Nb=1, S=ka=Rn=A=0.3, Pr=1.2, q=\varpi =Ec=\Upsilon = 0.1$
c0[1] =-0.7120631,c0[2] =-1.0616537 and c0[3] = -1.551661; (depend on the
 problem)
(*      Defines the initial guess    *)
U[1,0]= (1-Exp[-z])/(1+\varpi)+S;
U[2,0]= $\Upsilon$*Exp[-z]/(1+\Upsilon);
U[3,0]=Exp[-z];
(*                Print input data                  *)
PrintInput[{f[z], g[z], s[z]}];
(*    Get optimal convergence-control parameters    *)
(*c0[1]=c0[2]=c0[3]=h;
GetOptiVar[5, {}, {c0[1],c0[2],c0[3]}];*)
BVPh[1, 10];
```

B.2 MATLAB Codes for Problem in Chapter EIGHT

```
clc; close all;
a =0;b=16; theta=pi/12;Bi=0.1;So=0.1;s=0.3; Ma=0.2;
Pr= 0.72;ph=0.2;gamm=1; Gt=0.3;ka=0.3;Da=3;A=0.3;
```

```
x=a:0.05:b;
%  = vector that specifies an initial mesh.
%xinit=[0 0 0 0 0];
yinit=[0 0 0 0 0]; % Guess vector for the solution
init = bvpinit(x,yinit);% forms the initial guess for the bvp solver.
options = bvpset('Stats','on','RelTol',1e-7,'abstol',1e-6);
for Ec= [0.1 0.3 0.5 0.7]
f = @(x,y) [y(2)
y(3)
-(1-ph)^(2.5)*(1+7.96*ph)*(y(1)*y(3)-(1+(1/Da))*y(2)^2-A*(y(2)+0.5*x*y(3)))
+(Ma*((1-ph)^(2.5)*(1+2*ph)/(1-ph))+ka)*y(2)
-(1-ph)^(2.5)*(1-0.287*ph)*Gt*y(4)*cos(theta)
y(5)
-(Pr*(1-0.175*ph)*(401.226-399.38*ph)/(401.226+798.77*ph))*(y(1)*y(5))
-((401.226-399.38*ph)*Pr*Ec*y(3)^2)/((1-ph)^(2.5)*(401.226+798.77*ph))
-Pr*(401.226-399.38*ph)*So*exp(-gamm*x)/(401.226+798.77*ph)
-Pr*(y(4)*y(2)-A*(y(4)+0.5*x*y(5)))] ;
bc=@(ya,yb)[ ya(1)-s; ya(2)-1; ya(5)+Bi*(1-ya(4)); yb(2); yb(4)];
S=bvp4c(f,bc,init,options);
y = deval(S,x);% Evaluation of y at x (specified number of points by x)
fprintf('Reference values:y3(0)=-0.9663,y5(0)=-1\n')
fprintf(' Computed values:y3(0)=%6 .4f,y5(0)=%6 .4f \n',y(3,1),y(5,1))
disp('x         y1           y2            y3          y4        y5')
[x' y']
plot(x,y(4,:),'linewidth',1.5);
%plot(x,y(2,:),'linewidth',1.5);
hold on
end
% grid minor
legend('Ec=0.1','Ec=0.3','Ec=0.5','Ec=0.7');
axis tight; xlabel('\epsilon'); ylabel('H (\epsilon)');
%axis tight; xlabel('\epsilon'); ylabel('V^\prime(\epsilon)');
```